Wind Farm Effects on the Atmosphere

A meso-scale numerical modeling of the offshore boundary layer through parameterized turbine rotors

Master of Science Thesis

A.M. Striedinger P.



Wind Farm Effects on the Atmosphere

A meso-scale and numerical modeling of the offshore boundary layer through parameterized turbine rotors

MASTER OF SCIENCE THESIS

For the degree of Master of Science in Sustainable Energy Technology at Eindhoven University of Technology

A.M. Striedinger P.

24-5-2014

Department of Mechanical Engineering: Eindhoven University of Technology

Department of Wind Energy: Delft University of Technology

Wind Farm Effects on the Atmosphere A meso-scale numerical modeling of the offshore boundary layer through parameterized turbine rotors

© Copyright 2014 by Alberto Mario Striedinger Pinilla All rights reserved

Supervised by:

Dr ir H. Hartmann

Meteorological Research and Development department MeteoGroup Agro Business Park 99 6708 PV Wageningen The Netherlands

Prof. dr. G.J.W. van Bussel Dr. ir. W.A.A.M Bierbooms

Wind Energy Research Group Delft University of Technology Kluyverweg 1 2629 HS Delft The Netherlands



A.M. Striedinger P. Master of Science Thesis

"Be like water making its way through cracks. Do not be assertive, but adjust to the object, and you shall find a way around or through it. If nothing within you stays rigid, outward things will disclose themselves
Empty your mind, be formless, shapeless, like water. If you put water into a cup, it becomes the cup. You put water into a bottle and it becomes the bottle. You put it in a teapot, it becomes the teapot. Now, water can flow or it can crash. Be water, my friend"
-Bruce Lee 李小龍
If you ask me, this is what I want
With Most Love To My Parents Magally and Rafael , and my brother José

Acknowledgements

I would like to express my deepest gratitude to the Meteorological Research and Development department of MeteoGroup for taking me in for this project. My appreciation goes to Hugo Hartmann for being my supervisor at MeteoGroup and allowed me to work next to him, his assistance, patience, and incisive suggestions were key in accomplishing my thesis work. He is someone with a pedagogical instinct I would say; I enjoyed all discussions.

My thanks are extended to Clare Allen for her instructions on how to use the simulation software of WRF, and the guidance and remarks that come with being a first learner. Bas Vonk, for the access to the cluster and all issues associated with its use. Dirk Malda, for the discussions about the different wind farms that could have been analysed, and his insights.

Thanks to Gerald van der Grijn, for providing his contacts to acquire the wind farm and turbine data used for my validation study. It was finally through the Virtual Wakes Lab of Prof. R.J Barthelmie from the University of Indiana, that I was able to use measurements from the Middelgrunden Offshore wind farm. Measurements and more information are provided by Middelgrundens Vindmøllelaug through the Virtual Wakes Lab; I encourage other students to use it.

My grateful thanks to Robert Mureau, for his supervision during my last stage at the company, his meetings, feedbacks and recommendations on the meteorological aspects of interest. Thanks to Daniël van Dijke, for his suggestions on how to understand the code structure of WRF, and the data storage during the last stage of my work at the company. I also thank Prof. Wim van den berg for his group meetings and briefings on weather topics. If I happen not to mention more people from MeteoGorup is not out of disrespect, I was very welcomed at the company and I appreciate the friendliness of everybody, during conversations and outdoor activities.

I would also like to thank my academic supervisor Mr Bierbooms very much for his patience, rigorous feedback, and assistance on improving the writing of my thesis.

Last but not least, is my special and devoted gratitude to my beloved parents and my brother for their encouragements on the pursuit of my goals throughout this whole journey that has been my master studies. Here I say, that the present work is dedicated to them.

In this study, the offshore wind farm effects of Thanet (300 MW) in the U.K, and of Middelgrunden (40 MW) in Denmark were analyzed in a meso-scale numerical prediction model, whilst working at MeteoGroup. For the final analysis of Middelgrunden, the model is validated with measurement data from Middelgrundens Vindmøllelaug. The model uses parameterizations for the atmospheric flow, surface physics effects, and a turbine scheme based on a Drag disc concept. The scheme uses turbine data in relation to changes in the turbulent kinetic energy of the flow as it passes through the rotors.

The free stream is affected by the farm through local reductions of turbulence intensity aligned in front and in-between turbine rows, and the regions affected are as high as the turbine themselves. Wind speed near the surface is found to increase inside the wind farm (a phenomena often times unexpected), transporting turbulence downstream by advection. The simulations indicate that the added turbulence form turbine rotors promotes strong vertical transport of turbulent kinetic energy up in the atmosphere, and directly above the wind farms. Further, horizontal momentum exchanges is proven to be negligible behind turbine rotors in the downstream of the farm due to the lack of proper turbulent advection.

Local meteorology is affected as the air suddenly expands above the farm, increasing the height of the planetary boundary layer as a consequence. The expansion creates a vertical temperature gradient, separating cooler air masses above the rotor area, from similarly hotter air masses near the surface. The gradients obtained varied from -0.2° C to $+1^{\circ}$ C. Surface to air heat fluxes are lessen inside turbine arrays, whilst increased downstream in the farm wake. Additionally, the Local flow patterns are found to be crucial in determining the shape and a sense of direction of the wake downstream.

Finally, the meso-scale model with turbine scheme is found to mimic the interaction between the turbines and the atmosphere, to some extent due to uncertainties in the horizontal gradient of turbulence intensity. Further improvement is needed to produce a precise power forecast, which also depends on the model input data, such that a focus of attention is the correct prediction of wind direction. Further, the accurate representation of the turbine layout and number of turbines per grid location are essential to detail the turbulence inside the farm, but not for analyzing meso-scale effects. Winds speed and power ratio profiles were found in agreement with measurements.

A.M. Striedinger P. Master of Science Thesis

Contents

Conten	ts	V
List of F	igures	vii
Chapter	r-1 . Introduction	14
1.1.	Outline	17
Chapter	r-2. Concepts on Atmospheric Flow and Wind Energy	19
2.1.	Wind and The Offshore Environment	20
2.1	1.1. Atmospheric variables in the offshore relevant to wind farms	23
2.1	1.2. Long time scale wind speed changes	27
2.2.	Wind Turbine Basics	29
2.2	2.1. Model corrections to wind turbine analysis	31
2.2	2.2. Basics of turbine wake development, and wake boundaries	33
2.2	2.3. Wind turbine wakes inside turbine arrays	37
2.3.	Available Software for Wind Turbine and Wind Farm Simulation	39
2.4.	Numerical Weather Prediction	40
2.5.	Fitch Turbine Parameterization Scheme	42
Chapter	r-3 . Wind Farm Modeling with WRF	47
3.1.	Introduction to WRF	47
3.1	I.1. Computational grid in WRF	48
3.1	1.2. Atmospheric pressure levels and map scale factors	49
3.1	1.3. Input data and domain interaction	51
3.1	1.4. Numerical stability	52
3.2.	PBL and Physic Models in WRF	53
3.3.	Current Turbine Parameterization Scheme	54
Chapter	·	
4.1.	Site Description and Simulation Setup	60
4.2.	Flow Characteristics in the Background Wind	64
4.3.	Wind Speed and Turbulent Kinetic Energy Results	67
4.3	3.1. Wind speed results	67
4.3	3.2. Turbulent kinetic energy results	75
4.4.	Changes in local meteorology	82
4.5.	Turbine layout considerations and model physics on high resolution domains	87
4.6.	Computational time and file size in WRF simulations	90
Chapter	r-5. Validation Study Of Middelgrunden Offshore Wind Farm Reanalysis	92
5.1.	Site Description and Simulation Setup	93
5.2.	Data description and Method	95
5.3.	Analysis of the Free Stream Wind Speed	96
5.4.	Analysis of the Free Stream Turbulence Intensity	100
5.5	Analysis of Power Forecast and Performance	103

5.5.1.	Efficiency of the Turbine Scheme	109
5.5.2.	Wind speed deficit in the wake	112
5.5.3.	Increments and deficits of turbulence intensity and turbulent kinetic energy	113
Chapter-6.	Conclusions And Recommendations	115
6.1. Con	clusions	115
6.2. Reco	ommendations	116
Appendix-A.	Wind and The Environment	118
Appendix-B.	The Thanet Offshore Wind Farm	122
Appendix-C.	Information on Middelgrunden	144
Appendix-D.	Optional Turbine Scheme	165
Bibliography		186
List of Symbol	S	190

List of Figures

Figure 1: Levels in the Earth's Atmosphere [29]	20
Figure 2: Vertical structure of the Offshore PBL (left) ,height can be much higher [28], Geostrophic Wind (right) [1]	20
Figure 3: Schematic of Lapse rate (a): solid lines before sunrise, dashed lines (after) [1]. PBL components (b) [27]	22
Figure 4: Example of wind speed profiles of different atmospheric stability categories, adapted from [27]	
Figure 5: Turbulence Intensity (left) and Isotropic Turbulent kinetic energy (right) derived from wind turbine classes acco	
Equation 8. Reference turbulence intensities I_{ref} of 0.16, 0.14, 0.12 for Classes A, B, and C	_
Figure 6: Example of High and Low pressure center distributions in Europe; taken from KMNI. Blue lines represent cold f	
red lines represent warm fronts, and purple lines represent the combination of both fronts. Triangles the direction	
cold air to warm air, and the and semi-circles from warm air to cool air	
Figure 7: Effects of Pressure gradient on PBL height, low pressure center (left), and high pressure center (right), adapted	
[27]	
Figure 8: Histogram and Weibull Fit on Wind Speed probability distribution.	
Figure 9: Radial wind speed percentile distribution on Midelgrundden Offshore wind farm in Denmark for the first 15 da	
April 2001 (Wind Rose).	
Figure 10: Actuator Disc scheme [40]	
Figure 11: Performance Curves of 3MW Vestas V-112., 1.2 kg/m ³ air density: ideal and real thrust coefficients from Equa	
in relation to turbine power; adapted from [41].	
Figure 12: Blade Element Section. Incoming flow is represented by the local wind speed V_o , in a perpendicular direction	
rotor area	
Figure 13: Modified Tip/Hub loss factor for Vestas V-90 blade at constant 15 $^{\circ}$ inflow angle (ϕ)	
Figure 14: Effects of heavily loaded rotors for a correction factor F=0.75 due to tip effects only.	
Figure 15: Rotor schematics for Yaw mismatch and azimuth	
Figure 16: Jensen's wake model. Wake boundaries are defined by the red lines, and slope k for turbines wt1 and wt2	
Figure 17: Turbulent velocity ratios to free stream (a) [49]. Downstream wind speed deficit speed profiles from a turbine	
[26][26]	
Figure 18: Wind speed profile behind a small scale WT in a row. The experimental set up uses a rotor diameter D of 12 c	
hub height of 1 D [53]. The green arrows point to a sudden change in wind speed	
Figure 19: Sketch of rotor disc stream tube in wind tunnel with an open cross section [51]. The grey arrows indicate air	
recirculation near the wind tunnel walls.	36
Figure 20: Examples of vorticity for different flow cases (vorticity points). Flows shown in (a), absolute velocities at a sele	
section are shown in (b), and relative velocities to the center point are shown in (c). Lines in (a) show the flow patl	
fluid particles on it. The images are extracted from the web. Negative vorticity is anti-clockwise	
Figure 21: Smoke visualization photo showing tip vortices downstream a rotor. Flow orthogonal to rotor plane. Tip ratio	
and blade pitch angle of 2° , vorticity $\neq 0$; Adapted from [54]. Arrows indicate wind speed, in the inflow, in the wak	
outside the wake.	
Figure 22: Wake interferences inside turbine arrays. Single Wake Interference (SWI), Parallel SWI, Parallel Wake Interfer	
(PWI), and PWI on turbine array staggered configuration. Wake boundaries are drawn as red, and have been linear	
Figure 23: Parallel SWI as simulated with LES on Lillgrund offshore wind farm. Time averaged wind speed contour is norr	
to hub height wind speed in (a). Turbulent kinetic energy contour is normalized to hub height wind speed squared	
[56]	
Figure 24: Grid representation of terrain and height levels zk in Cartesian coordinates. Each plane represents a grid area	
certain height. Grid cells are contained between planes.	
Figure 25: Schematic depiction of a WT and a typical vertical grid configuration; taken from [11]	
Figure 26: Vertical wind speed profiles differences with the Fitch scheme on the Thanet offshore wind farm, v-wind is the positional wind (in the horizontal plane). The control mode for which all energy change is considered (CTR), black	
meridional wind (in the horizontal plane). The control mode for which all energy change is considered (CTRL, black	
momentum sink only (SINK, blue lines), TKE source only (TKE, red lines). The solid lines denote profiles over farm;	
lines indicate profiles 10 km downstream, and the horizontal dashed lines show the rotor area [12]	45

Figure 27: Horizontal wind speed contour e around the farm (a), horizontal wind speed profile at the farm location and in the wake (b), resultant turbulent kinetic energy contour around the farm (c), and resultant turbulent kinetic energy profile (d) from Fitch simulations on Thanet offshore wind farm in the UK (FARM- BACKGROUND) [12]46
Figure 28: WRF program structure: WPS on top, WRF model on bottom
Figure 29: Horizontal (X,Y) for easting and northing respectively, and the Vertical grid representation (k). Borders represent
vertical levels and horizontal grid distances. η represents atmospheric vertical pressure levels. Figure extracted from WRF manual
Figure 30: Vertical coordinate system in WRF, adapted from WRF User Manual49
Figure 31: Lambert conformal map projection for current simulations: Best suited for mid latitude domains; adapted from WRF manual
Figure 32: Example of domain setup. The Initial Domain is the main Parent Domain in this example, the remaining are all its nested domains. Domain 1 nests domain 1, and domain 3 nests domain 4. Consequently, there are two sets of nested
domains: Initial Domain with domains 1 and 2, and Initial Domain with domains 3 and 452
Figure 33: Simple Block Diagram of the Turbine Parameterization Scheme Algorithm in WRF57
Figure 34: Turbine power and performance coefficient data from generic function and manufactures data of 3MW and 2MW Vestas wind turbines
Figure 35: Geographical location of the Thanet Offshore wind farm. Farm location is marked in yellow and enclosed in dashed
lines. Other UK wind farms are shown as well. Image is taken from Google Earth59
Figure 36 Thanet offshore wind farm layout (see Appendix-B: C-2).
Figure 37: Power and coefficients of the 3 MW Vestas V-90. The simulation uses the generic functions in WRF62
Figure 38: Location of simulation domains from set #2, with a zoom on the 1 km domain from set #1 (d03). Red spots are Turbine grid locations
Figure 39: Resultant grid locations of WTs (●) on domains from simulation set# 2. Spatial resolutions of 4.5 km, 1.5 km, and 500 m (left to right). Red dashed lines enclose the comparison region for the three resolutions
Figure 40: Average Height over the Thanet offshore wind farm as seen on each domain. Height is represented by the -•- line, and the normalized vertical η levels are represented by the -•- line. Both are plotted against the WRF output levels: an number used to ease the data manipulation. The η vertical distribution is the standard configuration of MeteoGroup64 Figure 41: Weather maps on March 18, 2010 at 18:00 hrs (a), on March 19 at 00:00 hrs (b), and at 06:00 hrs (c). The exit of the English Channel is marked by a dotted circle. The light blue lines represent the near-surface isobars in hPa, dark blue lines with filled triangles represent cold fronts, pointing in the direction from cold air to warm air regions. The red lines with filled semi-circles depict warm fronts where the circles face towards the regions with cool air. Pictures are taken from the
KNMI website65
Figure 42: Wind Speed field from Venturi Effect at 10 m height (left), and at 67 m height (right). Both pictures taken from the 3 km resolution domain of simulation set #1 in BACKGROUND case (no wind farm implemented). Gap between UK and Europe is 34 km approx.
Figure 43 Illustration of Gap flows: (a) Idealized Funnel flow as gap winds, (b) example of gap flow when the Funnel Effect dominates in Nu'uanu Pali Pass in the Koolau Rang of eastern Oahu, Hawaii, (c) suggested gap flow though the English Channel. The channel/gap borders s are around 3 m to 100 m in height above sea level. White lines in (c) mark gap lengths of 170 km, 96.3 km, up to 35 km in the last line. Fist two pictures from UCAR
and 500 m (set #2) domains
Figure 45: Wind speeds at hub height (-Δ-) (left), and wind speeds at 10 m height (-•-) (right) as a function of domain resolution. Two vertical axis: wind speeds in [m/s] on FARM & BACKGROUND cases, and wind speed change in [%] on FARM — BACKGROUND cases. FARM cases are in blue lines, BACKGROUND cases are in black lines, and FARM — BACKGROUND cases are in green lines. All points are located within the wind farm location. Results from the 500 m grid (set #2) deviate from the trends. The location of the maximums suffered minor changes on each resolution.
Figure 46: Example of wind speed deficits in the middle row of the Thanet offshore wind farm (FARM case) in (a). The 1 km domain (set #1) represented as •, and the 500 m domain (set #2) as •. Solid lines represent linear fits to each domain result. The middle row is illustrated on the 500 m domain in (b), and contrasted to the 1 km domain representation in (c).

Figure 47: Wind speeds contours at 67 m above sea level (FARM case). Left to right: 9 km, 3 km, 1km domains (set #1), and the
500 m domain set #2 (below). Doted circles enclose the farm location, and show effects of the gap winds from the English
Channel near the turbines: merging of red/brown areas70
Figure 48: Contours of wind speeds changes at 67 m above sea level. Left to right: 9 km, 3 km, 1km domains (set #1): FARM –
BACKGROUND case. No relevant difference between 1 km , and 500 m (set #2) for this comparisons71
Figure 49: Wind speed contours at 9.8 m above sea level. Left to right: 9 km, 3 km & 1km domains from set #1 for (a) and (b);
domains of 1 km (set #1), and 500 m (set #2) domains in (c) and (d). FARM case is treated in (a) and (c) with bins of 0.05
m/s. The FARM – BACKGROUND case is treated in (b), and in (d) with bins of 2% and 4% change. RIGHT TAIL marked as (R),
AND left tail AS (L). Maximums and minimum values on all plots relate to their contoured area72
Figure 50: Wind speed deficit/decay profiles from the inflow to the downstream flow on the 1 km domain from set #1 (FARM –
BACKGROUND case). The Farm extends from the 10 th km. The vertical plane containing all points intersects the farm from
the pivot coordinates listed in Table 1073
Figure 51: Vertical profiles of wind speed from the inflow (-5 km) up to 27 km downstream of the farm. Plots from the 1 km
domain of set #1 (FARM – BACKGROUND case). The vertical plane containing all points intersects the farm from the pivot coordinates listed in Table 1074
Figure 52: Comparison of hub height wind speed development on the 500 m (set #2), 1km (set #1) grid resolutions with respect
to Jensen's wake model for the Off-shore (k=0.05), and On-shore (k=0.075)75
Figure 53: Contours of twice TKE at hub height, with turbine grid locations (FARM case). Left to right: 1 km (set #1), and 500 m
(set #2) domains. Bins of $0.1 \text{ m}^2/\text{s}^2$. qke_{max} values of $6.3 \text{ m}^2/\text{s}^2$ (left), and $7.4 \text{ m}^2/\text{s}^2$ (right) inside the farm76
Figure 54: Contours of twice TKE at 10 m above sea level, with turbine grid locations. Left to right: 1 km (set #1), and 500 m (set
#2) domains (FARM case), with bins: 0.1 m ² /s ² . Maximum <i>qke</i> values of 1.7 m ² /s ² (left), and 1.8 m ² /s ² (right) inside the
farm76
Figure 55 Example of Rotor Turbulence Intensity of the Thanet Offshore wind farm. See Appendix-B: B-177
Figure 56: Contorus of twice TKE. Left to right: 9 km, 3 km, and 1km domains from set #1 in (a) (b) (c), and 1 km (set #1) with
500 m (set #2) in (d). Figure (a) is FARM case at hub height with bins of 0.2 m ² /s ² . Figure (b) is FARM case at 10 m height
with bins of $0.1 \text{ m}^2/\text{s}^2$. Figures (c) and (d) are FARM – BACKGROUND cases at 10 m height with 0.05 and 0.1 m ² /s ² bins,
respectively. Maximum values displayed in (a), and (b) are found at the coast78
Figure 57: Average changes in twice <i>TKE</i> caused by the FARM presence on the 3 km, 1 km domains from set #1, and the 500 m
domain from set #2 (FARM – BACKGROUND case). Turbine locations, the Near wake and the Deep wake locations are
shown on the right
Figure 58: Contours of twice <i>TKE</i> to detail wake boundaries on the 3 km, 1 km domains from set #1, and on the 500 m domain
from set #2 (FARM-BACKGROUND case). Order: left to right. from left to right. Horizontal contour at 10 m height in (a), at
lower blade tip area in (b), and at hub height in (c). Vertical contour of positive TKE changes on the 500 m domain in (d),
and the negative changes on the 1 km and 500 m domains in (e). Hub height is marked by a dashed line80
Figure 59: Peripheral reductions of <i>TKE</i> in (a) and (b), and of Turbulence Intensity I_o in (c) and (d), at 67 m height for the FARM –
BACKGROUND case. Order: 1 km domain of set #1 in (a) and (c), and 500 m domain of set #2 in (b) and (d). Zones of
positive TKE in (1), coastal effects on turbulence in (2), wind transitions from coast through the offshore in (3), location of
the peripheral reductions in (4), and front reductions zones in (5)81
Figure 60: Vertical contour of temperature changes (a), and horizontal contour of surface-heat flux H_{sf} changes (a). All contours
are on the 1 km set #1 domain and from the FARM – BACKGROUND case82
Figure 61: Changes in H_{sf} inside the farm per domain resolution. Standard deviations are plotted as error bars83
Figure 62: Averaged Downward Heat flux to the surface $[-H_{sf}]$ for the period of 1958 – 2006 [71]. Left to right: annual mean (a),
and standard deviation (b). UK is located inside the dotted circle83
Figure 63: Monthly downward surface heat flux $[-H_{sf}]$ to the North sea at four locations (a): two near Thanet, and two on the
Equator; data is from 2009, and adapted from the WHOI OAFlux project [72]. Contour of upward surface-heat flux for the
BACKGROUND case in (b), with turbine grid location on the 1 km domains from set #1, at 12:00 hours, March 19 2010. The
contours in (b) illustrates that the sea coast on UK "gains heat", whilst the land releases heat84
Figure 64: Contour of Δh_* on the 1 km domain from set #1 (a), and Plot of average Δh_* inside the farm per domain resolution (b):
standard deviations are plotted as error bars85
Figure 65: Vorticity contours on the 500 m domain from set #2 at 4 different heights (FARM – BACKGROUND case): 10 m (a),
lower blade tip section at 33 m (b), hub height at 67 m (c), and higher blade tip at 109 m (d). Units in 10^{-5} s ⁻¹ 86

Figure 66: Illustration of the Free Atmospheric Radiation Process. Surface Albedo is the diffuse reflectivity of any surface.	07
Adapted from [73]	
	.67
Figure 68: Vertical Profiles of spatially averaged <i>TKE</i> on the BACKGROUND cases in (a). Solid lines represent the inflow profile	
(flow reaching the farm), and dotted lines indicate profiles just behind the farm location 'Near wake'. Arrow lines indicate the state of the state	te
the rotor areas. A zoom of the <i>TKE</i> profile on the rotor area is shown in (b). A sensitivity analysis of <i>TKE</i> with respect to	
momentum diffusivity (εt) by B. Matteo [78] is shown in (c): <i>TKE</i> profile flattens as diffusivity decreases	
Figure 69: Computational time simulations (a). Size of simulation domains in Mb as a function of grid cells per domain. The size	
in Mb can be further reduced by eliminating variables before executing WRF (b).	
Figure 70: Geographical location of the Middelgrunden Offshore wind farm. Background figure taken from Google earth. Turbi	
layout obtained from wind farm data and plotted in the UTM coordinate system: UTM zone 32	
Figure 71: Bonus 2 MW/76 Turbine Power and Coefficient Curves.	
Figure 72: Turbine locations on Domains.	
Figure~73:~Histograms~and~weibull~distribution~fits~of~free~streams.~Free~stream~in~MIDD~prior~and~post~wind~farm~installation	
(a). Free stream in OWEZ [30] prior and post wind farm installation (b). Forecast comparison of free stream in MIDD (c).	
Color arrows (←, Ļ) on all plots relate weibull distributions to their respective parameters, and (✓) indicates weibull	
displacements	.97
Figure 74: Differences in wind direction and wind speed per direction: WRF vs. Forecast data set	.98
Figure 75: Time series of WRF simulation result vs Forecast data on the 16 days simulation period. Values are 10 min averages	
Wind direction in (a), wind speed in (c). Dashed circles indicate important differences: Wind direction from the WEST in ((1),
undefined direction (NE or NW) in (2), and large errors in wind speed in (3). Time stamps with missing values on any WT	
are ignored, and the remaining series put together	.99
Figure 76: TI vs Wind speed from WRF simulation	101
Figure 77: TI vs Wind speed from April data set, with zoom in 4 – 16. Deduced from turbine data	101
Figure 78: TI vs Wind speed plots of the frees stream from all data sets (TIpw, I0na, I0pw, I0met) and simulation results T.I	
metmast. Variables described in section 5.2. TIpw speed-wise is based on same method as TIpw but not on direction. 1	102
Figure 79: Turbulence rose comparison for free stream TI from data set and WRF simulation. Highly turbulent rose distribution	n
from the forecast data set, and a more uniform and weaker distribution from the simulation. Atmospheric stability during	
the simulation is plotted through the Monin. L in meters	
Figure 80: Turbulence intensity as a function of wind direction, averaged quantities per same quantity of sample data on each	
direction bin. No range of turbulence intensity is shown per direction; see Figure 79 for such	
Figure 81: Time series analysis and differences between the simulation (WRF) and the Forecast data set. Wind farm power ite	
series (a). Error in wind farm power forecast (WRF – Forecast data set) values (b). Indicators for farm power larger than	
MW (c), and for inactive WTs (d). Free stream wind speed (e), and direction (f). Averaged 1-Cos(γ) from the Forecast dat	
set (g). Mean absolute value of γ of the farm (h), added γ due to wind direction error in simulations (i)	
Figure 82: Time series of errors in the simulation. Phase Error of wind farm power (a). Phase Error of wind farm power and Ev	
from V_{fs} , with nearly a perfect match (b). Resultant averaged error Ecp of the wind farm due to changes in V_{fs} (c).	
Comparison of compound errors and total compound error (d). Indicators for farm power larger than 2 MW (e)	107
Figure 83: Comparison of \mathbf{x}_{sn} efficiencies from different sources. Values are averaged on $+5^{\circ}$ centered direction bins each 10°	
Red are represented the standard deviation of \mathbf{x}_{sn} from the Forecast data set. Missing values from the 40° to 60° due to	
the lower number of data points for a representative average (simulations and forecast data set)	
Figure 84: Rose of Farm Efficiency \mathbf{x}_{max} from simulation results (WRF) and the Forecast data set per wind direction $+$ 15°	110
centered bins (above). Difference in \mathbf{x}_{max} from simulation results and the data set (below); directions are shown radially.	
Wind rose from forecast data set in (a), and wind rose from simulation in (b)	
Figure 85: Wind speed deficits (a) and power deficits ratios (b) to the outputs from the North and South WT for the 174° +15,	
and 354° + 15 directions.	112
Figure 86: TKE and I(u, wt), I0na ratios as seen from the South or North WT in MIDD for the 174° +15, and 354° + 15	
directions (a). Comparison to Frandsen's Model of turbulence intensity (b). SD are shown as error bars, dashed lines	140
indicate <i>unity values</i> , solid lines indicate locations with Ntc i, j = 2.	
Figure 87: Variation in turbulence intensity downstream between turbines with Frandsen's model, CTfrom Forecast data set,	
= 0.087 as obtained from WRF for the $174^{\circ} + 15$, and $354^{\circ} + 15$ directions, with 8-9 m/s winds	114

Figure 88: Representation of the terrain-following approach in the vertical coordinate of WRF1	120
Figure 89: Example of Turbulence Intensity of the Thanet Offshore wind farm1	122
Figure 90: Turbine layout of Thanet offshore wind farm	125
Figure 91: Wind speed contour plot at 67 m above sea level on the Thanet offshore wind farm from the 1 km grid resolution. 1	
March 2010. Bins of 0.2 m/s. Many turbine labels interlap each other but each group of turbines is evenly distributed1 Figure 92: Wind speed contour plot at 67 m above sea level on the Thanet offshore wind farm from the 500 m grid resolution.	126
19 March 2010 00:00 hrs . Bins of 0.2 m/s. Labels interlap each other but each group of turbines is evenly distributed1 Figure 93: Wind speed contour plot on the 500 m grid at 10 m height at the farm location. March 18, 2010, 15:00 hrs. Bins of 0.05 m/s. The surface winds increase in the flow direction on the site	
Figure 94: Wind speed contour plot on the 500 m grid at hub height at the farm location. March 18, 2010, 15:00 hrs. Bins of 0. m/s. The wake effects is shown as wind speed decays on the site	.25
Figure 95: Contour plot of turbulent kinetic energy TKE at hub height on the 500 m grid. March 19 2010, 00:00 hrs. Bins of 0.2	
m2 s-2. The SE coast of England is located at the left corner of the figure. Red spots on that corner are most likely due to the Dover hills in the south	O
Figure 96: Contour plot of turbulent kinetic energy TKE in pixel format at hub height on the 500 m grid: Zoom at the farm site.	
March 19, 2010, 00:00 hrs Bins of 0.05m2 s-2	
Figure 97: Wind speed contours at 33 m height (FARM case) . Left to right: simulation times yyyy-mm-dd: hh. Series #1: 3 km domain from simulation set #1. Series #2: 1 km domain from simulation set #1. Series #3: 500 m domain from simulation set #2	
Figure 98: Wind speed contours at 33 m height (FARM case) . Left to right: simulation times yyyy-mm-dd: hh. Series #1: 3 km domain from simulation set #1. Series #2: 1 km domain from simulation set #1. Series #3: 500 m domain from simulation set #2	
Figure 99: Wind speed contours at 67 m height (FARM case). Left to right: simulation times yyyy-mm-dd: hh. Series #1: 3 km domain from simulation set #1. Series #2: 1 km domain from simulation set #1. Series #3: 500 m domain from simulation	n
set #2	
Figure 100: Turbulent kinetic energy <i>TKE</i> at 67 m height (FARM case). Left to right: simulation times yyyy-mm-dd: hh. Series # 3 km domain from simulation set #1. Series #2: 1 km domain from simulation set #1. Series #3: 500 m domain from simulation set #2	
Figure 101: Wind speed contours at 67 m height (FARM case). Left to right: simulation times yyyy-mm-dd: hh. Series #1: 3 km	
domain from simulation set #1. Series #2: 1 km domain from simulation set #1. Series #3: 500 m domain from simulation set #2.	n
Figure 102: Turbulent kinetic energy <i>TKE</i> at 67 m height (FARM case) . Left to right: simulation times yyyy-mm-dd: hh. Series #	
3 km domain from simulation set #1. Series #2: 1 km domain from simulation set #1. Series #3: 500 m domain from	
simulation set #2	
() () () () () () () () () ()	135
Figure 104: Upward surface-heat flux H_{sf} contours with turbine grid locations (FARM – BACKGROUND case). Left to right: 9 km, 1 km domains from set #1, and 500 m domain from set #2 (below). Values indicate changes in H_{sf}	
Figure 105: Planetary boundary layer height h* contours with turbine grid locations (FARM – BACKGROUND case). Left to right km, 3 km, 1 km domains from set #1, and 500 m domain from set #2 (below)	
Figure 106: Vertical contours of Temperature (FARM – BACKGROUND case). Left to right: 9 km, 3 km, 1 km domains from set and 500 m domain from set #2. Top series is at simulation time of March 18, 15:00 hours, 2010. Bottom series at 18:00 hours. Farm is located from the 10 th km, and profiles are oriented in the flow direction at each simulation time	
Figure 107: Vertical contours of Temperature (FARM – BACKGROUND case). Left to right: 9 km, 3 km, 1 km domains from set and 500 m domain from set #2. Top series is at simulation time of March 19, 06:00 hours, 2010. Bottom series at 12:00 hours. Farm is located from the 10 th km, and profiles are oriented in the flow direction at each simulation time	
Figure 108: H_{sf} contours with turbine grid locations (FARM – BACKGROUND case). Left to right: simulation times yyyy-mm-dd: hh. Series #1: 3 km domain from simulation set #1. Series #2: 1 km domain from simulation set #1. Series #3: 500 m	

Figure 109: H_{sf} contours with turbine grid locations (FARM – BACKGROUND case) . Left to right: simulation times yyyy-mm-hh. Series #1: 3 km domain from simulation set #1. Series #2: 1 km domain from simulation set #1. Series #3: 500 m	
domain from simulation set #2	
Figure 110: PBLH contours with turbine grid locations (FARM – BACKGROUND case). Left to right: simulation times yyyy-mi hh. Series #1: 3 km domain from simulation set #1. Series #2: 1 km domain from simulation set #1. Series #3: 500 m	m-dd:
domain from simulation set #2	142
Figure 111: PBLH contours with turbine grid locations (FARM – BACKGROUND case). Left to right: simulation times yyyy-mine hh. Series #1: 3 km domain from simulation set #1. Series #2: 1 km domain from simulation set #1. Series #3: 500 m	m-dd:
domain from simulation set #2	143
Figure 112: Midelgrunden Offshore Wind Farm. Picture from Google Earth	
Figure 113: Wind roses for Middelgrunden site: Annual wind rose (left), for the period of March (middle), and for the perio	
April (right). All data from 2001-2014 from www.windfinder.com	
Figure 114: Meteological mast layout [79]	
Figure 115: Sactter widn speed for different dates (a), scatter turbulence intensity for different dates (b), scatter turbulence	
intsnity with respect to wind speed at 45 m (c), and wind direction histogram at 30 m heihgt (d). Raw data is extacted	d fron
[80]. All plots are met mast measurements.	
Figure 116: Extrapolation of wind speed distribution from 30 m to 50 m using zo of 0.03 m. Weibull fits are shown	147
Figure 117: Probability distribution of turbulence intensity of the free stream from the Forecast data set, and from the simulations in WRF.	147
Figure 118: Zoom in turbulence intensity with respect to wind speed from WRF simulations at met mast location, 50 m heig	_
Figure 119: Probability distribution of turbulence intensity from forecast data set, and from simulations. The data set has b	een
filtered to avoid readings from added turbulence due to the turbines	
Figure 120: Standard deviation diagram with area coverage in [%]	
Figure 121: Factor Fv, TI behavior with wind speed and turbulence intensity from Equation 56. The power –law distribut	
seen on the left, and the linear relation on the right. Linear approach takes the slope into account to extrapolate the	
results of the power-law distribution to higher values of turbulence intensity: TI > 0.04	
Figure 122: Resultant offset by using the power-law + linear distribution. Positive Offset indicate overestimation in the Fac	tor,
and negative Offset indicates underestimation of the Factor.	
Figure 123: Resultant offset by using the power-law + linear distribution. Positive Offset indicate overestimation in the Fac	
and negative Offset indicates underestimation of the Factor.	153
Figure 124: Approximation of Gv, σv , and $\sigma(p)$ Pavg- $\sigma(v3)$ Vavg3 over the power curve with 1 m/s bins	154
Figure 125: Farm efficiency from Case 2 vs wind direction in the MIDD farm.	155
Figure 126: Reanalysis time series of total turbine power output and wind speed for turbine WT01: North turbine	158
Figure 127: Reanalysis time series of total turbine power output and wind speed for turbine WT02	159
Figure 128: Reanalysis time series of total turbine power output and wind speed for turbine WT03	160
Figure 129: Reanalysis time series of total turbine power output and wind speed for turbine WT04	161
Figure 130: Reanalysis time series of total turbine power output and wind speed for turbine WT05	162
Figure 131: Reanalysis time series of total turbine power output and wind speed for turbine WT08	163
Figure 132: Reanalysis time series of total turbine power output and wind speed for turbine WT13	164
Figure 133: Calling Tree between turbine scheme and flow model in WRF	
Figure~134:~Elliptic~configuration~of~turbulence~intensity~distribution~based~on~turbine~spacing~parameters~s1~and~s2.~Green and~s2.	n
crosses represent the nearest turbines to the turbine under analysis.	167
Figure 135: OWEZ Offshore Wind Farm as digitized from available information on the web	168
Figure 136: Turbine vertical levels intersecting rotor area	170
Figure 137 Illustration of area moment analysis of rotor section above or below hub height	170
Figure 138: Illustration of area moment analysis for rotor section crossing hub height	
Figure 139:Wind speed profile in the wake of a wind turbine[44]	
Figure 140: Time linearization of turbulence	
Figure 141: Entry modules in the structure	
Figure 142: Algorithm inside the first module that calls the turbine scheme modules and dependencies	177

Figure 143: Tree for calling the PBL scheme and using variable from the module that reads the turbine information	177
Figure 144: Original and modified algorithm to set turbine locations to obtain turbines units per grid location (turb_der	ısity) and
total number	178
Figure 145: Initialization of qke , and turbine orientation per grid location $\theta turb$	179
Figure 146: Initialization of power, thrust, atmospheric stability and loop through rotor sections within k levels	179
Figure 147: Hub height wind speed interpolation for nacelle movement and turbine yaw assignment through function	
Yaw-movement, and air density reading	180
Figure 148: Section to correct turbine nacelle orientation	181
Figure 149: Final section to calculate ambient turbulence, and turbine performance coefficients	181
Figure 150: Code section to calculate the near wake distances	182
Figure 151: Code section for added turbulence intensity	183
Figure 152: Code for diagnostic variables	184
Figure 153: Final code to yield the average flapping moment	185

Chapter-1.Introduction

Wind energy has been present in humanity since early ages but it was only used as mechanical power for wind mills and navigation. It was not until the 1990's that the energy market started to consider wind as an alternative source of energy, the available wind turbines reached the megawatt capacity, and on the 21st century there was a growing trend for wind energy [1]. There are 3 major reasons why the trend happened. First of all, the concern about depleting fossil fuel reserves and the increasing energy consumption became vital topics to investigate for many countries. Secondly, the environmental awareness around the use of fossil fuels grew strong, and was embraced in few countries. On third, the technological feasibility of producing and commercializing wind turbines was at hand. There are now high capacity wind turbines available in the market like the 3MW Vestas V-90M, AREVA's M5000 (5MW), and the 6MW Turbina Sapiens from SIEMENS. Wind turbines exist as stand-alone machines or in arrays — 'wind farms'. With the current tendency towards renewables, wind energy has made a remarkable achievement in history by globally producing from 95 TWh to 314 TWh of electricity on the 2004-2009 period [2]. In Europe for example, the Dutch government has set goals of attaining 6 GW of offshore wind power by 2020. The offshore tendency has two main reasons. First, countries using wind energy are running out of appropriate land sites to build large wind farms. Second, the atmospheric conditions on the offshore provide more energy content with less power fluctuations than on land [3].

Most wind turbines have an overall efficiency of 40% [1]. Turbines in arrays experience wind speed deficits which influence wind farm design and power generation [3]. The speed deficits are expressed through 'wake models' as the downstream air from turbines follows a spiral shape profile, and disrupts the wind in front of other turbines. Once wind speed deficits are known, statistical models for power forecast based on them, on farm layout, and on turbine manufacturer's data can be implemented. Forecasting models have become a focus of attention within the academy and industry. Nonetheless, only few people have analyzed the climatological impacts generated by the operation of wind farms. For example, simulations of large-scale wind power like the studies done by David W. Keith et al. [4] and Daniel B. Barrie [5] suggest that air temperatures and wind flow patterns inside arrays cause large instabilities downstream. The turbines first altered the local climate after a few days, and oceanic winds weeks later. Barrie's analysis is an example of how a national U.S supply of wind power would affect the North Atlantic Ocean, with air pressure changes reaching the Irish seas in the matter of days¹. Keith's results indicate that a 10% increase in global power production form wind energy can significantly change the earth's general air circulation: polar cooling and low-latitude warming. Additionally, Keith also suggests that large amounts of wind power produce effects on seasonal temperature peaks², which is of vital importance for insect and plant ecosystems; hence, affecting local agriculture. Because of the

¹ In Barrie's article the effects are expressed in geo-potential height anomalies

² Values are sensitive towards wind turbine parameterization schemes.

complexity of atmospheric models, wind turbines were not modeled in detail. But rather proposed as local changes in the earth surface roughness³, having its roots in the expression developed by Lettau in 1969 [6] [7].

On a moderate spatial scale, wake effects are found to be persistent over several kilometers downstream regardless of the wind farm size. Thus, indicating that the local environment is also affected. Simulations from Baidya [8] in 2010 showed that wind farms change near-surface air temperatures, humidity, vertical heat fluxes, and near-surface air temperatures around 1 °C over 18–23 km downstream. Baidya also confirmed that the variability the effects depends on atmospheric stability; a property that indicates the tendency of the atmosphere to resist vertical motion or to suppress turbulence (commonly measured by the Monin-Obukhov Length). More modeling and experimentation are needed to further understand the effects of wind farms in the meso-scale atmosphere (5 to >100 km). The meso-scale atmosphere covers physical phenomena such as cloud formation and movement, snow and rain precipitation, long wave and short wave radiation, and surface-heat flux from large areas, among other aspects. Due to the various phenomena involved, their complexity and different spatial scale dependency, parameterizations of atmospheric phenomena are used in the analysis and forecast of the meso-scale atmosphere. It is worth mentioning at this point that the major constituent of uncertainty in wind resource analysis comes from the parameterizations of surface roughness, and atmospheric stability [9]. Turbine rotors are often parameterized with power and thrust coefficient data from manufactures, drag disc concepts, and basic formulations of turbulent kinetic energy and turbulence intensity. Few examples of recent turbine parameterization are Adams and Keith in 2007 [10], Baidya Roy in 2010 [8], Blahak et al. in 2010 [11], and Fitch et al. in 2012 [12].

On a smaller scale, atmospheric stability (very stable, stable, near-neutral, unstable, and very unstable⁴), and site location determine the variability of in-situ wind shear profiles and turbulence. Both are imperative for assessing fatigue damage of turbine blades. Each shear profile carries a unique loading case on the blades, proportional to the turbine hub height and rotor diameter; these two parameters are large for offshore wind turbines. Furthermore, power generation and long term energy yield estimates differ considerably from measured data when atmospheric stability changes. Consequently, wind shears can be larger than anticipated [13] [14] [15]. The occurrence of stability classes depends on site location and can be expressed through probability density functions (for wind speed as well). Bierbooms and Sathe [16] explain how different shear profiles modify fatigue damage under steady state conditions, taking as examples the Danish offshore sites of Rodsand and Vindeby. Their results showed that for Rodsand, the occurrence of different stability classes increased the fatigue damage by a factor of 3.2 with respect to the use of a single exponential shear profile, and a radical difference when using a logarithmic profile. But for Vindeby site, the damage attained differed only by a factor of 0.12, and 6.72 with respect to an exponential and logarithmic profile, respectively. The conclusion is that fluctuations on the local atmospheric stability of wind farm sites determine important changes in the fatigue damage of wind turbines.

³ The concept is introduced to shape wind profiles in logarithmic expressions. For further definition see [38] or section 2.1.1.

⁴ The classification of atmospheric stability is considered according to [16] [38].

An accurate way of capturing the loop process between the atmosphere and the turbines is by implementing Large Eddy Simulations (LES). For example, a wind filed with a certain wind speed profile approaches a wind farm (upstream flow), and once the flow reaches the turbines the local profile is modified. After a certain period, the farm presence alters the upstream flow, which once again reaches the wind farm, and the loop repeats itself. LES is derived from the Navier Stokes flow equations of motion and is a model that distinguishes the swirling of a fluid in different scales, allowing the model to handle unsteady anisotropic turbulent flows, and turbulent mixing effects caused by large structures. The spatial accuracy of LES is noticeable in the dissertation work of Ivanel [17] from the University of KTH in Sweden about understanding the mechanisms controlling the length of wakes, their interaction, and stability properties. In his study, an Actuator Line technique consisting of three rotating lines at hub height was implemented to represent the wind turbines at the Horns Rev Offshore Wind Farm. The technique used airfoil data and experimental corrections for turbine rotational effects, and achieved reasonable agreement with measurements of power generation. LES can also be used together with a simple wind turbine 'Drag Disc' concept and values of aerodynamic roughness. An example of such model is the work by Calaf, Meneveau, and Meyers [18]. Their results revealed that vertical fluxes of kinetic energy are of the same order of magnitude as the power extracted. Such models are also used in the assessment of optimal array turbine spacing in terrains with no topology (like on the offshore), by combining land and turbine cost ratios, and yielding optimum turbine spacing of approximately 15 rotor diameters (15 D) rather than the conventional 7 D spacing [19]; similar results were obtained by Cal et al. [20] in a wind tunnel experimental setup with a 3 by 3 turbine array.

Increments on air temperature around rotors have also been predicted by LES computations, together with the reduction in turbulent mixing and transport near the surface [21], wind speed deficits in the near wake (X < 5D) with some overestimation, and accurate speed profiles in the far wake (distances X > 20 D) [22]. But unlike models on moderate spatial scales, results with LES are extremely expensive: expertise, coding skills, and much computational power are required for any kind of simulations involving wind turbines. When the need for accuracy increases, so does the need for grid refinement on all coordinates, and the need for unsteady inflow input data [23]. All of which increase computational time. Additional literature highlighting the complexities of atmospheric turbulence and wake modeling are those by Mann [24], Bechmann's PhD Thesis [25], and Vermeer [26].

Bearing all previous information in mind, it is not surprising that aerodynamic and thermodynamic models of wind farm effects on the meso-scale atmosphere are important. As a result, a numerical study on the atmospheric effects of an offshore wind farms is proposed to the Company MeteoGroup. Lately, wind farms are being commissioned very close to each other and they can no longer be considered as separate bodies. Therefore, it is important to accurately represent the interaction between wind farms and the local atmosphere (numerical models), to subsequently infer the fluid interaction between wind farms close to each other. Such representation can be used to properly set measurement campaigns in the future, and help to achieve acceptable power generation from wind as a sustainable energy source. As a requisite, any numerical study must first be able to represents this flow interaction with an isolated wind farm. MeteoGroup has the computational capacity for such numerical analysis, and is running a meso-scale numerical weather prediction model for providing detailed weather forecasts on a daily

basis. This model includes a wind farm parameterization scheme, but it is unknown how well the model performs. The project therefore has two research aspects regarding wind farm interactions and the meso-scale model:

- \downarrow 1st: Is the current wind farm power parameterization scheme based on momentum sinks and turbulent kinetic energy generation able to mimic the interaction between a wind farm and the meso-scale atmosphere?
- lacktriangle 2^{nd} : For MeteoGroup: Is the turbine parameterization able to produce accurate predictions of power generation from a wind farm.

On the other hand, both interest are intrinsically related. If, in simple terms, the parameterization is able to mimic the wind farm to atmosphere interaction, then whatever is derived from such interaction is represented as well. Namely, that is power generation from the wind turbines as a consequence of the atmospheric flow conditions and turbine layout. The reverse, is not necessarily true.

The main objective of the thesis is thus to use the knowledge gained from the master studies and from the internship experience in MeteoGroup to answer the research aspects, and provide entry knowledge into the topic for future students. The answer will help in developing an understanding of the interaction between wind farms, and provide a commercial and economical value to research programs oriented into modeling wind farm effects in the meso-scale atmosphere. After the completion of this study, two subsequent research questions are left for discussion:

- $lack grade 3^{rd}$: How does the location and size of offshore wind farm affects their power generation, and fatigue damage
- lacksquare 4^{th} : How does the size and operation of offshore wind farms affects their interaction in terms of power generation and fatigue damage?

1.1. Outline

The current study consists of 3 steps focused on the parameterization of wind turbines in the meso-scale atmosphere to analyze wind farm effects and farm power performance. One parameterization (the Fitch Scheme) is currently implemented in the open source program WRF (Weather Research and Forecast) at MeteoGroup, and is investigated in the 1st step together with an introduction to atmospheric flow on the offshore, simple wind turbine modeling, and wind farm effects in Chapter-2. The 2nd step is to describe the aspects of WRF which are relevant to the simulations, like the physic models in Chapter-3, and an example case studying the sensitivity of the turbine scheme to different grid resolutions, along with the effects in the local environment in Chapter-4. The 3rd step is to perform a validation and verification study of the turbine scheme in Chapter-5, using weather input data and measurements from the Danish wind farm of Middelgrunden. Finally, conclusions and recommendations are presented in Chapter-6.

There are a variety of physical variable used to quantify the results, and are properly described in the Chapter-2; they appear in the next list:

- ↓ Turbulence Intensity: I_o or TI
 ↓ Turbulent Kinetic Energy: TKE
- ♣ Monin-Obukhov Length: L_{*}
- ightharpoonup Temperature: $T, \left(\frac{\partial T}{\partial z}\right)$
- ♣ Speed profiles
- ♣ Weibull distributions
- ₩ Wind rose
- ♣ Boundary Layer height : h_{*}
- lacktriangle Upward surface-heat flux: $H_{\rm sf}$
- **♣** Vorticity

Chapter-2. Concepts on Atmospheric Flow and Wind Energy

There are three options to parameterize wind farm effects on the atmosphere based on the spatial scale of interest. The 1st option is modeling the dynamics of each rotor to assess the added drag from the farm to the local boundary layer and how the wake interact downstream. Simulations in this category solve for the fluid dynamics around turbines with CFD models like LES or DES (Large, and Detached Eddy Simulations respectively.) Hence, they describe the flow characteristics within small spatial scales relative to the farm size. LES models are suitable for the analysis of power efficiency, layout design and turbine selection. If computational time is within industry practices, LES models can also be used for climatological forecasts by incorporating measurements.

The 2nd option is the "middle range" or meso-scale modeling between the wind farm and the local environment. The modeling focuses on changes in turbulent kinetic energy and induced drag forces on the flow, temperature changes, pressure variations, and atmospheric stability. Consequently, meso-scale modeling may not detail the flow dynamics inside wind farms unless turbine spacing falls on the spatial resolution of the model. Current meso-scale models parameterize wind farms as added aerodynamic roughness, induced drags, energy extraction and turbulence generation regions, or a combination of all. The 3rd option is synoptic modeling, a global concept dealing with effects on a larger spatial scale, where common wind farm parameterizations are expressions of increased aerodynamic roughness.

This chapter deals with meso-scale modeling by introductory concepts of the wind and the offshore environment in section 2.1, followed by an introduction to wind turbine and wake basics including modeling of single units and of wind farms dynamics in section 2.2. Section 2.3 discusses few software tools available for wind turbine and wind farm simulations, and the principles of numerical weather programming or NWP models is introduced in section 2.4. Finally, the current turbine parameterization in WRF, and used for the present study is explained and discussed in section 2.5.

A.M. Striedinger P. Master of Science Thesis

2.1. Wind and The Offshore Environment

The planetary boundary layer (PBL) is a small fluid layer from a 100 m to 2 km height on the bottom of the atmosphere, where most wind fluctuations occur (see Figure 1). A concept of the PBL is that these fluctuations are not experienced by the rest of the atmosphere [27]. Such concept is a debatable notion due to the pollution and green-house gas emissions affecting the earth's Ozone layer, and damaging our protection from UV-B radiation⁵. Hence, the analysis of phenomena inside the PBL (80% of the atmospheric mass⁶) is a relevant scientific endeavor, and wind farm analysis falls under such endeavor due to its operational dependence on boundary layer flow.

The upper section of the PBL is the Ekman sub layer (below the troposphere in Figure 2), and is recognized by small wind speed gradients, wind shears less or equal to 10% of those near the surface, and prominent changes in wind direction due to the earth Coriolis force [28].

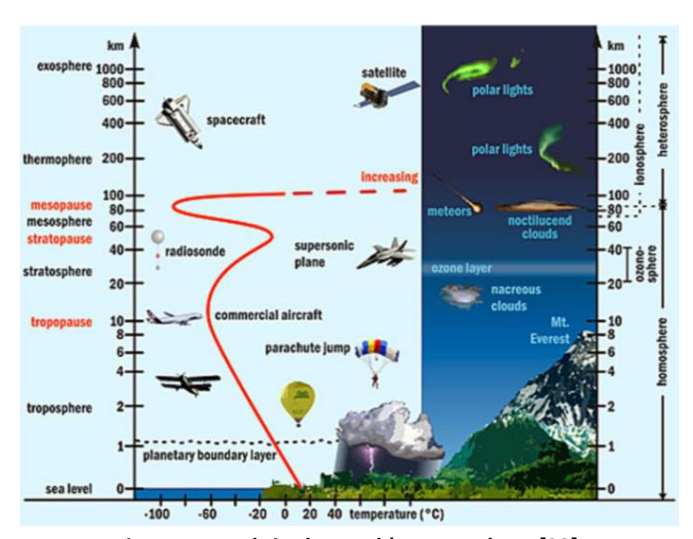


Figure 1: Levels in the Earth's Atmosphere [29].

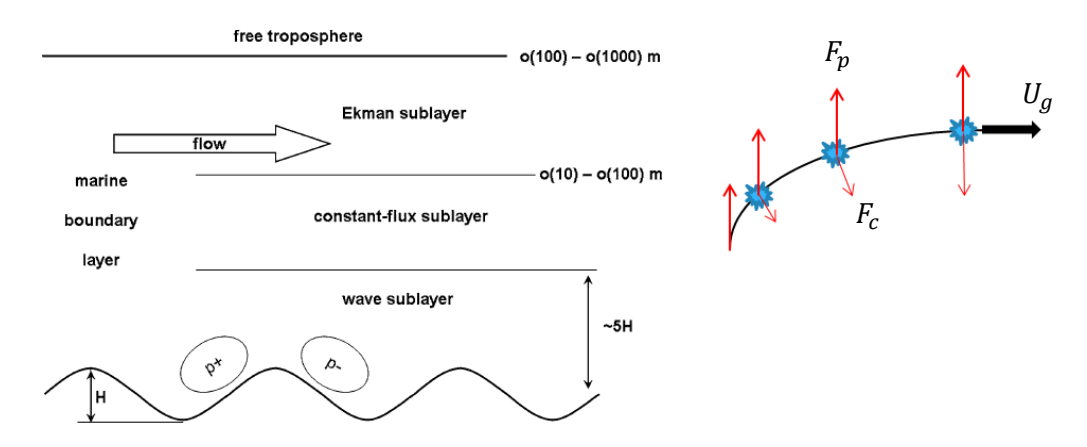


Figure 2: Vertical structure of the Offshore PBL (left), height can be much higher [28], Geostrophic Wind (right) [1].

⁵ Visit http://www.theozonehole.com/ for more information

⁶ Visit http://www.worldcat.org/title/mcgraw-hill-concise-encyclopedia-of-science-technology/oclc/300572607

Uneven radiation from the sun, greater at the equator and lower at the poles, sets a convective motion in the troposphere causing global air circulation, and strongly influenced by the earth's rotation. The changes in such heat transfer to the earth create pressure fields, moving the air from high to low pressure regions. Most pressure gradients are vertical, but coriolis forces and the gravitational pull favor horizontal gradients, such that most air moves horizontally in the Ekman sub layer and above it [28]. Most turbines reach this sub layer; hence, its wind shear characteristics make possible the extrapolation of near-surface wind speeds to hub heights, through a logarithmic function.

The previous statements are important when studying the effects of wind farms, by simplifying the wind speed above the PBL as a constant: Geostrophic wind $m{U}_{m{g}}.$ This is illustrated in Figure 2 and Equation 1; air parcels go up and acquire horizontal motion. U_g , arises from a balance between pressure and coriolis forces, where ϕ stands for latitude, and f_c for the coriolis parameter:

$$U_g = -\frac{1}{\rho f_c} \nabla P$$

$$f_c = 2\Omega_{earth} * \sin(\varphi)$$

Equation 1: Geostrophic wind and coriolis factor.

Shear stresses at the bottom of PBL become important as the non-slip condition creates waves with positive and negative pressure perturbations close to the sea surface (p^+, p^-) in Figure 2). The whole situation can be understood as the momentum exchange between the wave sub layer and the sea. The loss of momentum from the air is compensated by the thermal stratification of the atmosphere in steady conditions, during unstable conditions the waves are expected to be higher; this was proven in 1952 by data analysis from a North Atlantic weather ship [28].

Atmospheric stability is governed by the vertical temperature distribution due to the sun's radiation, and convection fluxes [1]. As a rule of thumb, the next definitions from the book of Roland Stull [27] should be understood: "Unstable air is that of light winds and a surface warmer than air, common in sunny days, warm air rises from the surface to heights of 1 to 4 km, and the turbulence is vigorous". Stable air on the other hand, is associated also with light winds but colder surfaces, as it occurs at nights, where turbulence is weak or not even existent, such that moving air parcels will always return to their initial states or oscillate around it. Boundary layer heights of stable atmosphere are typically 200 – 500 m [27]. The Neutral atmosphere is associated with modest to strong winds and little to no surface-heat transfer; often, a sign of bad weather predictions. A way to measure the atmospheric stability is through the Monin-Obukhov Length L_* ; explained in a later section. It uses the Lapse rate, which is the vertical temperature gradient of a section in the atmosphere. The lapse rate is further implemented to classify stability as well [30], and for a standard atmosphere, that is $288^{\circ}K$ at sea level and $216.7^{\circ}K$ at 10.8 km, the Lapse rate corresponds to -0.0066 °C/m [1].

$$\left(\frac{dT}{dz}\right)_{dry} \approx -\frac{9.8~^oK}{km} \qquad \quad \left(\frac{dT}{dz}\right)_{moist} = f(T) \approx -~\frac{5~^oK}{km}$$

Equation 2: Dry and moist adiabatic lapse rates.

Two important rates are the dry and moist adiabatic lapse rates (Equation 2), and the last one has a strong dependence on temperature. Figure 3 illustrates a boundary layer evolution from stable to unstable conditions, below the troposphere during one day. The capping inversion point in Figure 3 is where the Lapse rate changes to an opposite sign. The small region where the capping inversion lays is characterized by an intermittent turbulence, but with laminar flow over night [27]. The mixed layer is statically unstable (instability by means of buoyancy only). But when there is a tendency within static stability to form turbulence from wind shear, it is said to be dynamically unstable. Finally, the residual layer contains pollutants from the previous mixed layer but with less turbulence.

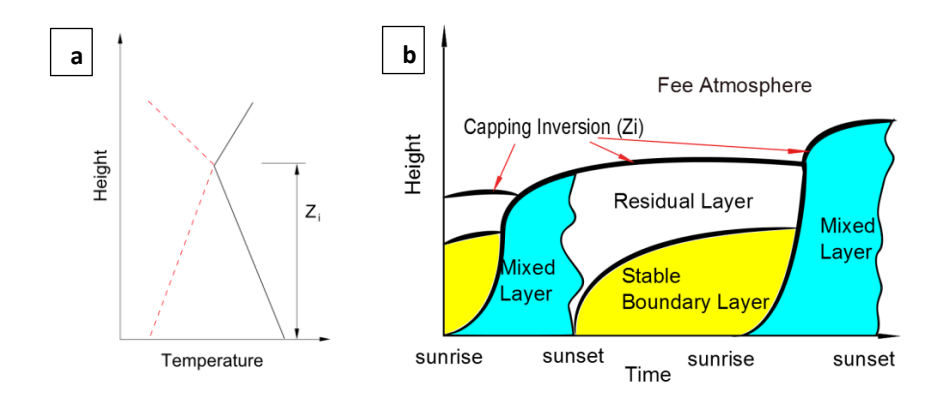


Figure 3: Schematic of Lapse rate (a): solid lines before sunrise, dashed lines (after) [1]. PBL components (b) [27].

Expressions for the wind shear stresses in the surface layer have been developed by means of the friction velocity u^* , and a roughness length z_o . The roughness length, also known as aerodynamic roughness, is not a measure of the real roughness of the surface but rather one that yields equivalent stresses. On the other hand, the friction velocity $u^* = \sqrt{\tau_o/\rho}$ is implemented to study the fluid per unit mass near the surface.

$$u^* = (\overline{u'w'}^2 + \overline{v'w'}^2)^{\frac{1}{4}} \qquad \cong \frac{\kappa U_{10}}{\ln[z_R/z_o]}$$
$$z_o = \alpha_c \frac{u^{*2}}{g}$$

Equation 3: Friction velocity expression (left), approximation (right), and Charnock Aerodynamic roughness (bottom).

The right hand expression of u^* in Equation 3 originates from the logarithmic law developed by Prandtl, and the expression of z_o is a simplification of the Charnock relation. Where z_o is related to the measured wind speed at z_R = 10 m height in the absence of turbulent data [30]. Equation 3 is further detailed in Appendix-A. Engineers have classified terrains according their representative aerodynamic roughness, these simple classifications provide reasonable predictions of wind speed profiles. Such an example is the Davenport Roughness classification in Table 1 (see Appendix-A for more).

Table 1: Davenport Roughness Classification [31].			
Aerodynamic	Landscape description		
Roughness: z_o m			
2×10^{-4}	Sea		
5×10^{-3}	Smooth		
$3 imes 10^{-2}$	Open		
0.10	Roughly Open		
0.25	Rough		
0.5	Very rough		
1	Closed		
> 2	Chaotic		

2.1.1. Atmospheric variables in the offshore relevant to wind farms

Atmospheric stability is the ability of the atmosphere to resist vertical motion or to suppress turbulence, where turbulence is defined as the random motion and rotation of wind, in the order of second to minutes⁷. Stability can be classified as static and dynamic, where static stability refers to the balance of buoyant forces on air parcel movement. Dynamic stability refers to the influence of shear stresses and buoyant forces on the movement. Under statically stable conditions, an air parcel with upward movement will return to its original position or start to oscillate periodically around it, contrary to its deviation under unstable conditions. But for high ratios of shear stress to buoyant forces, turbulence dominates parcel movement. Under dynamically stable conditions turbulence and buoyant forces are both attenuated such that equilibrium is attained. The PBL can contain regions with different stability. However, it is said to be unstable when at least one section is unstable.

Atmospheric stability is usually quantified by the Monin-Obukhov length L_{st} (Table 2, Equation 4) which includes the effects of humidity on the static air. The classification results in different types of wind speed profiles; examples are shown in Figure 4. Virtual temperature T_v in Equation 4 rescales temperature to define it in terms of water mixing ratios of the atmosphere, and surface-heat flux.

Table 2: Static stability and categorization with Obukhov's length [27].

Static Stability	Criteria	Criteria	PBL Stability	Criteria
Stable	$\frac{dT}{dz} > \left(\frac{dT}{dz}\right)_{dry}$	$\frac{dT}{dz} > \left(\frac{dT}{dz}\right)_{moist}$	Very stable	$0 < L_* < 200 \ m$
Neutrally Stable	$\frac{dT}{dT} \approx \left(\frac{dT}{dT}\right)$	$\frac{dT}{dt} \approx \left(\frac{dT}{dt}\right)$	Stable	$200 \le L_* < 1000 m$
	$ \overline{dz} \approx \left(\overline{dz}\right)_{dry} $	$\overline{dz} \sim \left(\overline{dz}\right)_{moist}$	Neutrally stable	$ L_* > 1000 m$
Unstable	All other	All other	Unstable	$-1000 \le L_* < -200 \ m$
			Very unstable	$-200 < L_* < 0 m$

A.M. Striedinger P.

⁷ Turbulence in wind speed is quantified as u', v', w' such that the complete velocity is $u = \bar{u} + u'$ on the x direction, and analogously on the other directions.

$$L_* = -\frac{T_v (u^*)^3}{\kappa g H_{sf}}$$

$$H_{sf} = \overline{T_v'w'}$$

$$T_v = T \left(\frac{p_o}{p}\right)^{\frac{R}{C_{p(a)}}} \quad or \quad T_v = 273.15 + T(1+0.61 \, r) \quad or \quad T_v = \frac{-H_{sf}}{c_{p(a)} \ u^* \, \rho_{\langle near-surface \rangle}}$$

Equation 4: Monin-Obukhov length L_* as a function of turbulence in the vertical direction (w'), virtual temperature T_v , pressure and humidity mixing ratio r. $c_{p_{(a)}}$ is the specific heat of dry air [28] [33] [34].

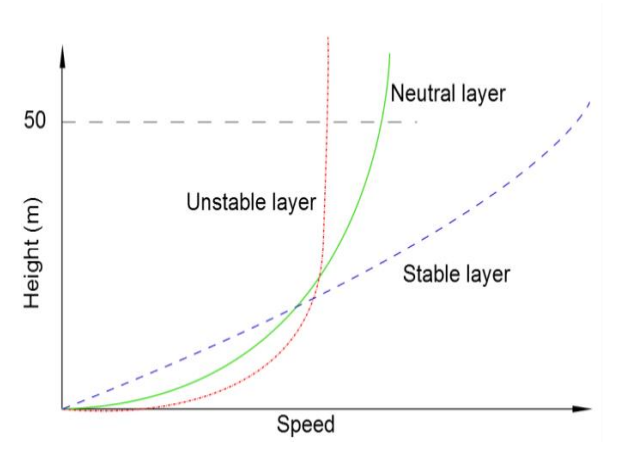


Figure 4: Example of wind speed profiles of different atmospheric stability categories, adapted from [27].

Under stable conditions, the vertical wind speed gradient remains nearly constant with height. For unstable conditions wind shear increases abruptly near the surface reaching a maximum at the lower part of the surface layer; wind speed remains constant afterwards (see Figure 4). The different wind speed profiles from Figure 4 can be derived with gradients functions from the similarity theory, and are applicable for the North Sea winds; see Equation 5.

Horizontal wind speed function:
$$u_{(z)} = \frac{u^*}{\kappa} \left[\ln \left(\frac{z}{z_o} \right) - \psi_m \right]$$
 Stable gradient function:
$$\psi_m = -5 \left(\frac{z}{L_*} \right)$$
 Unstable gradient function:
$$\psi_m = 2 \ln \left(\frac{1+x}{2} \right) + \ln \left(\frac{1+x^2}{2} \right) - 2 \operatorname{atan}(x) + \frac{\pi}{2}$$
 function (x):
$$x = \left(1 - 16 \left(\frac{z}{L_*} \right) \right)$$

Equation 5: Monin-Obukhov similarity theory applied to the North Sea wind [34].

From another perspective, Table 3 shows how variations in u^* and in z_0 induced changes from 6.1 m/s to 12.36 m/s on 10 m wind speed U_{10} measurements at Horns Rev under different stability classes. The results also point to a Charnock's constant α_c of 0.012 on that region of the North sea. Notice that increasing values of $\overline{z_o}$ indicate less stable atmosphere. Therefore, the similarity theory must be used together with measurements near the surface to accurately describe atmospheric stability, and simulate wind speeds at higher altitudes. Such measurements should be representative of the locations of interest.

Table 3: Mean parameters for different stability classes at Horns Rev (adapted from [36]). The last column is the sample profiles used to generate the results.

our to gonerate the results.							
	$\overline{\boldsymbol{L}_*}$	$\overline{u^*}$	$\overline{Z_o}$	$lpha_c$	U_{10}	Profiles	
Very stable	94 m	0.2 m/s	$0.5 \times 10^{-4} \ m$	1.23×10^{-2}	$6.10 \ m/s$	80	
Neutral	-1253 m	$0.47 \ m/s$	$2.7 \times 10^{-4} \ m$	1.20×10^{-2}	12.36 m/s	1253	
Unstable	-175 m	0.33 m/s	$1.3 \times 10^{-4} m$	1.17×10^{-2}	9.28 m/s	886	
Very Unstable	-74 m	0.25 m/s	$0.8 \times 10^{-4} \ m$	1.25×10^{-2}	7.33 m/s	940	

Standard deviations (σ_u, σ_v) of 10 min wind speed series quantify the turbulence from them. Turbulence can be expressed through the turbulent kinetic energy of the flow per unit mass TKE, and is made non-dimensional by means of the turbulence intensity I. Both variables are defined in Equation 6. But, depending on the location of interests and the atmospheric stability, the turbulence intensity can be simplified as isotropic; see Equation 7. The focus is on the horizontal contribution of TKE. Additionally, the relation between I and TKE is used in Appendix-D for an optional turbine parameterization.

$$I_{u} = \frac{\sigma_{u}}{\bar{u}}$$
 ; $\sigma_{u} = \sqrt{\frac{1}{N-1} \sum_{1}^{N} (u - \bar{u})^{2}} = \frac{1}{(u')^{22}}$

$$TKE = \frac{1}{2} \left[\sigma_{u}^{2} + \sigma_{v}^{2} + \sigma_{w}^{2} \right]$$

Equation 6: Turbulence intensity and turbulent kinetic energy.

$$\begin{split} TKE_{iso} &= \frac{1}{2} \Big(\sigma_{\langle horizontal \rangle}^2 + \sigma_w^2 \Big) \\ TKE_{iso} &= TKE_{\langle horizontal \rangle} + \frac{1}{3} TKE_{iso} \\ \Rightarrow TKE_{horizontal} &= \frac{2}{3} TKE_{iso} \quad ; \quad I = \frac{\sigma_{\langle horizontal \rangle}}{V_{hub}} = \frac{2}{V_{hub}} \sqrt{\frac{TKE_{iso}}{3}} \end{split}$$

Equation 7: Isotropic Turbulent Intensity, and its horizontal turbulent kinetic energy.

The IEC standard classifies wind turbines through wind classes, and each class represents the wind characteristic that turbines are exposed to. The classes are categorized by their turbulence intensity and the maximum expected wind speed during a period of 50 years; see Figure 5. Turbulence intensities from the classes are modeled through Equation 8. TKE increases as wind speed increases, but the opposite happens to turbulence intensity. IEC underestimates turbulence intensity at low wind speeds; i.e. speed less than 7 m/s in [28]. For higher wind speeds, the IEC standard produces few overestimations.

$$I_u = I_{ref} (0.75 + 5.6/\bar{u})$$

Equation 8: Turbulence intensity from the Normal Turbulence Model (NTM) in IEC standard [1] [37].

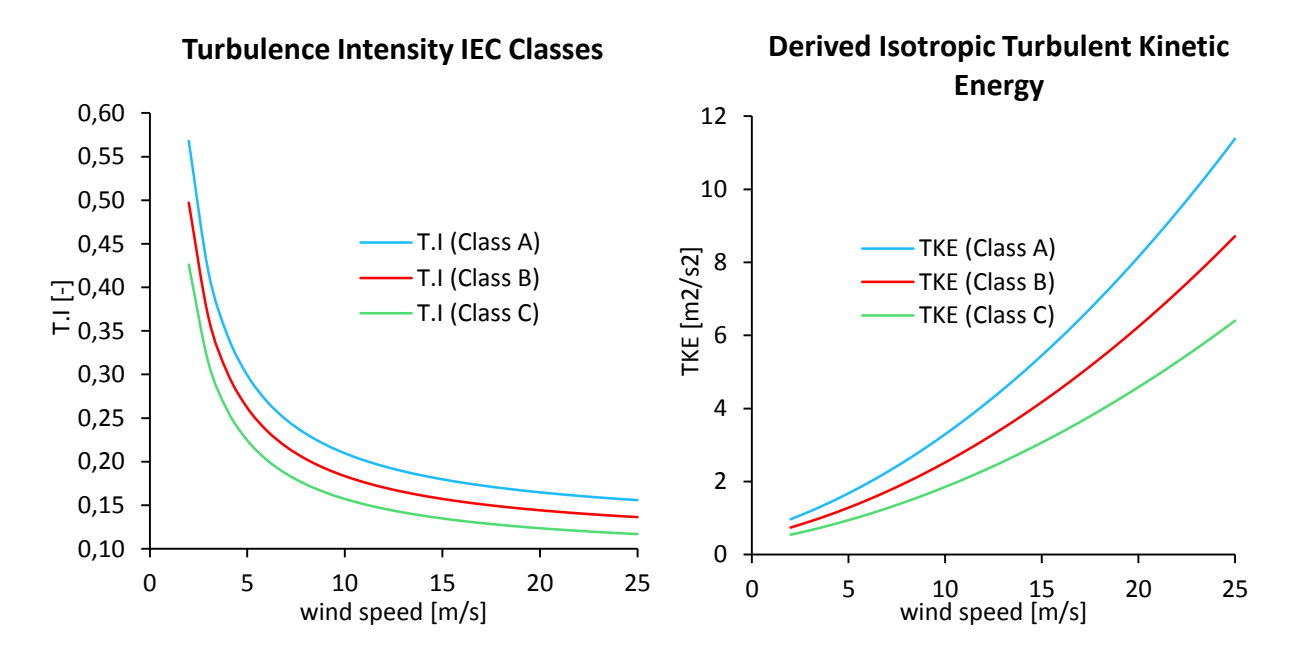


Figure 5: Turbulence Intensity (left) and Isotropic Turbulent kinetic energy (right) derived from wind turbine classes according to Equation 8. Reference turbulence intensities \emph{I}_{ref} of 0.16, 0.14, 0.12 for Classes A, B, and C.

In 1984, Panofsky and Dutton demonstrated that σ_u , and σ_v are proportional to the ratio of PBL height h_* to L_* during unstable conditions; see Equation 9. Under stable and neutral conditions, turbulence in the lower section of the surface layer is not strongly dependent on h_{st} but rather on the friction velocity u^* .

Unstable conditions:
$$\sigma_{u,v} = u^* \left(12 - 0.5 \ h_*/L_*\right)^{1/3}$$

$$\sigma_w = 1.3 \ u^* \left(1 - 3 \ z/L_*\right)^{1/3}$$
 Stable conditions:
$$\sigma_u = 2u^* \left[1 - (z/h_*)\right]^{3/4} \quad ; \quad \sigma_v = 2.2 \ u^* \left[1 - (z/h)\right]^{3/4}$$

$$\sigma_w = 1.73 \ u^* \left[1 - (z/h_*)\right]^{3/4}$$
 Neutral conditions:
$$\sigma_u = 2.5u^* \exp(-1.5 \ z/h_*) \quad ; \quad \sigma_v = 1.6 \ u^* \left[1 - 0.5(z/h)\right]$$

$$\sigma_w = 1.25 \ u^* \left[1 - 0.5(z/h_*)\right]$$

Equation 9: Wind speed variation in unstable, stable, and neutral conditions [38], [39].

Data suggests that the h_{st} is proportional the shear stress near the surface and inversely proportional to the coriolis factor under neutral conditions. But it depends on L_* as the atmosphere

A.M. Striedinger P. Master of Science Thesis becomes stable; see Equation 10. Under unstable conditions the h_* becomes dependent on the history of surface-heat flux H_{sf} to the air, and vertical wind speed [35]. Furthermore, measurements are needed to accurately describe the PBL height in unstable conditions.

> Neutral conditions: $h_* = 0.3 (u^*/f_c)$ $h_* = 0.4 (u^* L_* / f_c)^{1/2}$ Stable conditions :

Equation 10: Approximations of Planetary Boundary Layer height PBLH [35] [40].

2.1.2. Long time scale wind speed changes

Wind speed patterns change from month to month, altering the shape of local wind speed profiles over a region, from days to a complete season. Large forces determine wind speed direction, pressure, mean temperature changes and hence surface-heat fluxes. Moving pressure gradients disguised as pressure centers are developed and mix the air, their movement through large areas adds rotation to the winds in nearby regions of the pressure gradient (Figure 6). Wind circulates around and towards low pressure centers (L), whilst diverging from high pressure centers (H). The purple line in the figure represents the combination of two fronts separating air masses with very different temperatures; details about fronts are not explained.

Winds near high pressure regions, lower the local h_* and provide downward winds (see Figure 7). But when a low pressure centers passes, wind circulates towards the center and updrafts are generated from the surface layer. Additionally, local h_* increases, diminishing pollution and bringing rain near the pressure center.

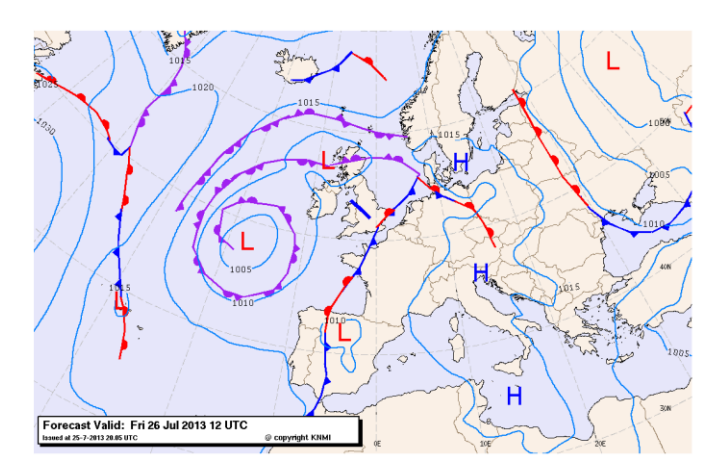


Figure 6: Example of High and Low pressure center distributions in Europe; taken from KMNI⁸. Blue lines represent cold fronts, red lines represent warm fronts, and purple lines represent the combination of both fronts. Triangles the direction from cold air to warm air, and the and semi-circles from warm air to cool air.

⁸ Visit http://www.knmi.nl/klimatologie/daggegevens/weerkaarten/index.cgi

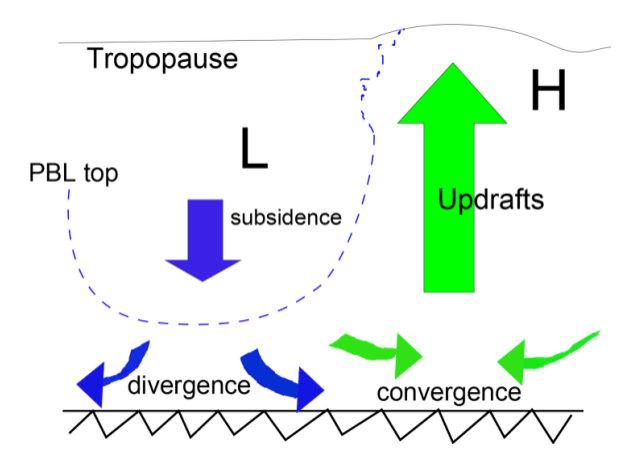


Figure 7: Effects of Pressure gradient on PBL height, low pressure center (left), and high pressure center (right), adapted from [27].

Wind speed variability is quantified by means of probability distribution functions; they are statistical fits for measured data over long periods of time, at certain heights. The most common function is the Weibull distribution; see Figure 8. Variability in wind speed direction is additionally presented in a polar plot commonly known as wind rose; see Figure 9.

Table 4: Probability functions of Wind Speeds for shape factors k, and scale parameters λ .

Category	Weibull Function
Cumulative for : ($V_i < V$)	$F = 1 - \exp\left[-\left(\frac{V}{\lambda}\right)^k\right]$
Frequency distribution for :	$k \left(V \right)^{k-1} \left[\left(V \right)^k \right]$
$(V - \frac{1}{2}dv < V < V + \frac{1}{2}dv)$	$f = \frac{k}{\lambda} \left(\frac{V}{\lambda} \right)^{k-1} \exp \left[-\left(\frac{V}{\lambda} \right)^{k} \right]$

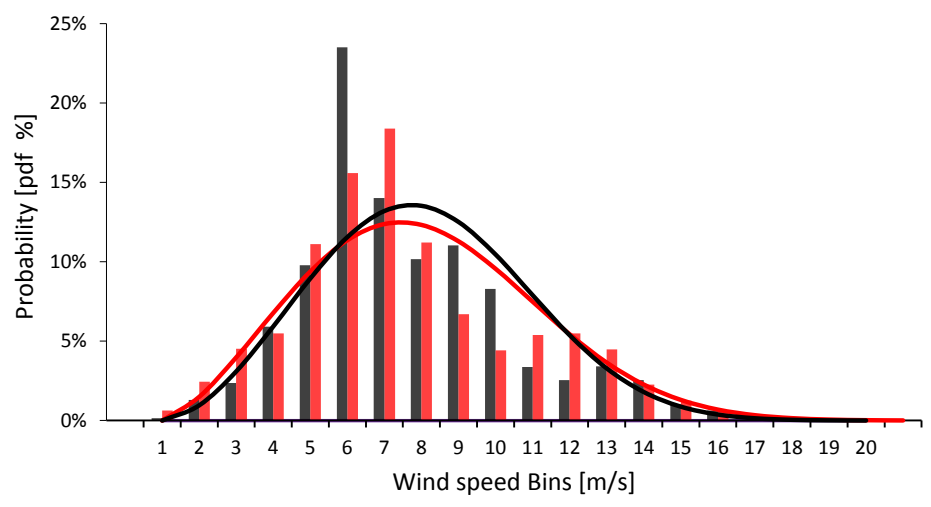


Figure 8: Histogram and Weibull Fit on Wind Speed probability distribution.

A.M. Striedinger P. Master of Science Thesis

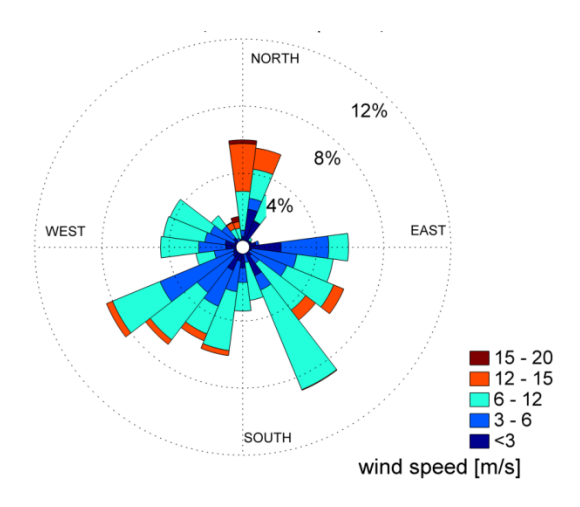


Figure 9: Radial wind speed percentile distribution on Midelgrundden Offshore wind farm in Denmark for the first 15 days of April 2001 (Wind Rose).

The directions from Figure 9 point to where the wind comes from: 0° points to the North, and 180° points to the South. Most of the measurements used for wind roses are done at 10 height, or close to hub height at a met mast located in the free stream.

Wind Turbine Basics 2.2.

The analysis of WTs can be simplified through the one-dimensional Momentum Theory, replacing the turbine by a drag disc, producing a pressure jump Δp and a velocity deficit across it. Wind speed is reduced as energy from the air is extracted through the rotor area (Figure 10). The reduction is represented with the axial induction coefficient a from Equation 11, influencing power and thrust by changing the power and thrust coefficients C_p , and C_T . The coefficients are functions of wind speed V_{∞} in the free stream, at hub height.

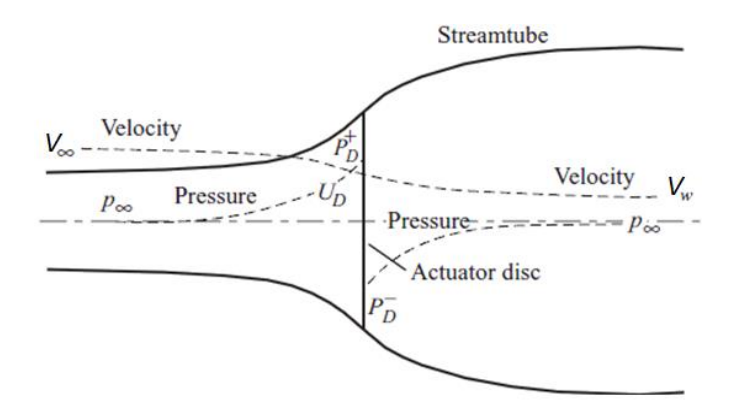


Figure 10: Actuator Disc scheme [40].

A.M. Striedinger P. Master of Science Thesis

$$P = \frac{1}{2} \rho A_{rot} (V_{\infty}^2 - V_{w}^2) U_2 = \frac{1}{2} \rho C_p V^3 A_{rot}$$

$$T = \dot{m_1} V_{\infty} - \dot{m_4} V_w = A_{rot} \Delta p = \frac{1}{2} \rho C_T V^2 A_{rot}$$

$$C_p = 4a(1 - a)^2$$

$$C_T \approx 4a(1 - a)$$

$$a = \frac{V_{\infty} - V_w}{2V_{\infty}}$$

$$0 < a < 1$$

Equation 11: Equations from Momentum Theory.

Experimental determination of the thrust coefficient is important due to its relation to fatigue damage and the incompatibilities of Momentum theory to describe heavily loaded rotor situations. Figure 11 shows the differences between C_p , and C_T curves from theory (ideal) and manufacturer's data; for that example, C_T is severely underestimated by theory. Unfortunately, low wind speeds occur more often that high wind speeds (i.e. 15 m/s). Therefore, turbine loading from a simple onedimensional momentum theory needs a modification if turbine data is not available.

When more detail is needed, lift and drag force distributions along the blades are required to express the torque, and thrust distributions on the turbine blades. The distributions depend on the relative wind speed V_{res} per blade section, which is a function of the flow speed, and turbine rotation Ω (Equation 12, and Figure 12). Consequently, force distributions on the blades are a function of a, an analogous tangential induction factor a', the angular twist of the blade θ , and the length of the blade section (Chord). Further, a' can be neglected if not much detail is needed.

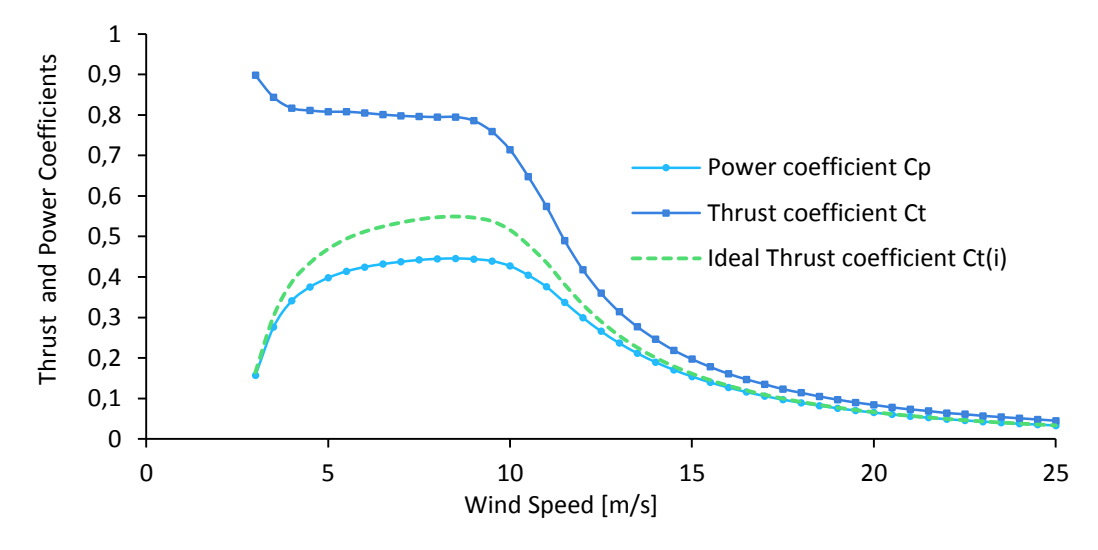


Figure 11: Performance Curves of 3MW Vestas V-112., 1.2 kg/m³ air density: ideal and real thrust coefficients from Equation 11, in relation to turbine power; adapted from [41].

A.M. Striedinger P.

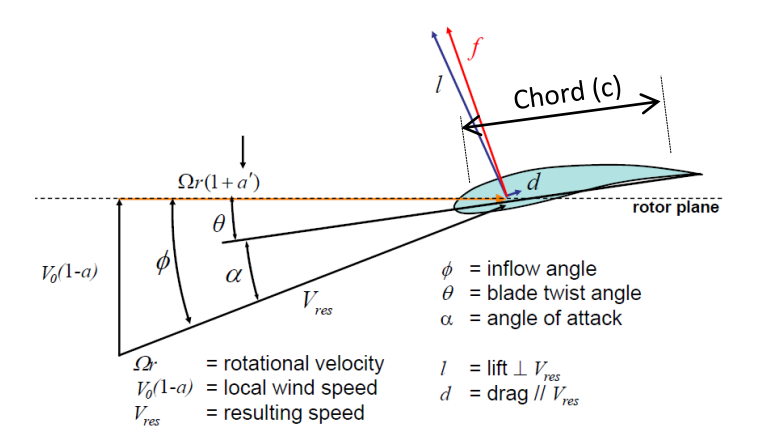


Figure 12: Blade Element Section. Incoming flow is represented by the local wind speed V_{or} in a perpendicular direction to the rotor area.

$$V_{res} = \sqrt[2]{V_o^2(1-a)^2 + [\Omega r(1+a')]^2}$$

Equation 12: Resultant wind speed on blade's immediate inflow field.

2.2.1. Model corrections to wind turbine analysis

Turbines experience unsteady effects such as Yaw Mismatch (out of range nacelle orientation), changes in the rotor Tilt Angle (with respect to horizon), and Heavily Loaded rotor situations. Power and thrust are also affected by tip and hub loses due to wake effects behind the turbine. Additionally, power loses due to tip and hub effects must be taken into account using correction factor F (Equation 13) that changes radially (Equation 14). Take for example its application in Figure 13, for a constant wind speed angle of 15° along the blades. These corrections are implemented in Appendix-D, to modify the current turbine parameterization scheme under evaluation. If necessary, the reader may jump to the next section.

$$C_T \approx 4aF(1-a)$$

$$C_p = 4aF(1-a)^2$$

Equation 13: Modified power and thrust coefficients from momentum theory.

$$F = \frac{2}{\pi} \cos^{-1} \left[e^{-f} \right] \qquad with \qquad f = \left[\frac{B(R-r)}{2r \sin \phi} \right|_{tip(r)} * \frac{B(r - R_{root})}{2r \sin \phi} \right|_{hub(r)}$$

Equation 14: Combined tip and hub loss correction factors in F, for Ct and Cp [41].

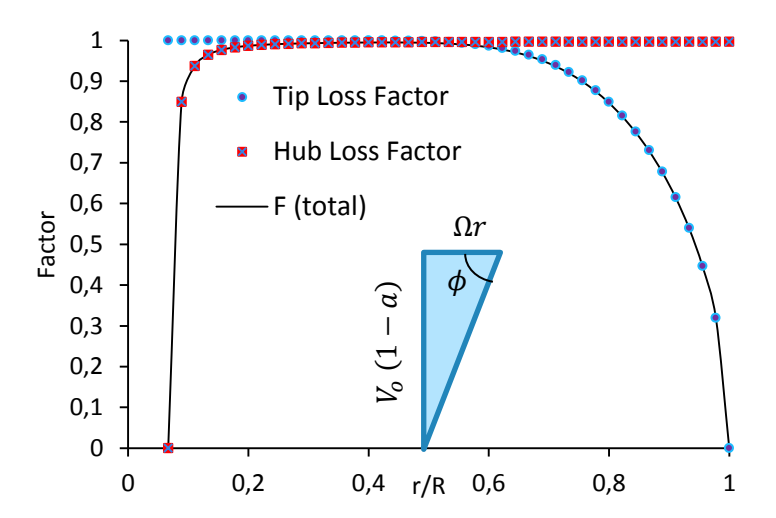


Figure 13: Modified Tip/Hub loss factor for Vestas V-90 blade at constant 15° inflow angle (ϕ) .

Heavily loaded rotor situations happen when a is greater than 0.4, but the rotor enters a turbulent state when a is greater than 0.5 [43] [44]. Flow from outside the wake enters and increases turbulence, so to account for this effect Glauert developed a C_T function based on a, and the loss coefficient factor F. The function has suffered changes since its conception, and the empirical modification by Buhl, yielding C_T values up to 2 is presented in Figure 14 and Equation 15 [43] [45].

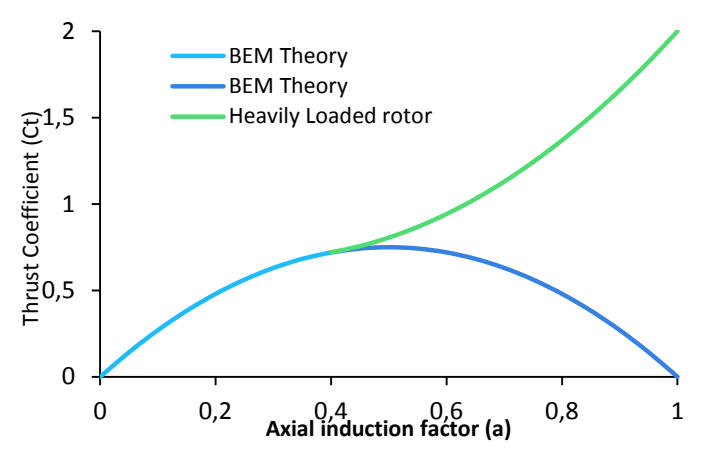


Figure 14: Effects of heavily loaded rotors for a correction factor F=0.75 due to tip effects only.

$$C_T = \frac{8}{9} + \left(4F - \frac{40}{9}\right)a + \left(\frac{50}{9} - 4F\right)a^2; \text{ with } a = \frac{18F - 20 - 3\sqrt{C_T(50 - 36F) + 12F(3F - 4)}}{36F - 50}$$

Equation 15: Thrust coefficient and axial induction factor corrections for heavily loaded rotor [45].. Use only for a>0.4.

The induction factor a for heavily loaded rotors is further corrected to account for Yaw mismatch (γ in Figure 15) by assuming steady inflow conditions with through Pit and Peters model used by NREL [43], modifying a into a_{skew} along the rotor blades. The model also accounts for rotor azimuth angle Ψ .

Rotor tilt angle β can also be included by replacing $\cos(\Psi)$ with $\sqrt{1-[\cos(\Psi)\cos(\beta)]^2}$ in Equation 16. This is because the reallocation of the blade has been titled down, and Ψ reduced to Ψ_2 (as projected on the rotor plane), and $r_{eq}\sin(\Psi_2)=r_{eq}\cos(\Psi)\cos(\beta)$. See that for $\beta=0$, Equation 16 is no longer modified. Tilt angles are provided in technical data sheets. But a simpler way to account for γ is to implement Glauert's correction based on momentum theory, changing C_p , and C_T in Equation 17.

$$a_{skew} = a \left[1 + \frac{15\pi r_{eq}}{32 R} \tan\left(\frac{\chi}{2}\right) \cos(\Psi) \right]$$
$$\chi \equiv (0.6a + 1)\gamma$$

Equation 16: Axial induction factor under Yaw mismatch γ and azimuth angle Ψ .

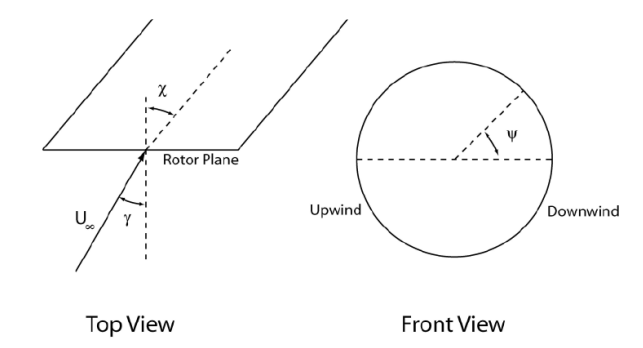


Figure 15: Rotor schematics for Yaw mismatch and azimuth.

$$C_p = 4a \left(\cos(\gamma) - a\right)\sqrt{1 - a[2\cos(\gamma) - a]}$$

$$C_T = 4a\sqrt{\sin^2(\gamma) + [\cos(\gamma) - a]^2}$$

Equation 17: Glauert's power coefficient based on momentum theory.

2.2.2. Basics of turbine wake development, and wake boundaries

Wake expansion determines wind speed deficits downstream of WT rotors¹⁰. This expansion is divided into two region: the near wake, and the far wake. The near wake region is a mixing region where velocity deficits are maximum, and there is no definite wind shear profile. The far wake, on the other hand, shows more definite profile along the region.

If the fluid dynamics is simplified, the Jensen model for wake expansion in Equation 18 and Figure 16 may be implemented. Further, the model does not distinguish between the near wake and the far wake. Rather, the wake is treated as the far wake only. The model considers an independent linear expansion of the wake. It further relates downstream hub height wind speed to C_T , rotor diameter D, the wake width, the turbine area exposed to the wake, and a tunable parameter k. According to DTU, a k of 0.05 is

⁹ Pit and Peters formulation has been modified an implemented in NREL's Blade Element Momentum Program

¹⁰ Remember the definition of wake presented in the introduction, as the spiral/ helical profile of the wind speed behind the rotor area.

recommended for offshore locations, whilst a k of 0.75 is for on-shore sites [46]. In Equation 18, $\left(\frac{A_{rea_int}}{A_{wt1}}\right) = 1$ serves for the description of a single turbine wake.

$$V_{\infty} = V_o \left[1 - \left(1 - \sqrt{1 - C_T} \right) \left[\frac{D_o}{D_o + 2kx} \right]^2 \left(\frac{A_{rea_int}}{A_{wt1}} \right) \right]$$

Equation 18: Jensen's wake model.

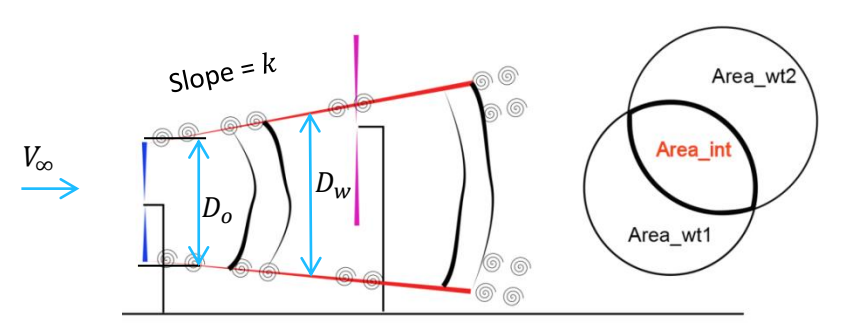


Figure 16: Jensen's wake model. Wake boundaries are defined by the red lines, and slope k for turbines wt1 and wt2.

To identify the origin on the far wake, Vermeulen [50] proposed an empirical relation for the length x_n of the near wake region, see Equation 19. It considers the contribution to wake growth from the atmosphere, shear generated-turbulence, and mechanical turbulence induced by the rotor: $\left(\frac{dr}{dx}\right)_{\alpha}$, $\left(\frac{dr}{dx}\right)_{m}$, $\left(\frac{dr}{dx}\right)_{\lambda}$; the expression is further detailed in Appendix-D. Consequently, analysis of the far wake corresponds to phenomena at distances larger than x_n .

$$x_{n} = \frac{n r_{o}}{\sqrt{\left(\frac{dr}{dx}\right)_{\alpha}^{2} + \left(\frac{dr}{dx}\right)_{m}^{2} + \left(\frac{dr}{dx}\right)_{\lambda}^{2}}}$$

Equation 19: Vermeulen's Expression for the near wake region X_n in terms of atmospheric turbulence intensity, turbine tip speed ratio, rotor diameter, and thrust coefficient.

In the far wake, Figure 17.a suggests an quasi axisymmetric development of the wind speed, such that profiles are nearly Gaussian. Maximum speed deficits in this region are located below hub height due to the presence of the turbine tower [44]. For example, deficits at 7 D are less than 10% of the free stream. Commonly, the far wake ends from 10 D to 15 D, but safe distances could reach 20 D [22]. Finally, turbulence in the far wake is minimum [48].

The distinction between the near wake and the far wake is uncertain. But often times, the near wake has a length of 2 – 5 D [44] [47], and the far wake starts form there on. Generally, mixing in the near wake takes place at its boundaries as it expands. Hence, air from the atmosphere mixes toward the center of the wake with two peak zones of increased turbulence intensity: the upper and lower boundaries of the wake, i.e. line of 2.5 D in Figure 17.b. In it, added turbulence decreases in the downstream, but is still present near the surface.

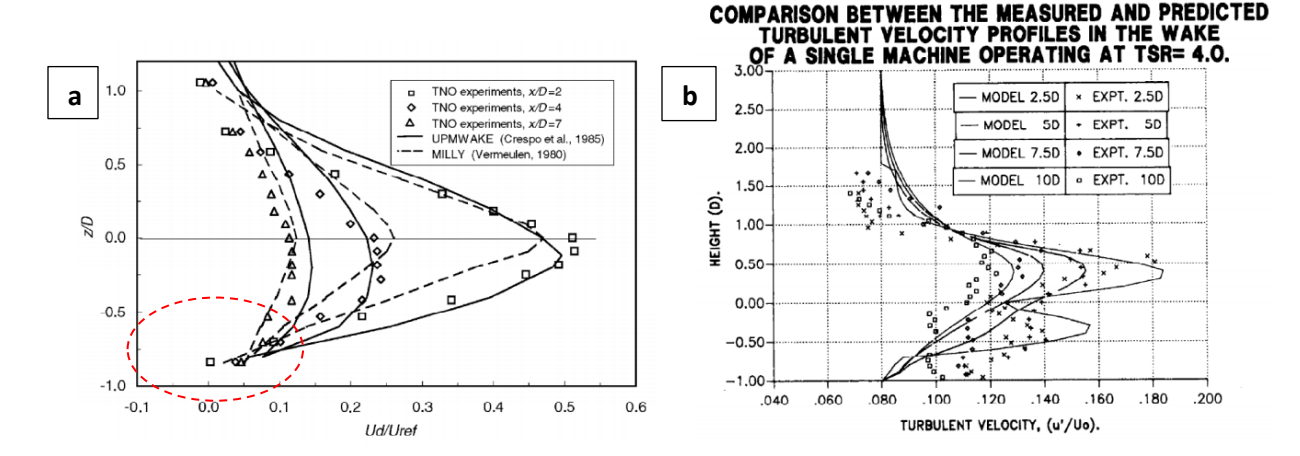


Figure 17: Turbulent velocity ratios to free stream (a) [49]. Downstream wind speed deficit speed profiles from a turbine (b) [26].

It is possible for winds near the surface to increase, as indicated by the red dotted circle in (a) for example; see x/D = 2 line (negative values of speed deficit). The increase is attenuated as a speed profile develops (lower sections in Figure 17.a, Figure 17.b). A wind tunnel experiment of a small scale array of WTs shows an increase of near-surface wind speed as a local phenomenon, affecting the profile near the ground; see green arrows in Figure 18. Figure 19 shows a simple wall-correction model for WTs tested inside an open wind tunnel section, and explains the principle behind the increase of near-surface wind [51]. Key features of this model are an algebraic expression for the axial momentum exchange between the wind tunnel and the room environment, and an expression suggested by Glauert [52] relating wind tunnel speed V_0 to an equivalent free stream speed V_{∞} . The model was verified with NS simulations and validated with measurements from a 500 kW Nordtank WT.

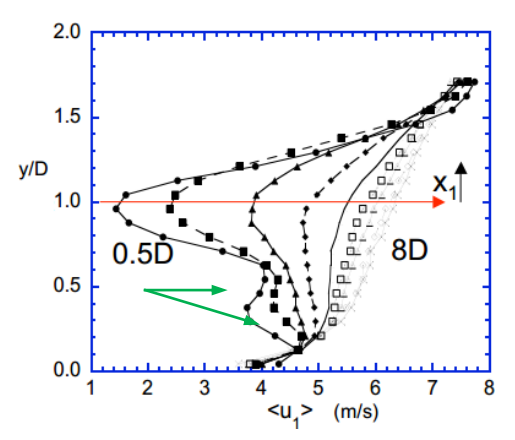


Figure 18: Wind speed profile behind a small scale WT in a row. The experimental set up uses a rotor diameter D of 12 cm and a hub height of 1 D [53]. The green arrows point to a sudden change in wind speed.

Master of Science Thesis A.M. Striedinger P.

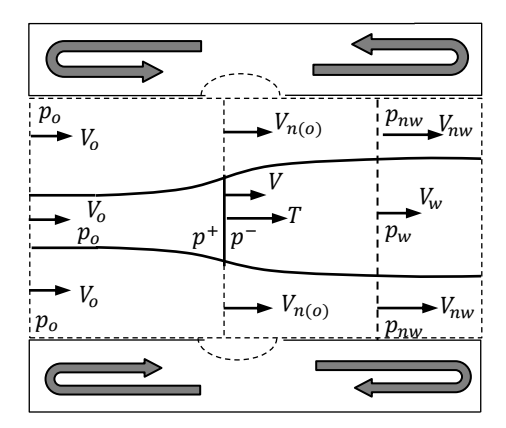


Figure 19: Sketch of rotor disc stream tube in wind tunnel with an open cross section [51]. The grey arrows indicate air recirculation near the wind tunnel walls.

Wind speed through the rotor disk decreases from V_o to V_w , and wind speed neat the tunnel walls V_n increases to V_{nw} due to mass conservation principle on the control volume of Figure 19 ($V_{n(o)} > V_o$, $V_{nw} > V_w$). The increase of V_n is higher for closed regions, as marked by the dotted lines. The momentum exchange between the wind tunnel and the room environment is proportional to C_T , and so is the increase in V_n , that for open sections is less than the tunnel speed V_o as the outer flow expands away from the wake boundaries. From here on, speed-up effects will represent the increase in wind speed in other regions due to the mass conservation principle. An example of speed-up effects inside a large offshore wind farm is presented in Chapter-4.

Another topic, is the flow vorticity, identified as 2 times the angular velocity vector of the flow at a center point; such center point may be fixed or moving in space. Vorticity can be generated when two currents flow parallel to each other, at a different speeds (i.e. shear flow). Such that the current with the highest speed starts to rotate inwards to the current of lowest speed (clock or anti-clockwise rotation, negative or positive). See Figure 20.

To better identify WT wakes, it is necessary to mark the boundaries of their expansion, and such is better expressed through vorticity plots behind the rotor. Vorticity plots in Figure 21 make a clear distinction between the flow inside and outside of the wake. The wind inside the wake is slower than that outside the wake, creating positive and negative vorticity at wake boundaries. For example, in a laminar flow of a pipeline with constant cross section the fluid goes parallel to the pipe axis. Faster at the axis, and almost stationary near the walls. The vorticity for this case will be zero at the axis, and maximum near the walls (shear is largest).

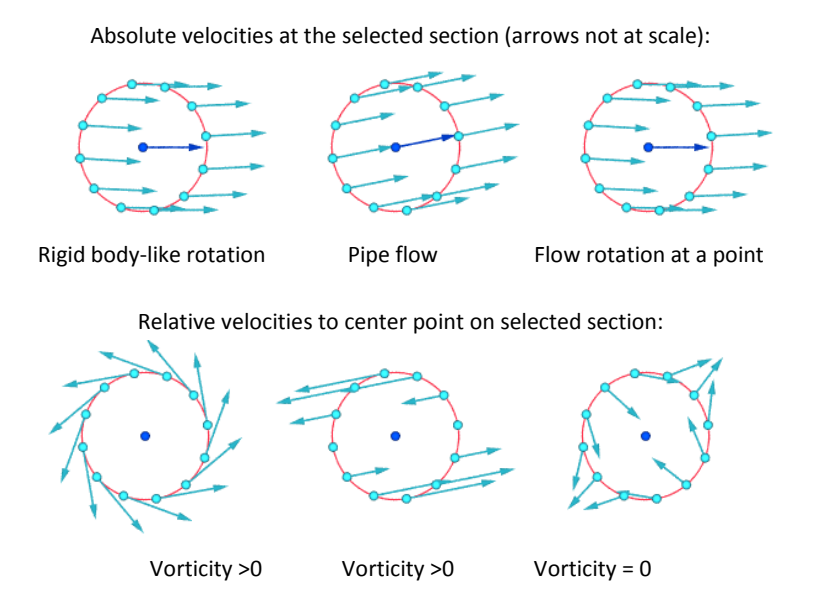


Figure 20: Examples of vorticity for different flow cases (vorticity points). Flows shown in (a), absolute velocities at a selected section are shown in (b), and relative velocities to the center point are shown in (c). Lines in (a) show the flow paths with fluid particles on it. The images are extracted from the web. Negative vorticity is anti-clockwise.

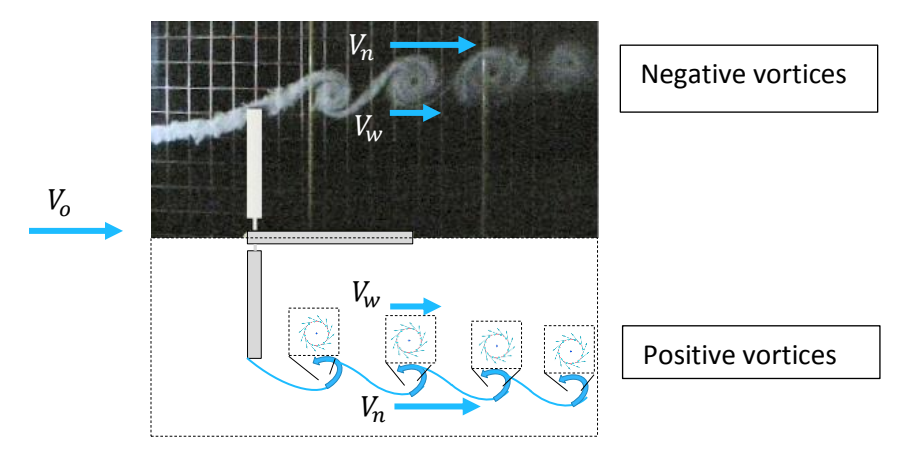


Figure 21: Smoke visualization photo showing tip vortices downstream a rotor. Flow orthogonal to rotor plane. Tip ratio of 8, and blade pitch angle of 2°, vorticity ≠ 0; Adapted from [54]. Arrows indicate wind speed, in the inflow, in the wake and outside the wake.

2.2.3. Wind turbine wakes inside turbine arrays

Wake effects are intensified inside arrays, and are responsible for power losses. Wind speed behind the rotors will experience a slower recovery than the expected behind a single wake. WTs in a row along the flow direction are named in-line WTs, and the wake effects in single in-line WTs are named single wake interference (SWI) because all wakes travel across the rotors without much deviation. When the deviation is such that the wake interference of in-line WTs affects neighboring WTs, the effects will be named parallel wake interference (PWI). A description of SWI, PWI and parallel SWI is presented in Figure 22. In PWI the wake boundaries from transverse WTs mix together. For parallel SWI, transverse

wake boundaries do not intercept but share the same outer flow. Such circumstance makes it possible to treat rows independently (i.e. Jensen Wake Model).

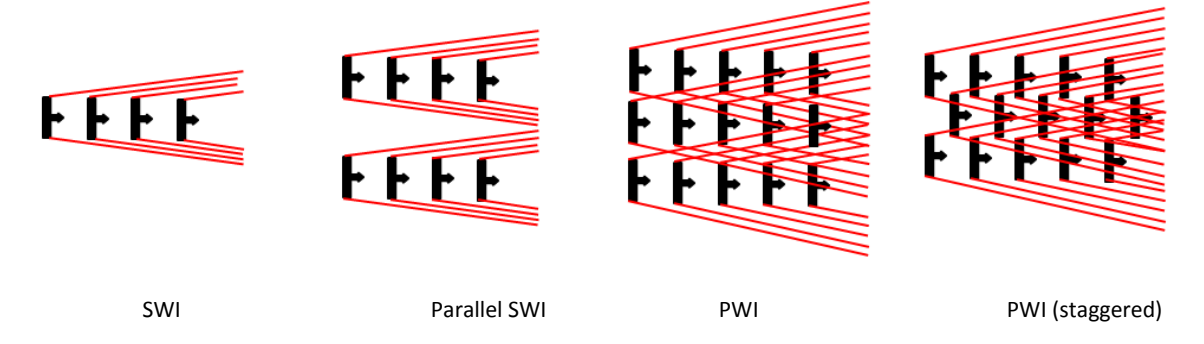


Figure 22: Wake interferences inside turbine arrays. Single Wake Interference (SWI), Parallel SWI, Parallel Wake Interference (PWI), and PWI on turbine array staggered configuration. Wake boundaries are drawn as red, and have been linearized.

Wake development has financial repercussions on wind farms because it determines the turbine layout. Take for example a recent analysis by J. Meyers and C. Meneveau [19] suggests an average spacing of 15 D between WTs is more suitable than the conventional range 7-10 D. Numerical CFD models are time consuming and therefore not feasible for every problem. The Jensen model is also used when analyzing wind farms (linearized PWI cases as well), but models based on local aerodynamic roughness are widely used in practice because they allow for flow simplifications.

$$Loses = 1 - \frac{P}{P_o}$$

Equation 20: Power or array losses in LES simulation from [55].

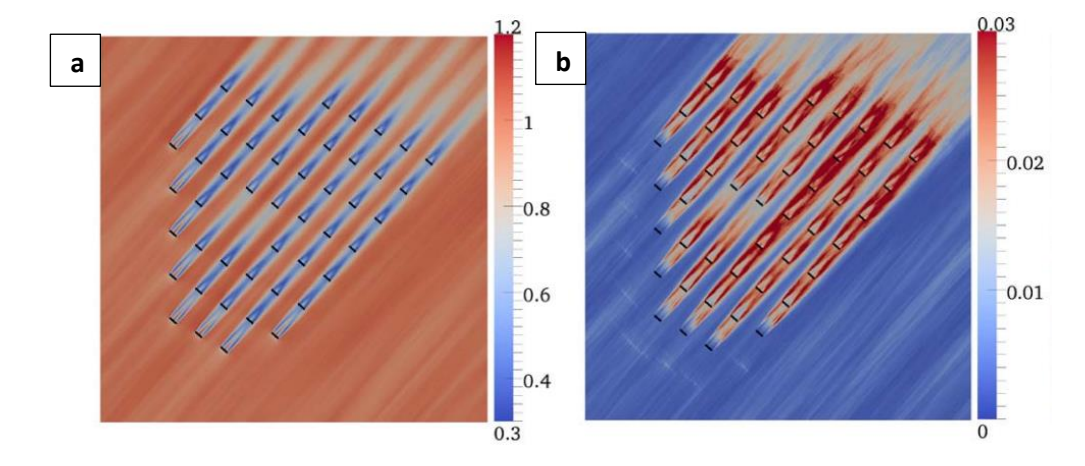


Figure 23: Parallel SWI as simulated with LES on Lillgrund offshore wind farm. Time averaged wind speed contour is normalized to hub height wind speed in (a). Turbulent kinetic energy contour is normalized to hub height wind speed squared in (b) [56].

An example of parallel SWI is shown in Figure 23, suggesting 35.51 % array losses with 33.4 MW of total production [55]. Where loses are defined with the average power of turbines P, and the average power of the turbines facing the free stream P_o (Equation 20); losses can be very large for faulty layouts. LES simulations also indicate that turbulence increases downstream until it becomes nearly isotropic.

The average speed deficits in the parallel SWI shows the same pattern as in Figure 22. PWI effects are more difficult to find.

Turbulent kinetic energy is related to the ambient turbulence intensity at hub height as in Equation 7, and has been a subject of study. Recognized models for the turbulence intensity behind WTs are those by Quarton and Ainslie in 1989, relating C_T and undisturbed turbulence intensity I_0 ; the model developed by Crespo and Hernandez, later modified by Hassan in 1992; and finally the model for added turbulence intensity ΔI_0 in the deep array proposed in 1999 by Thogersen and Frandsen presented in Equation 21, and Equation 22 [57] [58] [59].

$$\Delta I_o = \frac{1}{2} \left(I_o + \sqrt{I_o^2 + \left(\frac{0.36}{1 + 0.2\sqrt{s_1 s_2/C_T}} \right)^2} \right)$$

Equation 21: Added Turbulence Intensity turbine array per WT location; by Frandsen et al. [58].

$$I_{(u,x)} = \sqrt{I_o^2 + 0.129 \left(\frac{0.36}{1 + 0.2\sqrt{s_1 \xi/C_T}}\right)^3} \quad for \ 0 \le \xi \le s_2$$

Equation 22: Spatial development of turbulence intensity behind a WT. Downstream distance marked as ξ .

Frandsen's model accounts for turbine spacing s_1 and s_2 : transverse and in-line distances in rotor diameter ¹¹ respectively. However, the time dependence of turbulence intensity is not treated. Only the spatial development of the turbulence is accounted for in Equation 22. When taking I_o as the free stream, ΔI_o results in an average value for the turbine layout, but I_o is also taken from the upstream turbulence of each WT in the array. Turbulence intensities $I_{(u,wt)}$ at each WT can therefore, gradually increase or remain nearly constant. See more in Appendix-D.

2.3. Available Software for Wind Turbine and Wind Farm Simulation

There is a variety of software tools for design considerations such as XFOIL¹² developed by MIT and enhanced by ECN and TU Delft as RFOIL-3D to account for dynamic stall in blade profiles, a phenomena during which lift and drag coefficient behave out of data range (sudden drop in lift). Others are QBlade from TU Berlin, PROPID by the University of Illinois at Urbana-Champaign, and FAST and AeroDyn developed by NREL¹³. There are more open-source programs available, nevertheless only few of them are dedicated to analyze wind farms. Programs to be considered prominent in such analysis are WindPro

¹¹ For a detail expression of turbulence intensity as a function of downstream turbine spacing go to page 23, 24; equations 3.5 and 3.6 of [58].

¹² Visit http://web.mit.edu/drela/Public/web/xfoil/ to download XFOIL

¹³ Visit http://wind.nrel.gov/ for the suite of CAE tools available from NREL.

by EMD International, WAsP¹⁴ developed by the Wind Energy Department at DTU in Denmark, the CFD tools of FUGA and EllipSys also developed by DTU, WINDFARMER by GL Hassan, and SOWFA by NREL. Only SOFA and WindPro are open under the General Purpose License.

WindPro has three different wake models available, and one of them is Jensen's model but modified to account for different turbine heights and diameters in the same layout. The program can also use WASP as a calculator engine. The last is based on a geostrophic wind model, and ideal aerodynamic roughness at turbine sites; however the program now has evolved to include a CFD approach as well. Windfarmer, uses the model of Ainslie. SOFA uses CFD modeling for the atmospheric flow and combines it with its program FAST for blade calculations by modeling the turbine as an Actuator Line using lift and drag coefficient data from manufacturers. Furthermore, the aim of NREL (according to their website and presentations) is to couple WRF for the atmospheric input, OPEN-FOAM for the flow inside the wind farm and FAST for the turbine-flow interaction.

The program EllipSys is a home-built CFD tool that uses the RANS steady k-epsilon turbulence model as well as OPEN-FOAM but, it differentiates on its mesh generation package with no restrictions in geometrical aspect ratios, allowing for a smaller convergence time than Open-Foam [60]. More programs exist within the academic community, and for a general overview the reader is directed to [61].

The program WRF, short for Weather Research and Forecasting, has been updated with two recent turbine parameterization schemes to model wind farm effects in the atmosphere. The parameterizations were separately incorporated to WRF by Jimy Dudhia from UCAR, and Volker, Badger, Hahman, and Ott from DTU [62]. The last parameterization however, does not come in the standard package of WRF, only Dudhia's parameterization. It uses the Fitch scheme based on a Drag Disc concept, relating TKE changes to changes in thrust and power coefficients. Whereas Volker et al. produced a wind farm parameterization scheme independent of the meso-scale fluid model, and relying on classical far wake theory assuming that the far wake region can be described by means of a characteristic length (l) and a maximum velocity deficit (U_s). Their model has the advantage of being site specific, and their results were later plotted against measured wind farm data at Horns Rev and the Fitch scheme predictions.

2.4. **Numerical Weather Prediction**

Numerical weather predictions (NWP) exist to forecast climatological effects on local or global regions. There are 6 steps towards an accepted forecast: Gather observations, perform data assimilation, do numerical weather predictions, create the forecast with NWP model, do post processing, and evaluate final forecast [62]. The purpose of the data assimilation is to correct the forecast solution done by the NWP model by providing initial and boundary conditions. Every NWP model has its roots on solving the Navier-Stokes full equations of motions under certain assumptions: Hydrostatic (H), Quasi-Hydrostatic (QH), and Non-hydrostatic (NH) formulations. But, in all formulations the vertical coordinate is a derived

¹⁴ Visit http://www.wasp.dk/ for form information.

quantity from the hydrostatic pressure. The NH formulation is the complete Navier-Stokes formulation or the Euler equations (NS + heat conduction term, for inviscid fluid). The QH formulation neglects only the temporal changes and vertical velocity gradients, and any other external forcing in the vertical direction. The H formulation further neglects the cosine terms of the coriolis forces in the governing equations, where wind rotational effects at the earth poles result the same as those at the equator [63]. Consequently the H and QH formulations downgrade 3D flow situations into 2D problems. At the end, every formulation is expressed in a set of 7 equations to apply their assumptions:

- Equation of motion in the East-to-West direction
- Equation of motion in the North-to-South direction
- Equation of Temperature
- Equation of Humidity
- Equation of Continuity of mass
- Equation for the Surface pressure evolution

Regions of interest for NWP models are simulated in a computational grid shared inside a computer network. NWP models works on grid resolutions as coarse as 40x40 km, but are also used for high resolution grid from 1 to 2km grid cells. In the meteorological community, the resolution is often described in degrees of arc and not in km. That is to have a standard unit of resolution on the spherical earth. For practical purposes there is no difference, but computationally it simplifies the grid structure (more uniform spherical grid). The arc distance of 1° is constant (~ 111 km) along lines of constant longitude, but changes from 0 km to 111 km between the pole and the equator as shown in Table 5 along latitude lines.

Table 5: Length of 1° of Longitude along latitude lines of constant latitude

Latitude (°)									
Kilometers	111	109.6	104.6	96.5	85.4	71.7	55.8	38.3	19.4

NWP models use parameterization schemes to simplify and quickly find the solutions to the equations of motion. They also simplify sub-grid phenomena by relating their effects to variables at the grid scale. Examples of parameterizations are those for land surface (surface roughness approach), cloud microphysics, turbulent diffusion and air-surface interactions, radiative heat transfer, and drag on mountains. A common factor among NWP models is the increase of uncertainty with time: a next day forecast is generally more accurate than a 5-day forecast. Two major sources of uncertainty exits: Chaos, and model error [62]. Chaos plays a major role in the 5-days example of uncertainty, whilst model errors occur due to the lack of precision of the equations to capture specific details. Model error, like cloud positioning, which can alter results on precipitation forecasts. Further, missing values inside input data due to lack of weather observation points over the ocean and at mountains limit NWP accuracy.

Examples of global models are those from the European Center for Medium-Range Weather Forecasting (ECWMF) with a 40 km resolution grid, the Unified Model (UM) from the United Kingdom Meteorological Office with a 40 km resolution up to 4 km just for England (6-day forecast), and the NOAA's Global Forecast System (GFS) with a 35-70 km resolution grid. For regional climate The North American Meso-scale Model and the 12-hour forecast model Rapid Update Cycle (RUC). Finally, for high resolutions researchers use the Meso-scale Model v5 (MM5) with a maximum resolution of 4 km, the High Resolution limited Area Model (HIRLAM) up to 5 km resolution grids, and another example is WRF with proven maximum resolutions of 200 m.

Fitch Turbine Parameterization Scheme 2.5.

Ulrich Blahak [11] presented a model in the EWEC 2010 conference for a simple turbine parameterization on NWP models, in order to calculate the velocity deficits and energy changes within the local PBL. WTs are distributed in a grid and the vertical axis is denoted as height levels in the z direction. Only the rotor area, C_T , C_P are relevant for the parameterization.

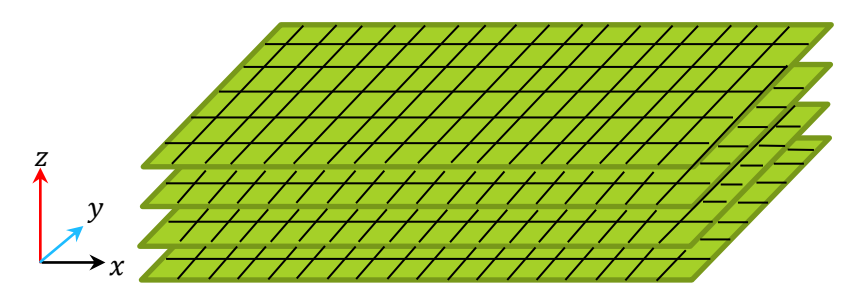


Figure 24: Grid representation of terrain and height levels z_k in Cartesian coordinates. Each plane represents a grid area at a certain height. Grid cells are contained between planes.

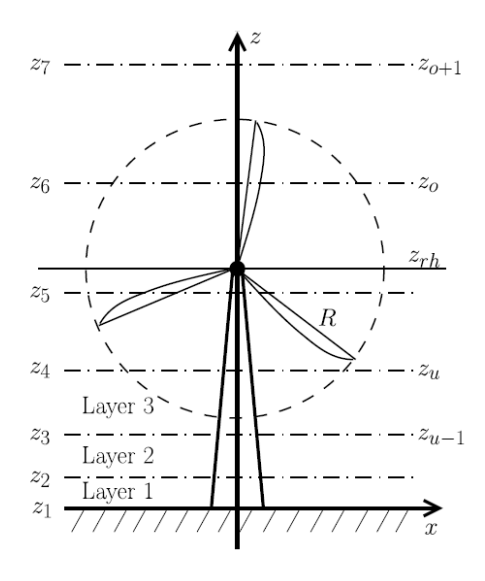


Figure 25: Schematic depiction of a WT and a typical vertical grid configuration; taken from [11].

Once WTs are distributed, each section of the rotor area intersecting a grid cell is considered as a source of turbulent kinetic energy and a region where kinetic energy decreases due to power extraction; see Figure 24, and Figure 25. Consequently, an immediate decrease in velocity occurs in the grid cells intersecting any rotor section, which affects the momentum balance equations in the surrounding grid cells.

Changes in the total kinetic energy $(KE_{wt}|_{tot})$ are expressed as a function of C_p , and a proportionality variable α is used to formulate the increase of the turbulent kinetic energy of the local atmosphere $(TKE_{wt}|_{atm})$. Both energy quantities account for the total energy change $(E_k|_{tot})$ in the local PBL; see Equation 23, and Equation 24. The analysis begins by evaluating the energy changes at the grid cells intersecting the lower tip blade section (Layer 3 on Figure 25), and continues in the vertical coordinate. The sub-indexes on all figures and equations indicate the coordinate to which the variables correspond (x, y, z respectively) with grid cells defined by their corresponding coordinate dimensions $(\Delta x \Delta y \Delta z)$. Additionally, each grid location has a turbine density factor value controlling the number of wind turbines it hosts (N_{tc}).

$$\left. \frac{\partial K E_{wt}}{\partial t} \right|_{\langle i,j,k \rangle} \right|_{atm} = \left. \frac{\partial}{\partial t} \left(\frac{1}{2} \rho V^2 \Delta x \Delta y \Delta z \right) \right|_{\langle i,j,k \rangle} = \rho V \left(\frac{\partial V}{\partial t} \right) (z_{k+1} - z_k) \Delta x \Delta y \right|_{\langle i,j,k \rangle}$$

Equation 23: Discretization of kinetic energy equation with coordinate system as (i,j,k).

$$\left. \frac{\partial KE_{wt}}{\partial t}_{ijk} \right|_{atm} = -\frac{C_p \rho V^3 A_{rot}}{2} \bigg|_{ijk} * N_{tc \langle i,j \rangle}$$

Equation 24: Final Equation for Energy Change per grid cell (i,j,k), and each A_{rot} indicates a rotor section are intersecting any grid cell like that in layer 3 from Figure 25.

The density factor $N_{tc (i,j)}$ is set constant, or different per grid location to approximate the real turbine layout configuration. On Blahak's proposal, $N_{tc \langle i,j \rangle}$ is considered constant. The final expressions for wind speed added changes are shown in Equation 25, as a result, the change in each wind component (u, v) is found by multiplying its corresponding fraction from the net wind speed; see Equation 25.

$$\begin{split} \left. \frac{\partial V}{\partial t} \right|_{\langle i,j,k \rangle} &= -\frac{C_p V^2 A_{rot}}{2(z_{k+1} - z_k) \Delta x \Delta y} \bigg|_{\langle i,j,k \rangle} * N_{tc \, \langle i,j \rangle} \\ \left. \frac{\partial u}{\partial t} \right|_{\langle i,j,k \rangle} &= \frac{u}{V} * \left(\frac{\partial V}{\partial t} \right) \bigg|_{\langle i,j,k \rangle} \; ; \; \left. \frac{\partial v}{\partial t} \right|_{\langle i,j,k \rangle} = \frac{v}{V} * \left(\frac{\partial V}{\partial t} \right) \bigg|_{\langle i,j,k \rangle} \end{split}$$

The change in TKE is set proportional to the total change in kinetic energy per grid cell through the coefficient α in Equation 26. Blahak considered $\alpha=0.2$ as an acceptable value, but also set limits to it: $0 \le \alpha \le (1 - C_p)/C_p$. Nonetheless, the value of α is to be found experimentally [11]. Further, Fitch et al. [12] proposed α as $(C_T - C_p)$ to make it turbine, and wins peed dependent, whilst maintaining energy conservation. Consequently, the change in mechanical energy of the flow is solely a functions of turbine thrust, a fraction is extracted for power production, whilst the remaining is transformed into TKE. See Equation 27 where TKE is divided by $[\rho \Delta x \Delta y (z_{k+1} - z_k)]$ to make it per unit mass.

$$\left. \frac{\partial TKE}{\partial x}_{ijk} \right|_{atm} = -\alpha * \left(\frac{\partial KE_{wt}}{\partial t}_{ijk} \right|_{atm} \right) = \frac{\alpha C_p \rho V^3 A_{rot}}{2} \bigg|_{(i,i,k)} * N_{tc \langle i,j \rangle}$$

Equation 26: Expression for Turbulent Kinetic Energy per grid cell and Fitch expression for coefficient α .

$$\left. \frac{\partial V}{\partial t} \right|_{\langle i,j,k \rangle} = -\frac{C_T V^2 A_{rot}}{2 \Delta z} \bigg|_{\langle i,j,k \rangle} * N_{tc \langle i,j \rangle} ; \qquad \left. \frac{\partial TKE}{\partial x} \right|_{ijk} \bigg|_{atm} = \frac{\left(C_T - C_p \right) \rho \ V^3 A_{rot}}{2} \bigg|_{\langle i,j,k \rangle} * N_{tc \langle i,j \rangle}$$

Equation 27: Fitch's expression for Turbulent Kinetic Energy per grid cell and change in wind speed.

Fitch et al. obtained qualitative and some quantitative agreement with wind speed deficits in a simulation of the wake downstream of an ideal offshore wind farm. The offshore site is to resemble flow effects from large turbine arrays like the Thanet Offshore wind farm in the UK. But data from the 5 MW Repower Turbine was used: a 126 m rotor diameter and 100 m hub height, covering an area of 10 km × 10 km ,and with operational wind speeds of 3.5 and 30 m/s. The flow physics was simplified by neglecting surface heat and moisture transfer, using a second order scheme for turbulent mixing, and the Charnock's relation for surface roughness on the sea (left hand of Equation 3), 10 m/s geostrophic wind with no meridional component at any height, and slightly deviated from the horizon [12].

Fitch's results were compared with measurements at Horns Rev and Nysted offshore wind farms in Denmark. However, both wind farms are smaller than Thanet wind farm. Fitch's simulations showed 10% wind speed deficit at hub height 10 m from downstream flow, which is closed to the measured data from Horn Rev and Nysted. Fitch also found persistent speed deficits within the Wind Farm, and a nonsymmetric power efficiency distribution within the turbine array. Velocity plots in Figure 26 indicate ideal speed profiles up to 600 m above sea level (4 D above hub height). Despite results from Fitch et al., no validation has been done with this model that is available in literature, except for the comparison done by Volker et al. from DTU [62]. Hence, most of the quantitative data from Fitch can only be used qualitatively. Yet, they reveal interesting phenomena:

- 👃 A speed-up effect near the surface, and shifted away from the main flow direction (Figure 26-a).
- Additional speed-up effects in the wake boundaries of the farm: upper and lateral sections (Figure 27-a, and Figure 27-b respectively).

Decrease of turbulence in the horizontal direction in the farm downstream, and the main increase of turbulence is in the vertical direction (see Figure 27-d).

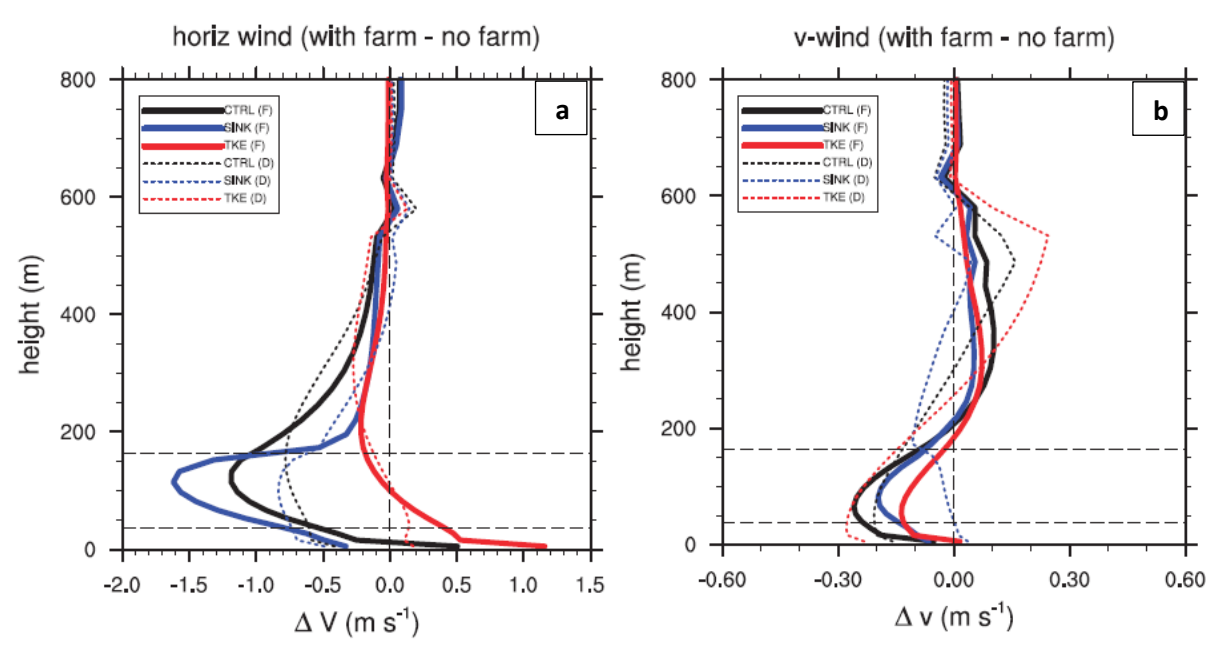


Figure 26: Vertical wind speed profiles differences with the Fitch scheme on the Thanet offshore wind farm, v-wind is the meridional wind (in the horizontal plane). The control mode for which all energy change is considered (CTRL, black lines), momentum sink only (SINK, blue lines), TKE source only (TKE, red lines). The solid lines denote profiles over farm; dashed lines indicate profiles 10 km downstream, and the horizontal dashed lines show the rotor area [12].

The profiles in Figure 26 are a result of isolating the farm effects from the BACKGROUND case (without wind farm). In subsequent chapters the isolated farm effects are denominated as FARM -BACKGROUND for all the case studies. The figure further shows how the flow moves upward to circumvent the farm as is forced to increase its speed at high altitudes. Unfortunately, results from variations in vertical and horizontal resolution reflected high sensitivity towards grid spacing in the horizontal directions, and overestimation of the TKE. The final formulation by Fitch and Blahak does not include rotational effects, the nacelle orientation is not considered either. The turbine density factor $N_{tc\langle i,i\rangle}$ of wind turbines also restricts the model to certain layouts of wind farms.

The Fitch scheme is the current turbine parameterization under evaluation and will be used to analyze the interaction between neighboring wind farms in the Dutch sea. The program using the flow model and the parameterization scheme will be introduced in the next chapter. A clear understanding of how the program simulates the meso-scale atmosphere is key for understanding the uncertainties and limitations of the results here presented, and those discussed in subsequent chapters.

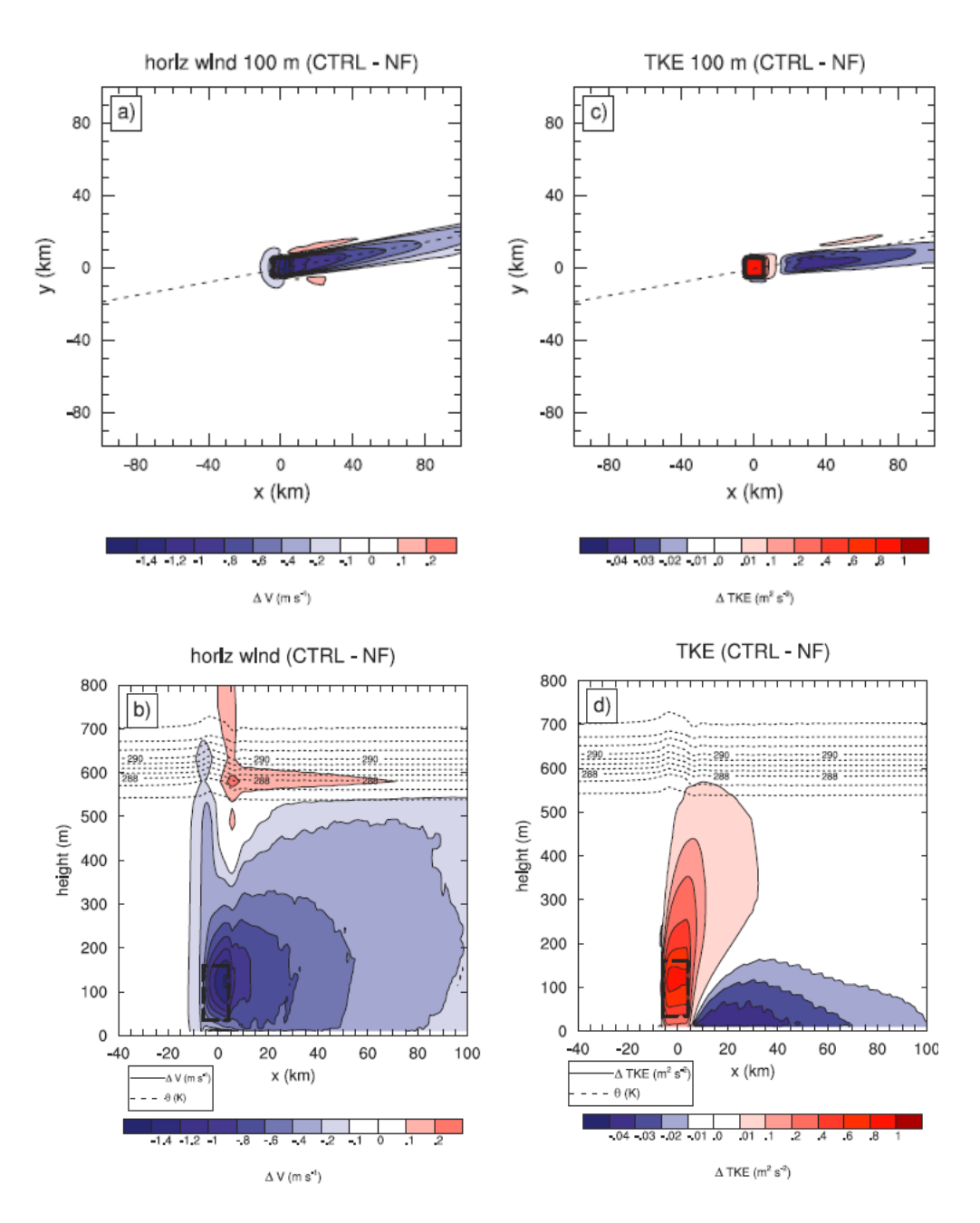


Figure 27: Horizontal wind speed contour e around the farm (a), horizontal wind speed profile at the farm location and in the wake (b), resultant turbulent kinetic energy contour around the farm (c), and resultant turbulent kinetic energy profile (d) from Fitch simulations on Thanet offshore wind farm in the UK (FARM- BACKGROUND) [12].

Chapter-3. Wind Farm Modeling with WRF

The "Weather Research and Forecasting" –WRF is a NWP program that is open source, and tailored for research and operational applications. WRF was developed and used since the 90's by the joint effort of the National Centre for Atmospheric Research in the U.S (NCAR), the National Centre for Environmental Prediction (NCEP), the Forecast System Laboratory (FSL), the Air Force Weather Agency (AFWA), the Naval Research Laboratory, the University of Oklahoma, and the Federal Aviation Administration (FAA) in the U.S. This chapter provides a brief introduction to how WRF works, followed by a description of the computational grid, and the variables stored in it (section 3.1). The input data, and the interaction between domains is also discussed in this section, and numerical stability constrains are presented. The chapter ends with a presentation of the physics schemes for the atmospheric flow modeling in section 3.2, and the code structure of the Fitch turbine parameterization in section 3.3.

3.1. Introduction to WRF

WRF solves the compressible non-hydrostatic Euler equations of motion¹⁵ in a conservative form, and pressure is resolved by a state law. The equations further account for moist and potential temperature, while neglecting viscosity because air can be treated as an inviscid fluid. Suffice to say, WRF relates atmospheric physics, mixing of turbulent flows, and the influence of earth's rotation on the equations of motion on a spherical coordinate system.

WRF consists of independent program sets, the first set is the preprocessing system WPS built to reconfigure input data and cope with the user settings. The WRF structure is shown in Figure 28, and with WPS the user creates grid domains around the latitude and longitude points of interest (a), creates a 3D pressure field and selects the vertical levels of importance in the local atmosphere (b), and makes horizontal interpolation of input variables to the output grid resolution (c). The last set consists of two programs: *real* and *ARW*, for the vertical interpolation of input data and the dynamic solver, respectively. For post processing, the program NCL from NCAR is implemented. Due to the meso-scale nature of WRF, it includes parameterizations schemes for physical phenomena like cloud formation, modeling of the planetary boundary layer, atmospheric and surface radiation, etc.

A.M. Striedinger P. Master of Science Thesis

_

¹⁵ If need, see section 2.4, or the complete equations of motion as used in WRF is presented in Appendix-A. An example of the equations is later shown in this section as well (Equation 31).

To know more about parameterization schemes, user settings, and WRF configuration options, the interested reader is referenced to the manuals and tutorials available at the WRF model user's web site¹⁶. The next sections deal with the computational grid, atmospheric pressure levels in the vertical coordinate, map scale factors, and numerical stability.

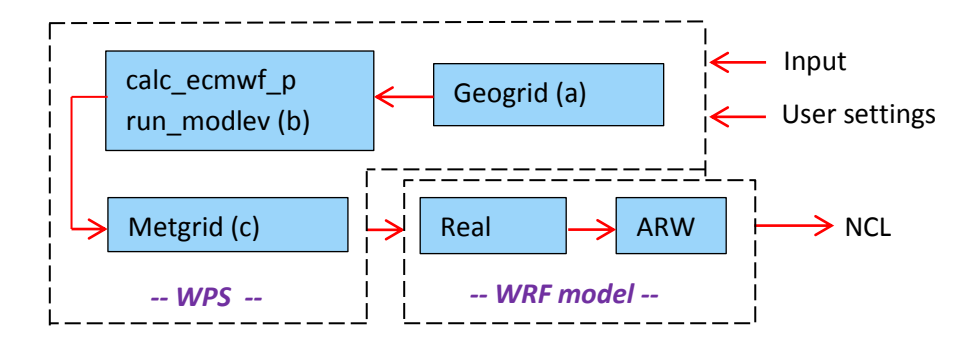


Figure 28: WRF program structure: WPS on top, WRF model on bottom.

3.1.1. Computational grid in WRF

The computational grid is the space used by the user to define the location of study, and is bounded to latitude and longitude reference points. The grid represents a mesh on an imaginary board storing input data and variables inside its nodes, borders, and center points. WRF uses a staggered grid, represented in Figure 29. Potential temperature (θ) , and velocities (u, v, w) are evaluated at center points and grid borders, respectively.

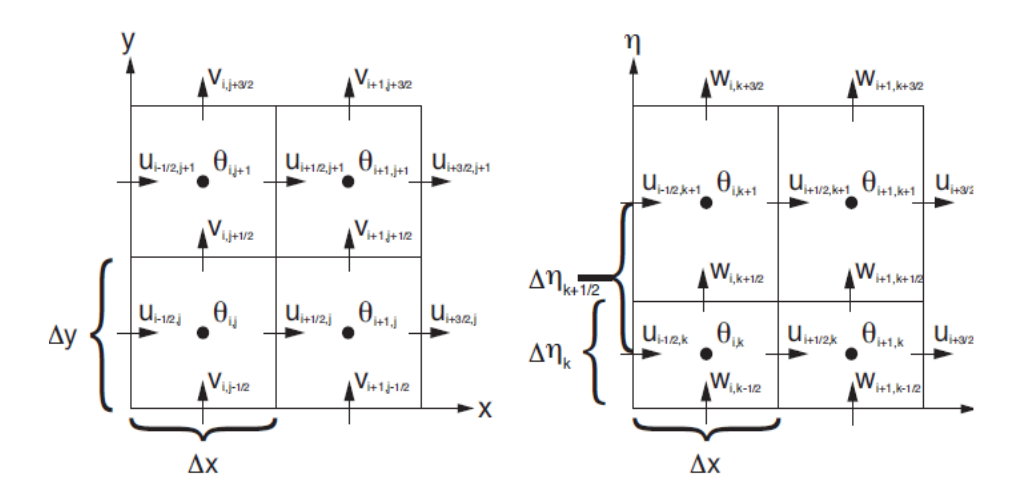


Figure 29: Horizontal (X,Y) for easting and northing respectively, and the Vertical grid representation (k). Borders represent vertical levels and horizontal grid distances. η represents atmospheric vertical pressure levels. Figure extracted from WRF manual.

¹⁶ Visit: http://www.mmm.ucar.edu/wrf/users/ and see User Support -> Tutorial

In general, diagnostic variables such as pressure p, and inverse density α are computed at center points¹⁷. The main advantages of using staggered grid cell vs. collocated cells (variables stored at same points) is the avoidance of discretization errors on pressure and velocity [66].

3.1.2. Atmospheric pressure levels and map scale factors

ARW is the solver for the compressible non-hydrostatic Euler equations in flux terms (flow rate per unit area). The equations are reformulated using a terrain-following approach, a hydrostatic-pressure vertical coordinate system. Each vertical coordinate (η) in the grid is an hydrostatic-pressure ratio (nondimensional): eta-levels. Therefore, the coordinate contains information on the vertical distance it represents above the ground. (see Figure 30, and Equation 28). Ground topology is represented with height as an output variable ¹⁸.

$$\eta = \frac{(p_{dh} - p_{dht})}{\mu_d}$$
 ; $\frac{\partial \eta}{\partial t} = \dot{\eta}$ where $\mu_d = p_{dhs} - p_{dht}$

Equation 28: Modified Vertical levels into Eta-levels for WRF.

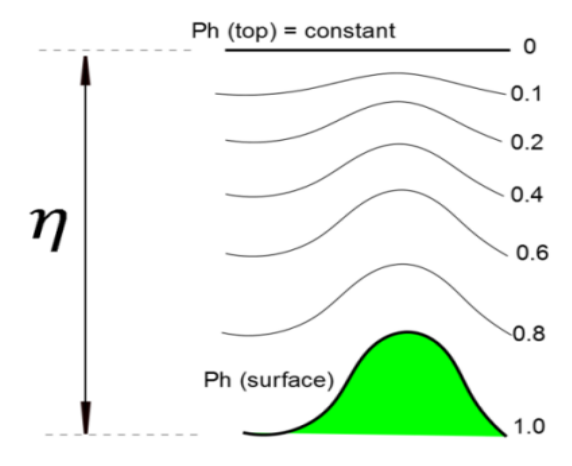


Figure 30: Vertical coordinate system in WRF, adapted from WRF User Manual.

Eta-levels (η) are normalized with respect to the top and surface hydrostatic-pressure differences at all times. For η to represent the dray air, the sub index d is used, so that dh, dht, dhs represent the hydrostatic pressures at certain level in the atmosphere, at the top, and at the bottom respectively. Momentum variables are also modified for the terrain following approach, and the gravitational field is

¹⁷ More can be found in the WRF physics description manual: http://www.mmm.ucar.edu/wrf/users/pub-doc.html

¹⁸ Flat terrains and the offshore are examples of terrains with no topology.

introduced with the geo-potential variable ϕ , such that pressure gradients are multiplied by gradients of ϕ . See Equation 29, and the complete governing equations in Appendix-A.

```
\phi = gz \mid geopotential ; \Theta = \mu_d \theta | New potential temperature field<sup>19</sup>
\mathbf{v} = (u, v, w) \mid velocity\ vector\ field; \mathbf{V} = (U, V, W) = \mu_d \mathbf{v} \mid modified\ vector\ field
                     \Omega = \mu_d \dot{\eta} | modified rate of vertical Eta gradients
```

Equation 29: Modified gravitational field, and momentum variables used in WRF with (d) representing dry air mass.

To obtain a domain like that of Figure 29, WRF implements spherical projections from the earth surface into a Cartesian grid system. Consequently, latitudes and longitudes are transformed into rectangular coordinate points. Figure 31 Illustrates the Lambert conformal projection used during this thesis work. For a full description of other projections see the WRF user manual.

The dotted lines in Figure 31 represent the resultant Cartesian plane of the Lambert projection. Latitudes from 30° to 60° have the least amount of distortion of projected distances on a flat map. All grid domains from the current simulations lay on that range. Horizontal grid spacing remains constant, but map factors (m_x, m_y) are introduced to indicate how much of the earth surface is being represented per grid surface, and each map factor depends on the type of spherical projections being implemented.

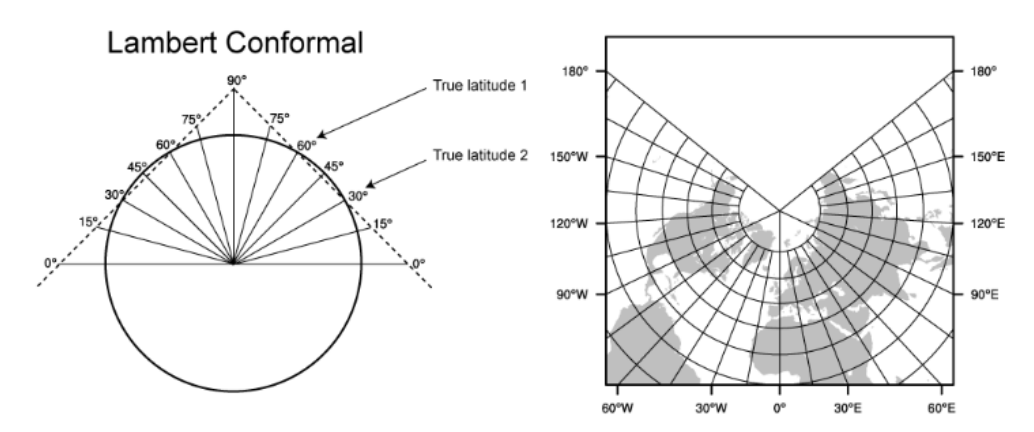


Figure 31: Lambert conformal map projection for current simulations: Best suited for mid latitude domains; adapted from WRF manual.

Map factors are explained in Equation 30. The ideal value distribution of map factors on any domain grid is 1 or close to 1, and for the Lambert Conformal projection that ideal distribution is achieved in the latitude range of 30°-60°. Further, the equations of motion in the west-east direction is shown in Equation 31.

¹⁹ Potential temperature was defined in section 3.1.2

$$\left(m_x,m_y\right) = \frac{(\Delta x,\Delta y)}{distance\ on\ earth} \quad ; \quad \mathbf{V} = \mu_d\left(\frac{u}{m_y},\frac{v}{m_x},\frac{w}{m_y}\right) \ ; \quad \mathbf{\Omega} = \mu_d\dot{\eta}/m_y$$

Equation 30: Map scale factor equation; factors are then inserted by diving U, V, W, Ω with m_w, m_w, m_w respectively.

$$\frac{\partial U}{\partial t} + m_x \left[\nabla \cdot u(U + V) \right] + \frac{\partial \Omega u}{\partial \eta} + \left(m_x / m_y \right) \left[\mu_d \frac{1}{\rho} \frac{\partial p}{\partial x} + (\rho_d / \rho) \frac{\partial p}{\partial \eta} \frac{\partial \phi}{\partial x} \right] = F_U$$

Equation 31: Non-hydrostatic Euler equation of motion in the x-grid direction (West-to-East direction).

Moist, rain and other gas-mixture fractions are accounted for in the mixture density ρ , and dry-air mass density ρ_d . In addition, the acceleration is expressed as F_U , where U is the corrected wind speed as $\frac{u}{m_{\nu}}$. Flux terms represent the flow through an area perpendicular to the direction of interest. Therefore, the map factor on each velocity component must modify the distances shaping the perpendicular area on each velocity (the area is $\Delta y_{(earth)}\Delta z$ for u) ²⁰. Consequently, velocity gradients are divided by their corresponding direction-wise map factors.

3.1.3. Input data and domain interaction

The input data from ECMWF used for this report is the ERA-Interim [67], consisting of weather simulations results coupled with observations at low resolution $(\Delta x > 40 \text{ km})^{21}$. ERA-Interim data is a simulation record of past events on the entire globe, together with operational measurements. Grid domains often have higher resolution than that of the input data, and data is interpolated to provide initial and boundary conditions to the domains. Depending on the differences in spatial resolution, few nested domains are located between the domain of interest and the input data to avoid interpolation errors (see Figure 32).

Figure 32 illustrates nested domains, where a parent domain provides boundary conditions to its inner domains, and main initial conditions are provided by input data. Each domain simulates over the area it encloses regardless of the presence of any other domain. Hence, domain 1 and domain 2 cover the UK in Figure 32. Therefore, phenomena in nested domains affect the simulation in the parent domains.

There are two options for the interaction of nested domains, namely feedback and with no feedback interaction; this is set prior to running the ARW solver. Once boundary conditions are given, parent domains wait for the response their nested domains before continuing their computational process. Domains without feedback don't have such a loop characteristic. More importantly, simulations with the

²⁰ The relations between areas and momentum fluxes can be reviewed on Chapter 3, page 79 of the second edition of "Transport Phenomena" by R.Byron Bird et al., and looking at the use of Δx , Δy , Δz in the formulations

²¹ Detail description of ERA-Interim data in http://icdc.zmaw.de/era_interim.html?&L=1

feedback option may run much slower than without feedback, and this is crucial if the period of evaluation is long.

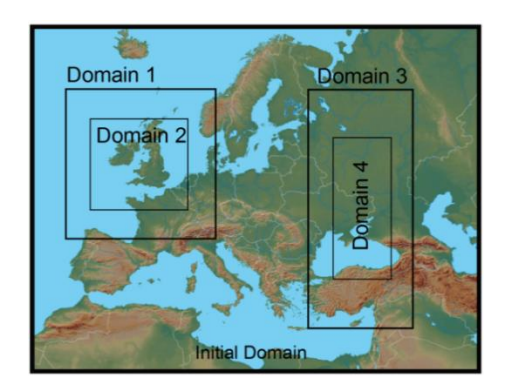


Figure 32: Example of domain setup. The Initial Domain is the main Parent Domain in this example, the remaining are all its nested domains. Domain 1 nests domain 1, and domain 3 nests domain 4. Consequently, there are two sets of nested domains: Initial Domain with domains 1 and 2, and Initial Domain with domains 3 and 4.

Numerical stability 3.1.4.

Map projection, grid size, and input time-steps are crucial for model stability, and their accurate values avoid numerical oscillations in the solution. There are two time constrains in order to achieve this goal: the model time-step constraint Δt_{max} and the acoustic time-step constraint $\Delta \tau$. These are for the advection and time integration schemes, respectively. See Equation 32.

$$\Delta t_{max} < \left(\frac{Cr}{\sqrt{3}}\right) \frac{\Delta x}{Speed_{\langle max \rangle}} \; ; \; \Delta \tau < \frac{0.5 * \Delta x}{Speed_{\langle sound \rangle}}$$

$$=> \Delta t_{max} < \left(\frac{Cr}{\sqrt{3}}\right) \frac{\Delta(x,y)}{Speed_{\langle max \rangle}} \bigg|_{\langle i,j,k \rangle} \; ; \; \Delta \tau < \frac{0.5 * \Delta(x,y)}{Speed_{\langle sound \rangle}} \bigg|_{\langle i,j \rangle}$$

Equation 32: Model time-step constraint (left) and acoustic time-step constraint (right), Cr is predefined by WRF, and Δx can be replaced by Δy . Both velocities are at grid cell center points; hence (see Figure 29).

The model time-step is an input defined by the user, and is bounded by the time constraints, and is easier than redoing pre-processing in WPS. Equation 30, Equation 31, and Equation 32 make clear the importance of a proper map projection, such that the simulation is not compromised. For example, for a 100 m/s wind speed above the PBL with an m of 1, a Cr limit of 1.42, a 3 km grid cell, and a sound speed of 300 m/s, the time constraints are 24.5 sec and 5 sec for Δt_{max} and Δau respectively. If the map factor is changed to 0.8, the new grid speed is 125 m/s, yielding a new Δt_{max} < 19.6 sec. Hence, if in any cell the model time-step is higher than 19.6 sec, then simulation becomes unstable. The previous example was simplistic and did not take into account the changes in wind speed through Equation 31 and the modification of map factors. But a similar situation may occur when the amount of intermediate eta levels near the surface is increased while maintaining a small grid size.

As the vertical grid spacing is reduced so do the terms in Equation 31 affected by the η coordinate, and to yield a similar flow acceleration F_U the value of the velocity gradient-terms must increase. As a consequence, the $Speed_{(max)}$ in Equation 32 can increase. The situation is mentioned in Chapter 6 when making the WRF-setup for a Danish offshore wind farm

3.2. PBL and Physic Models in WRF

There are many physic parameterization schemes in WRF. However, the current turbine parameterization is bounded to a specific scheme for the planetary boundary layer, and a surface layer scheme. Both schemes belong to the MYNN model [67]. The next table depicts the physical models used for the WRF simulations in the current study.

Table 6 Microphysics options implemented for WRF simulations.

Physics	Microphysics model			
Microphysics	Single-moment-6-class Scheme			
Long wave radiation	RRTM Scheme			
Short wave radiation	Goddard Shortwave Scheme			
Surface layer physics	MYNN Scheme			
Boundary layer physics	MYNN Scheme			
Cumulus physics	Grell-Devenyi ensemble scheme			

The microphysics scheme includes models for ice, snow, graupel, and is suitable for high resolution domains. The long wave radiation scheme stands for Rapid Radiative Transfer model that uses lookup tables for atmospheric radiative fluxes and heating rates, and increase computational efficiency. The short wave radiation scheme accounts for climatological ozone, and cloud effects. The MYNN Surface Layer scheme is in charge of estimating the surface roughness, friction velocity and air-surface heat fluxes to determine the atmospheric stability. The MYNN Boundary Layer scheme is used to model planetary boundary layer physics and express the turbulent kinetic energy TKE as a second order diffusion relation; see Equation 33. But the Cumulus Scheme is implemented only in low resolution domains, and models the physics of cloud formation.; these clouds are usually less than 2 km. At high resolutions, WRF is capable of solving the cumulus physics (example grid sizes: 500 m, 1 km-7 km), and its parameterization scheme is not needed.

Refereeing again to the PBL scheme, Equation 33 relates TKE per unit mass $q^2/2$ with potential temperature θ , wind shears, a length scale L, and stability functions S_M, S_H, S_q . Recalling the explanation of the turbine parameterization scheme in Section 2.5, the shear terms in the turbulence scheme together with a Δq^2 are influenced by the turbine operation, and a final value for TKE is obtained. More on this is highlighted in the next subsection.

$$u'w' = -LqS_{M} \frac{\partial \bar{u}}{\partial z}$$

$$v'w' = -LqS_{M} \frac{\partial \bar{v}}{\partial z}$$

$$w'\theta' = -LqS_{H} \frac{\partial \bar{\theta}}{\partial z}$$

$$-\left[w'\left(u'^{2} + v'^{2} + w'^{2} + \frac{2p}{\rho_{o}}\right)\right] = LqS_{q} \frac{\partial q^{2}}{\partial z}$$

$$\Rightarrow \frac{\partial q^{2}}{\partial t} = \frac{\partial}{\partial z} \left(LqS_{q} \frac{\partial q^{2}}{\partial z}\right) + 2Lq \left[S_{M} \left[\left(\frac{\partial \bar{u}}{\partial z}\right)^{2} + \left(\frac{\partial \bar{v}}{\partial z}\right)^{2}\right] - \frac{g}{\theta_{o}} S_{H} \frac{\partial \theta}{\partial z} - \frac{q^{2}}{B_{1}L^{2}}\right]$$

Equation 33: MYNN Turbulence parameterization scheme, where B₁ is a constant [67].

3.3. **Current Turbine Parameterization Scheme**

The current turbine parameterization scheme in WRF is based on the Fitch scheme. It uses turbine rated power, cut-in and cut-out wind speeds to generate a generic power curve, and the power and thrusts coefficient as a function of velocity. Once the boundary layer parameterization is initiated by WRF, turbine data is requested from user input files, and the turbine parameterization initiated as well. However for MeteoGroup there is now an additional option that enables the input of individual turbine power data, and coefficients such as C_T , C_P , and a. The following equations and block diagram illustrates how the parameterization scheme operates.

$$\begin{split} \frac{P}{\rho} &= 0.8*P_{max}*\left[0.5+0.5*\tanh\left(\frac{V-V_m+V_h}{V_h*0.6}\right)\right] \\ V_m &= \frac{1}{2}\left(V_{\langle out\rangle}+V_{\langle in\rangle}\right) \\ V_h &= \frac{1}{4}\left(V_{\langle out\rangle}-V_{\langle in\rangle}\right) \end{split}$$

Equation 34: Generic Power Functions, where P_{max} is given in MW.

$$\begin{split} for \ V > 2V_{\langle cut-in \rangle} \ \Rightarrow \ C_{p_i} = \left(\frac{P}{\rho}\right) * \frac{2*10^6}{V^3*A_{rot}} \\ for \ all \ other \ \ \Rightarrow \ C_p = C_{pi}e^{-\left[\frac{\left(V-2V_{\langle in \rangle}\right)^2}{V_{\langle n \rangle}}\right]} \end{split}$$

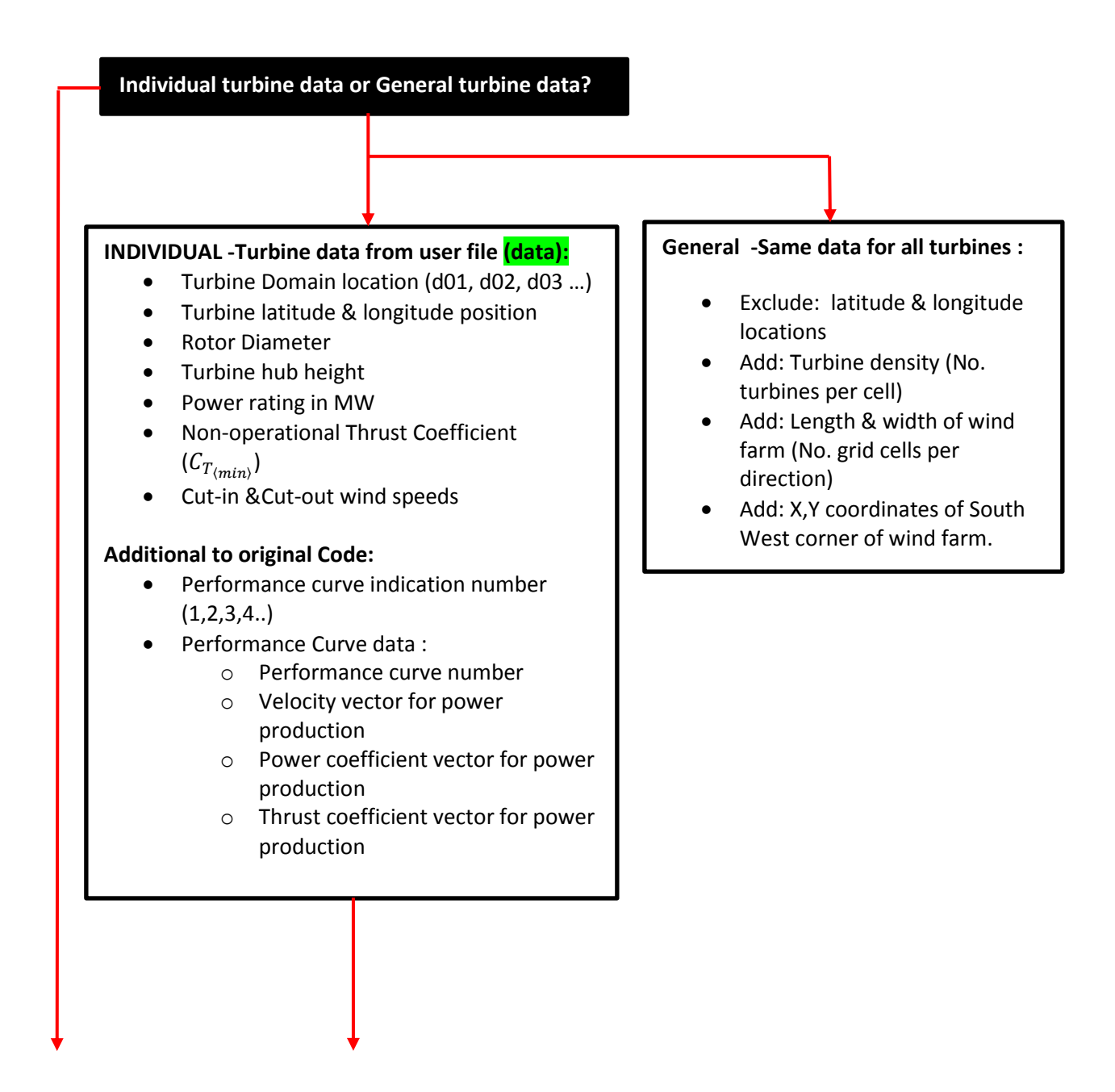
Equation 35: Generic power coefficient function.

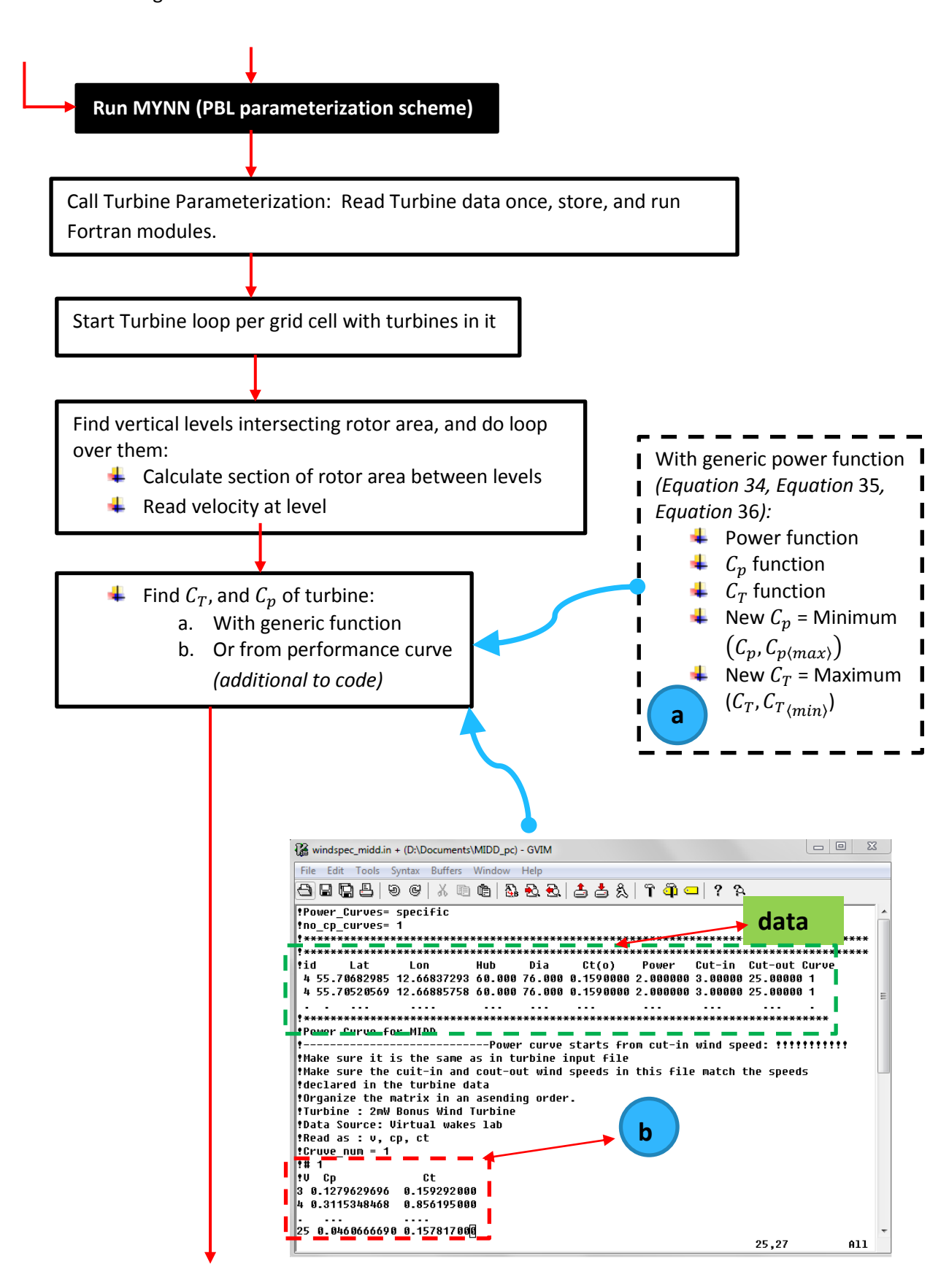
$$C_T = 1.75 C_p$$

Equation 36: Generic thrust coefficient function.

$$C_{P(max)} = 0.55 \text{ or } \frac{16}{27}$$
 $C_{T(min)} = C_{T(o)}$

Equation 37: limits for performance coefficients, where the minimum thrust coefficient is set as user input on a separate file with turbine locations.





- Calculate added turbulent kinetic energy per unit mass (Equation 27)
- Calculate change in horizontal velocity in X direction (Equation 25)
- Calculate change in horizontal velocity in Y direction (Equation 25)
- Add the changes to WRF variables gke, du, dv

Figure 33: Simple Block Diagram of the Turbine Parameterization Scheme Algorithm in WRF²².

The current generic power-function is modifiable and the user is not required to implement it (see Equation 34). The purpose of the function is to make the code faster, and give a sense of turbine dependence. Nonetheless the function is not useful for all turbines, and that is mentioned in the README file that comes with the new version of WRF.

The idea of generic functions in the parameterization scheme is an excellent concept as it allows fast operation to take place without overloading RAM memory space while doing the computations. This advantage is most likely targeted at heavy simulations to save computational time. Nonetheless, the contrast shown in Figure 34 between power performance from manufacturer's data of Vestas WTs and the generic functions indicate that the power is underestimated by the generic expressions. The C_T prediction is completely underestimated for wind speeds lower than $2 V_{(in)}$, and it is always overestimated for speeds close or larger than $V_{(rated)}$. The generic thrust coefficient achieved a low correlation factor of 0.672. That is, the generic C_T is accurate on 67% of wind speed operational range. Consequently, it is more reliable to include a loop to read coefficient data from an input file.

In the next chapters on wind farm situations results, both types of performance coefficient data will be implemented. The generic functions are implemented first in order to make a preliminary assessment, and real data is used on the simulations of one Danish offshore wind farm to obtain more reliable results.

²² The variable QKE in WRF indicates 2 times TKE.

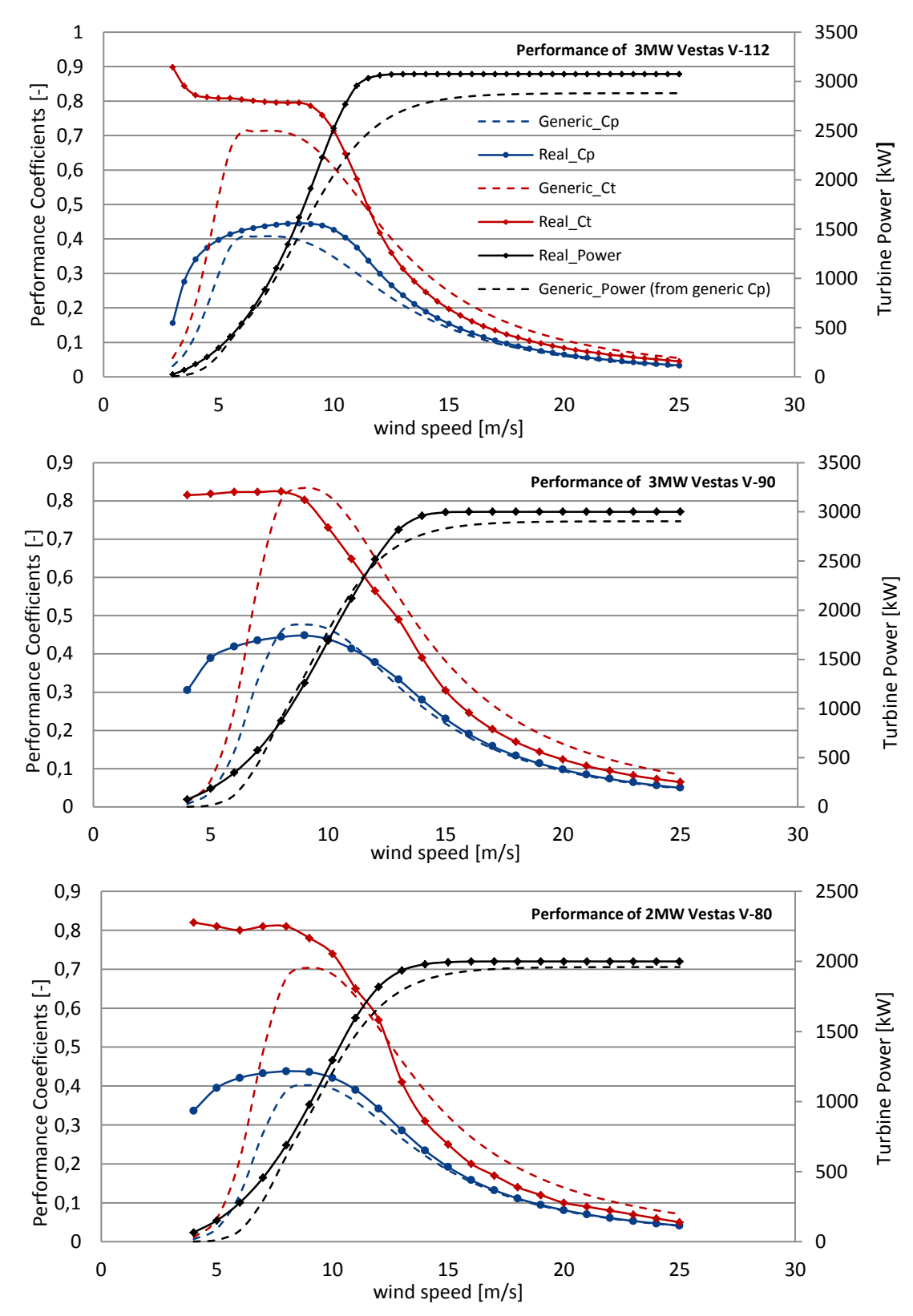


Figure 34: Turbine power and performance coefficient data from generic function and manufactures data of 3MW and 2MW Vestas wind turbines.

Chapter-4. Example Simulation Of The Thanet Offshore Wind Farm

Simulations of the Thanet offshore wind farm are done to select the proper grid size to use with the turbine parameterization scheme for simulations of large offshore wind farms; see Figure 35. Simulations are done at MeteoGroup. In WRF, the generic functions to compute power generation (Equation 35), and provide thrust and power coefficients (Equation 35 to Equation 37) are implemented. To provide the grid-sensitivity of the flow model and turbine scheme, the procedure in this chapter is oriented into in answering one research aspect:

↓ 1st: Is the current wind farm power parameterization scheme based on momentum sinks and turbulent kinetic energy generation able to mimic the interaction between a wind farm and the meso-scale atmosphere?



Figure 35: Geographical location of the Thanet Offshore wind farm. Farm location is marked in yellow and enclosed in dashed lines. Other UK wind farms are shown as well. Image is taken from Google Earth.

The offshore site is described in section 4.1, and the background wind of free stream is described in section 4.2. Further on, the sensitivity is expressed by comparing wind speeds and turbulent kinetic energy on different grid resolutions in section 4.3, and the effects on local meteorology in section 4.4. Effects of grid resolution on physics schemes are discussed in section 4.5. Computational time and data storage are explained in section 4.6. Finally, the topic performance in power forecast performance is discussed in Chapter-5.

4.1. Site Description and Simulation Setup

Located in Foreness Point, the Thanet Offshore win farm is close to the sea side town of Ramsgate, UK. The simulations of the farm take place during March 2010. March is a period of high gusts on southern England, with 8 m/s monthly average wind speeds, and a frequent 210° direction between 1959-2007 (from the south-east) [68]. During dawn hours the wind is calmer and more uniform than during the rest of the day.

The farm consists of 100 units of the 3 MW Vestas V-90 WTs, with 90 m in rotor diameter, and a 70 m hub height. Spacing between WTs is 800 m in the north-east direction, and 500 m in the north-west direction (between rows). The wind farm characteristics and turbine layout are described in Table 7 and in Figure 36. In addition, the generic power and thrust coefficient curves (C_p , C_T) being implemented are plotted in Figure 37.

Two sets of simulations are done to evaluate the performance of the turbine parameterization under different grid resolutions. Set #1 consists of three grid domains (d01, d02, d03)²³ with 9 km, 3 km, and 1 km horizontal resolutions respectively. Domains are organized such that d01 has d02 inside, and d02 has d03 inside (nested configuration). In addition, domain boundaries on set #1 share information via a feedback option²⁴. For the simulation set #1, WTs are located on the 1 km domain. Set #2 follows a similar configuration approach to set #1, but with four domains. A higher horizontal resolution of 500 m is placed on the 4th domain (d04), and the parent domains²⁵ of d04 have resolutions of 14.5 km, 4.5 km, and 1.5 km (d01, d02, d03) without a feedback option between them. WTs of the simulation set #2 are located on each domain.

With the feedback option, the presence of WTs on the most nested domain is perceived by all others. But without a feedback option, turbines need to be located on each domain. The configuration of the simulation sets, and size of domains are described in Table 8. Table 9 illustrates the WRF setup, together with the nested domain configuration from simulation set #2 in Figure 38, and a zoom-in on the 1 km domain from set #1. As disclosed in Table 8, both sets have similar domain sizes. Hence, the

²³ The domain nomenclature as d01, d02, d03, etc. is used to familiarize the reader with the nomenclature used inside WRF, and facilitate the setup visualization in Figure 38.

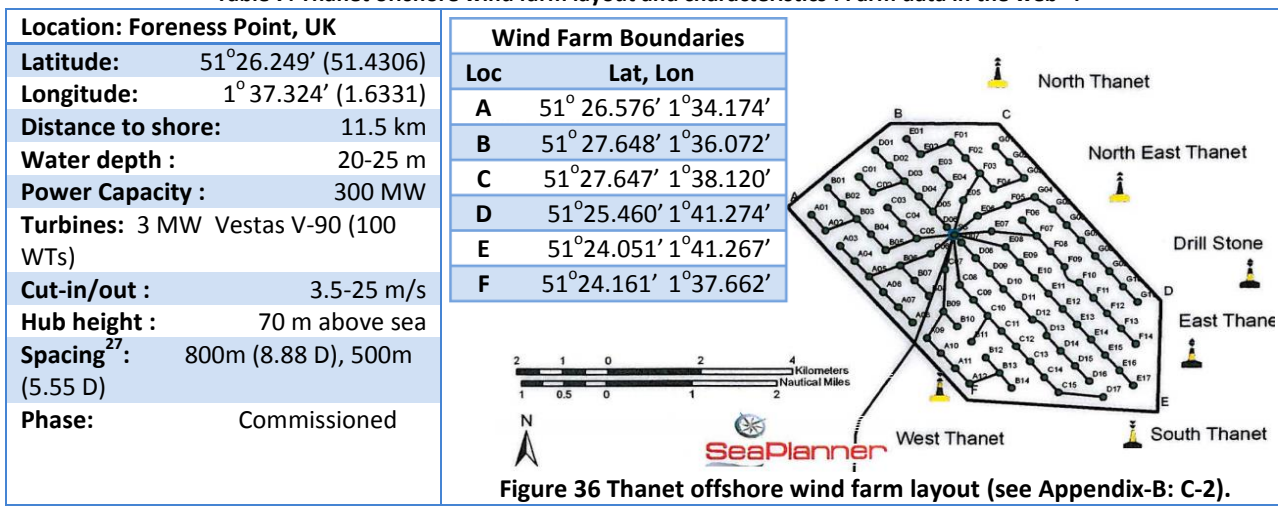
²⁴ Remember the definition of feedback as a loop process between nested domains through their shared boundary conditions

²⁵ In a top to bottom description of domains, a nested domain is that inside a parent domain.

configuration in Figure 38 is representative for both of them: each domain is marked by its name and grid size.

All simulation domains are large enough to cover most atmospheric effects from the wind farm. Additionally, the separation between nested domains is set from 10 to 20 grid points to ease a proper assignment of the boundary conditions. These separations are suggested by MeteoGroup due to their experiences on successful, and accurate simulations with WRF.

Table 7: Thanet offshore wind farm layout and characteristics: Farm data in the web²⁶.



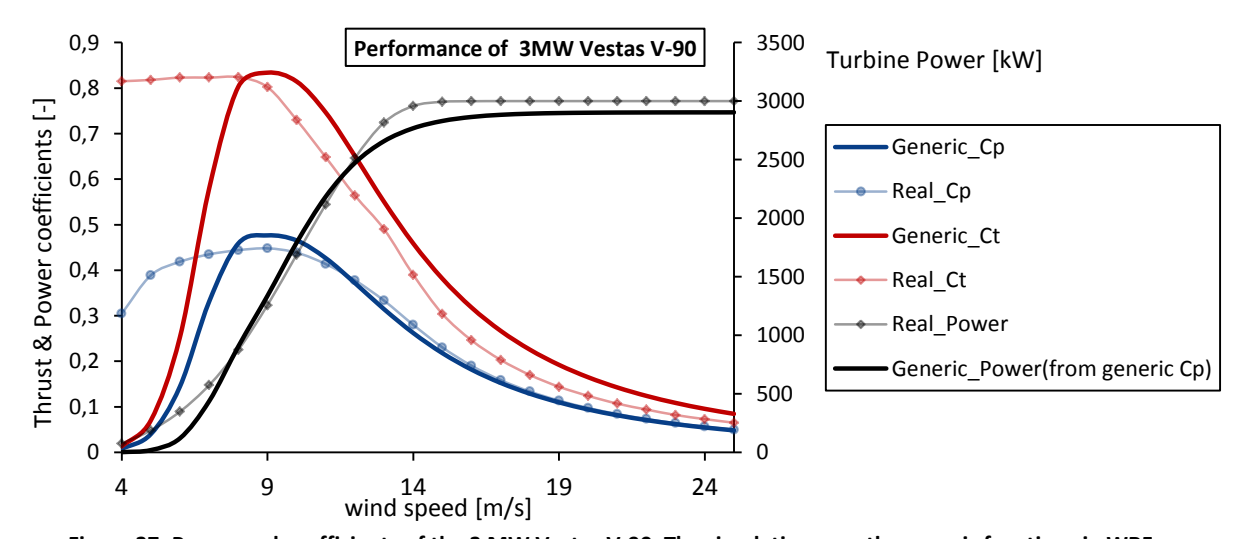


Figure 37: Power and coefficients of the 3 MW Vestas V-90. The simulation uses the generic functions in WRF.

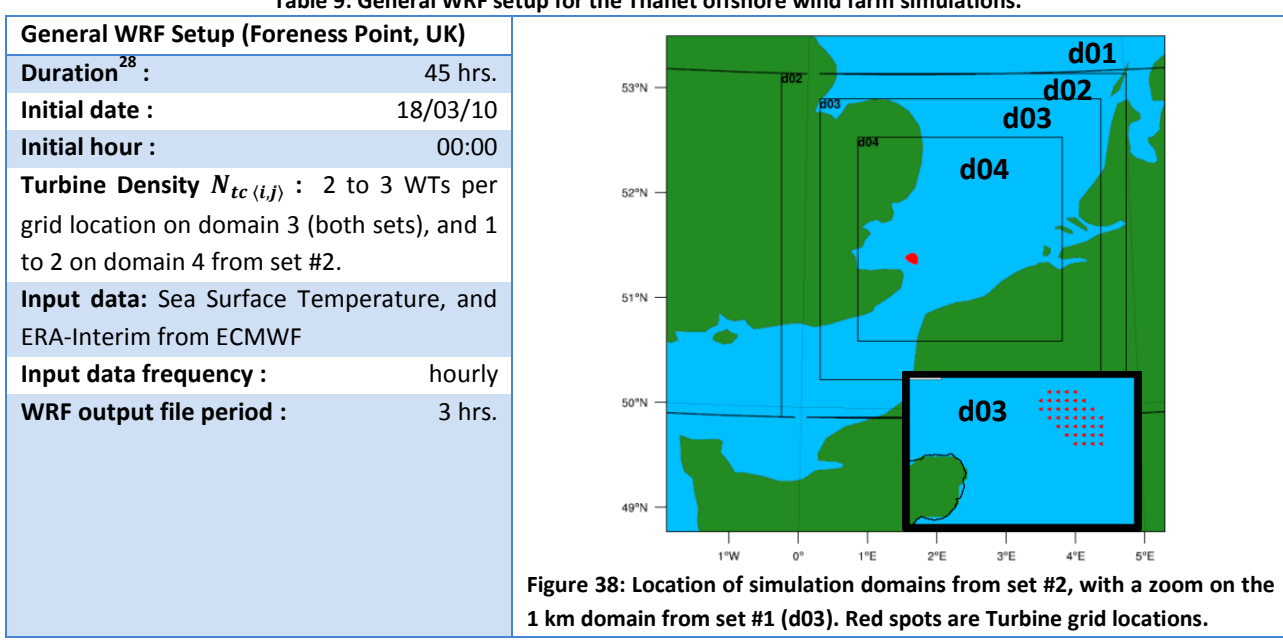
²⁶ General wind farm data, and turbine layout was obtained from Vattenfall web site: http://www.vattenfall.co.uk/en/thanet-offshore-wind-farm.htm. Additional data was found in the LORC data base: http://www.lorc.dk/offshore-wind-farms-map/thanet

²⁷ Turbine spacing is also measured as rotors distances, 1 D = 90 m

Table 8: Domain configuration fore WRF simulations of the Thanet Offshore wind farm, (mxn) represents horizontal grid size, with 39 vertical levels. Each set contains simulations of the flow with and without the wind farm on place.

Domains	Simulation set #1:	Simulation set # 2:		
	Resolution & Size	Resolution &Size		
Parent domain (d01)	9km (100x100): 81*10 ⁴ km ²	14.5km (80x80): 134.56*10 ⁴ km ²		
Nested domain (d02)	3km (100x100): 9*10 ⁴ km ²	4.5km (82x82): 10.7*10 ⁴ km ²		
Nested domain (d03)	1km(100x100): 10 ⁴ km ²	1.5km (151x151): 5.13*10 ⁴ km ²		
Nested domain(d04)	[-]	500m (271x271): 1.8*10 ⁴ km ²		
Turbine Locations	On d03	On all domains		

Table 9: General WRF setup for the Thanet offshore wind farm simulations.



Each WT in the wind farm is associated to a grid location per domain, and does not need to be unique per WT. Such association depends on the horizontal resolution of the domains, and their coordinate origin (as defined by the user). Differences in turbine grid locations are shown for the simulation set #2 in Figure 39, with 22 locations on the 1.5 km domain, and 89 on the 500 m domain. Similarly, the 1 km domain of the simulation set #1 has 39 locations for the 100 WTs to be allocated on. Two additional examples with wind speed contours can be found in Appendix-B: B-3 (Figure 91 to Figure 94).

²⁸ The first 12 hours count as a spin-up time in WRF to initialize the system, hence outputs in this range are disregarded.

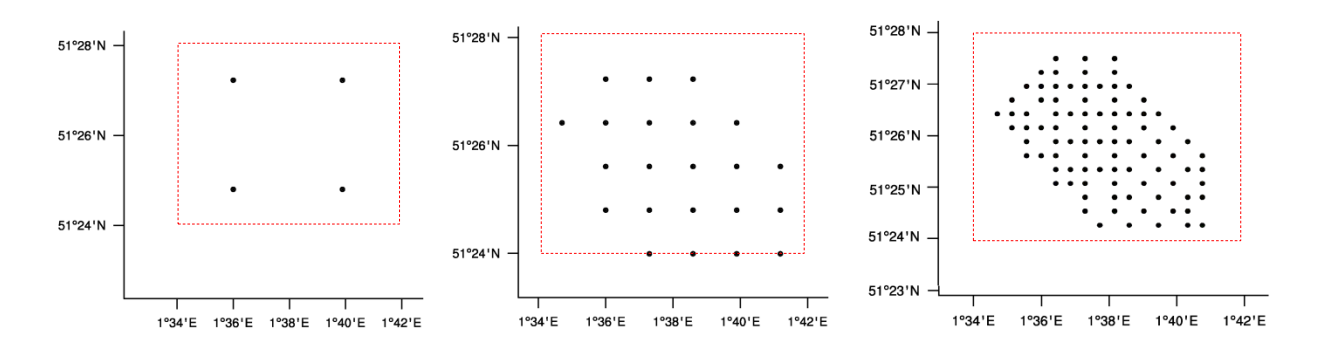


Figure 39: Resultant grid locations of WTs (●) on domains from simulation set# 2. Spatial resolutions of 4.5 km, 1.5 km, and 500 m (left to right). Red dashed lines enclose the comparison region for the three resolutions.

The simulation results and discussion of the next sections are related to the general characteristics listed in Table 10. One example is the height at which the contours of wind speeds and other variables are displayed. A description of each grid level (k), their associated heights and η levels are shown in Table 11 and presented graphically in Figure 40 (η levels were explained in section 3.1.2.).

Table 10: General characteristics of the comparison of simulation results from WRF.

Object	Description	Object	Description
Date	March 19, 2010 @ 00:00 hrs.	Contour Bins	Each 0.2 m/s, or relative change of 2%
Turbine locations	If applicable, represented by $ullet$, $oldsymbol{\Delta}$	Vertical contours	Horizontal distance vs. height with origin at point 51.408 Lat, 1.593 Lon, in flow
Coast lines	Solid black lines on horizontal contour	direction.	
TKE contours	($qke=$ twice TKE from MYNN schen	ne) ²⁹ .	_

Table 11: Intermediate η vertical levels and heights covering the turbine region from sea surface to upper blade tip.

$\eta_{(k+1/2)}$	Height at	Height at
	$\eta_{(k+1/2)}$	$\eta_{(k+1)}$
[-]	[m]	[m]
0.9988	9.814	19.628
0.9959	33.573	47.518
0.9919	66.477	85.436
0.9867	109.473	133.51

²⁹ The turbine parameterization scheme treats $qke=\sigma_u^2+\sigma_v^2+\sigma_w^2=2*TKE$ in this manner.

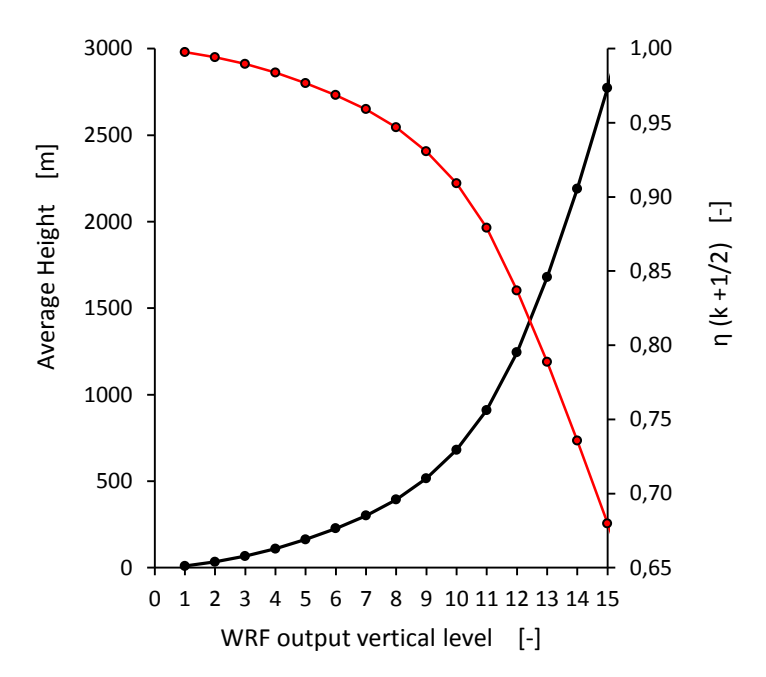


Figure 40: Average Height over the Thanet offshore wind farm as seen on each domain. Height is represented by the -e- line, and the normalized vertical η levels are represented by the -o- line. Both are plotted against the WRF output levels: an number used to ease the data manipulation. The η vertical distribution is the standard configuration of MeteoGroup.

Unlike the results of Fitch et al. [12], where the vertical coordinate is divided into many sections near the surface to provide more detail on the wind speeds through the rotor, the current grid configuration intersects the rotor area in 4 sections only (Table 11). Such fact is due to the low vertical resolution of the model input data near the surface³⁰. Numerical instability increased once the vertical resolution near the surface was set higher on the 1 km and 500 m domains. This action was an attempt to replicate Fitch's strategy, which turned incompatible with the current long wave radiation scheme in WRF (revisit Table 6). As a consequence, time-step constraints were not satisfied.

4.2. Flow Characteristics in the Background Wind

It is important to reproduce flow patterns in order to simulate real flow scenarios, and therefore test the competence of the atmospheric flow model to reproduce them while running the turbine scheme for different resolutions. Consequently, a situation with non-uniform flow is analyzed. The model competence is not tested to its limits under uniform flow situations because to achieve so, WRF needs to be run under "idealized" configuration. An idealized configuration allows the user to manipulate

³⁰ The model used input data from ECWMF (European Center for Middle Range Weather Forecast). This input data is for reanalysis purposes of past events only, consisting of both modelling, and observational data. The name given is ERA-Interim data.

characteristics of the flow scenario for versatility. But for most configurations some physics in WRF are disabled: radiation, surface fluxes, and frictional effects³¹.

The date selected for the comparison of simulation results is March 19, 2010 at 00:00 hours (dawn), and happens to provide a non-uniform flow case. Yet, it is simple enough to be analyzed for the purpose of this chapter. Results at other times are shown in Appendix-B. During dawn hours the wind is calmer and more uniform than during the rest of the day. The farm location allows to witness the wind transition from land to sea, vice versa, and strong winds from the exit of the English Channel to which the farm is exposed to (see cost lines in Figure 42). A low pressure center (L) on the North of the UK moves the air in an anticlockwise direction as seen in Figure 41. Such that the pressure center drives the flow through the English Chanel and strengths a Venturi Effect (follow purple line³²).

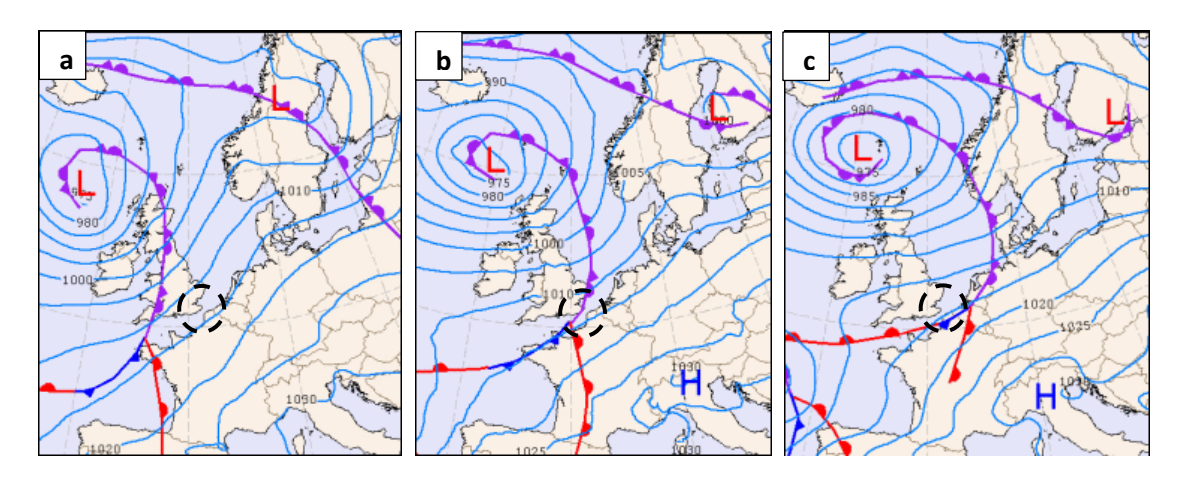


Figure 41: Weather maps on March 18, 2010 at 18:00 hrs (a), on March 19 at 00:00 hrs (b), and at 06:00 hrs (c). The exit of the English Channel is marked by a dotted circle. The light blue lines represent the near-surface isobars in hPa, dark blue lines with filled triangles represent cold fronts, pointing in the direction from cold air to warm air regions. The red lines with filled semi-circles depict warm fronts where the circles face towards the regions with cool air. Pictures are taken from the KNMI website ³³.

When the air is forced to exit the English Chanel, the sudden change in cross sectional area causes the 10 m wind speeds near the sea to increase up to 11.5 m/s at the very exit of the Channel. The wind speeds remain higher than 9 m/s after entering the open sea (winds of 8 - 9 m/s). Such an effect is idealized as a Funnel or Venturi effect, but the strongest winds do not occur at the shortest constrictions of the gap, that separates Europe from the U.K. At hub height the wind speed flied is less uniform, the wind increases up to 16.2 - 16.6 m/s at the gap exit, and remains higher than the sea winds of 14 m/s; see Figure 42. Figure 43 illustrates 2 examples of pure Gap flow courtesy of UCAR online courses in meteorology³⁴, and a representation of the flow case in the English Channel from Google Earth.

³¹ See physics modeling during idealized simulations discussed in Chapter 4 of the User's Guide for Advanced Research WRF (ARW) Modelling System, and its section of "Initialization for Ideal Cases". See also http://www.mmm.ucar.edu/wrf/users/docs/user_guide/users_guide_chap4.html

³² See recommended video on weather map readings: http://www.youtube.com/watch?v=bd7DcVnrSL8

³³ For the complete weather charts visit http://www.knmi.nl/klimatologie/daggegevens/weerkaarten/

³⁴ http://www.meted.ucar.edu/mesoprim/gapwinds/print.htm

The current location of the Thanet Offshore wind farm is close to the exit of the English Channel, but not directly at it as to experience strong gap winds more frequently. The gap winds from the channel are also influenced by the land-sea winds due to the presence of low level coastlines along the channel exit (as shown in Figure 43-c). From a purely perspective of energy resource, it would be interesting to evaluate the sitting of turbines next to the exit of the Channel, or at any similar location. This inquiry however, falls out of the scope of the present study.

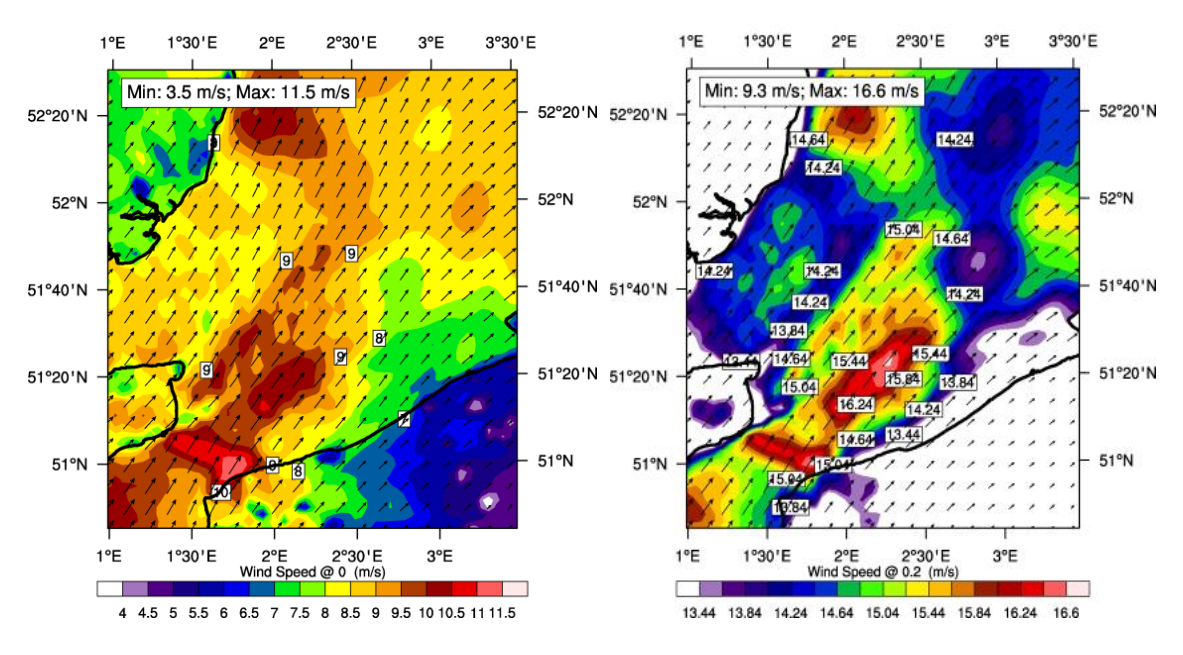


Figure 42: Wind Speed field from Venturi Effect at 10 m height (left), and at 67 m height (right). Both pictures taken from the 3 km resolution domain of simulation set #1 in BACKGROUND case (no wind farm implemented). Gap between UK and Europe is 34 km approx.



Figure 43 Illustration of Gap flows: (a) Idealized Funnel flow as gap winds, (b) example of gap flow when the Funnel Effect dominates in Nu'uanu Pali Pass in the Koolau Rang of eastern Oahu, Hawaii, (c) suggested gap flow though the English Channel. The channel/gap borders s are around 3 m to 100 m in height above sea level. White lines in (c) mark gap lengths of 170 km, 96.3 km, up to 35 km in the last line. Fist two pictures from UCAR.

Wind Speed and Turbulent Kinetic Energy Results **4.3**.

Results from the two simulations sets are compared in two ways. The first is a comparison of the model solutions including the turbine scheme (FARM case), and the second is a comparison of the solutions to their BACKGROUND cases: the net results when the wind farm is placed at the offshore location (FARM – BACKGROUND case). Changes in the wind field at hub height and at 10 m above sea level are compared, followed by the differences in turbulent kinetic energy per domain/grid resolution, and its development from the inflow through the farm site and downstream. Key findings in turbulence intensity are also mentioned, gap winds from the English Channel discussed, and their effects highlighted.

From the second simulation set, only results on domain 4 (500 m resolution) were considered relevant for the comparisons to those from set #1. Results on the 4.5 km, and 1.5 km domains from set #2 showed similar wind speed and turbulence patterns to those found on the 3 km, and 1km from set #1; therefore, conveying no additional information. It would have been more proficient to compare results from all resolution domains in more detail and display them in this chapter. Unfortunately, the comparison was not possible due to time constraints.

From this point forward, each grid resolution will be immediately associated to its domain, i.e. 500 m domain from the simulation set #2, 1 km from set #1, 3 km from set #1, and the 9 km from set #1.

4.3.1. Wind speed results

The 1 km and 500 m domains with 2 to 3 and 1 to 2 WTs per location respectively, show the major regions of speed deficits inside the farm. A zoom on wind speed contours at hub height from both domains is illustrated in Figure 44. The most affected regions are marked with light purple at the farm location, and with red color at the outside. Wind speed deficits are not exactly turbine-specific on the 1 km domain (set #1), and on the 500 m domain (set #2) a more detailed wake development along rows is generated. Turbine layout has greater impact on the 500 m domain, but not in contrast to simulations discussed in literature (Figure 23, Section 2.2.3). On the other hand, results from WRF show expected wind speed deficits in the downstream of the farm, and are marked with blue-scale colors. This is shown in later figures.

When comparing wind speeds at hub height to their respective values on the BACKGROUND cases, maximum deficits in wind speed are very different per domain. At 00:00 hours there are maximum speed deficits of 6.3%, 15.7%, 19.6%, and 17.4% on the 9 km, 3 km, 1 km, and 500 m domains respectively³⁵. Such deficits inside the farm are a measure of the wake strength; see Figure 45. As it can be seen, speed deficits on the 500 m domain deviate from the trends established by the other domains. Nevertheless, their respective background wind speeds at hub height are more similar, corresponding to 13, 14, 14.4, and 15m/s respectively.

³⁵ Refer to Table 8 for the description of domains

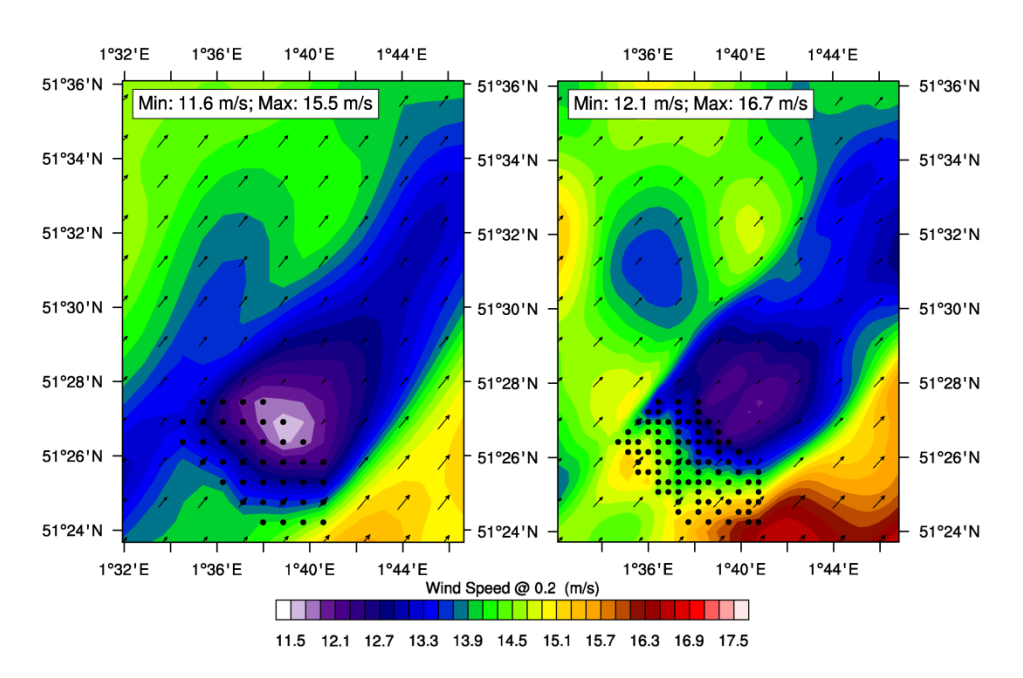


Figure 44: Wind speed contours at 67 m height above sea level with turbine locations (FARM case). Left to right: 1 km (set #1, and 500 m (set #2) domains.

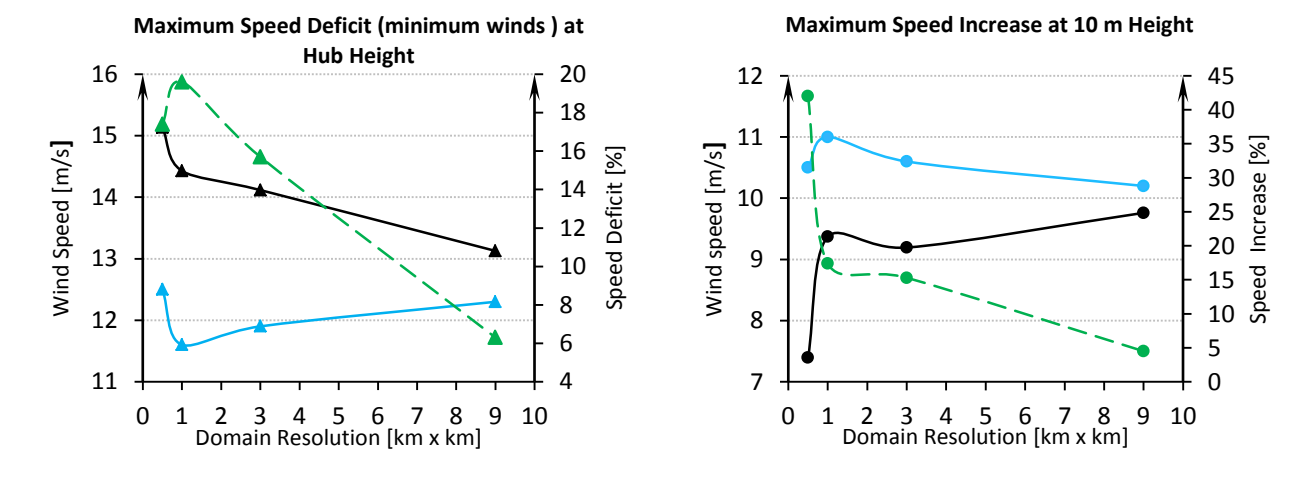


Figure 45: Wind speeds at hub height (-Δ-) (left), and wind speeds at 10 m height (-Φ-) (right) as a function of domain resolution. Two vertical axis: wind speeds in [m/s] on FARM & BACKGROUND cases, and wind speed change in [%] on FARM -BACKGROUND cases. FARM cases are in blue lines, BACKGROUND cases are in black lines, and FARM - BACKGROUND cases are in green lines. All points are located within the wind farm location. Results from the 500 m grid (set #2) deviate from the trends. The location of the maximums suffered minor changes on each resolution.

The change in 10 m winds on the 500 m domain (-•-) follows the trend from the previous domains but with higher values than the expected: a maximum increase of 42% inside the array, and 44% behind the farm³⁶.Results suggest that this resolution has affected the flow patterns near the surface, and consequently the flow in the array. For example, the off-trend value of Maximum wind speed on the FARM and BACKGROUDN cases (-o-,-o-). Wind speeds at 10 m were expected to decrease inside the farm location, but local speed-ups discussed in section 2.2.2 and also found by Fitch et al [12] may appear due to mass conservation³⁷. Similar speed-ups at hub height, due to turbine layout and resulting in local increase of power generation, were found by MSc. Svetlozar [69] at the same time results here were analyzed. His results did not use speed measurements near the sea surface, but it is suspected that they were also affected. Consequently, maximum 10 m wind speeds from Figure 45 measure the immediate inflow to the farm or local speed-ups inside the farm.

Overall, wind speed deficits on the finest domains develop similarly. For example, wind speed ranges from 14.6 to 12.5 m/s and from 13.7 to 11.7 m/s in the middle rows on the 500 m and 1 km domains respectively; see Figure 46. The most important difference is however, the partial attenuations of speed deficits captured on the 500 m domain, yielding a lower gradient $\left|\frac{\partial V}{\partial x}\right|$ as the wind flows through the turbine row. Such case suggests a relative overestimation of wake effects inside the array for coarser resolutions.

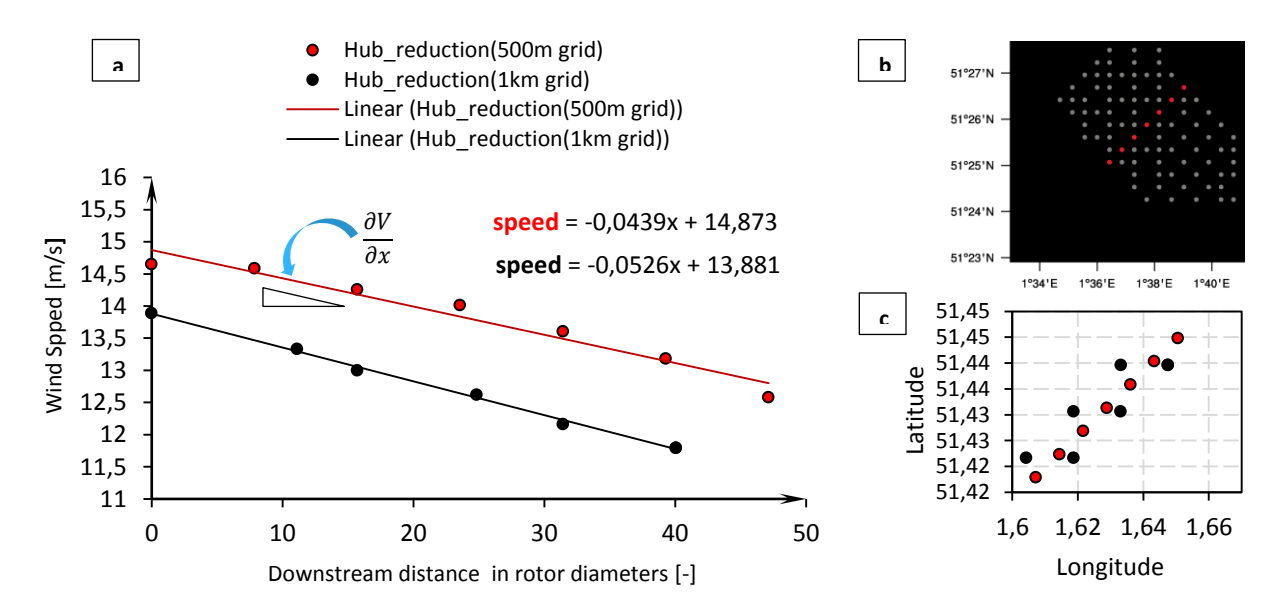


Figure 46: Example of wind speed deficits in the middle row of the Thanet offshore wind farm (FARM case) in (a). The 1 km domain (set #1) represented as •, and the 500 m domain (set #2) as •. Solid lines represent linear fits to each domain result. The middle row is illustrated on the 500 m domain in (b), and contrasted to the 1 km domain representation in (c).

³⁶ Single points were not selected for Figure 45 because the turbine locations are different per domain, and thus increasing the uncertainty when selecting the locations. Neither were domain average wind speeds because the convey no information about the wake by themselves.

³⁷ See Figure 19, and Figure 26 if necessary.

A more detailed wake development on the 500 m domain brings changes in the near wake of the farm. For example, the near wake of the farm starts further downstream of the farm on the 500 m domain than on the others. Such that wind speed continues to decrease behind the farm reaching a minimum of 12.1 m/s or 19.6% (FARM - BACKGROUND case). Downstream, recovery starts due to mixing.

Contour plots are useful for describing the wind field around the farm, and the wake development behind it. Figure 47 and Figure 48 show the convergence of downstream hub height wind speed as the grid resolution increases. For example the farm wake on the 3 km, and 1 km domains cover similar spatial boundaries with wind speeds ranging from 12.to 14 m/s (-11.6% to -2% approx.); see Figure 48.

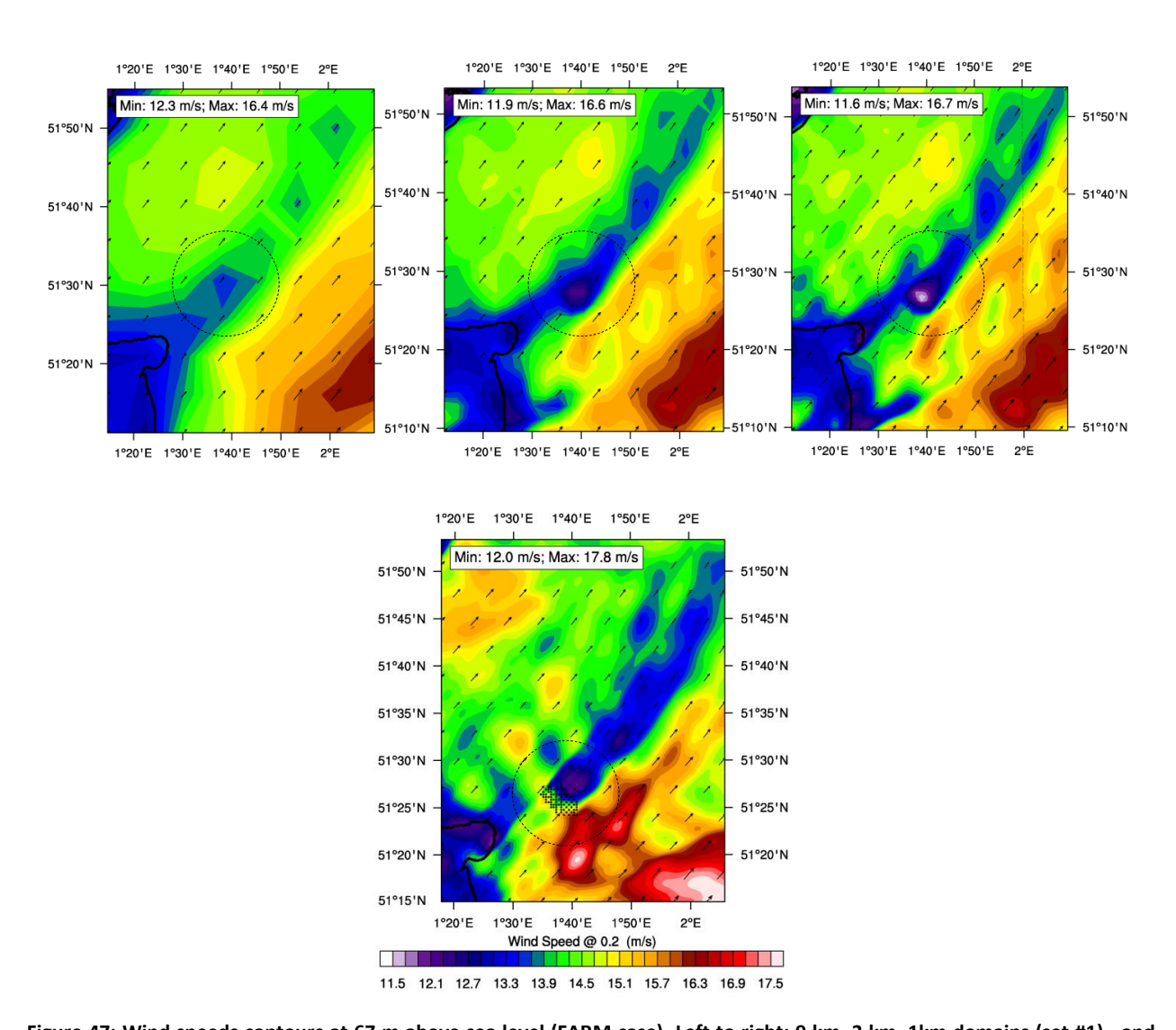


Figure 47: Wind speeds contours at 67 m above sea level (FARM case). Left to right: 9 km, 3 km, 1km domains (set #1), and the 500 m domain set #2 (below). Doted circles enclose the farm location, and show effects of the gap winds from the English Channel near the turbines: merging of red/brown areas.

A.M. Striedinger P. Master of Science Thesis

No relevant difference was found between wind speed contours downstream the farm, on the 1 km and 500 m domains for the FARM - BACKGROUND case. In addition, the far wake extends + 54 km approx. on all domains and a north-easterly direction³⁸.

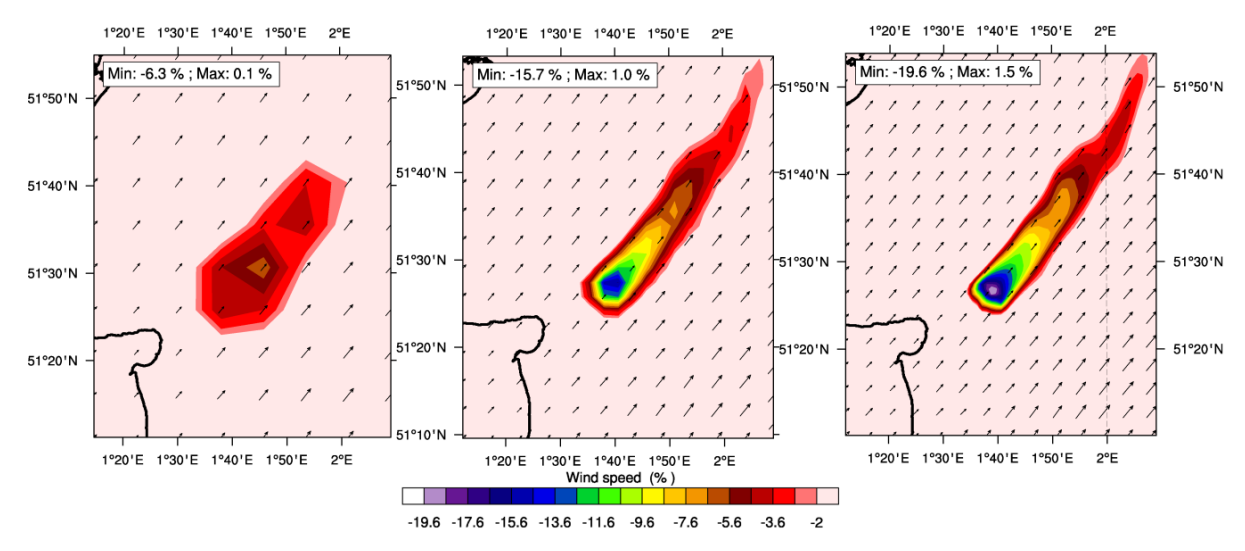


Figure 48: Contours of wind speeds changes at 67 m above sea level. Left to right: 9 km, 3 km, and 1 km domains (set #1): FARM - BACKGROUND case. No relevant difference between 1 km, and 500 m (set #2) for this comparisons.

Gap winds appear on all grid domains, with less intensity on the 9 km domain, and most pronounced on the 500 m domain. Land winds are lower than sea winds as expected, and their transition from the coast to the offshore is interrupted by the farm presence. These winds merge with the gap winds from the English Channel, which is notorious at the southeastern corner of the farm: blue region fuses with red/brown areas regions as in Figure 47.

At 10 m height, wind farm wake effects are undistinguishable on the 9 km domain (FARM case); see Figure 49-a. Such 10 m winds were expected to decrease with a similar pattern to the wind speed at hub height (Figure 47). Nonetheless, the 1 km, and 500 m domains capture speed-up effects near the sea surface. In general, 10 m wind speeds increase up to the last WTs in the flow direction, and are attenuated downstream; see box region on Figure 49-a. The speed-up is strengthened at the southeastern corner of the farm up to 11 m/s due to the gap winds, yielding a tow-tail flow pattern downstream of the farm as seen on the 3 km contour of Figure 49-a (right plot). The figure is for the simulation set# 1.

Figure 49-b isolates the 10 m wake effects in wind speed from simulation set #1, by comparing the changes in wind speed from all domains of FARM - BACKGROUND case. Local seep-ups near the sea surface are found ranging from 11% to 15% inside the farm on the 3 km and 1 km domains. Fitch et al. [12] suggest that such speed-ups are caused by an increase of TKE near the surface, due to the turbine parameterization.

³⁸ The wake length is calculated from the range of wind speed deficit on both simulations, Latitude 51° 27′ N, Longitude 1⁰ 39' E to Latitude 51⁰ 50'N, Longitude 2⁰ 6'E.

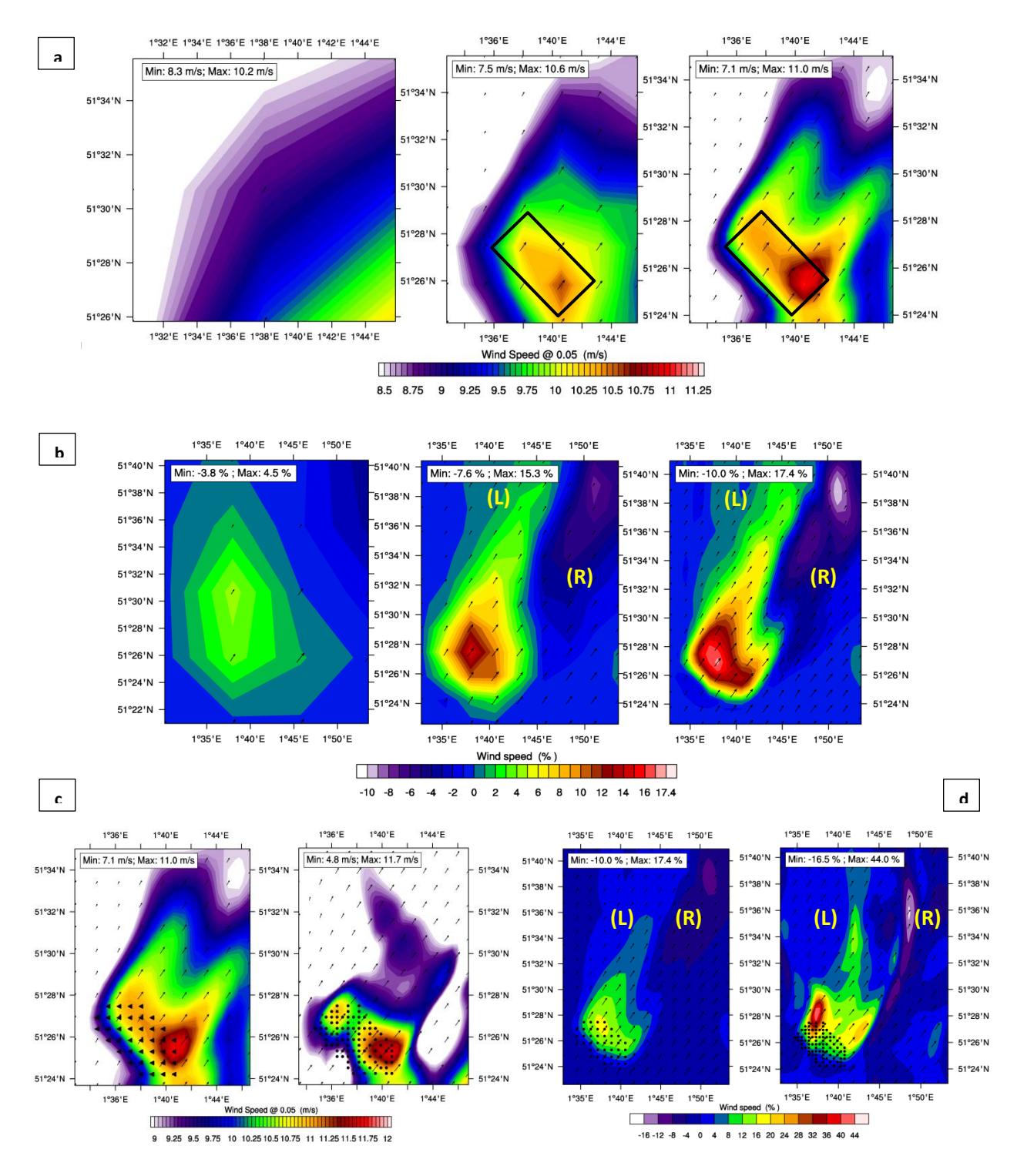


Figure 49: Wind speed contours at 9.8 m above sea level. Left to right: 9 km, 3 km & 1km domains from set #1 for (a) and (b); domains of 1 km (set #1), and 500 m (set #2) domains in (c) and (d). FARM case is treated in (a) and (c) with bins of 0.05 m/s. The FARM - BACKGROUND case is treated in (b), and in (d) with bins of 2% and 4% change. RIGHT TAIL marked as (R), AND left tail AS (L). Maximums and minimum values on all plots relate to their contoured area.

A.M. Striedinger P. Master of Science Thesis

The effects of the two-tail wake behind the farm is felt in the downstream as well in Figure 49-b, d. There are two sections: a right tail (R), and a left tail (L). Where (R) is set on a purple color scale, and shows expected downstream wind speed deficits with maximums of 7.6%, 10%, and 16.5% for the 3km, 1km, and 500 m domains with respect to the background winds. Whereas, (L) is set on a green scale, and shows wind speed attenuations from an 8% increase back to background conditions (0%), and from 15% to 0% on the 500 m domain (set #2). Both tail sections show a decrease of wind speed in the flow direction.

It is suggested but not proven, that the wake division at 10 m height into two sections is due to the intersection between the gap winds and the sea winds at the southeast of the farm site (BACKGROUND case). Both streams meet, and once the farm is placed (FARM case), a momentum transfer from the strong gap winds to the weaker sea winds (L) is enhanced due to air mixing inside the farm. Why does a momentum exchange go in that direction? Because, momentum is always transferred from the faster to the slower moving layers, unless external forces are applied. Hence, the location of the farm with respect to the gap winds influences the wake division at 10 m height.

On the other hand, it is curious to notice that (R) on the 500 m domain seems to be located at a wake boundary rather than being part of the wake as on previous domains. In addition, the two tail shape characteristic found in the FARM case is no longer present (Figure 49-c), and there are less speedup regions inside the farm. This situation indicates a different trend in mixing inside the farm than on previous domains. It is uncertain at this moment what factors caused the 500 m domain to produce such a very different flow scenario near the sea surface.

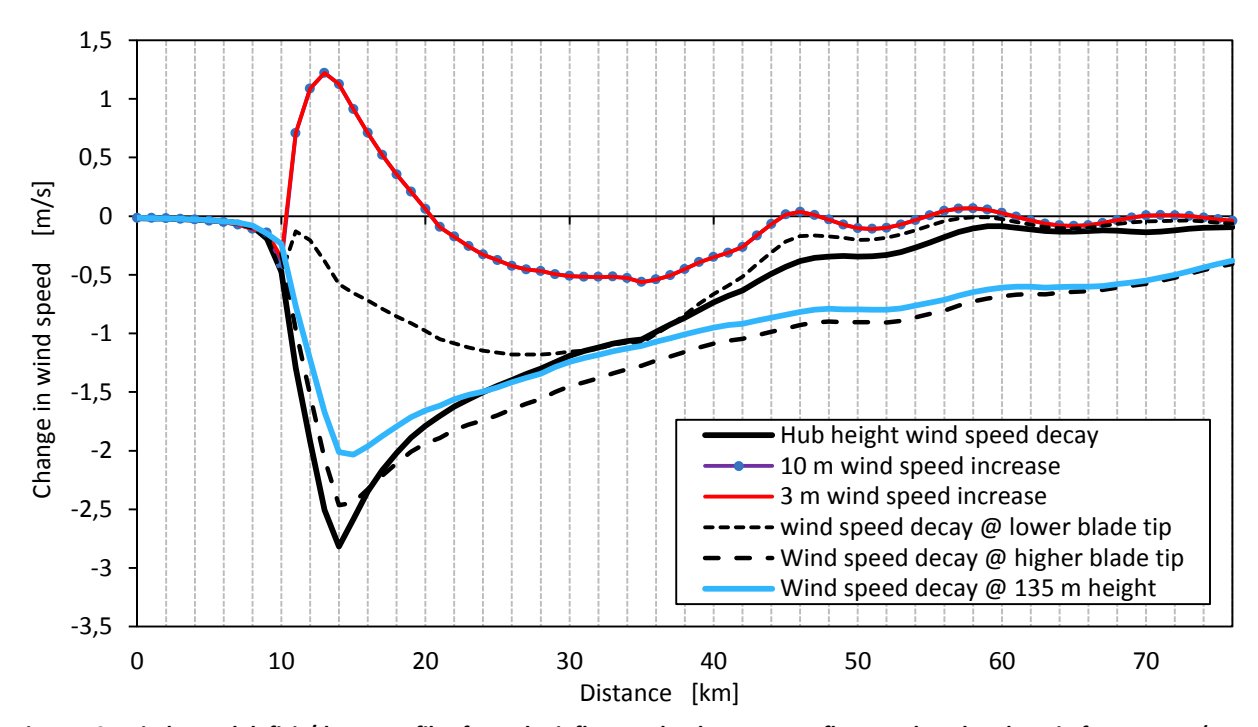


Figure 50: Wind speed deficit/decay profiles from the inflow to the downstream flow on the 1 km domain from set #1 (FARM - BACKGROUND case). The Farm extends from the 10th km. The vertical plane containing all points intersects the farm from the pivot coordinates listed in Table 10.

From another perspective, changes in wind speed development along the farm are plotted in Figure 50: from 3 m to 135 m above the surface. Wind speed deficits decrease with height above the hub as expected because the turbine rotors are no longer presented: i.e. at 135 m height. The speed-up effects near the surface become important below the lower blade tip region, opposing turbine drag and producing maximum wind speed deficits in the wake of the farm as a consequence. Figure 51 shows the vertical profile of wind speed as it passes through the farm and into the farm wake.

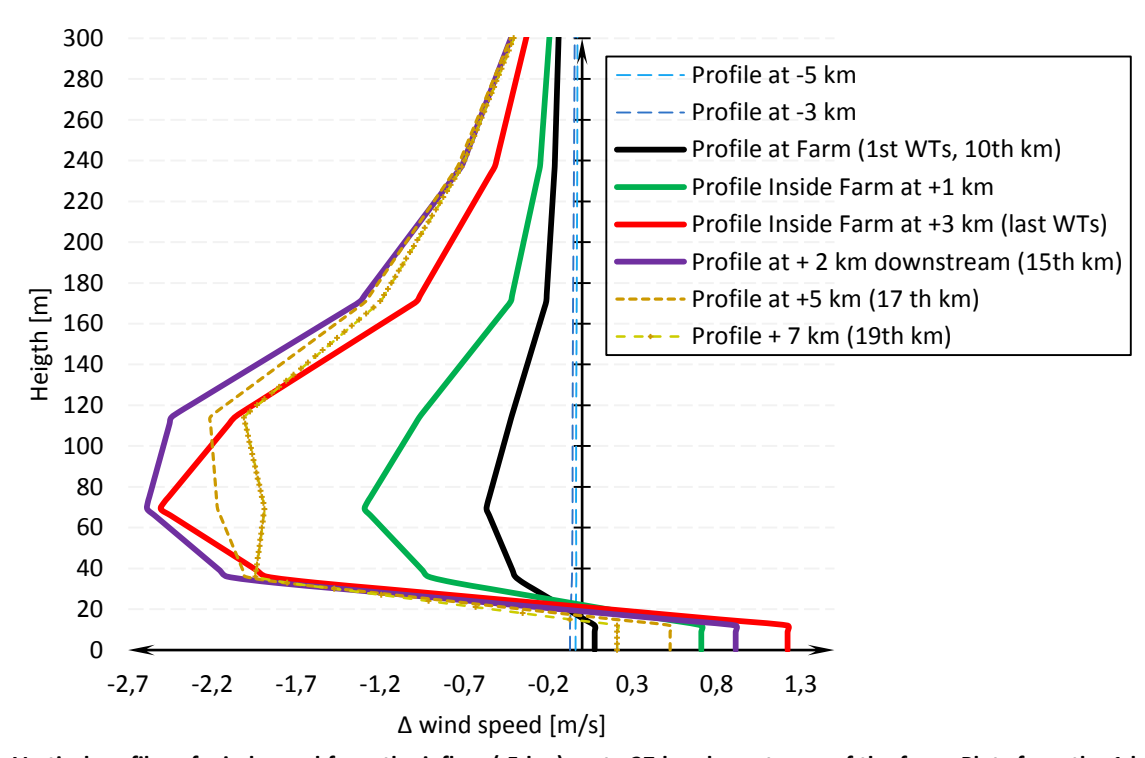


Figure 51: Vertical profiles of wind speed from the inflow (-5 km) up to 27 km downstream of the farm. Plots from the 1 km domain of set #1 (FARM - BACKGROUND case). The vertical plane containing all points intersects the farm from the pivot coordinates listed in Table 10.

5.3.1.1. Comparison to Jensen's wake model

The wind speed development at hub height predicted with the Jensen model is calculated using an Excel spread sheet, without including surface reflection [69], nor PWI³⁹. The model considers a an independent linear wake expansion per turbine row⁴⁰. The flexibility of the model lays in the tuning of the wake expansion through the parameter k. According to DTU, a k of 0.05 is recommended for offshore locations, whilst k of 0.75 for on-shore [45].

³⁹ PWI was defined in section 2.2.3 as the interaction of wakes from parallel turbine rows.

⁴⁰ The Jensen model, linear wake development is defined in Equation 18 from section 2.2.2.

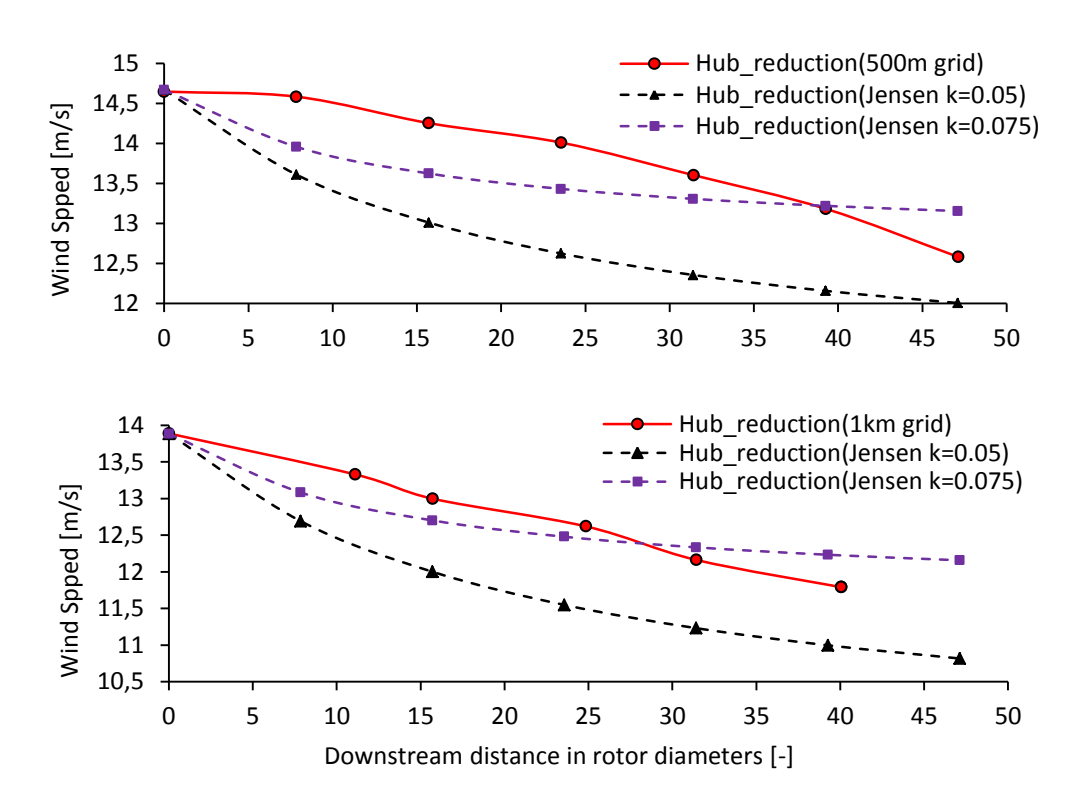


Figure 52: Comparison of hub height wind speed development on the 500 m (set #2), 1km (set #1) grid resolutions with respect to Jensen's wake model for the Off-shore (k=0.05), and On-shore (k=0.075).

Wind speeds at hub height in Figure 52 are plotted on real locations for the Jensen model, and on grid locations for the simulations results. The comparisons are for the middle row (Figure 46-c). Wind speeds from the Jensen model converge along the row towards a constant value. Such behavior is not found on either simulation. Rather, speeds decrease at a constant rate yielding minimum values behind the last WTs. The same was found at other rows (Appendix-B: B-3).

According to the comparison, simulated wind speeds at hub height are overestimated on most WTs, but the opposite happens on the last WTs. Therefore, an over prediction of power production is possible, and as will be presented in the validation study from Chapter-5. Another consequence is that wind speed deficits in the farm's far wake could be yielding deeper wakes than in reality. P. Volker et. al [64] reached to the same conclusions, but on the far wake of the Horns Rev wind farm by using met mast data and a logarithmic approximation to values at 70 m height. In their results the turbine scheme overestimates the total energy extracted from the flow. But hub height speed deficits inside the array were accurate enough.

Turbulent kinetic energy results 4.3.2.

Turbulence is best captured on the 1 km and 500 m domains as shown in Figure 53, with qke_{max} of 6.3 and 7.4 m^2/s^2 at hub height (qke = twice TKE from MYNN scheme). Such value is more than twice its corresponding on the 9 km domain, and is located at the same region of maximum wind speed deficits (as in Figure 44). Analogously, qke_{max} of 1.7 and 1.8 m^2/s^2 at 10 m height correspond to speed-up effects near surface on the southeastern corner of the turbine array; see Figure 54. Further, the 500 m domain provides a more turbine-specific generation of turbulence⁴¹.

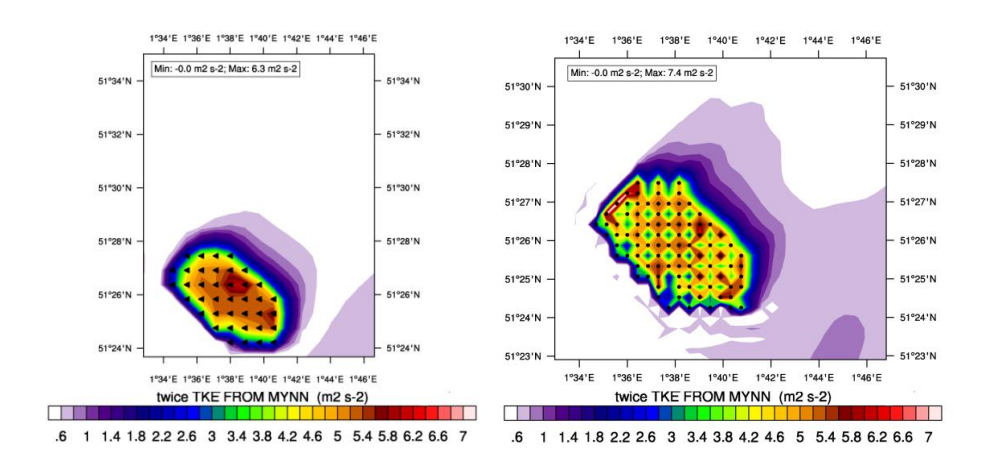


Figure 53: Contours of twice TKE at hub height, with turbine grid locations (FARM case). Left to right: 1 km (set #1), and 500 m (set #2) domains. Bins of 0.1 m²/s². qke_{max} values of 6.3 m²/s² (left), and 7.4 m²/s² (right) inside the farm.

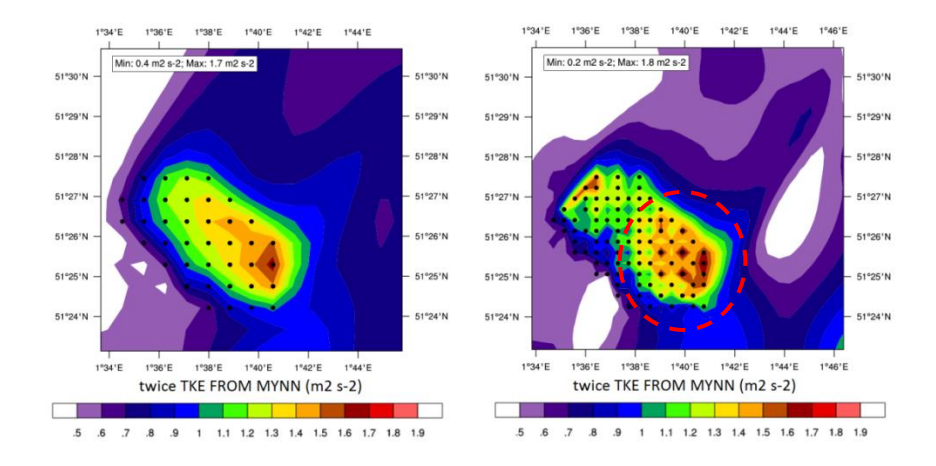


Figure 54: Contours of twice TKE at 10 m above sea level, with turbine grid locations. Left to right: 1 km (set #1), and 500 m (set #2) domains (FARM case), with bins: 0.1 m²/s². Maximum qke values of 1.7 m²/s² (left), and 1.8 m²/s² (right) inside the farm.

The turbulent kinetic energy TKE through the rotors is around 2.5 m²/s² (qke of 5 m²/s²), representing major turbulence intensities I_u of 14% – 16% on most domains (3km, 1 km, 500 m). Consequently, most WTs are momentarily brought to a Wind Class C (IEC 2005 Standard ⁴²), which is the climate that most WTs are exposed to; see (--) in Figure 55. Whilst, qke outside the farm ranges from

⁴¹ The parameterization in WRF treats qke as an output variable of the simulation, such that $qke=\sigma_u^2+\sigma_v^2+\sigma_w^2$ ⁴² Equation 7 to calculate the horizontal turbulence intensity equivalents. If needed, revisit Section 2.1.1. I_0 outside farm with average 13.3 m/s flow, and range of I_0 inside farm with wind speed deficits of 13.5 m/s to 11.6 m/s. IEC classification with same speed deficits. See Appendix-B: B-1 for details.

0.6 to 0.8 m²/s², representing I_0 areas of 4.7% – 5.5%. The previous values of turbulence intensity are representative for offshore sites according to literature [28]⁴³.

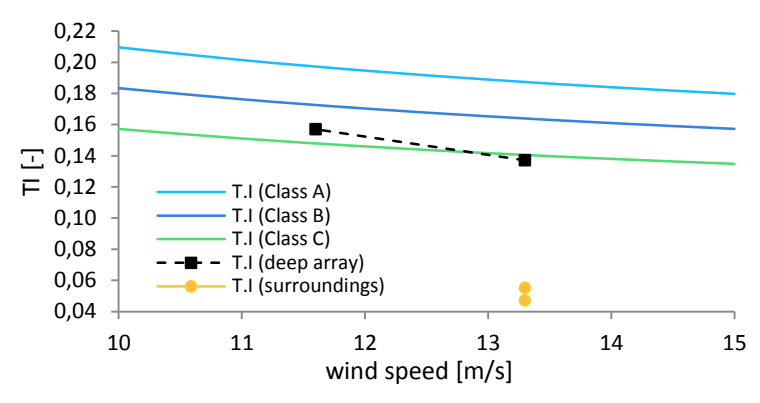


Figure 55 Example of Rotor Turbulence Intensity of the Thanet Offshore wind farm. See Appendix-B: B-1.

Given a fixed number of WTs in a wind farm, grid locations can contain more than one of them: high $N_{tc\langle i,j\rangle}$ ⁴⁴. For high $N_{tc\langle i,j\rangle}$ locations, the effect of one WTs is multiplied by the number of them per location. This approach yields more uniform areas of TKE increase on the 1 km domain than on the 500 m domain.

Results on coarser resolutions do not capture all turbulence patterns. For example, the 3 km domain shows maximum hub height TKE at the center of the farm (Figure 56-a). This situation cannot happen under the current flow and turbine characteristics, all WTs have same rotor diameters and thrust coefficient curves. It is possible to consider the TKE results on the 3 km domain if two or more wind streams meet towards the farm center. In addition, TKE patterns from Figure 56 suffice to disregard the use of the 9 km resolution for wind farm simulations of similar size to Thanet.

Unlike at the rotor area, there is no TKE generation embedded in the numerical modeling near the sea surface. But results in Figure 56-b and (c) indicate that TKE at 10 m increases up to 0.85 m^2/s^2 inside the farm due to vertical transport of turbulence (qke_{max} of 1.7 m^2/s^2 in Figure 54). There are at least three possible explanations for such increase (+0.05 to +0.9 m²/s²): tower effects, wake "surface reflection", or numerical uncertainty.

Towers are not included in the turbine parameterization scheme, and numerical accuracy is unlikely to cause such an increase over the entire region with the specific zones shown. It is more likely that numerical uncertainty will give small discrepancies when comparing simulation results to real data. Surface reflection [69] is a feasible option as it entails the interaction between the sea surface and the wake expansion from the rotor area, such that turbulence is transported vertically. Hence, the nearsurface TKE can change.

 $^{^{43}}$ See Chapter 5 Offshore winds of [28] and Figure 5.19 for FINO 1 data.

 $^{^{44}}N_{tc(i,j)}$ was defined as WTs per grid location. This value is different per location on each domain.

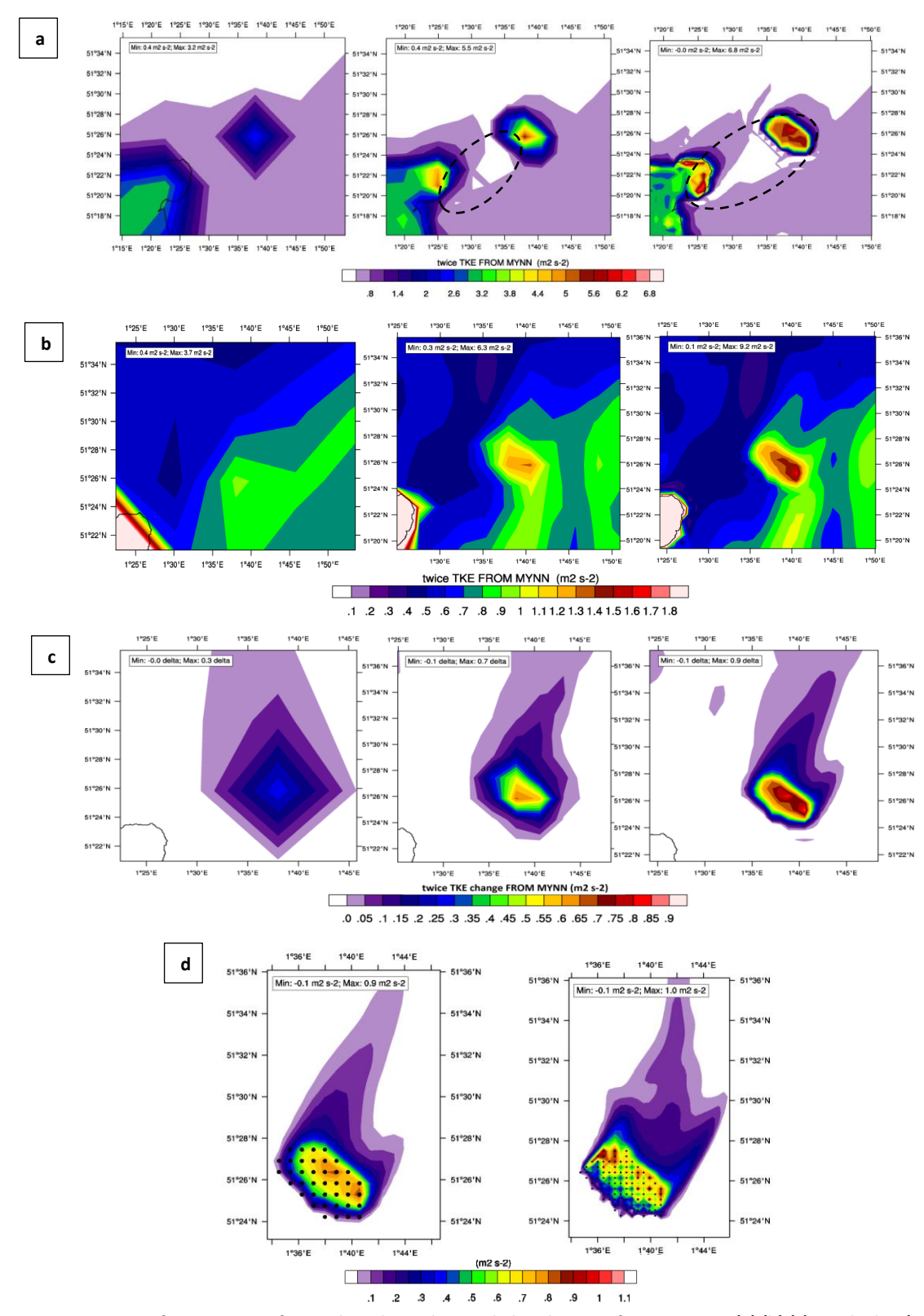


Figure 56: Contours of twice TKE. Left to right: 9 km, 3 km, and 1km domains from set #1 in (a) (b) (c), and 1 km (set #1) with 500 m (set #2) in (d). Figure (a) is FARM case at hub height with bins of 0.2 m²/s². Figure (b) is FARM case at 10 m height with bins of 0.1 m²/s². Figures (c) and (d) are FARM - BACKGROUND cases at 10 m height with 0.05 and 0.1 m²/s² bins, respectively. Maximum values displayed in (a), and (b) are found at the coast.

As expected, major changes in TKE happen inside the farm, but changes in the free stream are also important. Contrary to hub height wind speed deficits (Figure 44 ,and Figure 47), the increment of TKE is not as strong in the flow direction. Thus, turbulence dissipates downstream, in addition to a predominant upward vertical transport. The simulation results from WRF show that the vertical transport of TKE reached 300 m height (2.2 D above upper blade tip), from a qke_{max} of 5 m²/s² to 0.1 m^2/s^2 approx. Vertical transport of TKE was found by Fitch et al. [12], and by Meneveau [18] as well. For example, Fitch et al. found major transport up to 2.7 - 3.6 D above the upper blade tip: +0.1, and +0.01 m²/s² respectively. Results from both researchers indicate that momentum exchange is negligible in the horizontal direction, which is suggested by the present study. It is proposed here that such momentum exchange is negligible due to low advection of TKE in the flow direction, caused by the wind speed deficits behind the rotors; see Equation 38.

Vertical profile changes of TKE are shown in Figure 57, emphasizing the difference between the deep array and the near wake on the 500 m and 1 km domains. The deep array refers to TKE inside the farm, and the near wake to the TKE behind it⁴⁵. Simulation results differ mostly inside the farm, whilst TKE in the near wake is very low. Furthermore, wind speed deficits weaken with height, slightly improving the advection of TKE above the rotor (Equation 38). Plots from Figure 58 provide more assurance on the suggestion that *TKE* has a main vertical transport.

$$\frac{\partial TKE}{\partial t}\Big|_{advected} = -\vec{V} \cdot \nabla TKE$$

Equation 38: Advection of TKE. Wind speed decay prevents the increase of TKE in the flow direction.

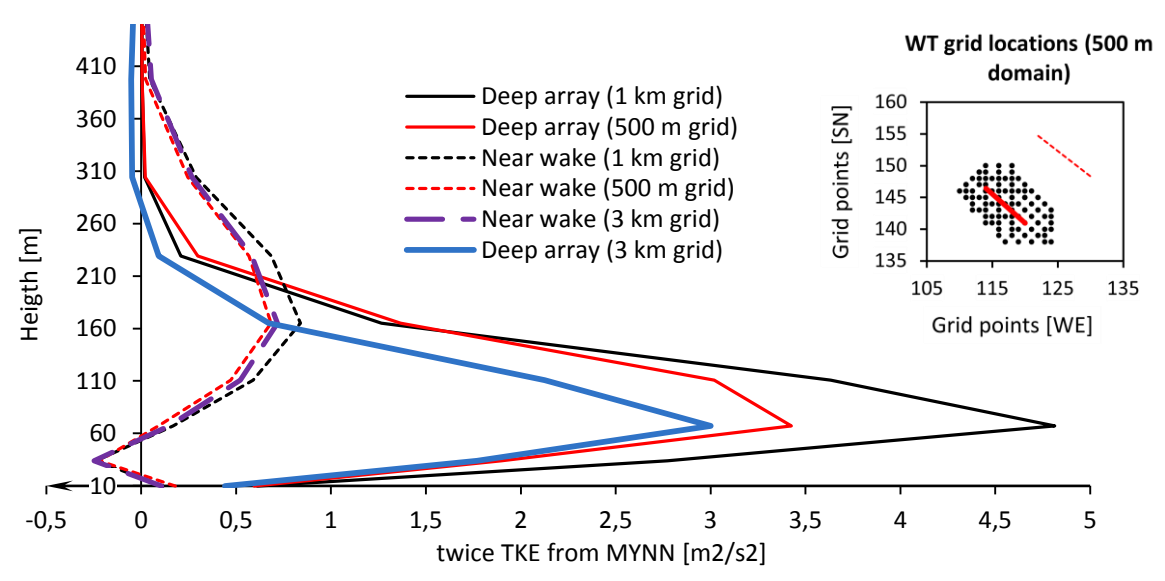


Figure 57: Average changes in twice TKE caused by the FARM presence on the 3 km, 1 km domains from set #1, and the 500 m domain from set #2 (FARM - BACKGROUND case). Turbine locations, the Near wake and the Deep wake locations are shown on the right.

⁴⁵ The distance between the wind farm and the near wake was set arbitrary for illustrative purposes, and is not used for further calculations. The location selected is approximately where the hub height wind speeds start to recover.

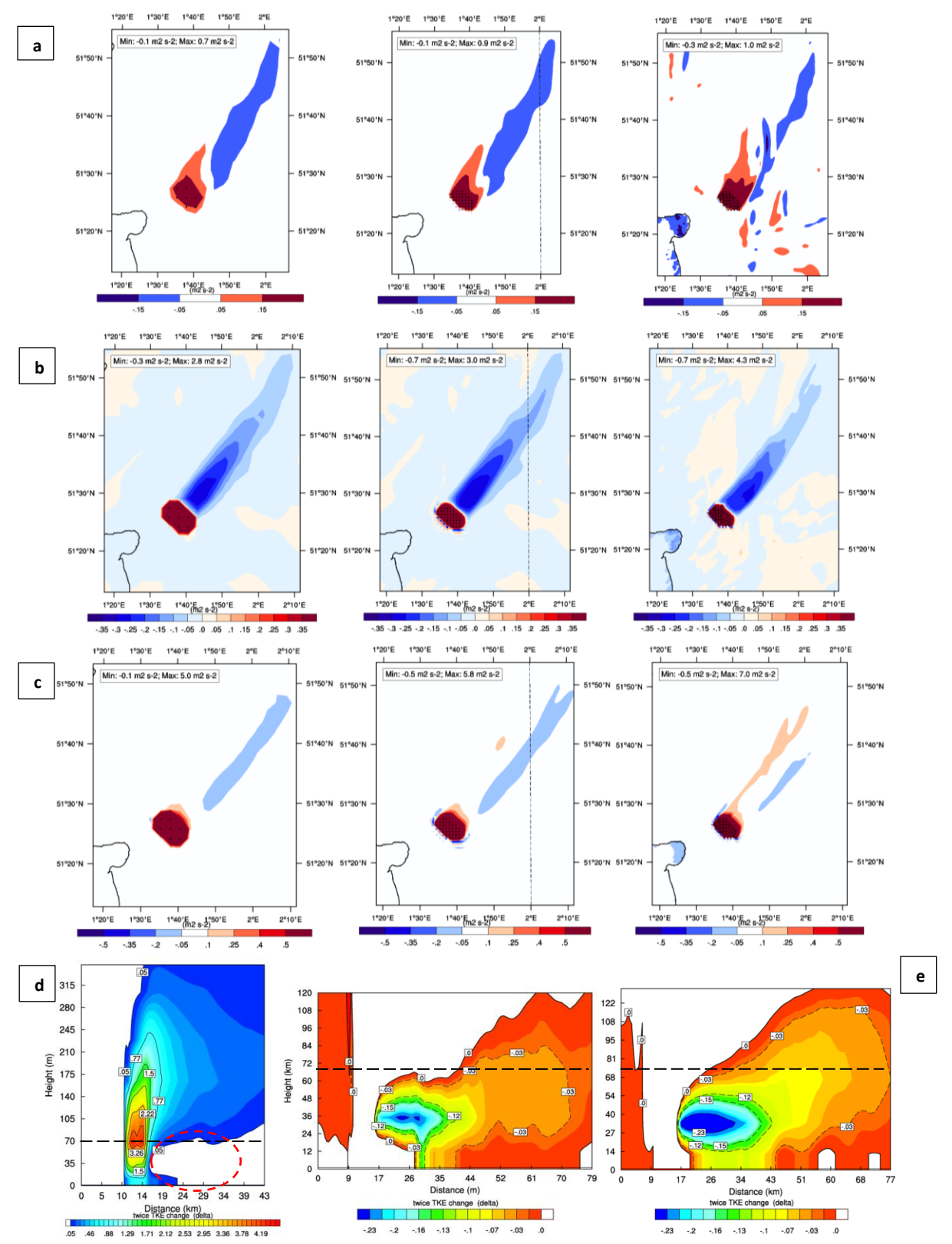


Figure 58: Contours of twice TKE to detail wake boundaries on the 3 km, 1 km domains from set #1, and on the 500 m domain from set #2 (FARM-BACKGROUND case). Order: left to right. from left to right. Horizontal contour at 10 m height in (a), at lower blade tip area in (b), and at hub height in (c). Vertical contour of positive TKE changes on the 500 m domain in (d), and the negative changes on the 1 km and 500 m domains in (e). Hub height is marked by a dashed line.

The decrease of horizontal TKE transport with time is captured by a negative wake in the FARM— BACKGRUND cases. This situation, creates a region of increased TKE, and one of negative change. The negative region starts downstream the wind farm, and is stronger below the hub height. Both TKE regions, and the spatial development of the farm wake are shown in Figure 58 for the 3 km, 1km, and 500 m domains. Figure 58-a, (b), (c) are horizontal contours, whereas (d) and (e)are vertical contours.

It has been discussed that 10 m wind speeds increase inside the farm, thereto they promote TKEadvection near the sea surface (through Equation 38), pushing downstream the negative region of the wake near the surface. It starts at the kilometer 21st on 1 km domain, and at kilometer 26th on 500 m domain (Figure 58-e). Generally, the wake length on both resolutions and its vertical development are similar. It is found to persist 46 - 56 km downstream approx. (8.2 - 10 times the farm length), with highest impact on the first 10 km downstream (at hub height), and absolute changes larger than 0.23 m²/s². Results also suggest that turbulence is higher on the wake boundaries as already discussed in section 2.2.2.

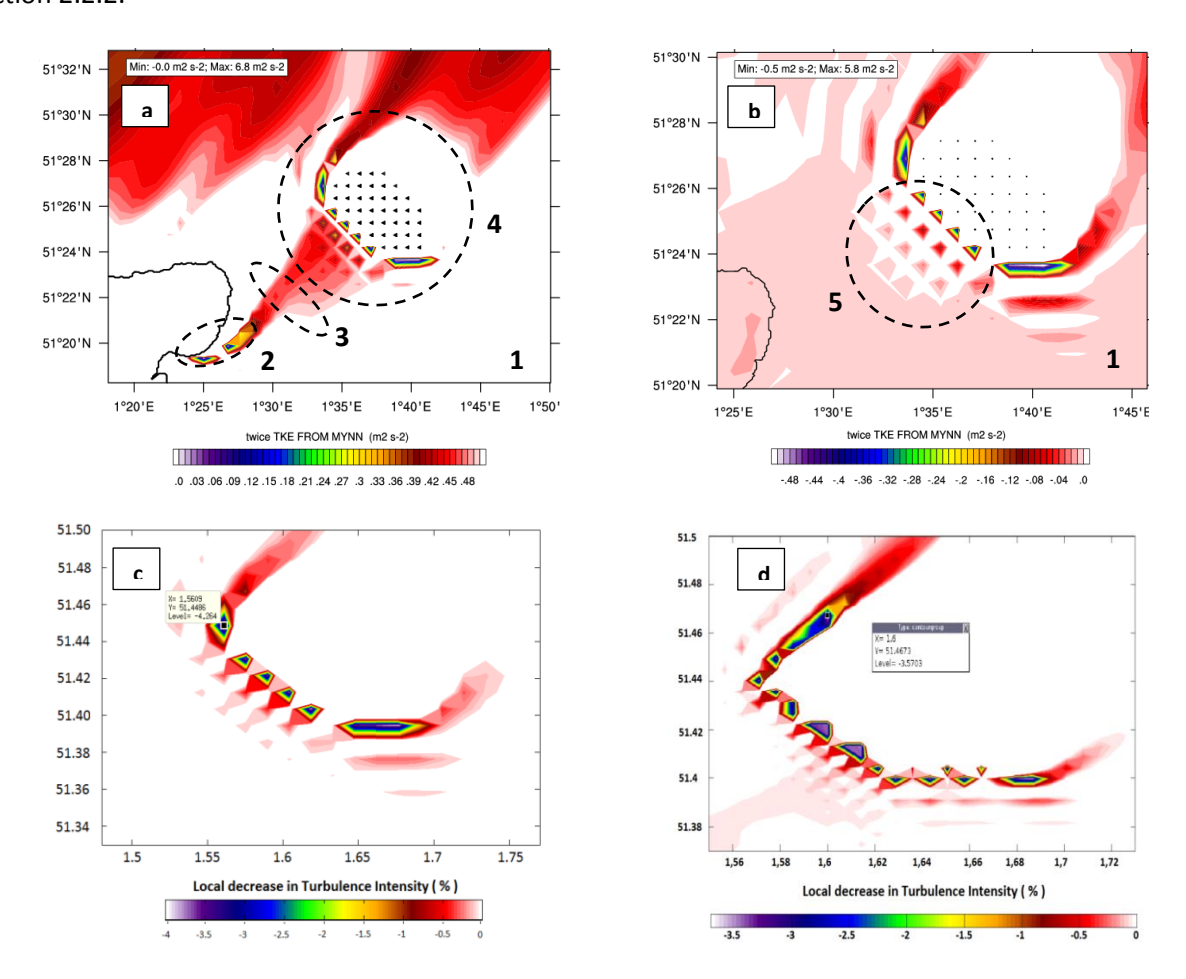


Figure 59: Peripheral reductions of TKE in (a) and (b), and of Turbulence Intensity I_o in (c) and (d), at 67 m height for the FARM - BACKGROUND case. Order: 1 km domain of set #1 in (a) and (c), and 500 m domain of set #2 in (b) and (d). Zones of positive TKE in (1), coastal effects on turbulence in (2), wind transitions from coast through the offshore in (3), location of the peripheral reductions in (4), and front reductions zones in (5).

Master of Science Thesis A.M. Striedinger P.

Changes in the free stream in front of the first WTs of the array (inflow) are shown in Figure 59. Figure 59-a, and (b) indicate local reductions of inflow TKE concentrated at half the perimeter of the farm. Turbulence decreases locally near the coast (a) to then recover and decrease again in front of the array with maximum deficits of $0.5 m^2/s^2 qke$ at the center of peripheral locations (b). The front peripherals lay between WT rows staring from 10 m height and above (5). Turbulence intensity I_0 in Figure 59-c and (d) shows similar patterns with maximum reductions of 4% surrounded by areas of ΔI_0 < -3%. On the other hand, none of the TKE and I_o reduction regions present smooth contours or transitions on either the 1 km or 500 m domain. Hence, a higher resolution is needed for such details.

4.4. Changes in local meteorology

Local meteorology is also affected by the farm presence through changes variables such as air temperature, upward surface-heat flux H_{Sf} , planetary boundary layer height h_{st} , and vorticity among others. Results on the 500 m and the 1 km domains provide similar features.

Changes in temperature are rather small in comparison to changes in other variables. However they do have an important pattern. A vertical gradient in temperature is developed, separating cooler air masses above the rotor area, from similarly hotter air masses below it. For example, temperature changes reached maximum values of +1°C, and -0.2°C, yielding +10% and -2% relative changes in the FARM - BACKGROUND case. Because the BACKGRUND temperature field is practically homogeneous, the temperature gradient causes heat transfer from the surface; see Figure 60-a. The plot suggest that energy in the form of heat goes up and is also transported downstream.

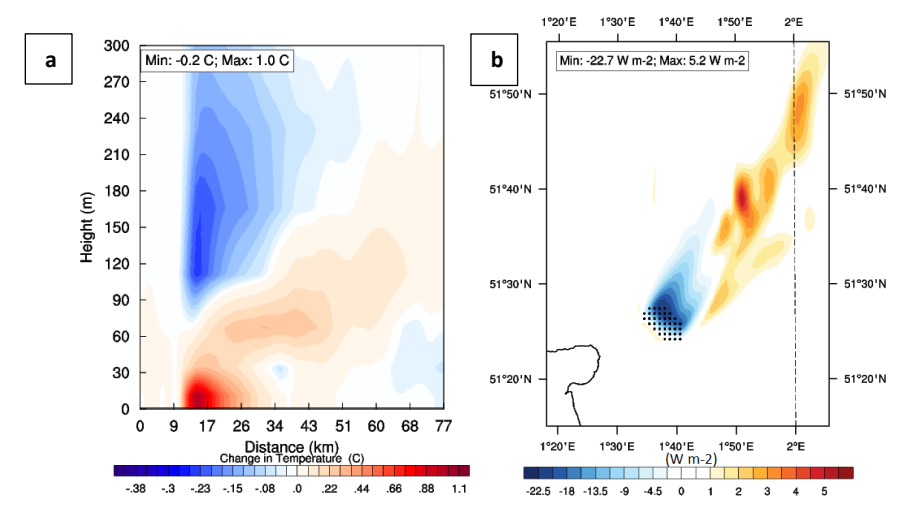


Figure 60: Vertical contour of temperature changes (a), and horizontal contour of surface-heat flux H_{sf} changes (a). All contours are on the 1 km set #1 domain and from the FARM - BACKGROUND case.

The warm up of air near the surface, decreases H_{sf} inside the farm site. Depending on the surface temperature and initial conditions, the total H_{sf} could be zero, negative or more negative. The decrease of the heat flux inside the farm as shown in Figure 60-b is not uniform, but rather proportional to the TKE generation pattern near the surface (Figure 56-d, Figure 58-a). Surface-heat flux increases

downstream, with minimum Δ of -5.2 W/m², and extends along the farm wake. Results also show that both high grid resolutions yield similar trends; see plot in Figure 61.

On land, H_{sf} is commonly positive during the day, and negative during the night [39]: i.e. watersurface is colder than the air above. Positive H_{sf} indicates TKE generation by buoyancy, whilst negative H_{sf} consumes/destroys TKE [71]. Commonly, unstable atmospheres promote upward surface-heat flux, whilst stable atmosphere the opposite. This situation has to do with the fact that stable atmosphere suppresses vertical transport of turbulence (for positive H_{sf}). We need to remember that stable boundary layers often happen during dawn hours as well, like in the example above. Hence, \mathcal{H}_{sf} is negative in dawn hours and the farm is making it more negative at the site.

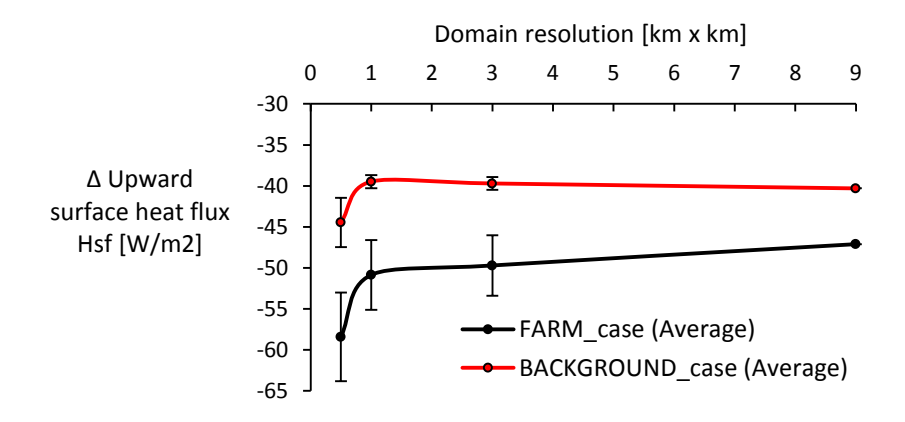


Figure 61: Changes in H_{sf} inside the farm per domain resolution. Standard deviations are plotted as error bars.

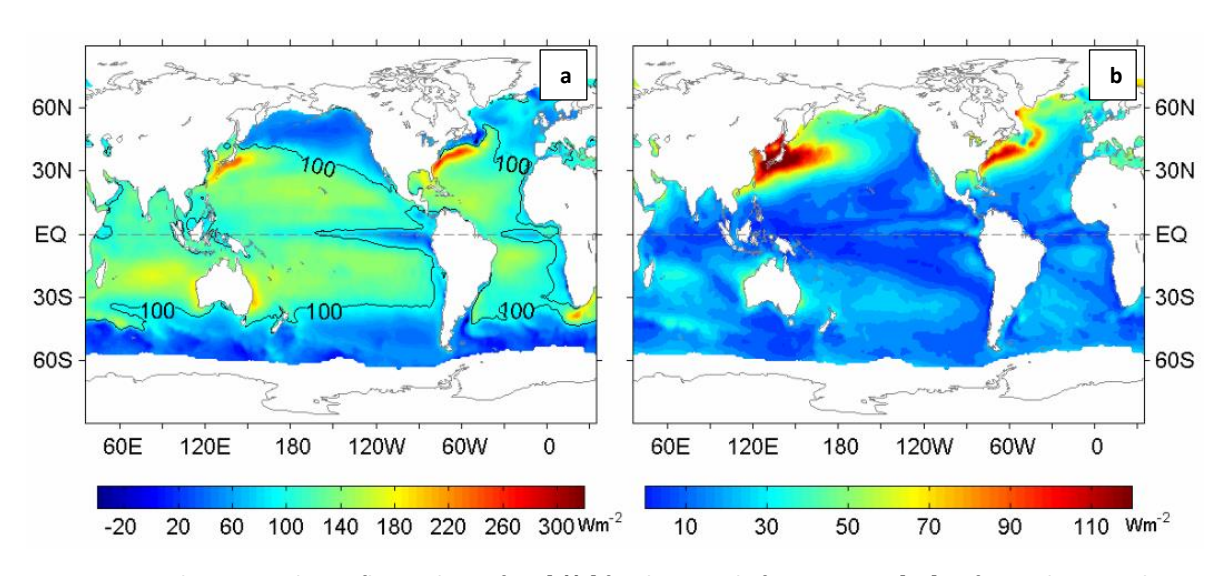


Figure 62: Averaged Downward Heat flux to the surface [-H_{st}] for the period of 1958 – 2006 [71]. Left to right: annual mean (a), and standard deviation (b). UK is located inside the dotted circle.

A.M. Striedinger P. Master of Science Thesis

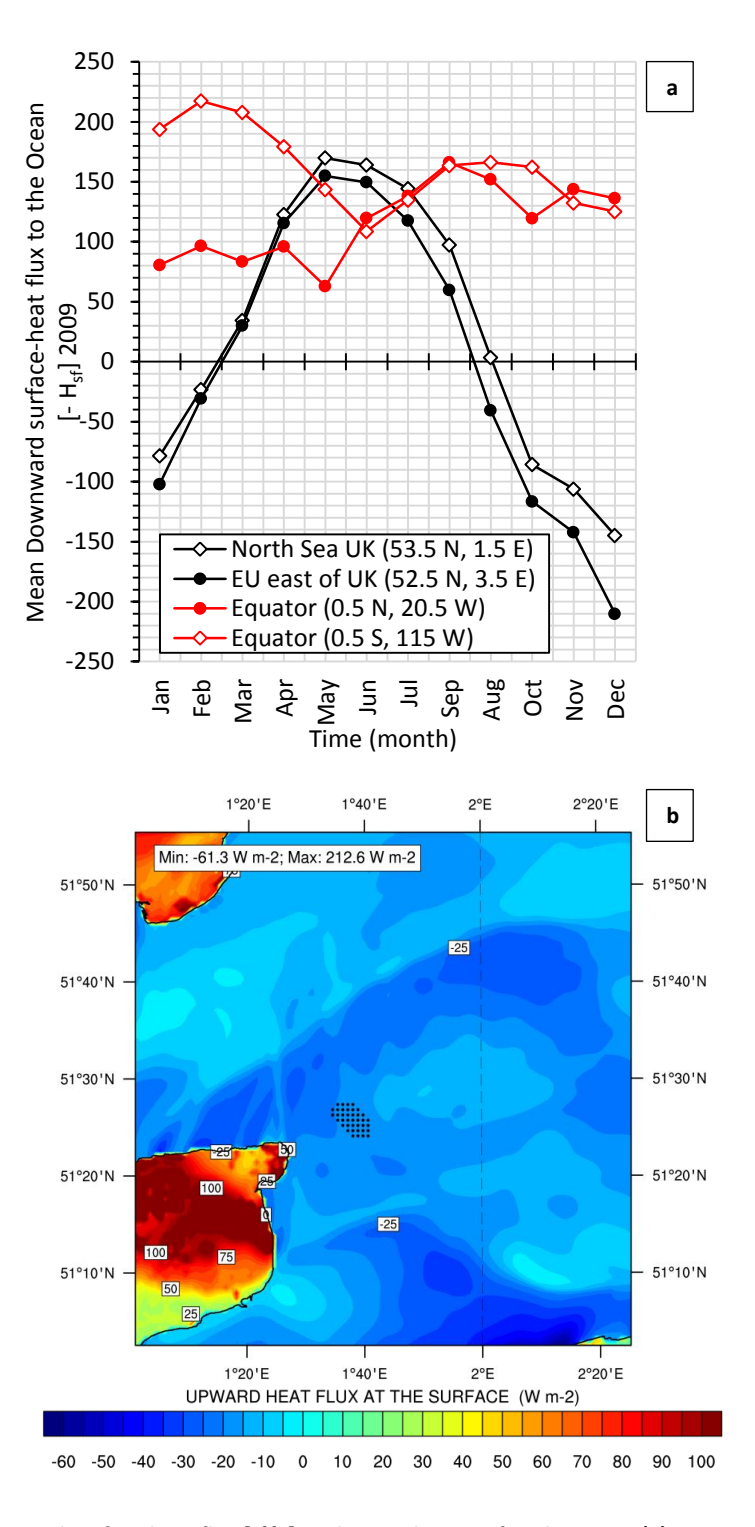


Figure 63: Monthly downward surface heat flux [-H_{sf}] to the North sea at four locations (a): two near Thanet, and two on the Equator; data is from 2009, and adapted from the WHOI OAFlux project [72]. Contour of upward surface-heat flux for the BACKGROUND case in (b), with turbine grid location on the 1 km domains from set #1, at 12:00 hours, March 19 2010. The contours in (b) illustrates that the sea coast on UK "gains heat", whilst the land releases heat.

As weather seasons evolve during the year, they have an impact on the surface-heat transfers from the ocean, and H_{sf} diurnal cycles start to change, as they depend on the latitude and longitude positions

of interest. Consequently, H_{sf} on day time may be negative. That is, the sea "gains heat" or experiences a downward heat flux. On the equator, this situation is strong and highly expected along the entire year, due to the high levels of solar radiation. On the North sea, the variation in H_{sf} is higher. Figure 62 shows Lat/Lon dependency of annual H_{sf} , whilst Figure 63-a shows the seasonal effect, and Figure 63-b shows H_{sf} from simulation (BACKGROUND case) on the 1 km domain at noon. The figure shows downward flux on the offshore and upward flux on land. Hence, for current study March is a period on which the North Sea "gains heat".

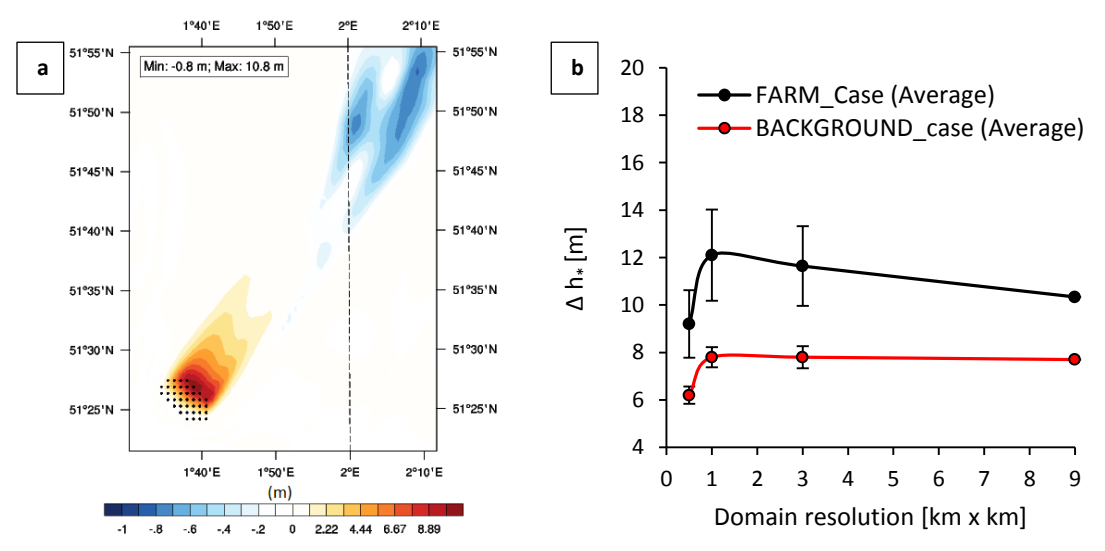


Figure 64: Contour of Δh_{*} on the 1 km domain from set #1 (a), and Plot of average Δh_{*} inside the farm per domain resolution (b): standard deviations are plotted as error bars.

Figure 64 shows the changes in h_* inside and above the farm site (Δ), where the h_* reaches peak values above the last WTs (in the flow direction): i.e. maximum Δh_* of +11 m on the 1 km domain (a). In addition, the Δh_* pattern is found to be the same as the pattern in ΔH_{sf} (Figure 60-b & Figure 64-a). The explanation for such a change is very simple and obeys the mass conversation law in an open control volume analysis:

As the rotor wind speed decays inside the farm, wind speed must increase on other regions in order to compensate for the loss of mass transport through the rotor areas :i.e. speed-ups near the surface. Section 2.2.2 explained that speed-ups can occur, pronounced on regions where the flow "cannot expand" like near the surface, where the option for the flow is to increase its speed and/or expand sideways. This fact is because the water acts as a rigid surface preventing air from expanding downwards. Above the turbine rotors, the wind can expand in order to circumvent the rotors and, it does not need to accelerate because there is no "rigid surface" high above WTs. The expansion above the rotors can be complex, but its vertical projection is measured by the Δh_* Furthermore, the decrease in temperature above the rotor in Figure 60-a also suggest air expansion.

The influence of local flow patterns on the shape of the farm wake and possibly its strength can be observed by measuring the changes in vorticity of the flow. Vorticity is quantified as 2 times the angular velocity vector of the flow at a center point; such center point may be fixed or moving in space. Vorticity can be generated when two currents flow next to each other, at a different speeds (i.e. shear flow). Such that the current with the highest speed starts to rotate inwards to the current with the lowest speed (clock or anti-clockwise rotation, negative or positive). For example, vorticity plots in Figure 65 make a clear distinction between the flow inside and outside of the wake. The wind inside the wake is slower than that outside the wake, creating positive and negative vorticity at wake boundaries.

It was explained earlier that the Thanet wind farm is subject to gap winds from the English Chanel at the southeast. The vorticity has increased along the wake border making a clear division between the mixing in the wake and the outer flow to the right. There is some amount of mixing inside the wake but nor relay marked by the abrupt changes in vorticity shown here. Further, the calmer winds on the west of the farm add negative vorticity to the downstream, such the trail of negative vorticity is the wake boundary on the left. It is also important to highlight that the changes in the vorticity field are also presented inside the farm. One therefore, could argue the changes in vorticity originate inside the farm and increase was we get close to the wake boundaries. For more plots on meteorological variable see Appendix-B:B-4.

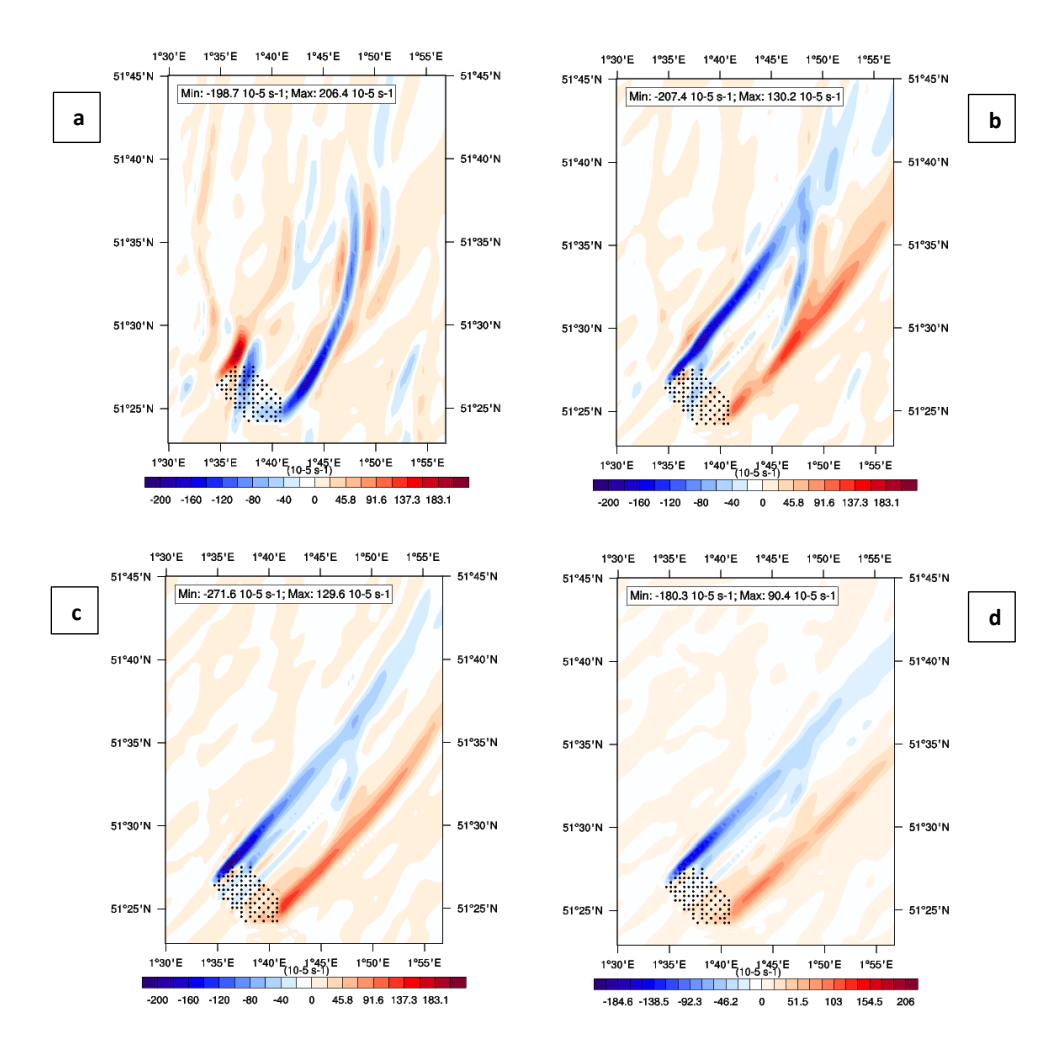


Figure 65: Vorticity contours on the 500 m domain from set #2 at 4 different heights (FARM - BACKGROUND case): 10 m (a), lower blade tip section at 33 m (b), hub height at 67 m (c), and higher blade tip at 109 m (d). Units in 10⁻⁵ s⁻¹.

Turbine layout considerations and model physics on high 4.5. resolution domains

The 500 m domain from set #2 allows more turbine grid locations than the 1 km domain from set #1: 89 and 39 locations respectively, due to the short spacing between WTs (500 to 880 m). Simulation results suggest that the previous situation yields a considerable difference in the BACKGROUND wind conditions of both domains (direction, speeds, and patterns). Major differences are found in the BAKCOGRUND winds, near the sea surface on both domain. Nevertheless, such a difference in the wind conditions is not proportional to the changes suffered on the coarser resolutions. Thus, indicating the influence of micro-scale flow effects in the farm site on 500 m domain. Most micro-scale effects near the surface are controlled by the surface-layer physics, and the radiation schemes in WRF. The surface effects are then transmitted to the PBL scheme, which derives the winds in the boundary layer; see Figure 66 and Figure 67.

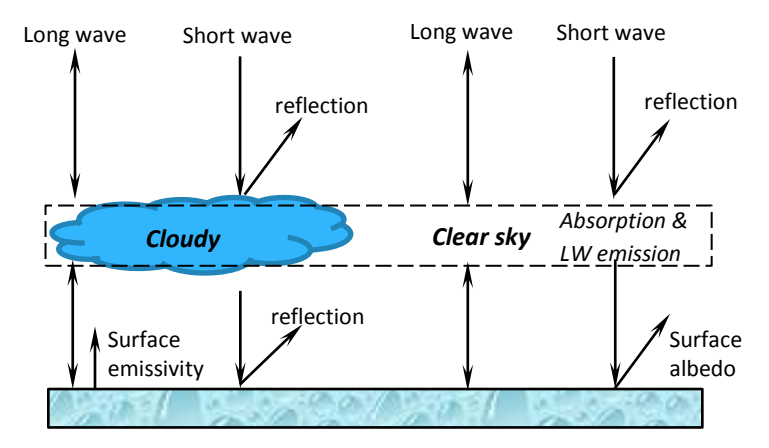


Figure 66: Illustration of the Free Atmospheric Radiation Process. Surface Albedo is the diffuse reflectivity of any surface. Adapted from [73].

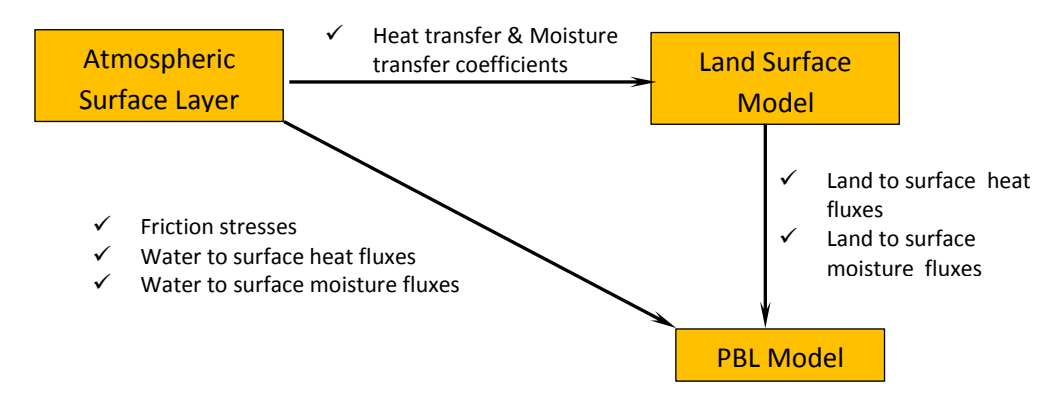


Figure 67: Diagram of Surface Physics Components in WRF. Each block indicate a computing module. Adapted from [73].

Master of Science Thesis A.M. Striedinger P.

Heat and moisture fluxes depend on the aerodynamic roughness length (defined in section 2.1), which depends on the winds at the water surface. Hence, this relation is key in the simulation of large offshore wind farms. The treatment and further analysis for this relation falls out of the present study due to time constraints.

Most physics schemes inside WRF are meant for simulations of the meso-scale atmosphere, and the 500 m resolution may fall out of it. The WRF user manual, and literature recommend using LES for high resolution domains because it resolves for the energy contained in the turbulence, with good agreement with measurements in the far wake [18] [22] [25] [75] [76]⁴⁶. LES is more computationally demanding, time consuming and it does not incorporate the current turbine parameterization. Consequently, changes in flow physics schemes were not studied.

Nevertheless, two factors can explain why the flow behaves so differently on the 500 m domain. The 1^{st} reason is 'empty' grid cells between tribune locations (spacing ≥ 5.5 D) in the 500 m domain, providing distance and time for the development of the near wake region of some turbines (of 2D-5D [23]). Therefore, an expected partial wind speed recovery is captured inside the farm, yielding a slightly weaker wake inside the farm and behind it. The 2nd reason is the influence of topography, like land-sea wind transitions due to changes in resolution [77]: high resolution produces more accurate topography, and low resolutions smooth it. Topography affects pressure differences, air circulation, and buoyant forces in the air, which in turn drive local winds. In addition, land-sea transitions affects the evolution of wind speed profiles. Consequently, inflow winds are dependent on grid resolution due to the farm's proximity to land. It is therefore proposed that the grid resolution and its implication on the topography of the coast, micro scale flow effects, and turbine locations, are causing the main differences in results from both domains; these are:

- Wind speed near the sea surface (i.e. Figure 45, Figure 49)
- Wake strength inside the farm (i.e. Figure 53, Figure 57)
- Strength of the Farm's near wake (i.e. Figure 58-b, and Figure 58-e)
- Turbulent kinetic energy transport of the wind approaching the farm (i.e. Figure 68-a, b)

Differences in the turbulent kinetic energy transport can be described from the inflow up to the winds downstream of the wind farm (BACKGROUND case). At the farm location, rotor sections are of importance: Above hub height, and below hub height. For Figure 68 the following points can be suggested:

 \bot The average TKE density of the inflow (on rotor area) is similar on the 3 km and 1 km set #1 domains, and lower on the 500 m domain from set #2: 19.7 m^3/s^2 for the 500 m, 25 m^3/s^2 for 1km, and 23.5 m^3/s^2 for 3 km.

⁴⁶ See also http://www.mmm.ucar.edu/wrf/users/FAQ.html and look for the question "Can I run both ideal and real case LES simulation? For the real case, is there anything special I need to do?" and daily news at http://www2.ucar.edu/for-staff/daily/calendar/2013-09-12/mesoscale-modeling-high-not-turbulence-resolvingresolution

- The 500 m grid caries more turbulent energy than other domains below hub height, but less above it.
- Above the rotor area, the south hills of the UK add a peak of TKE. The peak is most visible in the inflow and disappears as the flow transits forward. It is most likely due to a peak in turbulent stresses. Otherwise the profile would have presented only the peak 25 m above sea level, and a rapid decrease with height. A similar decrease is stated by Meneveau et. al. [18] on their LES simulations.
- \blacksquare The TKE peak above the rotor area is lessen on the 500 m, and according to B. Matteo [78] it could be due to a change in the diffusivity of momentum ε_t in each domain. As the ε_t decreases, it would flatten the TKE profile. Figure 68.c shows the flattened TKE profile from LES simulations, and the tendency as diffusivity changes.

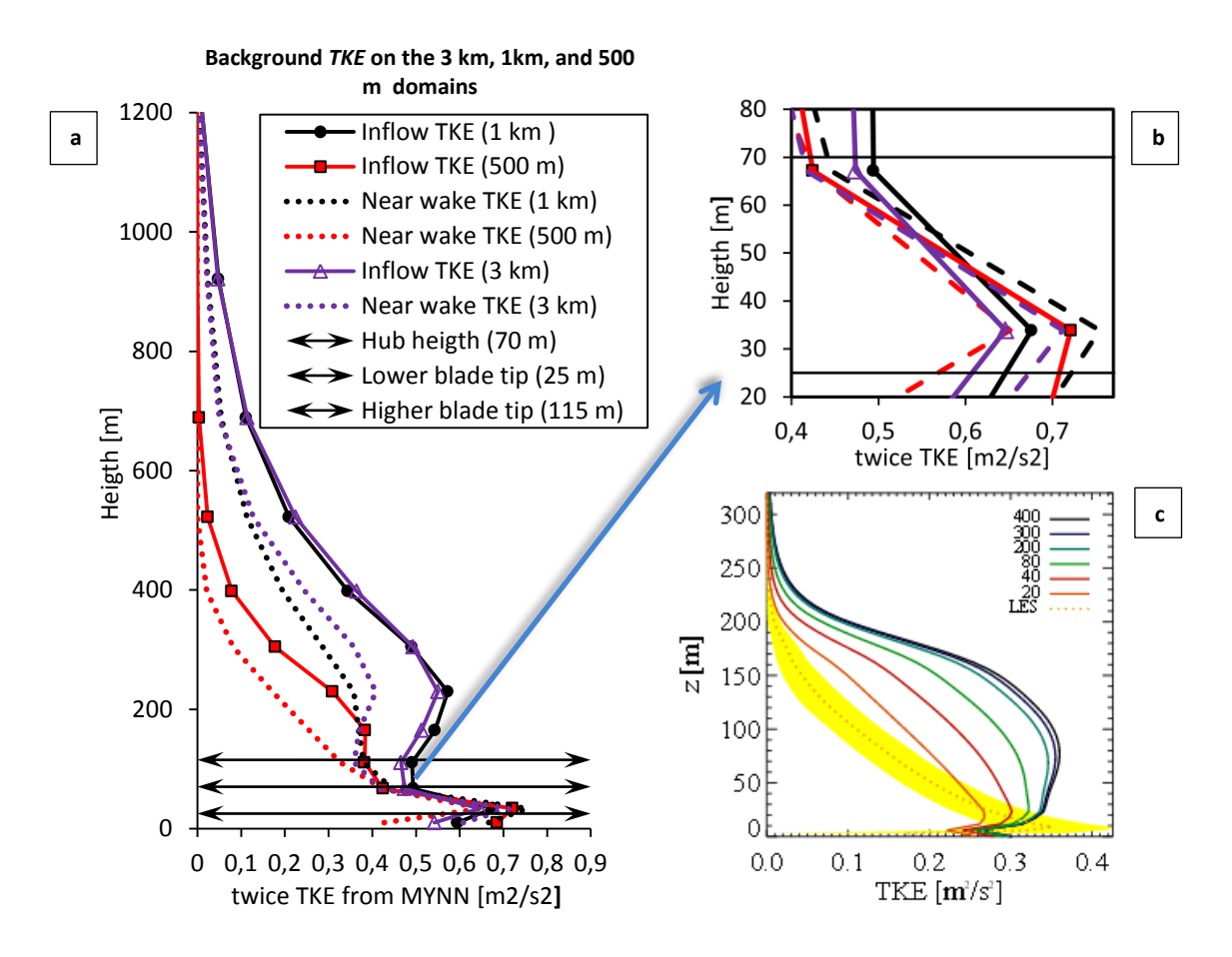


Figure 68: Vertical Profiles of spatially averaged TKE on the BACKGROUND cases in (a). Solid lines represent the inflow profile (flow reaching the farm), and dotted lines indicate profiles just behind the farm location 'Near wake'. Arrow lines indicate the rotor areas. A zoom of the TKE profile on the rotor area is shown in (b). A sensitivity analysis of TKE with respect to momentum diffusivity (ε_t) by B. Matteo [78] is shown in (c): TKE profile flattens as diffusivity decreases.

The eddy diffusivity ε_t of momentum (m^2/s) is related to the turbulent shear stresses $\bar{\tau}_{ij}^t$ through Equation 39. The higher the diffusivity, the more important the turbulent stress are in shaping the

Master of Science Thesis A.M. Striedinger P.

TKE profile because TKE is a measure of the turbulent shear stresses. The stresses are derived from the equations of motion for turbulent flow. In simpler words, as ε_t decreases, the spatial change of wind speed increases (turbulent part, i.e. $u'_{Z+\Delta Z}-u'_Z$). With time, this change becomes higher. Because TKEmeasures the energy in (u', v', w'), TKE is higher at the points where the spatial difference in the turbulent speed is higher. On Figure 68, the previous statement means that the TKE profiles moves locally to the right.

$$\overline{\tau_{ij}}^t = \rho \overline{v'_i v'_j}$$

$$\overline{\tau_{ij}}^t = -\rho \varepsilon_t \frac{\partial \overline{v_j}}{\partial x_i}$$

Equation 39 Relation of Turbulent shear stresses $\bar{\tau}_{ii}^t$ to the eddy diffusivity of momentum ε_t .

4.6. Computational time and file size in WRF simulations

Computational time is defined here as the real time needed to perform the commutation and generate the results. On the other hand, the simulation time is reserved for the time that is being represented by the simulations: i.e. March 19, 2010 at 00:00 hours. The simulation time is discrete and depends on the input time-step defined by the user. This input time is transformed into a stability parameter for the simulation, as explained in section 3.1.4.

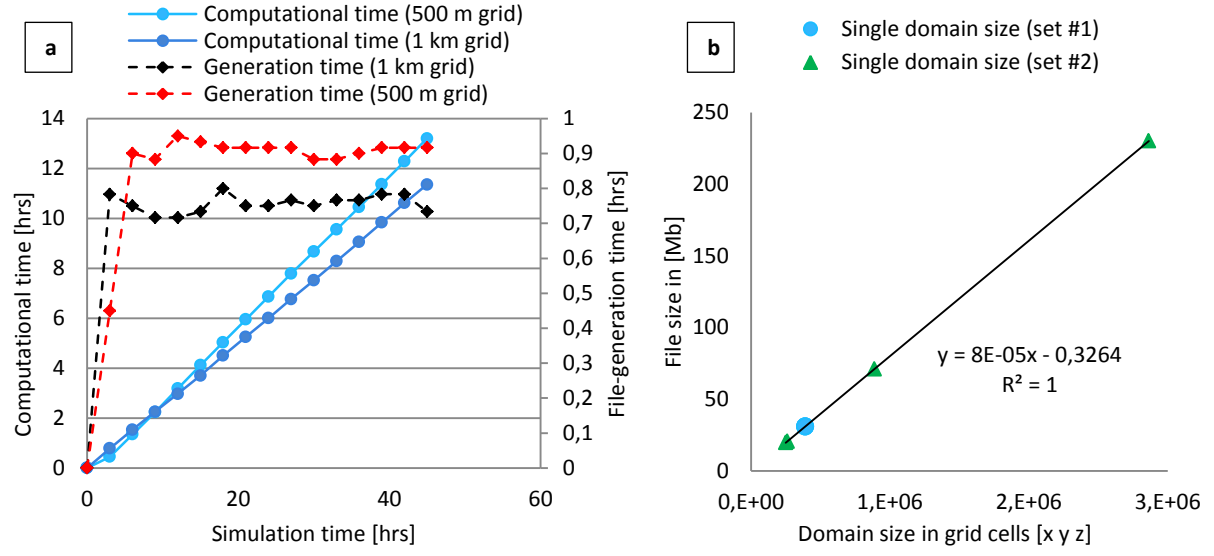


Figure 69: Computational time simulations (a). Size of simulation domains in Mb as a function of grid cells per domain. The size in Mb can be further reduced by eliminating variables before executing WRF (b).

For the current simulation sets the adaptive time-step configuration was selected, such that WRF would select the proper time-steps to comply with the stability constraints, whilst optimizing for a fast computation. In addition, the computational time required for each result or output file from WRF was nearly constant (generation time); see red and black lines in Figure 69-a. Each generation time is derived from the date tag of the output files from WRF. Hence, adding the generation times gives the total

A.M. Striedinger P. Master of Science Thesis computational time of the study; this is also shown in Figure 69-a. The computational time was 11.35 hours for a simulation time of 45 hours on the 1km domain resolution from set #1, and 13.2 hours on the 50 m domain resolution from set #2. The simulation used 54 cores in a Linux server to produce the results.

According to Figure 69-a the predicted computational time for a simulation time of 1 month would be 8 days (24hr/day) on a 1km domain resolution, and 9 days on a 500 m resolution. Therefore, it is estimated that 3 month of computational time are needed to simulate an annual energy yield (in GWh) of an offshore wind farm with similar size to Thanet. The previous prediction can be used for specific wind energy resource assessments, and influence future decisions regarding the construction of large offshore wind farms.

WRF has a special approach when creating nested domains of different resolutions. This approach is the grid ratio between nested domains, i.e. grid ratio of 3 between the domain 3 (1 km resolution) and the domain 2 (9 km resolution). Grid ratios must be odd numbers, this is a constrain in WRF, and is one of the reasons why the 500 m domain is located on the simulation set #2. A consequence of this constraint is the change in size of nested domains, the higher the grid ratio and the resolution, the bigger the domain in order to represent a certain surface area. The domain size is measured in the number of grid cells, and producing a certain size in Mb of each domain output file. See Figure 69-b.

The file size in Mb is linearly proportional to the domain size in grid cells. The size of the 500 m domain is the biggest of all, with 2.864 E+06 grid cells (230 Mb), and occupying a surface are of 1.8 E+04 km² (Table 8). The surface area on the 1 km domain from set #1 is 1 E+04 km² with 0.39 E+06 grid cells and a file size of 31 Mb. Therefore, a two fold increase in domain size has yielded a 7.6 fold increase in a single file size. The previous fact has immediate consequences in the storage capacity of the computer or server where the simulations are run. On the contrary, the computational time did not change considerably between results on the 1 km and 500 domains.

High resolutions like that of the 500 m domain may not be suitable for large project where storage is a key feature, as it will increase computational costs. Results suggest that a 1km resolution or a domain yielding 1 to 3 WTs per grid location, may suffice for the modeling of wind farm effects in the meso-scale atmosphere.

Chapter-5 . Validation Study Of Middelgrunden Offshore Wind Farm Reanalysis

This chapter deals with the partial validation of the current turbine parameterization in WRF with the purpose to expand the findings of Chapter-4 with respect the answering the $\mathbf{1}^{st}$ research question, whilst providing an answer to the $\mathbf{2}^{nd}$ research question:

4 2nd For MeteoGroup: Is the turbine parameterization able to produce accurate predictions of power generation from wind farm.

The wind farm to be analyzed is the Middelgrunden offshore wind farm (MIDD), built in 2000 as the world's largest offshore farm at that time (Figure 70). The approach in this chapter is to describe the offshore site and simulation setup in section 5.1. The input data for the model and free stream conditions around MIDD are described in section 5.2. The accuracy of the atmospheric model physics in capturing the free stream is described in section 5.3 & 5.4, and the accuracy of power forecast and performance of the flow model + turbine scheme are discussed in section 5.5: efficiency of power generation, speed deficits, and turbulence generation. Finally, conclusions and recommendations from this thesis work are presented in the next chapter.



Figure 70: Geographical location of the Middelgrunden Offshore wind farm. Background figure taken from Google earth. Turbine layout obtained from wind farm data and plotted in the UTM coordinate system: UTM zone 32.

A.M. Striedinger P. Master of Science Thesis

Site Description and Simulation Setup 5.1.

Located in Øresund between Denmark and Sweden, MIDD sets 2 km east of the Copenhagen harbor [80]. Wind direction is dominant from the southwest during the year, with an eastern bias each month. According to measurements from a weather station at København-Kastrup⁴⁷, westerly winds are frequent in March (248°, 293°), with a switch to south-easterly winds in April (157°). The annual average wind speed is 6 m/s, and monthly averages deviate $\frac{+}{0.23}$ m/s. Because the simulation time covers the beginning of April 2001, the transition of wind direction between March and April is important, and it was captured by the flow model using ERA-Interim input data⁴⁸. More information on the offshore site is given in Appendix-C. When pertinent, such information is presented.

MIDD consists of 20 2MW Bonus WTs of 76 m rotor diameter and a 64 m hub height. They are oriented from south to north in a bow shape, with a 2.4 D spacing (154 m); see Table 12. Thrust and power coefficients C_T , C_p from the manufacturer are implemented for the current validation study; see Figure 71.

Table 12: Middelgrunden Offshore Wind Farm (MIDD) Location.					
Location: Amager, Denmark (Copenhagen, Sjaelland)					
Latitude: 55°41.454	55°41.454 (55.6909)		ut: 3-25 m/s		
Longitude: 12°40.248	(12.6708)	Hub heig	ht : 64 m		
Distance to shore:	2 km	Spacing:	182 m (2.4 D)		
Water depth:	3-5 km	Phase:	Commissioned		
Power Capacity:	40 MW	Wind Farm Boundaries			
Turbines: AN Bonus		Turb	Lat, Lon		
2MW/76 (20 WTs)		WT 01	55 ⁰ 42.09, 12 ⁰ 40.1		
		WT 20	55 ⁰ 40 546 12 ⁰ 40 1		

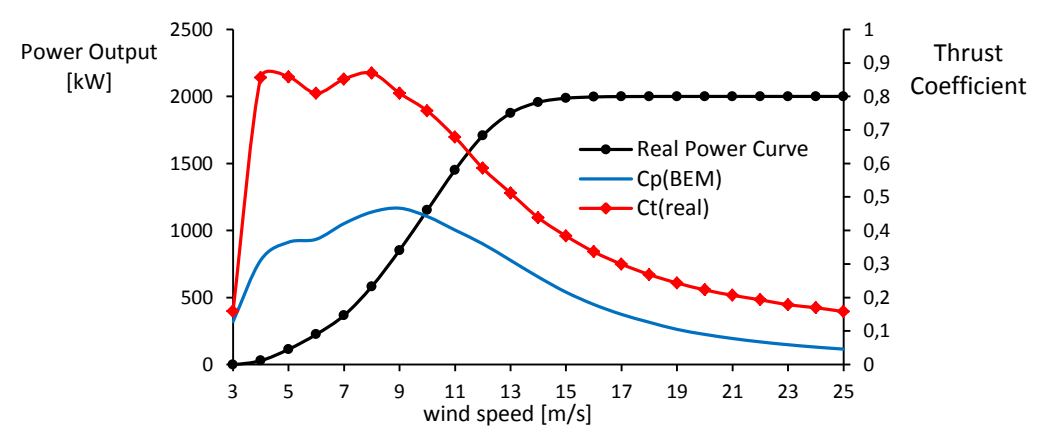


Figure 71: Bonus 2 MW/76 Turbine Power and Coefficient Curves.

Master of Science Thesis

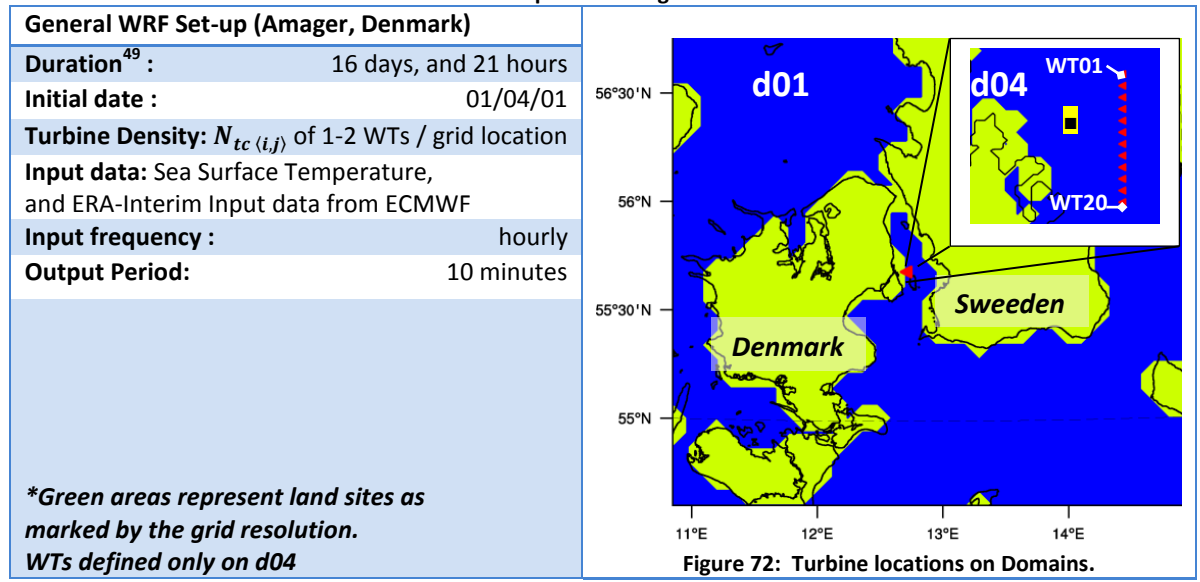
⁴⁷ Information of wind speed and direction can be verified in http://www.windfinder.com/windstats/windstatistic koebenhavn-kastrup.htm&fspot=marina kastrupin ⁴⁸ ERA-Interim input data has been defined in Chapter-4.

Table 13: Domain configuration for the WRF simulation of MIDD, domain size (mxn) represents horizontal plane of the gridded domains.

Domains	Resolution & Size		
Parent domain (d01)	22.5km (36x36): 62*10 ⁴ km ²		
Nested domain (d02)	7.5km (37x37): 7.29*10 ⁴ km ²		
Nested domain (d03)	1.5km (36x36): 2.756*10 ³ km ²		
Nested domain (d04)	300m (36x36): 110 km ²		
Turbine Locations of interest	At d04		

Short spacing between WTs demands a high resolution grid, for which 4 domains are implemented in a nested configuration yielding a final 300 m grid (d04): WTs are defined on this domain. See Table 13 for domain configurations. The location of each WT is automatically adjusted to the grid resolution. Consequently, a total of 12 grid locations is used: 8 locations with 2 WTs each, and 4 points with 1 WT each. Unfortunately, the bow shape of the farm layout is lost in the configuration, and is not distinguishable in the grid. Analogously to the Thanet results from Chapter-4, the current WRF configuration has 4 vertical intersections in the rotor area, and an attempt to increase the vertical resolution produced numerical instabilities in the output hydrostatic pressure fields at all grid levels.





⁴⁹ The first 12 hours count as a spin-up time in WRF to initialize the system, hence outputs in this range are disregarded.

5.2. Data description and Method

In order to assess the efficiency of the turbine scheme in WRF, it is important to validate the inflow wind conditions with available measurements, and see if the weather conditions at which the data was taken are represented during the simulation. Accordingly, the validation and verification data sets are first described. Secondly, there is a description of the "free stream" or undisturbed wind as produced in the simulation, and as inferred from the data sets.

Simulation results are compared with three data sets, and an external data source; see Table 15. The data sets are the Forecast data set, April data set, and Met mast data set. Information from the Met mast data set is prior to the farm operation. The met mast was located at 55° 42.1N, and 12° 39.45 E [80]. It has a height of 50 m, and wind measurements (V, σ) are referenced to heights of approximately 10 m, 30 m, and 50 m above sea level. Interpolations for intermediary heights are also included. More information on the meteorological mas set is given in Appendix-C: C-1. The external data source is the work on wind farm wakes by R. J. Barthelmie et al. [79] (See Table 15). Sample plots on met mast measurements and wind farm performance are extracted from this source.

Table 15: Description of data sets for validation and verification of simulation results

Data sources ⁵⁰	Description
Forecast data set	Measurements from the South or North turbines (WT20 or WT01) for the "free stream" wind
	, and independent turbine data. Duration: Simulation time
April data set	Same as Forecast data set but for the "free stream" only, and different duration: 2001 – 2004, for the month of April only.
Metmast data set	Measurements from met mast data (■). Duration 1997 – 1999 ⁵¹
R. J. Barthelmie et al. [79]	Analysis of met mast data, wind farm efficiency, power generation, and wake effects. Duration: 2001 – 2004, annual info as [*].

SCADA data describing the turbine performance in a 10 min series were given for the forecast and April data sets (averaged quantities). The output variables from the SCADA are mean and standard deviations of active power (P_{avg} , σ_p), yaw angle (not mismatch), nacelle and turbine wind speed, the orientation of each WT, and whether they are active or not (i.e. a WT could be active but not producing power). In order to determine the wind direction of the free stream only WT01 and WT20 are used such that they fulfilled the following criteria:

- No missing values of wind direction from either WT
- 4 If both WTs point in the same quadrant, assume reading from the WT01 or WT20 correspondingly: 90° – 270° (WT20), else WT01.
- 4 If readings from both Wt20 & WT01 point to different quadrants, check the orientation of the WTs (pointing South or North), and read from WT01 or WT20 accordingly.

⁵⁰ 2001-2004 data available for Nacelle wind speed, for the period of 2001-2002 Turbine wind speed is provided in the virtual wakes lab of Indiana University (collection of measurements). Such wind speeds are different than Nacelle speed. See Acknowledgements.

⁵¹ Location of met mast (\blacksquare) is an approximation, and the mast ran until January 2000 before being destroyed by a ship [79].

Values of turbulence intensity from the Forecast and April data sets are obtained in two different ways; they are named as TI_{pow} , and I_{0na} for each data set. A third alternative I_{0pw} , based on the method by Jorgensen is obtained from R. J. Barthelmie et al. [80]. The method relates σ_p , and V_{avg} with the power curve of WTs as expressed in Equation 41, yielding a constant ratio B of 0.797 for the MIDD site 52 . TI_{now} is based on the mathematical expression derived during this study (Equation 40). It is only valid from cut-in to cut-out wind speeds. The equation uses turbulence intensity as a function of P_{avg} , σ_p , and V_{avg} through constants a, b, and m; See Appendix-C for the complete derivation. Both TI_{pow} , , and I_{0pw} are used for the free stream. On the other hand, I_{0na} is based on nacelle wind speed measurements only (σ_{na}/V_{na}) . Therefore, it is used to quantify wake effects inside the farm (section 5.5).

$$\frac{\sigma_p}{P_{ava}} \cong m \, T I_{pow}^2 + T I_{pow} \left(\frac{a}{V_{ava}} + C - 0.04m \right)$$

Equation 40: Turbulence intensity TI_{pow} from measurements of P_{avg} , and σ_p with a=1.04, c=2.082, m=2.67 for $TI_{pow} \ge 0.04$.

$$B = \frac{\sigma_p}{\left(\frac{dP}{dV}\right) V_{avg} I_{0pw}}$$

Equation 41: Derived turbulence intensity I_{0pw} . Method of Jorgensen, based on Thomsen and Markilde Petersen; see [79].

Wind speeds used to describe the free stream from the simulation are obtained from the 300 m domain, and at the grid location resembling the meteorological mast latitude and longitude coordinates (height of 50 m with interpolation). Finally, the simulation variables to be used are wind speed, wind direction, turbulence intensity (derived from TKE in Equation 7), atmospheric stability, power generation and efficiency.

5.3. Analysis of the Free Stream Wind Speed

Weibull and histograms are used to represent the probability distributions of wind speeds in the free stream, prior and during wind farm operation. (Figure 73). Prior to the operation of MIDD, the Metmast data set indicates a free stream with an average power density (PD) of 430 – 480 w/m2 from 30 m up to 50 m height above sea level; see Figure 73-a. The annual distribution favored 6 – 7 m/s wind speed at 30 m, and 68% of the time the winds were less than 9m/s. As height increases (50 m), the low aerodynamic roughness of the site (z_0 = 0.03 m [30])makes winds of 8 –9 m/s most often. On the other hand, the **April** data set indicates a decrease in the energy carried by the frees stream due to the farm operation. The averaged PD is lowered to 281 w/m2 at 50 m, and an average wind speed of 6 m/s. Consequently, the weibull distribution of the April data set is displaced to the left. This effect is expected because the wind farm exerts a drag force on the wind field, and as such, the wind reduces its speed when reaching the farm. In addition, the farm consumes energy from the free stream (lowering PD).

⁵² The value of B is not calculated but rather taken from R. J. Barthelmie et al. [79].

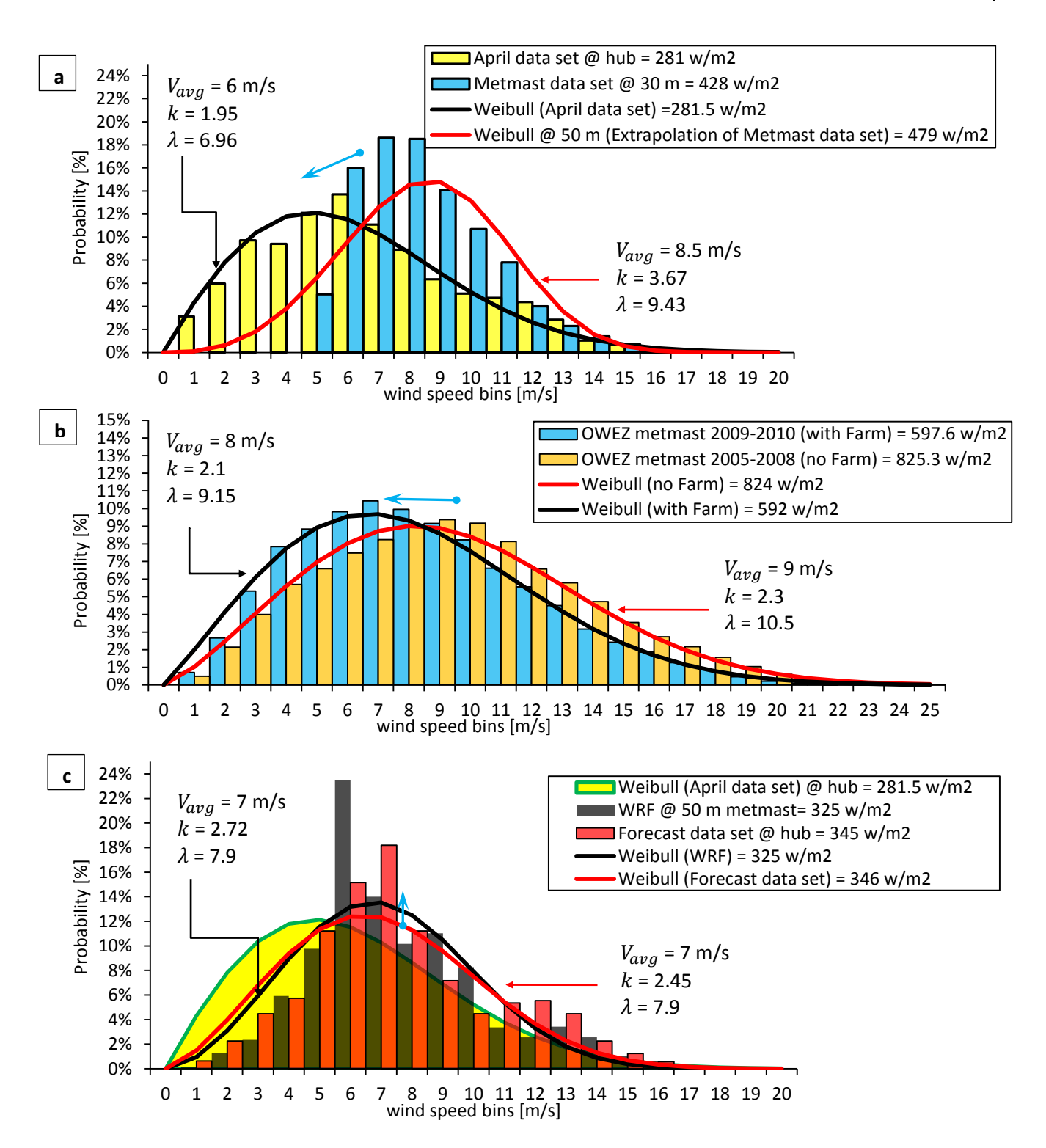


Figure 73: Histograms and weibull distribution fits of free streams. Free stream in MIDD prior and post wind farm installation (a). Free stream in OWEZ [30] 53 prior and post wind farm installation (b). Forecast comparison of free stream in MIDD (c). Color arrows (←, I₂) on all plots relate weibull distributions to their respective parameters, and (∠) indicates weibull displacements.

 $^{^{\}rm 53}$ Data from OWEZ meteorological mast is available online at: http://www.noordzeewind.nl/en/knowledge/reportsdata/ per month per year.

Such case is verified with met mast measurements from the met mast of the Dutch offshore wind farm of OWEZ in Figure 73-b; the wind farm became operational in 2007-2008. It is evident from the wind distributions at 70 m height that the free stream carried more energy before the installation/operation of OWEZ (825 vs. 597 w/m²). Think of the farm effect on the frees stream in the following manner: some of the probability of high winds is moved to the lower winds, shifting the weibull to the left and yielding a lower average wind speed. For the OWEZ case the weibull also shifts upwards because the reduction in PD is not as much or as for the MIDD case.

One could argue that a data set more extended that the April data set would provide a more similar pattern to the OWEZ change in weibull distributions. But, the annual average wind speed is 6 m/s, with $^+$ 0.23 m/s deviations each month. Consequently, the shape factors k and the bell-shape pivot points of the distributions per month are similar. This situations preserves the weibull shift characteristic of the figure presented. Nonetheless, there are few aspects to be mentioned about the weibull shifts:

- 🖶 Distribution for the OWEZ case are derived from a met mast; Hence, they are more confident.
- Distributions for the MIDD on the April data set may include wind speed reduction effects from WT rotors, slightly lowering the weibull downwards.

Looking at Figure 73-c, the average inflow wind speed from the WRF simulation time is 7 m/s, the same as calculated from the Forecast data set. On both cases the probability of low wind speed is similar: scale factors λ of 7.9, a similar k. The main difference is a more frequent 6 m/s wind in the simulation (23.5% of the time vs. 16%), resulting in a lower average PD (325 vs. 345 W/m²). It is suggested that the lowering the of the weibull on the forecast data set is due to using turbine data.

It is important to state that the Forecast data set and the WRF simulation capture the transition from westerly to south-easterly flow; see Figure 74. Nevertheless, winds are prominent from the southeast in WRF, whilst data sample shows a more symmetric distribution between the southwest and the southeast; the magnitude of wind speed per direction are similar; and both sets provide no winds around 50° approx. Furthermore, measurements from **Metmast data set**, and from weather station at København-Kastrup confirm both wind roses from, supporting high probability of south-easterly winds.

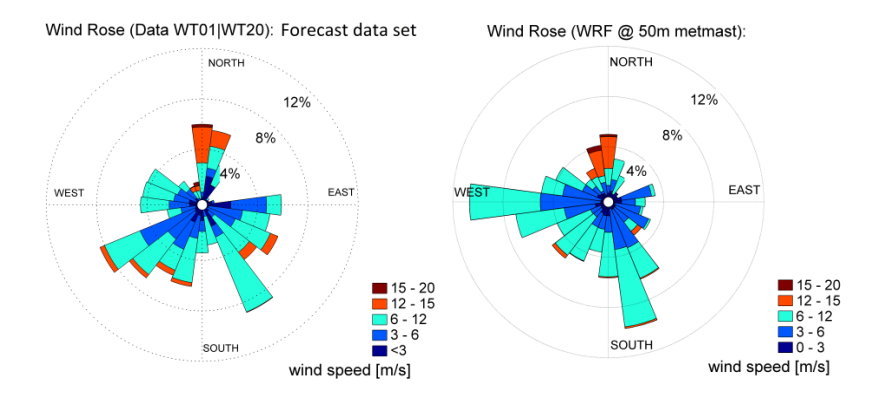


Figure 74: Differences in wind direction and wind speed per direction: WRF vs. Forecast data set.

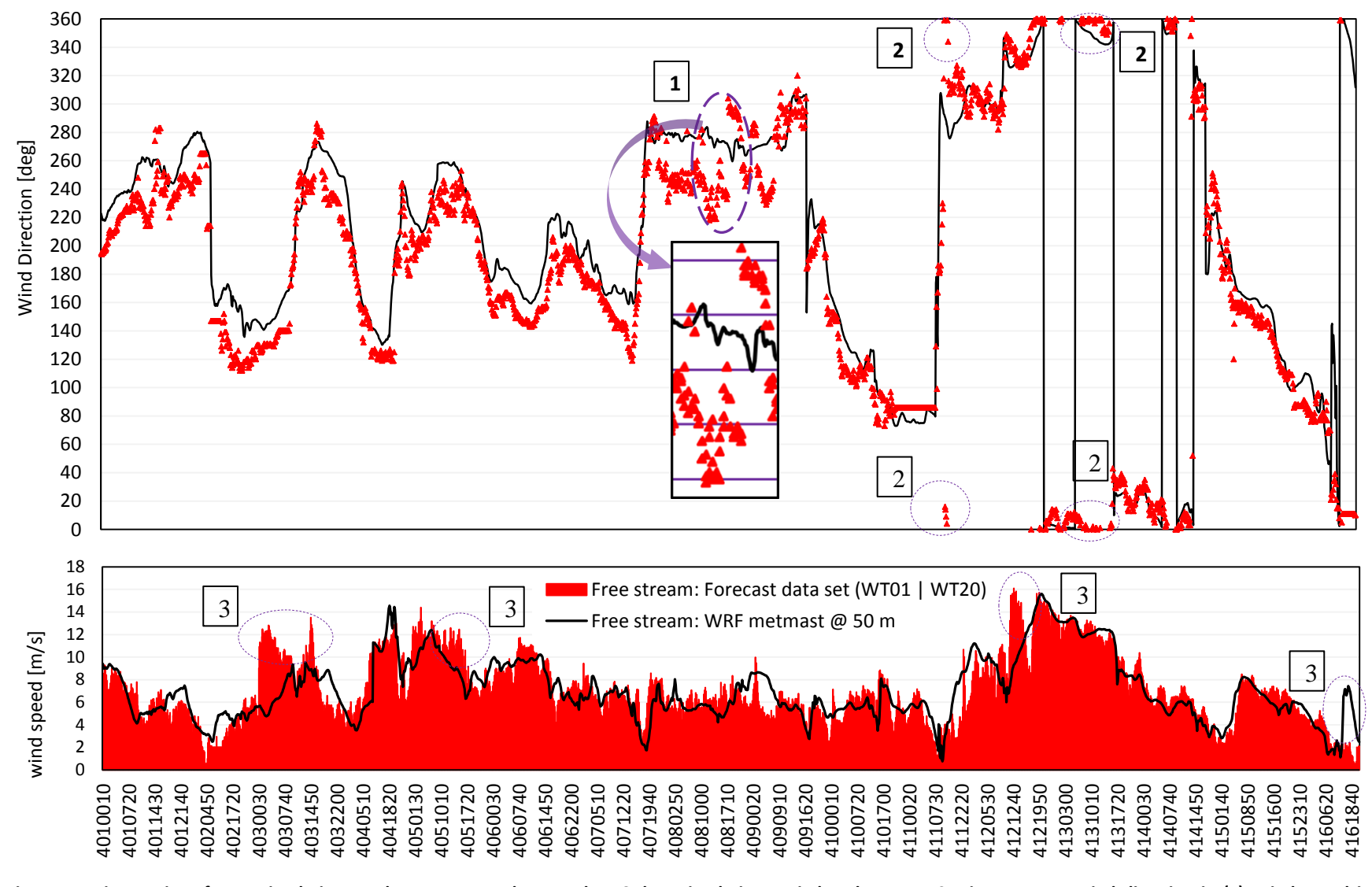


Figure 75: Time series of WRF simulation result vs. Forecast data on the 16 days simulation period. Values are 10 min averages. Wind direction in (a), wind speed in (c). Dashed circles indicate important differences: Wind direction from the WEST in (1), undefined direction (NE or NW) in (2), and large errors in wind speed in (3). Time stamps with missing values on any WT are ignored, and the remaining series put together.

A.M. Striedinger P. Master of Science Thesis

Bias [%] SD [%] Bias SD Wind Speed 26% 51% 1,33 m/s 1,27 m/s 25,15° **Wind Direction** 13% 1% 2,08°

Table 16: Summary of Reanalysis Errors in the Free Stream simulation.

Time series of wind speed and wind direction in Figure 75 show how accurate if the free stream forecast from simulation; both series (Forecast data and WRF) follow the same trend. There is however a large relative error in the simulation (Bias[%]) about 26% with a large deviation (SD[%]). The error is only 1.3 m/s but it spikes in few periods due to the SD, is more prominent on high wind speeds⁵⁴ of the data set series (see spikes in the plot). In the remaining of the series, errors are 0 – 2.6 m/s; see summary in Table 16. For meteorological purposes the error may be considered as low but not necessarily for a wind farm analysis as $P \propto V^3$.

On the other hand, the resultant wind direction deviates with a bias of 25°, the trend is more similar as the SD is negligible but such bias is important for the farm power output analysis. Because the power performance of the farm depends on the wind direction, as they shape the wake patterns of the bowshaped farm of MIDD.

Analysis of the Free Stream Turbulence Intensity 5.4.

Turbulence remained relatively low before the farm installation, that is I_{0met} was between 0.05 and 0.14 during 87% of the time, with highest occurrence around 0.07 (17% of the time) [81]. Furthermore, it remained practically constant with wind speed, once averaged. The simulation produced slightly different values: $TI_{metmast}$ from remained 84% of the time between 0.05 and 0.14, and never exceeded 0.2. On the other hand, the results from the Forecast data set correspond to a probability of 49% for TI_{nw} between 0.05 and 0.14, and 13% for TI_{nw} lower than 0.05. Further, TI_{nw} is greater than 0.2 during 28% of the time⁵⁵: this is due to capture of added turbulence intensity from the North and South WTs. Once the values greater than 0.2 are discarded from the statistics, TI_{nw} remains 22% of the time below 0.05, and 79% between 0.05 and 0.14. Consequently, it the distributions of TI_{pw} and $TI_{metmast}$ are similar. For complete histograms of turbulence intensity see Appendix-C: C-1

Nonetheless, due to the lack of data points on certain wind speeds from the simulation (1 m/s bins), TI results are more representative in the 4 -10 m/s interval; see Figure 76. The interval is therefore used to compare all data sets. The average sample per speed bin is 6.3% of the complete simulation, and only bins with 6.3 $^+$ 0.5 (or $^+$ 10%) of sample points were considered appropriate for an average TI to represent them in a TI vs wind plot. Unfortunately the simulation did not last longer so to avoid the use of the comparison interval. On such a hypothetical case the simulation could have been directly contrasted with the **April data set** in Figure 77.

⁵⁴ The time series is mostly low wind speeds, and the high wind speed refer to the highest values among these low wind speeds. i.e. a relative high value.

⁵⁵ The notation for turbulence intensity is defined in section 5.2.

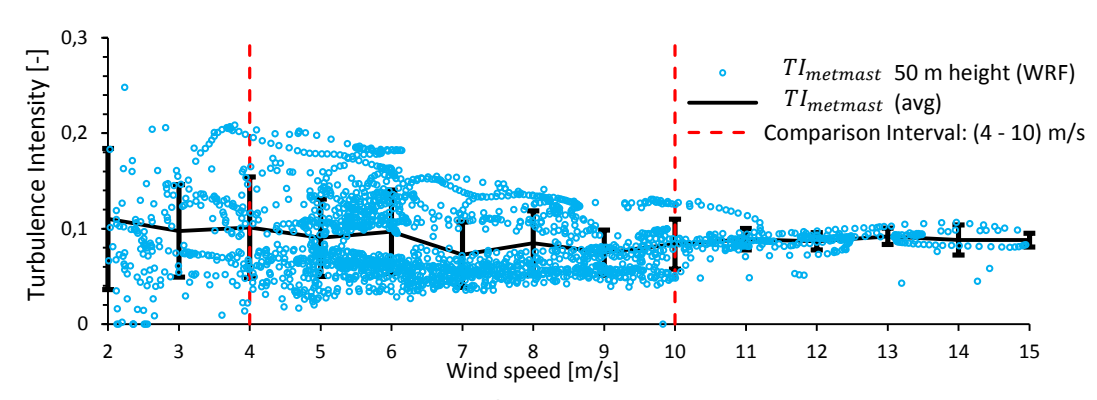


Figure 76: TI vs Wind speed from WRF simulation

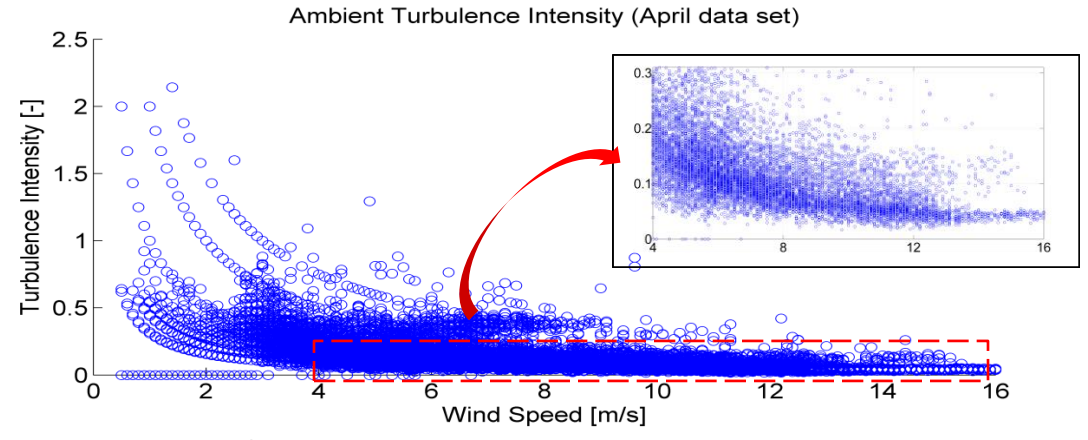


Figure 77: TI vs Wind speed from April data set, with zoom in 4 - 16. Deduced from turbine data.

Figure 78 plots turbulence intensity TI results from all data sources, where I_{0met} and $TI_{metmast}$ were expected to show the lowest values. I_{0na} is larger on all wind speed bins as expected from the previous section, and TI_{pw} values are remarkably similar to those from I_{0pw} , except that the there is no peak at rated wind speed which suggests TI_{pw} to be more useful. Therefore, the results partially validate its formulation.

Ideally the simulated $TI_{metmast}$ should be similar to TI_{pw} , and I_{0pw} , but they differ much inside the comparison interval. One could argue that TI_{pw} , and I_{0pw} are the highest because they represent turbulence on the rotor area and not at hub height. None the less, the differences in turbulence intensity from the lower blade tip to the upper blade tip is less than 1% according to [79]. One major contributor to the high values of TI_{pw} , and I_{0pw} is rather the use of one significant digit to register σ_u : low values appear lower, and high values appear higher. This is in addition to the inherent capture of added TI of the methods used. The overestimation seems more evident at low wind speeds because TI is inherently higher for them. At higher wind speeds, the difference is not that noticeable.

Master of Science Thesis A.M. Striedinger P.

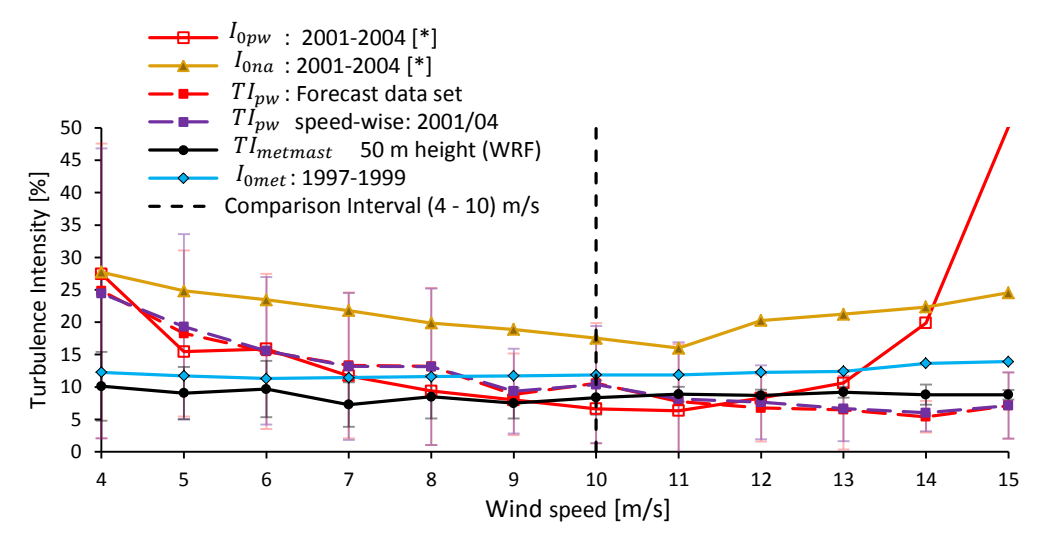


Figure 78: $TI \ vs$ Wind speed plots of the frees stream from all data sets ($TI_{pw}, I_{0na}, I_{0pw}, I_{0met}$) and simulation results T.I met mast. Variables described in section 5.2. TI_{pw} speed-wise is based on same method as TI_{pw} but not on direction.

Turbulence is compared per direction bins in the wind roses of Figure 79: It is evident that there is not much occurrence of north-easterly winds. The Forecast data set shows a less uniform distribution of TI, whereas the simulation indicates a much calmer and uniform flow. Such calmed flow represents a very stable atmosphere in the simulation: Monin-Obukhov⁵⁶ length L_* remains between 0 and 200 m. This very stable atmosphere is the responsible for suppressing most of the turbulence in the simulated flow, producing a less variant wind rose.

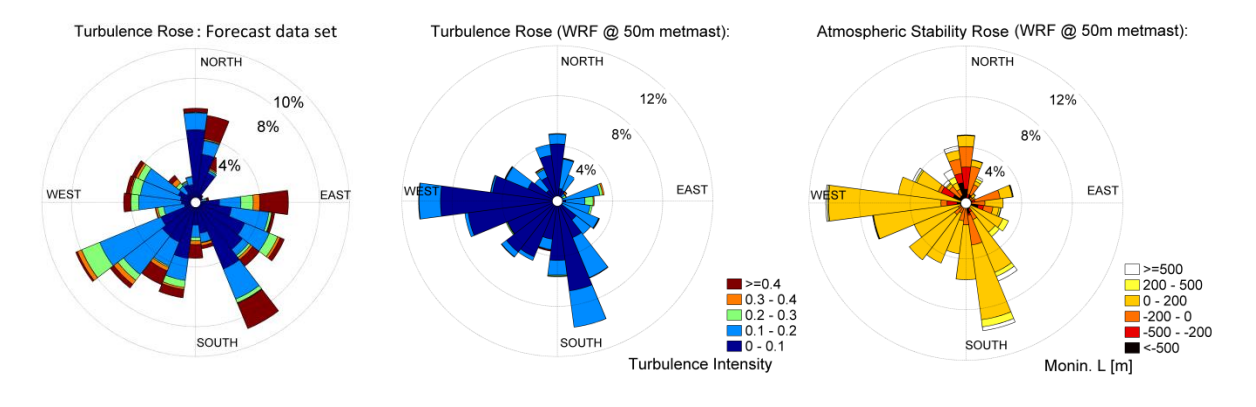


Figure 79: Turbulence rose comparison for free stream TI from data set and WRF simulation. Highly turbulent rose distribution from the forecast data set, and a more uniform and weaker distribution from the simulation. Atmospheric stability during the simulation is plotted through the Monin. L in meters.

To average TI per direction bin is necessary to have sufficient sample data per bin. There was no much samples for some bins during the simulation⁵⁷. Therefore, bins had to be made irregular in Figure 80 for all data sets. There are peaks of turbulence from the North-East direction caused by wind speed lower than the 3 m/s cut-in from that quadrant. As stated in Chapter-2, TI increases with decreasing

 $^{^{56}}L_{\star}$ is a measure of atmospheric stability as stated in section 2.1.1.

⁵⁷ The reader can verify this fact in Appendix-C: C-1

wind speed. Further, there is an underestimation on $TI_{metmast}$ in contrast to I_{0met} from south-westerly and north-easterly winds (180° to 360°). An explanation is that inflow TI is locally reduced affected by the farm presence as it was proven in Chapter-4 (Figure 50). How much less should this reduction be?, this is uncertain due to factors like model input data and resolution affecting topographical features, etc.

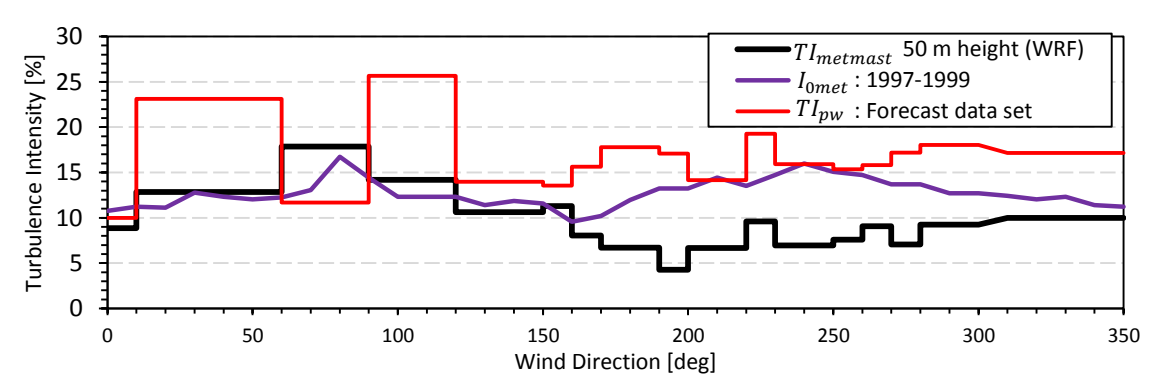


Figure 80: Turbulence intensity as a function of wind direction, averaged quantities per same quantity of sample data on each direction bin. No range of turbulence intensity is shown per direction; see Figure 79 for such.

It is suggested that for longer periods of simulations, WRF results would show better similarities to the Forecast and Metmast data sets. But may still produce a less turbulent free stream. The evidence for such a statement are the similarities in wind speed distributions and wind directions plots from section 5.3, and the similar TI vs Wind trend between $TI_{metmast}$ and I_{0met} . The strength of this suggestion is debatable but at this moment it cannot be proved nor disproved tacitly.

5.5. Analysis of Power Forecast and Performance

Most frequent winds are around 6-7 m/s, as such, power production from MIDD is relatively low for the period chosen. In addition, not all WTs were active during the simulation period, at most 4 WTs were inactive at the same time: turbine inactivity is indicated in the Forecast data set⁵⁸. It is important to recall that the 10 min series here presented covers an average of 1 to 2 WTs per location. Such that on certain cases, WT power is multiplied by two to obtain the total power production. When doing this, accuracy is lost because the wake effects between such WTs are never taken into consideration by the solver.

Despite differences in turbine layout, the power series from the WRF simulation and the forecast data set behave similarly. There are however, differences like the an prediction of -35 MW between days 2 and 3 of the simulation. Bear in mind, that the farm has a 40 MW rated power. It is not entirely sure why there are such discrepancies, only that they are primarily caused by the error in the free stream wind speed of the simulation. Remaining errors in the power forecast are lower that example provided, but never with an acceptable accuracy for a profitable forecast. It is shown in this section that the error is rooted in the inaccuracy of the wind speed simulations of the free stream; they explain most of the

⁵⁸ Inactivity can also be considered as WTs not in operation due to any external reason.

variation of the power error (its standard deviation σ_{pw}), and nearly half of average error :bias and offset. Where offset is defined as the net differences in power production $\|Power_{(WRF)} - Power_{(WRF)}\|$ $Power_{(data)}$. The average offset is about 250%. That is, a net differences 2.5 times the value predicted with WRF; approximately 4.5 MW. Large values of offset are mostly due to cases of wind speed near cutin. such that power is very low (Forecast data set). Whereas the nearly constant error in wind direction forecast influences the remaining of the average error of the power forecast, by miss representing the wake case inside the farm. The direct consequence is a decrease in the efficiency of power production.

Figure 81 offers a plot summary relating power to wind direction, free stream wind speed, and yaw miss match γ (the angle between the wind and the nacelle orientation)⁵⁹. On average $Power_{data}$ is a slightly larger than $Power_{(WRF)}$; see Figure 81-a. This fact, is reflected by a negative bias error of -1.9 MW, and a standard deviation σ_{nw} of 6.9 MW. The series error is plotted in Figure 81–b, where the 4.5 MW offset is more evident. Notice also that the columns in Figure 81–c indicate when $Power_{(data)}$ or Power_(WRF) is larger than 2 MW, and the number of inactive turbines is shown in (d). The plots of free stream wind speed and direction are repeated in (e) and (f).

Yaw mismatch γ is presented in the **Forecast data set**, therefore there are slight decrements of the C_p of each WT. The best case is when γ = 0, which is fulfilled with flows perpendicular (\perp) to the rotor blades. The fraction of the wind not \perp is expressed through $1 - Cos(\gamma)$ in plot (g), it has been averaged over the farm on each time stamp. For instance, 1 - Cos (γ) of 0.45 indicates that 45% of the wind is not L, a value of 1 indicates that the wind does not flow through the rotor at all, and values > 1 indicate the wind flows from behind WTs (no power generation). The effect of $Cos(\gamma)$ on C_p is measured through Glauert's momentum theory in Equation 17. For example, an axial induction factor a of 0.15 yields a C_p of 0.435 for γ =0. For γ = 30° C_p is reduced to 0.375, and for γ = 45° (50 % of the flow \perp), C_p is reduced to 0.3. This is are minimum reductions in WT power generation of -15%, and -31%. This is even hypnotizing that a does not decrease.

Fortunately, γ remains low so that in average 8.8% of the flow is not \perp . There are only few times when the wind direction causes almost no power generation, and these are marked with dashed squares in Figure 81-a, and (g). The average γ of the farm is displayed in (h) and its range over the farm is marked in blue areas (see black line). The bias error in free stream wind direction sets a nearly constant offset between the real γ , and the one it would be if considering the wind direction from the simulations (red line).

The γ offset (Figure 81.i) is not taken into account for the power generation because the real WT yaw was not tracked during the simulation. This situation makes one wonder that even if the turbine parameterization is to correct for γ , the error could be higher instead of decreasing as ideally expected. A yaw- tracking algorithm within the parameterization would have got to be implemented, and not just an update on the measured γ .

A.M. Striedinger P.

⁵⁹ Yaw, and γ have been defined in Section 2.2.1 in Equation 15.

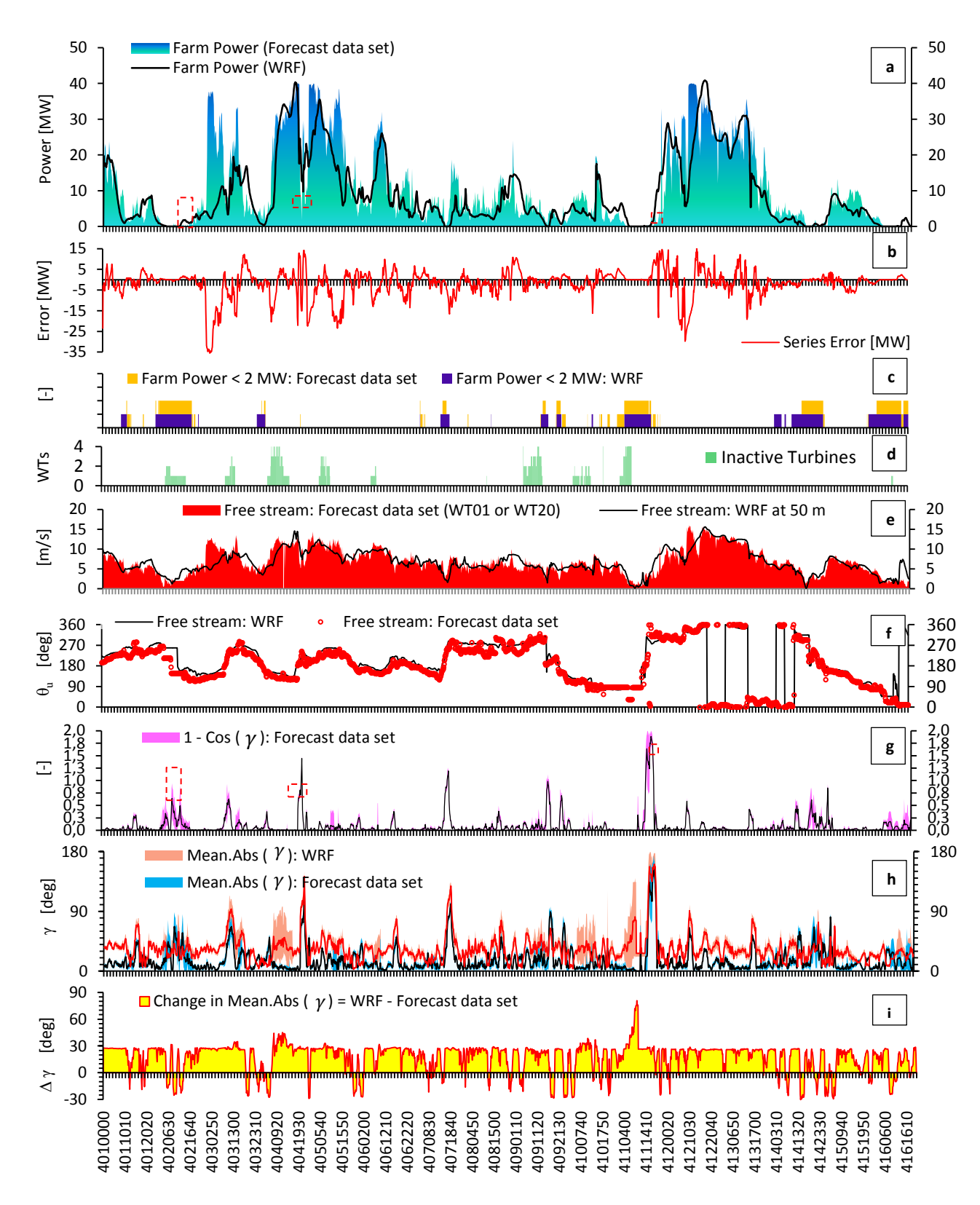


Figure 81: Time series analysis and differences between the simulation (WRF) and the Forecast data set. Wind farm power item series (a). Error in wind farm power forecast (WRF – Forecast data set) values (b). Indicators for farm power larger than 2 MW (c), and for inactive WTs (d). Free stream wind speed (e), and direction (f). Averaged 1-Cos(γ) from the Forecast data set (g). Mean absolute value of γ of the farm (h), added γ due to wind direction error in simulations (i).

One option would be to use a constant rotational speed (yawing speed) for the nacelle orientation by using manufacturer's data. For example, the maximum yawing speed of the 3 MW V-90 at 60 Hz from $Vestas^{60}\text{, is }0.5^{\circ}\text{/s. The optional turbine parameterization in Appendix-D treats the yaw in this manner.}$

Finally, the error in wind farm power generation is quantified in two types: Series Errors, and Phase Errors: $\left(\frac{Power_{(wrf)}-Power_{(data)}}{Power_{(wrf)}}\right)$. Both types are calculated for the complete simulation, and for the situations with $Power_{(WRF)} > 100$ kW, and > 2MW. This is done to avoid the largest phase errors due to low power production; see Error! Not a valid bookmark self-reference. for errors in [MW] and in [%].Notice, that the phase error σ_{pw} is reduced from an astonishing 4362% to 140 – 200 %. Such fact, ensures that the largest errors are due to WT operations at near cut-in wind speeds. The negative phase error bias, and the large offset (-45 %, and 74% for > 2MW) confirms that the model + turbine scheme behaves poorly for an accurate power forecast. But it doesn't say why at the moment.

••	, bu.,		• ••			
Error Types	For Farm Po	wer (WRF)				
Series Errors [MW]:	Complete Simulation	> 100 KW	> 2MW			
Bias	-1,9	-1,9	-2,1			
σ_{pw}	6,9	6,9	6,9			
Offset	4,5	4,6	5,2			
Min	-35,6					
Max	16,					
Phase Errors [%]:	Complete Simulation	> 100 KW	> 2MW			
Bias	-222%	-61%	-45%			
σ_{pw}	4362%	200%	140%			
Offset	250%	95%	74%			
Min	-195340%	-3455%	-1605%			
Max	100)%				

Table 17: Error types and values: Bias, Standard deviation (σ_{pw}), Offset, Minimums (Min), Maximums (Max).

The relation of phase errors in free stream can be related to the phase errors in farm power by using the momentum theory (section 2.2), such as changes in C_p due to a change in velocity. Consequently, Equation 42 relates error in C_p to error in wind speed per turbine.

$$Phase \; Error_{(wt)} \; = \; \frac{\frac{1}{2}\rho A_{rot} \left[C_{p(wt)}V^3\right]_{wrf} - \frac{1}{2}\rho A_{rot} \left[C_{p(wt)}V^3\right]_{data}}{\frac{1}{2}\rho A_{rot} \left[C_{p(wt)}V^3\right]_{wrf}} = 1 - \left(\frac{C_{p(wt)_{data}}}{C_{p(wt)_{wrf}}}\right) \left(\frac{V_{data}}{V_{wrf}}\right)^3$$

Equation 42: Equation of the Phase Error in Farm Power.

 $^{^{60}}$ The technical data sheet used for This yawing speed is the "General Specification" company document from 2004. Find it online at: http://www.gov.pe.ca/photos/sites/envengfor/file/950010R1 V90-GeneralSpecification.pdf

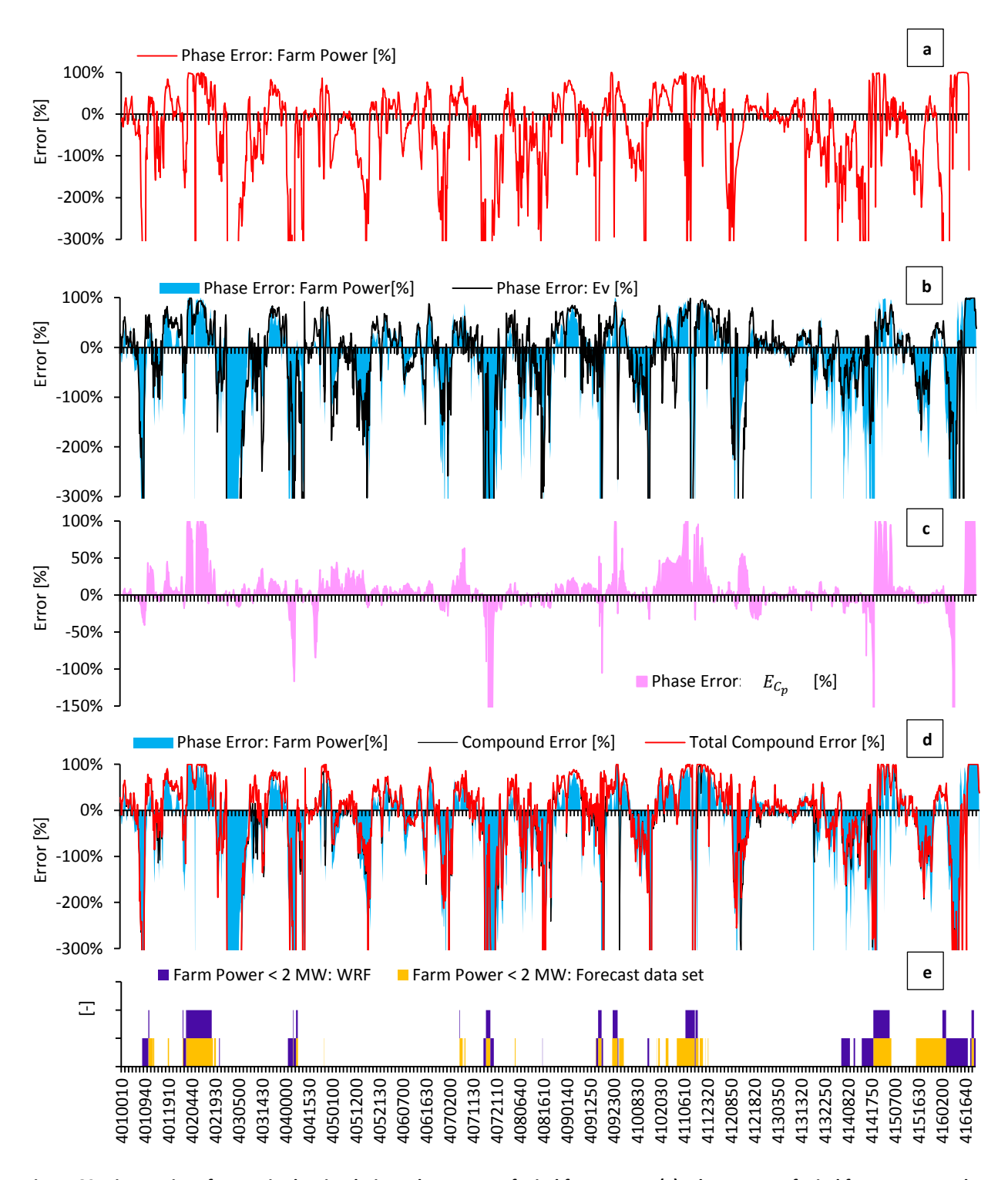


Figure 82: Time series of errors in the simulation. Phase Error of wind farm power (a). Phase Error of wind farm power and Ev from V_{fs} , with nearly a perfect match (b). Resultant averaged error Ecp of the wind farm due to changes in V_{fs} (c). Comparison of compound errors and total compound error (d). Indicators for farm power larger than 2 MW (e).

One can further extend Equation 42 to relate the errors in the free stream wind speed V_{∞} , to the power coefficient of each turbine $C_{p(wt,V_{\infty})}$ on each time stamp, caused by the differences in V_{∞} between the simulation and the forecast data set. This is done by referring to the manufactures power data of V_{∞} vs. C_p . This phase error relation is named the Compound Error in Equation 43, and $Total\ Compound\ Error$ when γ is considered with $C_{p(wt,V_{\infty},\gamma)}$ with Equation 17. Where E_V , and E_{C_n} are the respective wind speed and power coefficient phase errors.

$$Compound\ Error = 1 - \left(\frac{C_{p(wt,V_{\infty})_{data}}}{C_{p(wt,V_{\infty})_{wrf}}}\right) \left(\frac{V_{\infty(data)}}{V_{\infty(wrf)}}\right)^{3} = E_{V} + E_{C_{p}} - \left(E_{C_{p}}E_{V}\right)$$

Equation 43: Compound Error formulation.

Because there are several WTs in the wind farm and the main Phase Error is set for the farm power, E_{C_n} is treated individually as $E_{C_n(wt_i)}$. Further, the farm average is taken on each time stamp, the reason for this is that the phase errors are ratios and not direct quantities (Equation 44).

$$E_{C_p} = \frac{\sum_{i}^{n} E_{C_p(wt_i)}}{n}$$

Equation 44: Phase Error of power coefficient.

The final relation of phase errors is plotted in Figure 82, with the *Phase Error* in (a). Once E_V is compared to Phase Error in (b), it is clear that both are extremely similar, so that the error in V_{∞} explains the majority of the errors in of the power forecast: The corresponding $E_{\mathcal{C}_p}$ as a function V_{∞} is plotted in (c). After comparing both compound errors in (d), correlation factors $f_{(x,y)}$ are calculated between them and the Phase Error; see Equation 45 and Table 18. The factor is a statistical measure of the similarity between time series (x, and y), and ranges from -1 to 1.

$$f_{(x,y)} = \frac{\sum \left((x - x_{avg})(y - y_{avg}) \right)}{\sqrt{\sum (x - x_{avg})^2 \sum (y - y_{avg})^2}}$$

Table 18: Correlation factor between phase errors in power forecast and compound errors.

$f_{(x,y)}$ for:	y =Compound Error	y=Total Compound Error		
x = Farm Power (WRF) > 100 KW	0,858	0,869		
x = Farm Power (WRF) > 2 MW	0,983	0,942		

There is no relation for $f_{(x,y)}=0$, a strong linear relation for $f_{(x,y)}=1$, and a strong inverse relation $\left(x \propto \frac{1}{v}\right)$ for $f_{(x,y)} = -1$. For $Power_{(wrf)} > 100$ kW, $f_{(x,y)}$ around 0.8, and larger than 0.9 for $Power_{(wrf)} > 2$ MW. On the later, the $f_{(x,y)}$ of the $Total\ Compound\ Error$ is the lowest, and may be due to the following:

- Uncertainty in Glauert's power coefficient (Equation 17)
- lacktriangle Uncertainty in averaging $E_{C_p(wt_i)}$ to E_{C_p}
- lacktriangle Uncertainty in $E_{\mathcal{C}_n(wt_i)}$ itself due to the incorrect representation of V per WT location on the computational domain

But on what characteristics are the compound errors and the *Phase Error* alike? This is better represented in Table 19. The bias of the compound errors is almost half of the *Phase Error*, the offsets are relatively more similar, but the error oscillation σ_{pw} are almost a perfect match. Hence, the errors in the frees stream wind speed forecast are responsible for the oscillations and error trend of the power forecast.

Table 19: Compariosns of Phase Error, Compound Error, and Total Compound Error. Yellow lables indicate good relations, blue label indicate bad realtions.

Error Type	Phase E	Error	Compoun	d Error	Total Compound Error		
[%]	> 100 KW	> 2MW	> 100 KW	> 2MW	>100 KW	>2 MW	
Bias	-61%	-45%	-36%	<mark>-26%</mark>	-26%	-21%	
SD	200%	<mark>140%</mark>	219%	<mark>150%</mark>	172%	<mark>149%</mark>	
Offset	95%	<mark>74%</mark>	86%	<mark>70%</mark>	77%	<mark>56%</mark>	
Min	-3455%	<mark>-1605%</mark>	-4278%	- <mark>1675%</mark>	-1670%	<mark>-1670%</mark>	
Max	100%	100%	100%	100%	100%	100%	

Additionally, the separate cause affecting the bias and offset error in the power forecast is the bias error in the wind direction forecast form WRF. As stated at the beginning of this section, now let's explain why. Take for example, the predominant southerly direction in the simulations shown in Figure 74, in contrast to the southeasterly direction in the Forecast data set. The efficiency is much lower in the first case, than in the later; hence, for case with similar free stream and $\gamma = 0$ the power production is definitely much lower in the simulations. The farm efficiency is the lowest for northerly and southerly winds, because that is the turbine row is oriented like that. Hence, producing a strong wake interference. The previous statements indicates the frees stream is not being forecasted accurately enough to produce an accurate farm power forecast.

5.5.1. **Efficiency of the Turbine Scheme**

Wind farm performances is quantified by its efficiency in power generation (x) as a function of wind direction only. In this case, the influence of the wind farm layout on farm power is targeted. In addition, the dynamic errors of the power series (previous section) are no longer influential because time is not taken into account. The ability of the turbine parameterization scheme to represent the turbine characteristics is isolated from the ability (or lack of) of the atmospheric flow model + input data to accurately forecast the free stream.

Wind farm efficiency is defined as $\aleph=rac{Farm\,Power}{20*FP_0}$, where FP_0 stands for the base power; there are two ways to select the base power, and hence obtain different x:

Master of Science Thesis A.M. Striedinger P.

- + FP_0 as power from the south or north WT depending on wind direction (same methodology of section 5.2); this case produces \aleph_{sn}
- ullet FP_0 as the maximum turbine power within the farm on each wind direction. This case produces \aleph_{max}

The case with $\kappa_{\rm sn}$ is implemented by R. J. Barthelmie et al. [80] as well, and is plotted as a an annual average Annual Mean [*]. For the case of \aleph_{max} , one would expect that the maximum power would also be from the north or south WTs, but due this is not always the case due to farm layout. Sometimes maximum power is found near the middle of the row. For the $\kappa_{\rm sn}$ case, the efficiency is averaged $^+$ 5° on each $10^{\rm o}$ direction bin, and the complete time series is used. Winds from the north or south are split in two different bins, $[0^{\circ} - 5^{\circ}]$ for the 0° bin, and $[355^{\circ} - 360^{\circ}]$ for the 360° , to differentiate the effects due to the bow shape of the farm. Due to the low occurrence of the 40° to 60° direction bins, the amount of data points available did not suffice for an accurate average on that range. The scatter data illustrating this statement is given in Appendix-C: C-3

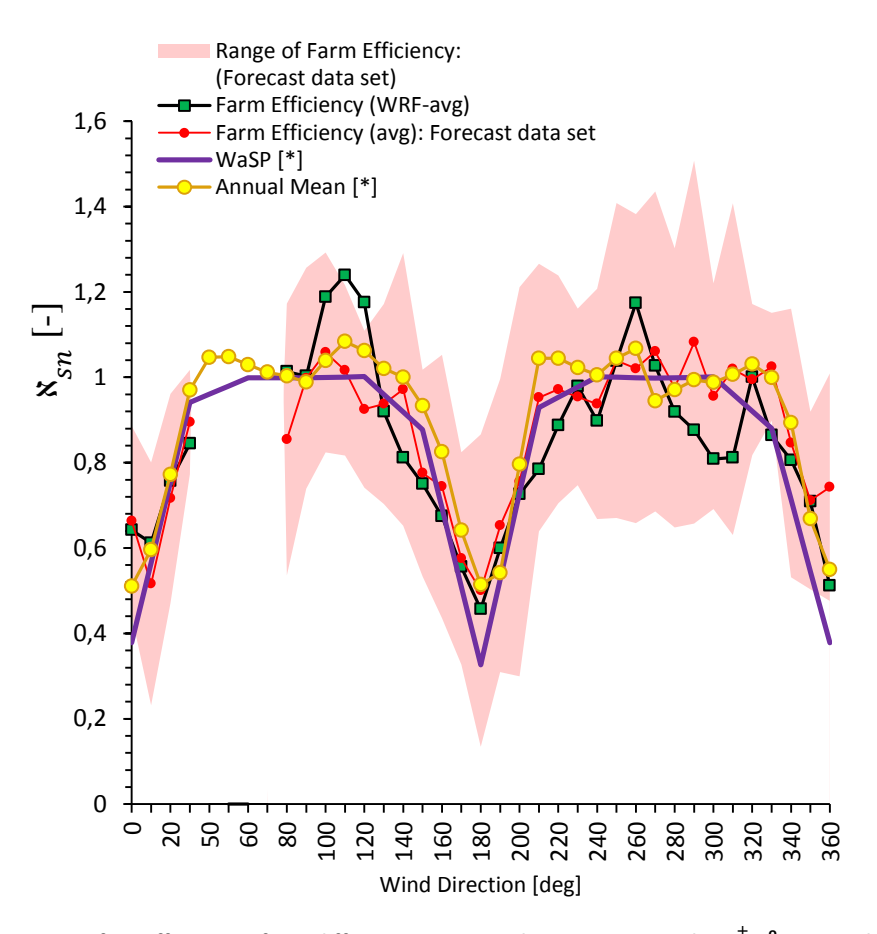


Figure 83: Comparison of \aleph_{sn} efficiencies from different sources. Values are averaged on $\frac{+}{5}$ ocentered direction bins each 10°. Red are represented the standard deviation of \aleph_{sn} from the Forecast data set. Missing values from the 40° to 60° due to the lower number of data points for a representative average (simulations and forecast data set).

Averages of \aleph_{sn} are shown in Figure 83, for which simulations remained within the standard deviation of the data (Range of Farm Efficiency). Efficiencies are also compared to WaSP predictions

(extracted from [78]). As expected, $\kappa_{\rm sn}$ is lowest for southerly and northerly winds, and all plots match best around 180° direction (southerly), with maximum avlues for westerly and easterly winds. The trend shows slithly lower efficiecies from the simulation. Notheless, it is quite remarkable for a model that does not include the commplete farm layout.

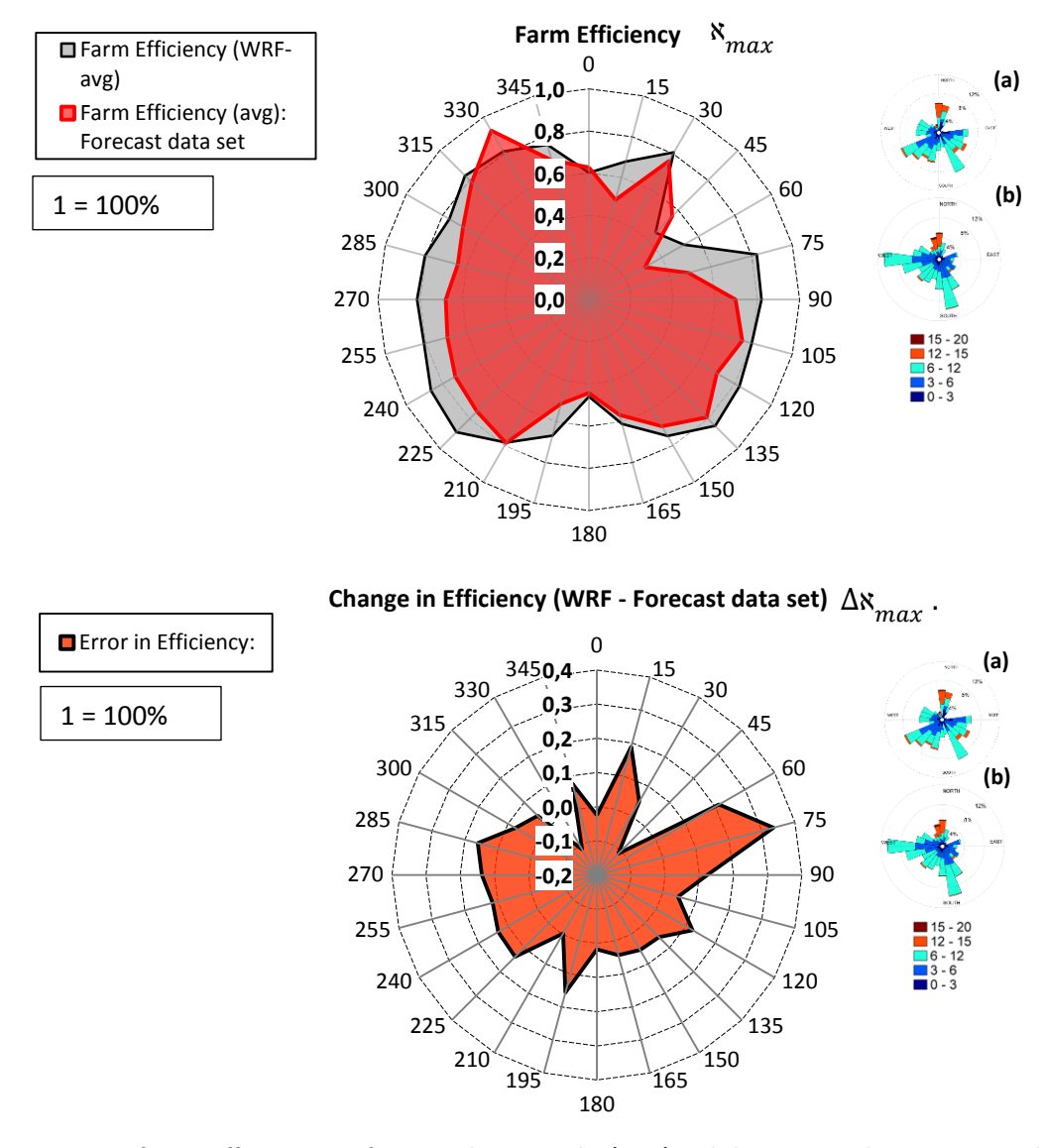


Figure 84: Rose of Farm Efficiency \aleph_{max} from simulation results (WRF) and the Forecast data set per wind direction $\frac{+}{-}$ 15° centered bins (above). Difference in N_{max} from simulation results and the data set (below); directions are shown radially. Wind rose from forecast data set in (a), and wind rose from simulation in (b).

For the second case of \aleph_{max} in Figure 84 the situation is slightly different, but it is evident that the turbine scheme assumes a more efficient power generation than the real case. It is only in a few sectors that \aleph_{max} from the data set and the simulation is relatively the same, i.e. south, north, 30° and 210°. The κ_{max} plot is shown in Figure 84-a and the difference in κ_{max} from the simulations and the data set is displayed in (b).

5.5.2. Wind speed deficit in the wake

Wind speed deficits at hub height measure the strength of the wake inside the farm. Speed ratios are calculated with respect to the north or south WTs, along the row for 8 – 9 m/s wind speeds; see Figure 85. The wake is stronger on this direction as proven by the efficiency plots in Figure 83 and Figure 84. Simulation results indicate a spatial convergence of wind speed downstream, and very similar to that obtained from the forecast data set. Having a bow shape as wind farm layout seems to avoid a the single wake interference from all WTs, batching the wake-affected WTs in few units. Such a situation produces large deviations on the wind speed ratios of Figure 85⁶¹.

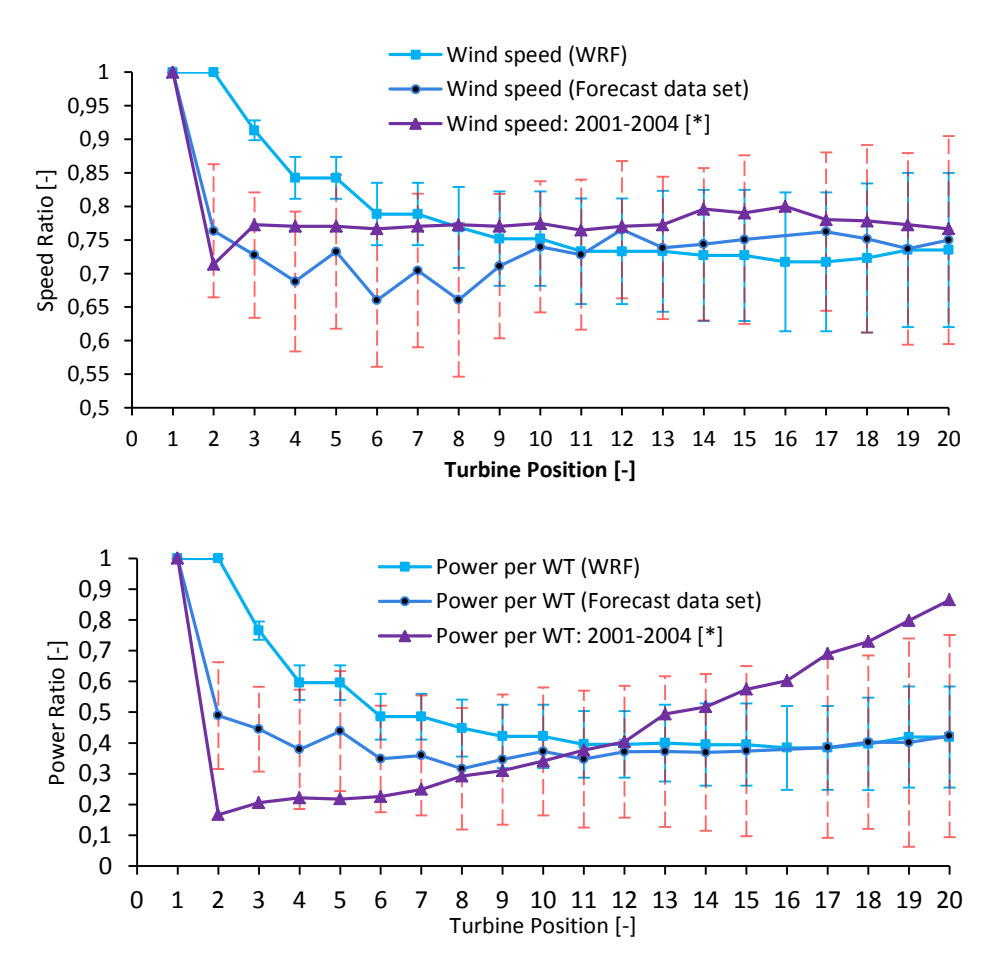


Figure 85: Wind speed deficits (a) and power deficits ratios (b) to the outputs from the North and South WT for the $174^{\circ} \pm 15$, and $354^{\circ} + 15$ directions.

Simulation results follow a smother trend, with a slight overestimation of wake effects on the first WTs. In contrast, speed ratios remain constant in the annual mean [*]. On the long run, the wake center is shifted from the hub, and the layout allows each downstream WT to interact with a decreased area of the wake expansion from its upstream WT. Consequently, the power ratio sharply decreases at the 2nd

⁶¹ WT on position 15 is disregarded due to missing values.

WT, and starts increasing along the bow in the annual mean [*]. Such behavior is contrary to the simulation results and the forecast data set. Both have a similar behavior to that of the wind speed ratios but with better convergence. Nevertheless, such contrast in power ratios is shown for the reader to understand the layout effects in annual power generation.

5.5.3. Increments and deficits of turbulence intensity and turbulent kinetic energy

Ratios of turbulence intensity and turbulent kinetic energy per WT (TKE, $I_{(u,wt)}$) are shown in Figure 86a, also with respect to the south or north WTs. Dashed lines connect TKE and $I_{(u,wt)}$ values on grid locations with one WT only (unity values). The remaining values for locations with more WTs ($N_{tc(i,j)} > 1$) are taken as $TKE/N_{tc\langle i,j\rangle}$, and later used for $I_{(u,wt)}$. Such approach overestimates TKE, and underestimates $I_{(u,wt)}$ in contrast to *unity values*: solid vs. dashed lines. The simulated TKE decreases as the wake develops, whereas $I_{(u,wt)}$ increases immediately and remains nearly constant.

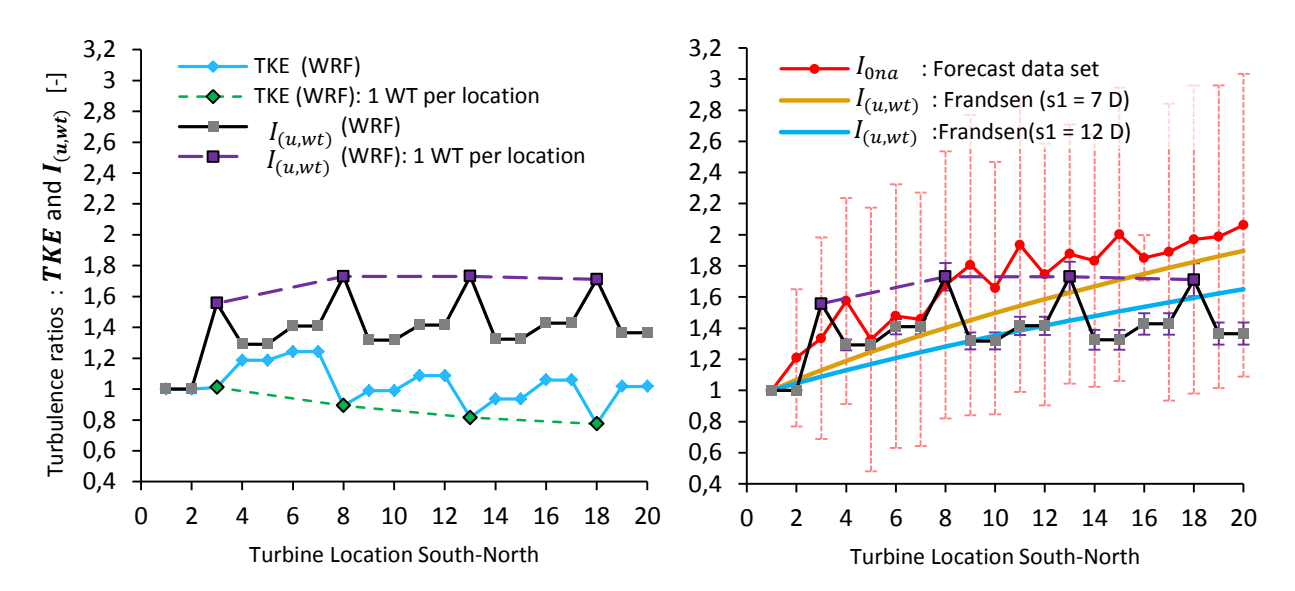


Figure 86: TKE and $I_{(u,wt)}$, I_{0na} ratios as seen from the South or North WT in MIDD for the 174 $^{\circ}$ $^{+}$ 15, and 354 $^{\circ}$ $^{+}$ 15 directions (a). Comparison to Frandsen's Model of turbulence intensity (b). SD are shown as error bars, dashed lines indicate unity values, solid lines indicate locations with $N_{tc (i,i)} = 2$.

Comparisons to the Forecast data set I_{0na} and the Frandsen's model (Equation 22), are clear on Figure 86-b. The data set shows a gradually increasing I_{0na} along the bow, where only the unity values have the lowest error. But the trend in I_{0na} is to rapidly increase downstream, such that most values are larger than the simulated $I_{(u,wt)}$. This fact is partially understood given that the simulation takes $I_{(u,wt)}$ as an averaged value around the hub, and not behind it. It is notorious then, that $I_{(u,wt)}$ values on locations with $N_{tc\langle i,j\rangle} > 1$ are not accurate enough. On the other hand, the data set shows large deviations adding uncertainty to the exact values of $I_{(u,wt)}$.

The solution from Frandsen's model in Figure 86-b used speed ratios from the forecast data set and their corresponding C_T per WT. Spacing is 2.4 D downstream, but there is no explicit transverse spacing; rather, it changes along the farm. Additionally, this distance is somewhat diagonal to the WTs as a consequence of the layout. Therefore, a transverse turbine spacing should be selected as an average value or independently per WT⁶². Hence, spacing of 7 D and 12 D are selected to compare the results⁶³.

The prediction form the model suggest a more gradual increase in $I_{(u,wt)}$ than that of I_{0na} . Turbulence intensity decreases behind WT rotors and it is also expressed by the model in $I_{(u,x)}$ from Figure 87. Generally, there are two reasons explaining the gradual increase:

- ♣ 1st: The small spacing along WTs affecting locations with 2 WTs
- **♣** 2nd: The very low speed ratios on the first WTs of the wake (Figure 85)

 1^{st} : Given that downstream spacing is low, $I_{(u,x)}$ may not converge in-between WTs due to the lack of turbulence dissipation. Therefore, the undissipated turbulence is the initial value of $I_{(u,x)}$ on each WT location (before the peaks). For example, the complete bottom sector in Figure 87 gradually shifts upwards.

 $\mathbf{2}^{ ext{nd}}$: The low speed ratios correspond to high \mathcal{C}_T values, indicating higher added $I_{(u,\chi)}$ on the first WTs (height of peaks in Figure 87). Consequently, the initial value of $I_{(u,x)}$ on each WT increases, and so does the immediate $I_{(u,wt)}$.

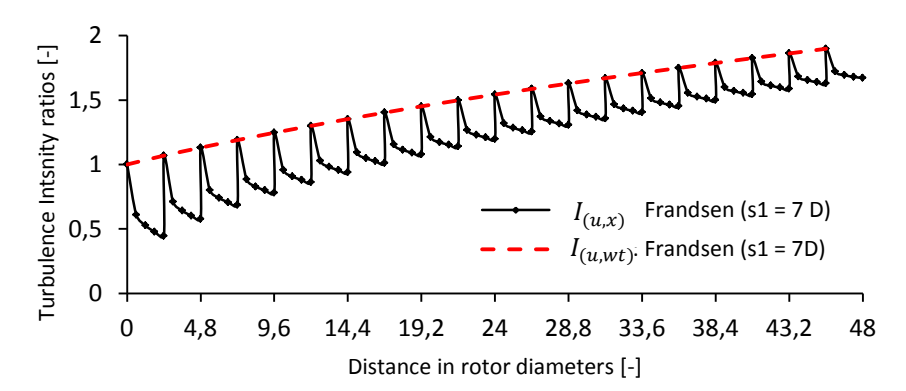


Figure 87: Variation in turbulence intensity downstream between turbines with Frandsen's model, C_T from Forecast data set, I_0 = 0.087 as obtained from WRF for the 174° $^+$ 15, and 354° $^+$ 15 directions, with 8-9 m/s winds.

⁶² This is required by the model, and is also implemented in the parameterization found in Appendix-D.

 $^{^{63}}$ Some argue the spacing between WTs in the offshore should be larger than 7 D, and Appendix-D states why 12 D should also be considered; an analogy to in-line spacing.

Chapter-6. Conclusions And Recommendations

6.1. **Conclusions**

In this study, the offshore wind farm effects of Thanet in the U.K (300 MW), and of Middelgrunden in Denmark (40 MW) were simulated in WRF. The program solves the compressible Non-Hydrostatic Euler equations of motion, in relation to the spherical earth. Parameterizations were used for modeling of the planetary boundary layer, and turbine operation. The objectives were to validate the parameterizations for accurate wind farm power forecasts, and to simulate the effects on the local atmosphere.

The simulation of Thanet suggests that high-end resolutions (1 to 2 WTs/location) should be used for accurate wake effects inside a farm. Whereas, mid-end resolutions (2 to 3 WTs/location) suffice to account for farm effects into the meso-scale atmosphere, including local changes in meteorology. The characteristic that separates high-end from mid-end resolutions, is that on high-end grids the flow model can take into account the multiple wake expansions inside the farm due to the so called empty grid cells in the numerical representation of the farm layout. On the other hand, simulations on high-end resolutions use more computational memory.

The current study reveals that the free stream is affected by the farm presence through local reductions of turbulence intensity aligned in front and in-between turbine rows. Such reductions start at 10 m above the surface onto regions as tall as the turbines. High-end resolutions are recommended if these reductions are to be further investigated. Another unexpected phenomena was the strong speedup effects of near-surface winds inside an array. They transport turbulence downstream, and may affect the behavior of the waves in the offshore, affecting the fatigue damage of turbine towers. Unfortunately, this effect was not further explored but it is certainly recommended to do so.

Results also indicate the strongest turbulence effect is its vertical transport up in the atmosphere, just above the wind farm. Horizontal momentum exchange is negligible behind the farm due to a lack of turbulent advection caused by the downstream wind speed decay. This negligibility was corroborated by Fitch et. al [12], and by Meneau[18]. Local meteorology is also affected as the air expands above the farm, locally increasing the height of the planetary boundary layer. The expansion separates cooler air masses above the rotor area, from similarly hotter masses below the rotor; values registered varied from -0.2°C to +1°C, also with little transport downstream. Such warm-up near the surface decreases the upward surface-heat fluxes inside the farm, whilst increasing them in the downstream. Both effects are proportional to the turbulent kinetic energy patterns of the flow. Finally, the flow vorticity was found to better contour the wake boundaries also indicating mixing in the wake, and local flow patterns were

A.M. Striedinger P.

crucial in determining the shape and of direction of the farm wake. The previous remarks suggest that vorticity studies of turbine wakes could be used to further enhance the turbine parameterization.

An important conclusion is that the parameterizations capture the expected wind farm effects, and mimic the interaction between the farm and the meso-scale atmosphere to some extent; but the complete model needs further enhancement. The deficits of hub height wind speeds through the rotors have a good validation with measurements inside the farm. But a comparison to the Jensen wake model, suggests that wind speeds in the far wake are overestimated. Indirect measurements of the horizontal gradient of turbulence intensity inside the farm suggest the same: The turbine parameterization used in WRF did not perform better than the Farndsen's model. Further, P. Volker et. al [64] reached the same conclusions about the far wake based on measurements in the far wake of the Horns Rev wind farm.

Finally, the farm power series suggests the need for an accurate tracking of the wind direction, and nacelle orientation if the model is to be used for acceptable power forecasts. Nevertheless, results followed closely the power time series form measurements. Despite the issues with wind direction, the resulted power efficiency of the farm was within the range of measured efficiencies. The farm curvature of MIDD proved to be important on assessing the efficiency. As a consequence, an accurate replication of wind farm layout inside the model is crucial for further simulations.

6.2. Recommendations

With a few modifications and a new study with a larger turbine spacing, it is possible to make the MYNN model + turbine parameterization suitable for short term power forecast:

- Turbine layout must be carefully replicated to avoid more than 1 WT/location.
- lacktriangle A feature to correct or estimate nacelle orientation is recommended so to assess the uncertainty of the atmospheric flow model independently of the turbine scheme.
- An increase in the vertical resolution of WRF from the surface to the rotor will aid in detailing the wind speed and power deficits in the first turbines because model microphysics were found to be crucial for high resolutions.
- 🖶 For locations with topography, resolution plays a key role, and the results here are not sufficient to make accurate statements on such cases; this should be investigated separately. Because free stream is also affected by the farm presence, it is interesting and perhaps financially thought-provoking to evaluate the model on Dutch offshore neighboring wind farms and measure the effect on farm power performance, and annual energy production as affected by the changes in free stream.
- Speed-up effects near the sea surface are related to the waves striking the turbine towers. It is therefore, important to evaluate the frequency of speed-ups near the surface.
- 🖶 Finally, a parameterization is proposed to compare the experimental result of added turbulence by Frandsen's model to the current WRF scheme. The parameterization linearizes the near wake development in time, and accounts for errors due to nacelle miss orientation

based on a nacelle rotational speed found in most turbine data sheet; and a reformulation on the energy balance used for the current scheme; see Appendix-D.

With respect to the atmospheric flow model and parameterisation the following can be said and is left open to debate:

- ♣ The frees ream turbulence at high resolutions should be evaluated on sites close to coast-lines in order to determine the locations where uncertainty and inaccuracy of the flow model is most likely to determine the inefficiency of the turbine parameterization.
- LES simulation can be performed with the turbine parameterization as there is more reference in literature about LES turbine and wind farm modelling.

Appendix-A. Wind and The Environment

The full equations of motion in turbulent flow have additional expression for turbulent stress and for velocity fluctuations, which are denominated as $(\bar{\tau}^v + \bar{\tau}^t) \& (\bar{V} + V')$ respectively. Their derivation can be found in averaging the equations in time. This in turn introduces the time-averaged viscous momentum flux as ($\bar{\tau}^v$), and the *turbulent* momentum flux tensor as ($\bar{\tau}^t$):

$$\overline{\tau_{ij}}^t = \rho \overline{v'_i v'_j}$$

$$\overline{\tau_{xx}}^v = -2\mu \frac{\partial \overline{u}}{\partial x} \qquad \overline{\tau_{xy}}^v = \overline{\tau_{yx}}^v = -\mu \left(\frac{\partial \overline{v}}{\partial x} + \frac{\partial \overline{u}}{\partial y}\right)$$

The previous formulation enables the tensor notation as follows, and used by Prandtl for an expression on the turbulent flux tensor:

$$\nabla \cdot \overline{V} = 0 \quad \text{and} \quad \nabla \cdot V' = 0$$

$$\frac{\partial}{\partial t} \rho \overline{V} + \left[\nabla \cdot \rho \overline{V} \overline{V} \right] = -\nabla \overline{p} - \left[\nabla \cdot (\overline{\tau}^v + \overline{\tau}^t) \right] + \rho g$$

$$\overline{\tau_{ij}}^t = -\rho l^2 \left| \frac{\partial v_j}{\partial x_i} \right| \frac{\partial v_j}{\partial x_i}$$

In order to derive the logarithmic law wind of speed profile we have to assume developed flow near the surface, very little to no fluid deformation with the non-slip condition, replace the mixing length \boldsymbol{l} with κz where κ is the van Karman constant, and further consider the fluid motion to be simplified as 2-D with one axis in the horizon. Consequently, the following expressions:

$$0 = -\frac{\partial \bar{p}}{\partial x} - \frac{\partial}{\partial z} \left[\overline{\tau_{zx}}^t + \overline{\tau_{zx}}^v \right]$$

$$= -\frac{\partial \bar{p}}{\partial x} + \frac{\partial}{\partial z} \mu \left[\frac{\partial \bar{u}}{\partial z} + \frac{\partial \bar{w}}{\partial x} \right] + \frac{\partial}{\partial z} \left[\rho l^2 \left| \frac{\partial \bar{u}}{\partial z} \right| \frac{\partial \bar{u}}{\partial z} \right]$$

Change in Fluid deformation ≈ 0

By moving the pressure term to the left, and integrating both sides from the surface to a certain height **z** with the surface stress being $\tau_o = \frac{u^*}{o}$, we obtain:

$$z\left(\frac{\partial \bar{p}}{\partial x}\right) + \tau_o = \rho l^2 \left|\frac{\partial u}{\partial z}\right| \frac{\partial u}{\partial z}$$

Neglecting the horizontal pressure gradients near the surface simplifies the solution. Nonetheless, the assumption indicates a solution that does not hold in the wind turbine rotor area for example, where pressure gradients are non-negligible. The solution then is a simple logarithmic wind speed profile based on the aerodynamic roughness z_o :

$$\int_{z_0}^{z} \frac{u^*}{\kappa z} dz = \int_{0}^{u} du$$

$$u_{(z)} = \frac{u^*}{\kappa} \ln \left(\frac{z}{z_0} \right)$$

Equation 46: Logarithmic expression of wind speed profile with aerodynamic roughness z_o

A-1. Update to the aerodynamic roughness classifications

The article by Jon Wieringa from 1992 [31] used data from sixty field experiments and compared them with popular aerodynamic roughness reviews. A final series of tables with explanations of aerodynamic roughness (z_0) values is presented in the article, few of them are illustrated here; see Table 20. The aerodynamic roughness does not have to represent the real roughness patterns on a surface, but when used in the flow equations it shall emulate real near-surface shear stress. Furthermore, the concept of z_o is widely used on wind farm analysis tools. Therefore, the reader can find the information provided here very useful.

Table 20:Aerodynamic Roughness classifications.

Terrain	$\boldsymbol{z_o}$	Davenport 1960	Oke1978	ESDU Smedman 1978	Cook 1985
Flat snow	0.0003	-	0.0002	0.0001	0.003
Flat land	0.0003	0.006	0.0003	0.005	0.003
Fallow ground	0.002	0.015	0.001 - 0.01	-	0.01
Short grass	0.013	0.015	0.003 - 0.01	0.008	0.01
Long grass	0.034	0.04	0.04 - 0.1	0.02 - 0.05	0.01
Cropped farmland	0.04 - 0.18	0.11	0.04 - 0.2	0.05 - 0.1	0.03
Mature pine forest	1.2	0.8	1.0 - 6.0	0.4	0.3
Low suburb	0.6	1.3	-	0.4 - 0.6	0.3
Regular town	1.1	1.3	-	0.6 – 0.9	0.8

A-2. Complete Non-Hydrostatic Euler Moist-Equations of Motion

The expressions here described corresponded to the equations of motion as implemented in the Weather Research and Forecast model tool WRF. The coordinate system is defined on a dry-air mass basis, and as a pressure ratio. Hence, the vertical coordinate η is as follows.

$$\eta = \frac{(p_{dh} - p_{dht})}{\mu_d} \qquad \mu_d = p_{dhs} - p_{dht}$$

Equation 47 Vertical coordinate in WRF.

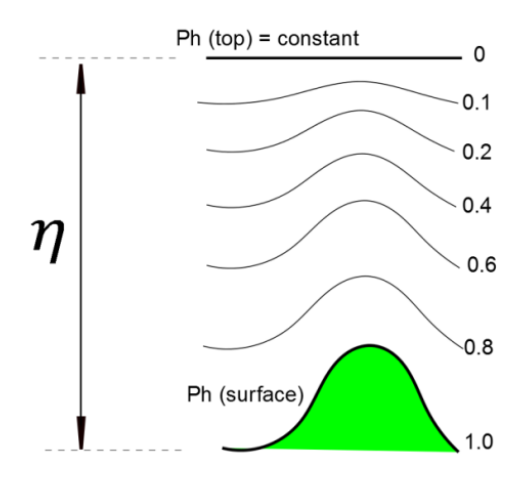


Figure 88: Representation of the terrain-following approach in the vertical coordinate of WRF.

Where μ_d represents the mass of dry air per unit area, and dh, dht, dhs represent the hydrostatic pressures at certain level in the atmosphere, at the top, and at the bottom (respectively). Table 21, Equation 48, and Equation 49 describe the final compressible Euler equations of motions including map projections, to be solved the ARW dynamic solver. Height z is taken into account with the definition of geo-potential $\phi = gz$. Wind speed velocities v, potential temperature θ , and pressure changes $\dot{\eta}$ are modified for the inclusion of moist, yielding V, Θ , Ω , respectively.

$$\mathbf{V} = (U, V, W) = \mu_d \mathbf{v} \quad \mathbf{\Omega} = \mu_d \dot{\eta} \quad \Theta = \mu_d \theta$$
$$\mathbf{v} = (u, v, w)$$

Equation 48: Moist dependent atmospheric variables.

To track pressure changes, the gas equation of state is used as a function of the ratio of heat capacities γ for dry air, the dry-gas constant R_d , and the total air inverse density α which is a function of all the physical states: dry, vapor, cloud, rain, ice, etc. Because the grid spacing $(\Delta x, \Delta y)$ is constant all over the computational grid, map scale factors are used to account for the real area grid cells represent on the spherical earth. Momentum variables are then multiplied by these scale factors m_{χ}, m_{γ} , which also affect the forcing terms F in Equation 48. Finally Coriolis (Ω_e as earth rotation), curvature effects (earth radius r_e), and change in grid distances are introduced to the forcing term expressions of F.

Table 21: Terminology for the Complete Non0hydrostatic-moist Euler Equations of Motion used in WRF.

Mixing ratios (mass/mass dry air) for vapor, cloud, rain, ice, etc. Ratio of dry air heat capacities
$$\gamma = c_p/c_v = 1.4$$
 Inverse density
$$\alpha = \alpha_d \left(1 + \sum q_m\right)$$
 Change in density
$$\frac{\partial \phi}{\partial \eta} = -\alpha_d \mu_d$$
 Map scale factor
$$(m_x, m_y) = \frac{(\Delta x, \Delta y)}{distance \ on \ earth}$$
 Momentum variable vectors
$$V = \mu_d \left(\frac{u}{m_y}, \frac{v}{m_x}, \frac{w}{m_y}\right) ; \ \Omega = \mu_d \dot{\eta}/m_y$$
 Pressure
$$p = p_o \left(\frac{R_d \theta_m}{p_o \alpha_d}\right)^{\gamma}$$
 Moist potential temperature
$$p_m = \theta(1 + R_v q_v/R_d)$$
 Mixing terms vector
$$q_m = \mu_d q_m$$
 Coriolis factors ($\psi = latitude$)
$$f_c = 2\Omega_e \sin \psi$$

$$e = 2\Omega_e \cos \psi$$

Velocity Forcing terms

$$F_{U_{cor}} = \frac{m_x}{m_y} \left[fV + \frac{uV}{r_e} \tan \psi \right] - \frac{uW}{r_e} - eW \cos \alpha_r$$

$$F_{V_{cor}} = \frac{m_y}{m_u} \left[-fUV - \frac{uU}{r_e} \tan \psi - \frac{vW}{r_e} + eW \sin \alpha_r \right]$$

$$F_{W_{cor}} = +e \left(U \cos \alpha_r - \left(m_x/m_y \right) V \sin \alpha_r \right) + \left(\frac{uU + \left(m_x/m_y \right) vV}{r_e} \right)$$

$$\begin{split} F_{U} &= \frac{\partial U}{\partial t} + m_{x} [\nabla \cdot u(U+V)] + \frac{\partial \Omega u}{\partial \eta} + (m_{x}/m_{y}) \left[\mu_{d} \alpha \frac{\partial p}{\partial x} + (\alpha/\alpha_{d}) \frac{\partial p}{\partial \eta} \frac{\partial \phi}{\partial x} \right] \\ F_{V} &= \frac{\partial V}{\partial t} + m_{y} [\nabla \cdot v(U+V)] + (m_{y}/m_{x}) \left[\frac{\partial \Omega v}{\partial \eta} + \mu_{d} \alpha \frac{\partial p}{\partial y} + (\alpha/\alpha_{d}) \frac{\partial p}{\partial \eta} \frac{\partial \phi}{\partial y} \right] \\ F_{W} &= \frac{\partial W}{\partial t} + m_{x} [\nabla \cdot w(U+V)] + \frac{\partial \Omega v}{\partial \eta} - \frac{g}{m_{y}} \left((\alpha/\alpha_{d}) \frac{\partial p}{\partial \eta} - \mu_{d} \right) \\ F_{\Theta} &= \frac{\partial \Theta}{\partial t} + m_{x} m_{y} (\nabla \cdot \theta(U+V)) + m_{y} \frac{\partial \Omega \theta}{\partial \eta} = \\ 0 &= \frac{\partial \mu_{d}}{\partial t} + m_{x} m_{y} [\nabla \cdot (U+V)] + m_{y} \frac{\partial \Omega}{\partial \eta} \\ 0 &= \frac{\partial \phi}{\partial t} + \frac{1}{\mu_{d}} \left[m_{x} m_{y} \left(U \frac{\partial \phi}{\partial x} + V \frac{\partial \phi}{\partial y} \right) + m_{y} \Omega \frac{\partial \phi}{\partial \eta} - m_{y} g W \right] \\ F_{Q_{m}} &= \frac{\partial Q_{m}}{\partial t} + m_{x} m_{y} \frac{\partial U q_{m}}{\partial x} + \frac{\partial V q_{m}}{\partial y} + m_{y} \frac{\partial \Omega q_{m}}{\partial \eta} = \end{split}$$

Equation 49: Complete non-hydrostatic-moist Euler Equations of motion

Appendix-B. The Thanet Offshore Wind Farm

B-1. Examples of wind turbine classes in IEC standard.

For the results displayed of turbulent kinetic energy of the wind farm, most turbines show values of turbulence intensity that would momentarily classify them as in between Full Wind Class B or C. These calcification does not apply all the time, and more data is needed to generalize the turbines as in either one of them. Therefore, the results shown and here explained are only illustrating the net effect of turbines in the deep array on the turbine classes according the simulated flow scenarios.

Example:

On March 19, 2010 the qke results at hub height indicate major areas of 5 m^2/s^2 , with speeds from 13.5 m/s to 11.6 m/s inside the array. Outside the farm, the wind field has major areas of 13.5 + 5 m/s and qke between 0.6 m^2/s^2 and 0.8 m^2/s^2 . Such values can be converted into isotropic turbulence intensity on turbine locations $I_{(u,wt)}$, and that in the free stream as I_o . Both in the main flow direction, as follows.

$$I = \frac{\sqrt{\frac{2}{3}qke}}{V_{hub}}$$

$$I_{\max(u,wt)} \in \left[\frac{\sqrt{\frac{2}{3}*5}}{13.5}, \frac{\sqrt{\frac{2}{3}*5}}{11.6}\right] \Rightarrow I_{\max(u,wt)} \in [0.135, 0.157]$$

$$I_o \in \left[\frac{\sqrt{\frac{2}{3}*0.6}}{13.5}, \frac{\sqrt{\frac{2}{3}*0.8}}{13.3}\right] \Rightarrow I_o \in [0.047, 0.055]$$

Equation 50: Isotropic turbulence intensity values. For qke = 2*TKE from MYNN Scheme.

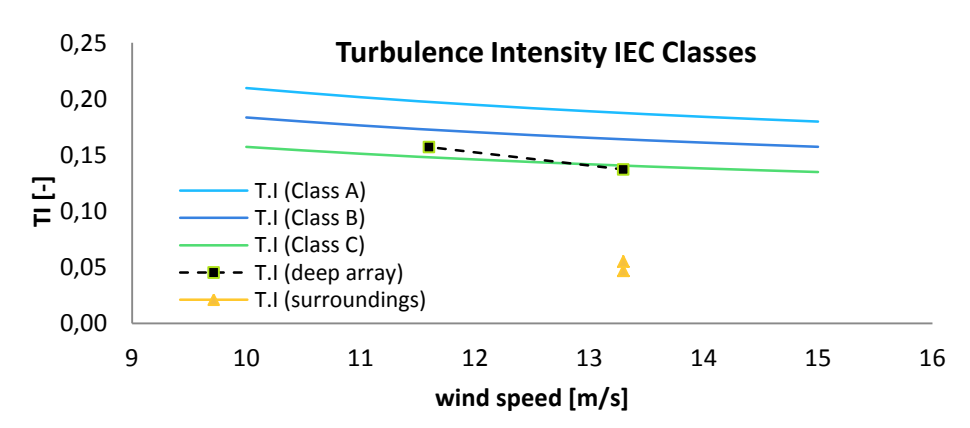


Figure 89: Example of Turbulence Intensity of the Thanet Offshore wind farm.

Consequently, the majority of turbines have a turbulence intensity within $I_{\max(u,wt)}$. The IEC classification criteria is established by comparing the isotropic turbulence intensities to the wind speed classes in Figure 89. The classes estipulate the most likely wind reaching the turbines. The comparison yields that most turbines in the deep array behave as Class C. The wind farm has momentarily increase the turbulence of the site by 2.5 fold increase.

B-2. Wind Farm Characteristics

This appendix section contains general information on the Thanet offshore wind farm and additional results from the WRF simulations performed at MeteoGroup. Information from the Thanet offshore wind farm was collected from public sources in the internet, and no private right is to be derived from them. Turbine and Farm information can be found in the following web sites:

- http://www.lorc.dk/offshore-wind-farms-map/thanet
- http://www.vattenfall.co.uk/en/thanet-offshore-wind-farm.htm

The next tables summarize the general information regarding the farm and the location of turbine on the simulation domains. Additional plots of *TKE* and wind speed contours are given at the end.

Table 22: Thanet offshore wind farm configuration and general information.

Location		Array Configuration	
Name	Thanet Offshore Wind Farm	Not Uniform	
Phase	Commissioned	Number of rows	7
Location	Foreness Point	Number of Columns	17 (vary in length)
Region	Ken	Number of Turbines	100
Country	England / U.K	Inline turbine spacing	500 m
Sea	North Sea	Between row spacing	800 m
GPS Latitude	51.4306	Composition overview	,
GPS Longitude	1.6331	(Number of rows/	1/12 (1 st)
Distance to Shore	11.3 – 11.5 km	turbines per row)	2/14 (2 nd & 3 rd)
Water Depth	20 - 25 m		1/15
			2/17
			1/11
Turbine Description ar	nd Energy Production	Annual Productions:	
Farm Power	300MW	2012	821.68 GWh/yr.
Turbine Power	3 MW	2011	823.88 GWh/yr.
Turbine	Vestas V-90	2010⁶⁴	377.89 GWh/yr.
Rotor diameter	90 m	Historic Mean	741.12 GWh/yr.
Hub height	70 m	Annual mean speed	8.76 m/s
Cut in speed (V_{in})	3.5-4 m/s	10-yr mean (2000-2010)	10.06 m/s
Cut out speed (V_{out})	25 m/s		
Rated speed	14 m/s		

A.M. Striedinger P.

⁶⁴ The wind farm construction ended in September 2010. Such is the reason suggested for the low annual power production from the farm that year.

Table 23: Turbine Locations at offshore site with input parameters. Cut- in speed as 3.5 m/s , Cut out 25 m/s, and Power 3MW. Grid point locations from South to North (SN), and from West to East (WE) are set form domain 3, and domain 4 with 1km and 500m grid resolutions respectively.

No	Lat	Lon	Hub	Dia	Ct(o)	Power	V_{in}	V_{out}	SN_{d03}	WE_{D04}	SN_{d04}	WE_{D04}
1	51.441	1.577	70	90	0.158	3	3.5	25	45	40	146	110
2	51.438	1.582	70	90	0.158	3	3.5	25	45	40	146	111
3	51.435	1.587	70	90	0.158	3	3.5	25	44	41	145	111
4	51.432	1.591	70	90	0.158	3	3.5	25	44	41	144	112
5	51.429	1.596	70	90	0.158	3	3.5	25	44	41	143	112
6	51.425	1.600	70	90	0.158	3	3.5	25	43	42	143	113
7	51.422	1.605	70	90	0.158	3	3.5	25	43	42	142	114
8	51.419	1.610	70	90	0.158	3	3.5	25	43	42	141	114
9	51.416	1.614	70	90	0.158	3	3.5	25	42	43	141	115
10	51.413	1.619	70	90	0.158	3	3.5	25	42	43	140	116
11	51.409	1.624	70	90	0.158	3	3.5	25	42	43	139	116
12	51.406	1.628	70	90	0.158	3	3.5	25	41	44	138	117
13	51.447	1.582	70	90	0.158	3	3.5	25	46	40	147	111
14	51.444	1.587	70	90	0.158	3	3.5	25	45	41	147	111
15	51.441	1.592	70	90	0.158	3	3.5	25	45	41	146	112
16	51.437	1.596	70	90	0.158	3	3.5	25	45	41	145	112
17	51.434	1.601	70	90	0.158	3	3.5	25	44	42	145	113
18	51.431	1.605	70	90	0.158	3	3.5	25	44	42	144	114
19	51.428	1.610	70	90	0.158	3	3.5	25	44	42	143	114
20	51.425	1.615	70	90	0.158	3	3.5	25	43	43	142	115
21	51.421	1.619	70	90	0.158	3	3.5	25	43	43	142	116
22	51.418	1.624	70	90	0.158	3	3.5	25	43	43	141	116
23	51.415	1.618	70	90	0.158	3	3.5	25	42	43	140	116
24	51.412	1.633	70	90	0.158	3	3.5	25	42	44	140	118
25	51.409	1.638	70	90	0.158	3	3.5	25	42	44	139	118
26	51.405	1.642	70	90	0.158	3	3.5	25	41	45	138	119
27	51.449	1.592	70	90	0.158	3	3.5	25	46	41	148	112
28	51.449	1.596	70	90	0.158	3	3.5	25	46	41	148	113
29	51.443	1.601	70	90	0.158	3	3.5	25	45	42	147	113
30	51.440	1.606	70	90	0.158	3	3.5	25	45	42	146	114
31	51.437	1.610	70	90	0.158	3	3.5	25	45	42	145	114
32	51.433	1.615	70	90	0.158	3	3.5	25	44	43	144	115
33	51.430	1.620	70	90	0.158	3	3.5	25	44	43	144	116
34	51.427	1.624	70	90	0.158	3	3.5	25	44	43	143	116
35	51.424	1.629	70	90	0.158	3	3.5	25	43	44	142	117
36	51.421	1.633	70	90	0.158	3	3.5	25	43	44	142	118
37	51.417	1.638	70	90	0.158	3	3.5	25	43	44	141	118
38	51.414	1.643	70	90	0.158	3	3.5	25	42	45	140	119
39	51.411	1.647	70	90	0.158	3	3.5	25	42	45	139	120
40	51.408	1.652	70	90	0.158	3	3.5	25	41	45	139	120
41	51.405	1.656	70	90	0.158	3	3.5	25	41	46	138	121
42	51.455	1.597	70	90	0.158	3	3.5	25	47	41	149	113
43	51.452	1.601	70	90	0.158	3	3.5	25	46	42	149	113
44	51.449	1.606	70	90	0.158	3	3.5	25	46	42	148	114
45	51.446	1.611	70	90	0.158	3	3.5	25	46	42	147	114
46	51.442	1.615	70	90	0.158	3	3.5	25	45	43	146	115
47	51.439	1.620	70	90	0.158	3	3.5	25	45	43	146	116
48	51.436	1.624	70	90	0.158	3	3.5	25	45	43	145	116
49	51.433	1.629	70	90	0.158	3	3.5	25	44	44	144	117
50	51.430	1.634	70	90	0.158	3	3.5	25	44	44	144	118
51	51.426	1.638	70	90	0.158	3	3.5	25	44	44	143	118
52	51.423	1.643	70	90	0.158	3	3.5	25	43	45	142	119
53	51.420	1.648	70	90	0.158	3	3.5	25	43	45	141	120
54	51.417	1.652	70	90	0.158	3	3.5	25	42	45	141	120
55	51.413	1.657	70	90	0.158	3	3.5	25	42	46	140	121
56	51.410	1.661	70	90	0.158	3	3.5	25	42	46	139	122
57	51.407	1.666	70	90	0.158	3	3.5	25	41	46	139	122
58	51.404	1.671	70	90	0.158	3	3.5	25	41	47	138	123
30	31.707	1.0/1	, 0	50	0.130	,	٥.5	23	71	7/	130	14.0

59	51.458	1.606	70	90	0.158	3	3.5	25	47	42	150	114
60	51.454	1.611	70	90	0.158	3	3.5	25	47	42	149	114
61	51.451	1.615	70	90	0.158	3	3.5	25	46	43	148	115
62	51.448	1.620	70	90	0.158	3	3.5	25	46	43	148	116
63	51.445	1.625	70	90	0.158	3	3.5	25	46	43	147	116
64	51.442	1.629	70	90	0.158	3	3.5	25	45	44	146	117
65	51.438	1.634	70	90	0.158	3	3.5	25	45	44	146	118
66	51.435	1.639	70	90	0.158	3	3.5	25	45	44	145	118
67	51.432	1.643	70	90	0.158	3	3.5	25	44	45	144	119
68	51.429	1.648	70	90	0.158	3	3.5	25	44	45	143	120
69	51.426	1.652	70	90	0.158	3	3.5	25	43	45	143	120
70	51.422	1.657	70	90	0.158	3	3.5	25	43	46	142	121
71	51.419	1.662	70	90	0.158	3	3.5	25	43	46	141	122
72	51.416	1.666	70	90	0.158	3	3.5	25	42	46	141	122
73	51.413	1.671	70	90	0.158	3	3.5	25	42	47	140	123
74	51.410	1.675	70	90	0.158	3	3.5	25	42	47	139	123
75	51.406	1.680	70	90	0.158	3	3.5	25	41	47	138	124
76	51.457	1.620	70	90	0.158	3	3.5	25	47	43	150	116
77	51.454	1.625	70	90	0.158	3	3.5	25	47	43	149	116
78	51.450	1.630	70	90	0.158	3	3.5	25	46	44	148	117
79	51.447	1.634	70	90	0.158	3	3.5	25	46	44	148	118
80	51.444	1.639	70	90	0.158	3	3.5	25	45	44	147	118
81	51.441	1.643	70	90	0.158	3	3.5	25	45	45	146	119
82	51.438	1.648	70	90	0.158	3	3.5	25	45	45	145	120
83	51.434	1.653	70	90	0.158	3	3.5	25	44	45	145	120
84	51.431	1.657	70	90	0.158	3	3.5	25	44	46	144	121
85	51.428	1.662	70	90	0.158	3	3.5	25	44	46	143	122
86	51.425	1.667	70	90	0.158	3	3.5	25	43	46	143	122
87	51.422	1.671	70	90	0.158	3	3.5	25	43	47	142	123
88	51.418	1.676	70	90	0.158	3	3.5	25	43	47	141	124
89	51.415	1.680	70	90	0.158	3	3.5	25	42	47	140	124
90	51.456	1.634	70	90	0.158	3	3.5	25	47	44	150	118
91	51.453	1.639	70	90	0.158	3	3.5	25	46	44	149	118
92	51.450	1.644	70	90	0.158	3	3.5	25	46	45	148	119
93	51.440	1.647	70	90	0.158	3	3.5	25	45	45	146	120
94	51.443	1.653	70	90	0.158	3	3.5	25	45	45	147	120
95	51.440	1.658	70	90	0.158	3	3.5	25	45	46	146	121
96	51.437	1.662	70	90	0.158	3	3.5	25	45	46	145	122
97	51.434	1.667	70	90	0.158	3	3.5	25	44	46	145	122
98	51.430	1.671	70	90	0.158	3	3.5	25	44	47	144	123
99	51.427	1.676	70	90	0.158	3	3.5	25	44	47	143	124
100	51.424	1.681	70	90	0.158	3	3.5	25	43	47	142	124

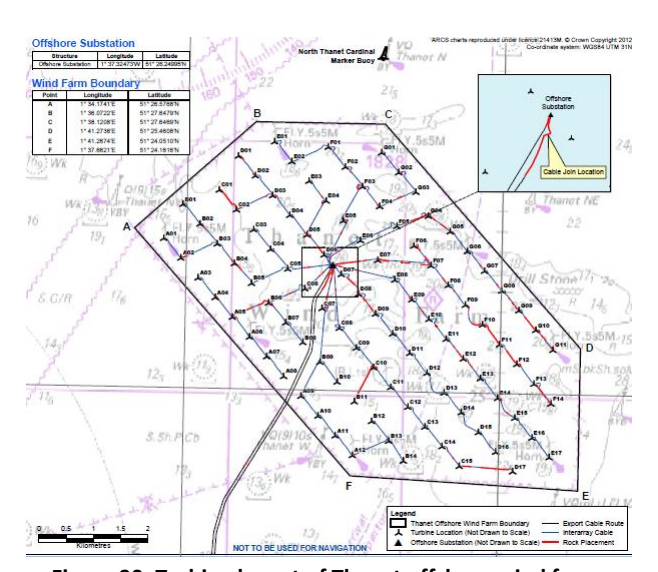


Figure 90: Turbine layout of Thanet offshore wind farm.

Effect of Resolution to Wind Farm Layout and Resultant Wind Speed B-3. and TKE Contours.

Simulations have proven that the current turbine parameterization scheme under the MYNN PBL and surface physics schemes, is dependent on the horizontal resolution of the computational grid. The wind speed deficits inside the farm are more turbine-specific on the highest resolution (500 m domain). The turbine grid locations are shown for the 1 km, and 500 m domain resolutions in Figure 91 to Figure 96 for the contours of wind speeds at hub height. Their corresponding production of turbulent kinetic energy is shown in Figure 95, and Figure 96. The differences in turbulence generation from the coast and from the farm are highlighted, where the turbulence generation inside the farm is very well represents the turbine layout.

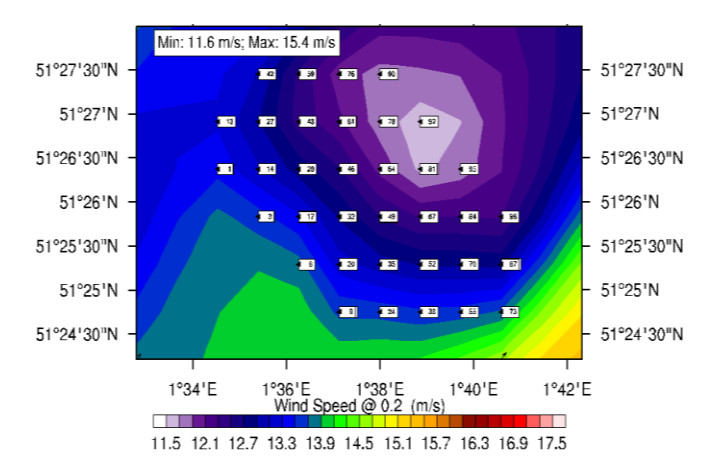


Figure 91: Wind speed contour plot at 67 m above sea level on the Thanet offshore wind farm from the 1 km grid resolution. 19 March 2010. Bins of 0.2 m/s. Many turbine labels interlap each other but each group of turbines is evenly distributed.

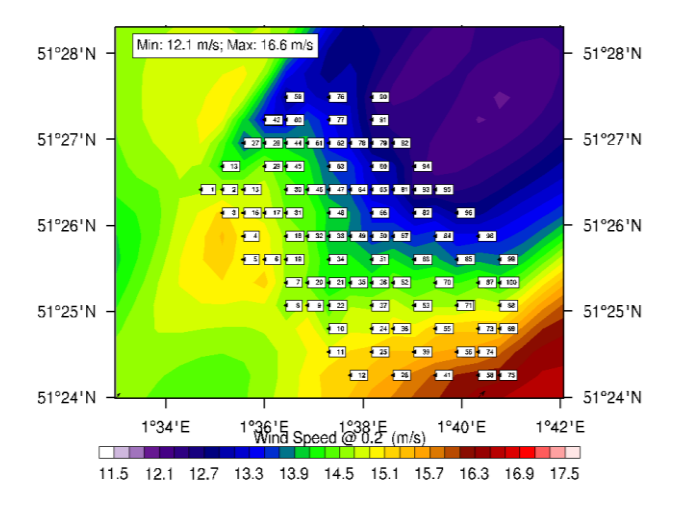


Figure 92: Wind speed contour plot at 67 m above sea level on the Thanet offshore wind farm from the 500 m grid resolution. 19 March 2010 00:00 hrs . Bins of 0.2 m/s. Labels interlap each other but each group of turbines is evenly distributed.

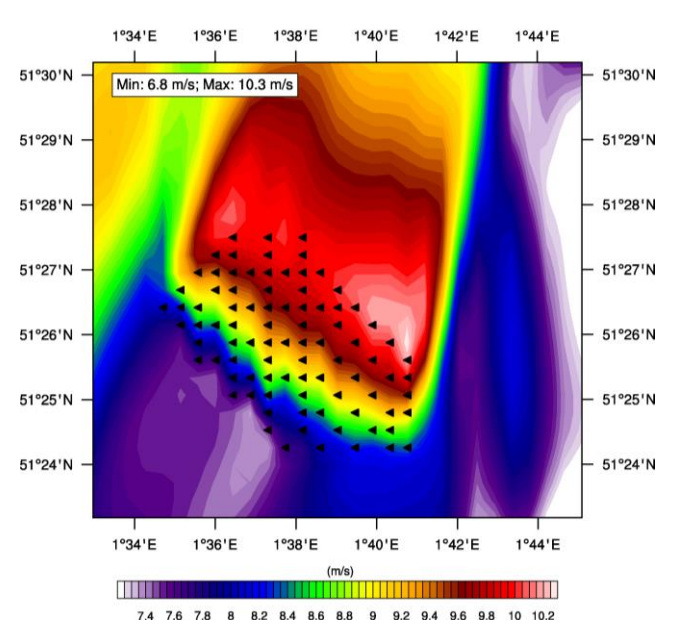


Figure 93: Wind speed contour plot on the 500 m grid at 10 m height at the farm location. March 18, 2010, 15:00 hrs. Bins of 0.05 m/s. The surface winds increase in the flow direction on the site.

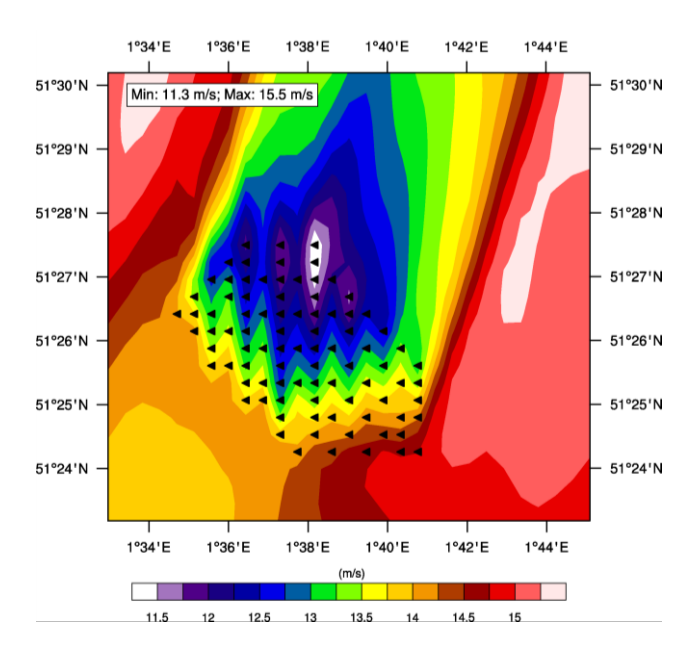


Figure 94: Wind speed contour plot on the 500 m grid at hub height at the farm location. March 18, 2010, 15:00 hrs. Bins of 0.25 m/s. The wake effects is shown as wind speed decays on the site.

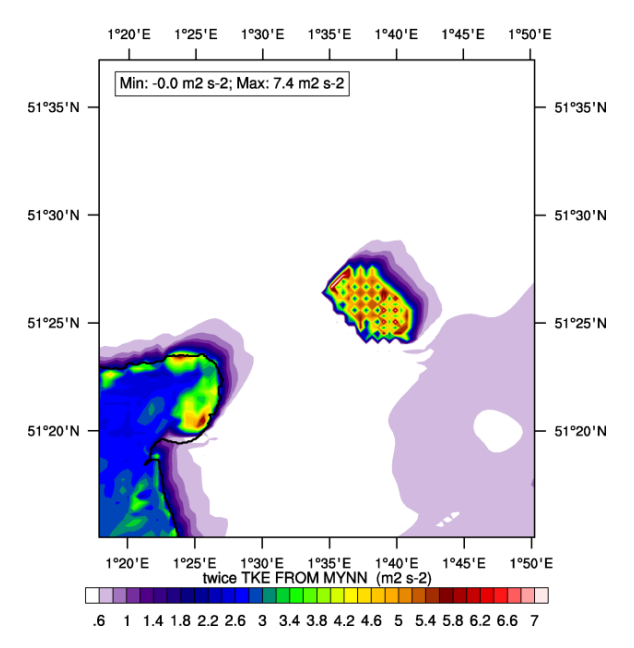


Figure 95: Contour plot of turbulent kinetic energy TKE at hub height on the 500 m grid. March 19 2010, 00:00 hrs. Bins of 0.2 m2 s-2. The SE coast of England is located at the left corner of the figure. Red spots on that corner are most likely due to the Dover hills in the south.

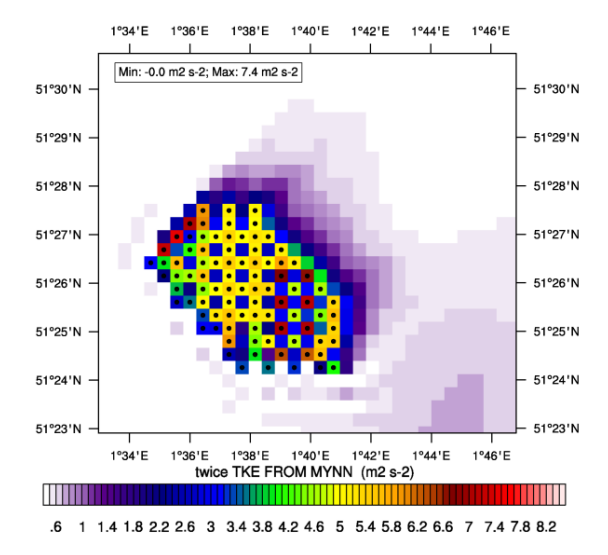


Figure 96: Contour plot of turbulent kinetic energy TKE in pixel format at hub height on the 500 m grid: Zoom at the farm site. March 19, 2010, 00:00 hrs Bins of 0.05m2 s-2.

The following figures show the time development of wind speed at 33 m height from the simulation set#1. After wards, wind speed and TKE at 67 m height are compared for their corresponding domains and simulation times. The period selected is March 18, 18 hrs to March 19, 12 hrs.

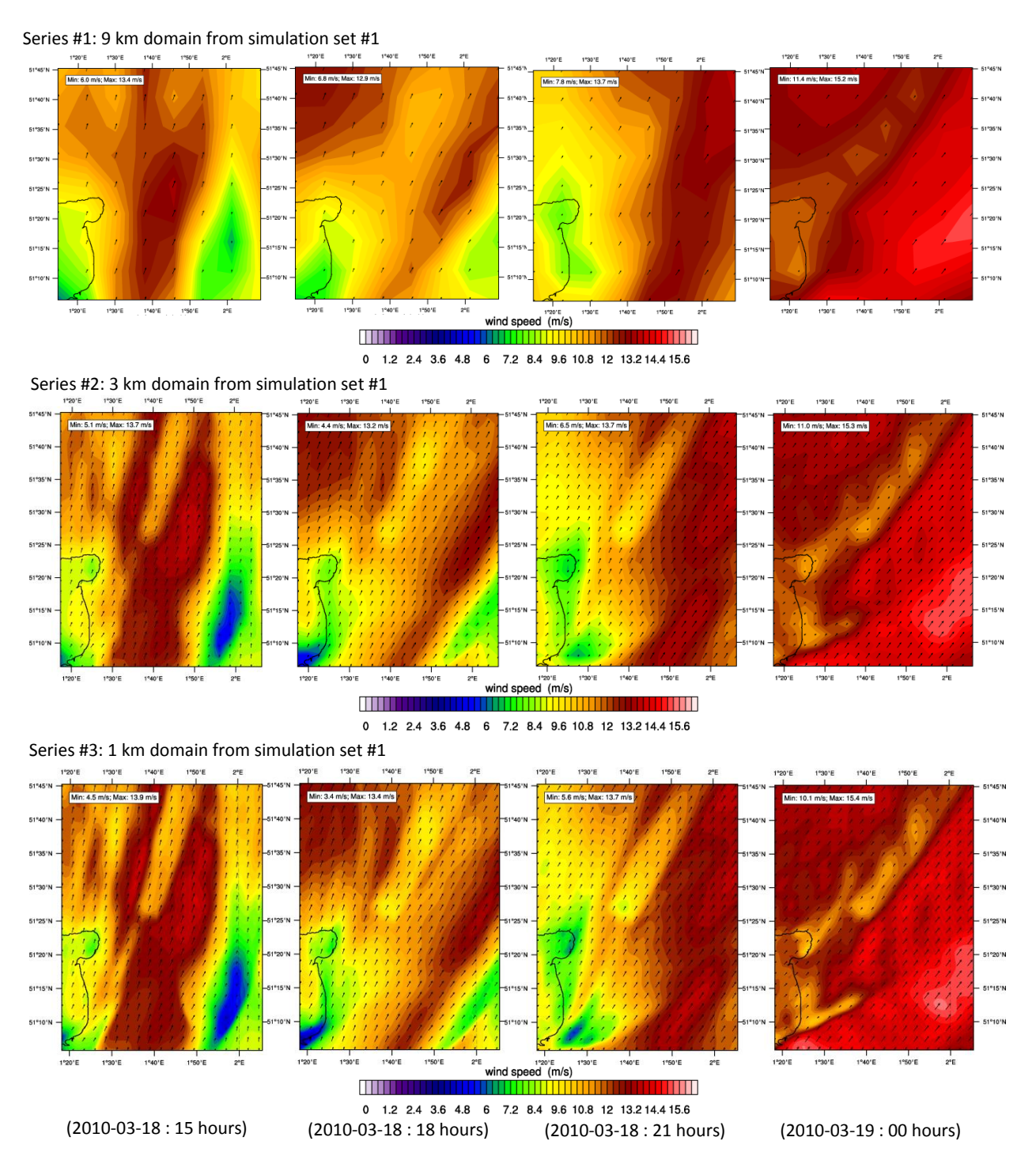


Figure 97: Wind speed contours at 33 m height (FARM case) . Left to right: simulation times yyyy-mm-dd: hh. Series #1: 3 km domain from simulation set #1. Series #2: 1 km domain from simulation set #1. Series #3: 500 m domain from simulation set #2.

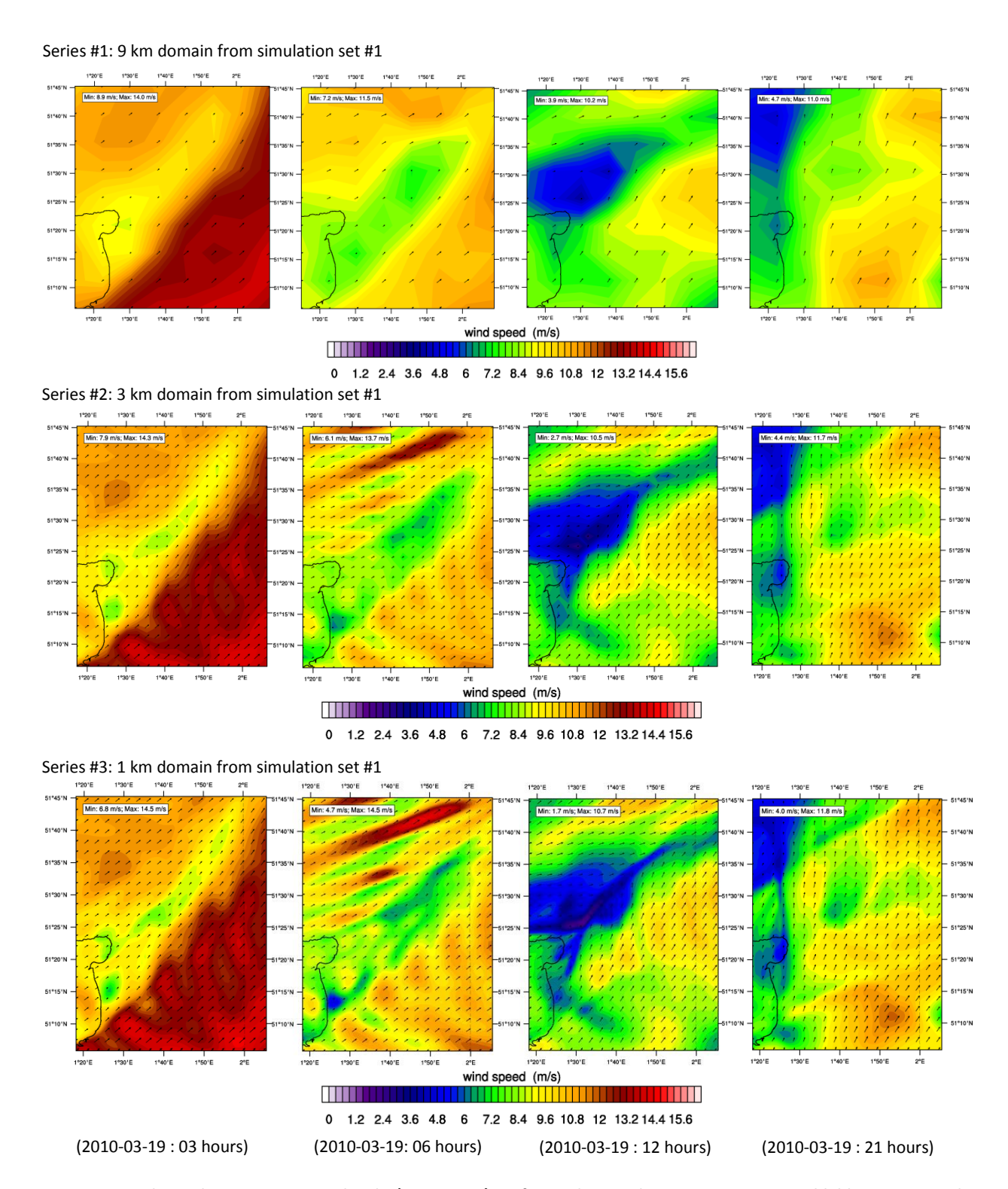


Figure 98: Wind speed contours at 33 m height (FARM case). Left to right: simulation times yyyy-mm-dd: hh. Series #1: 3 km domain from simulation set #1. Series #2: 1 km domain from simulation set #1. Series #3: 500 m domain from simulation set #2.

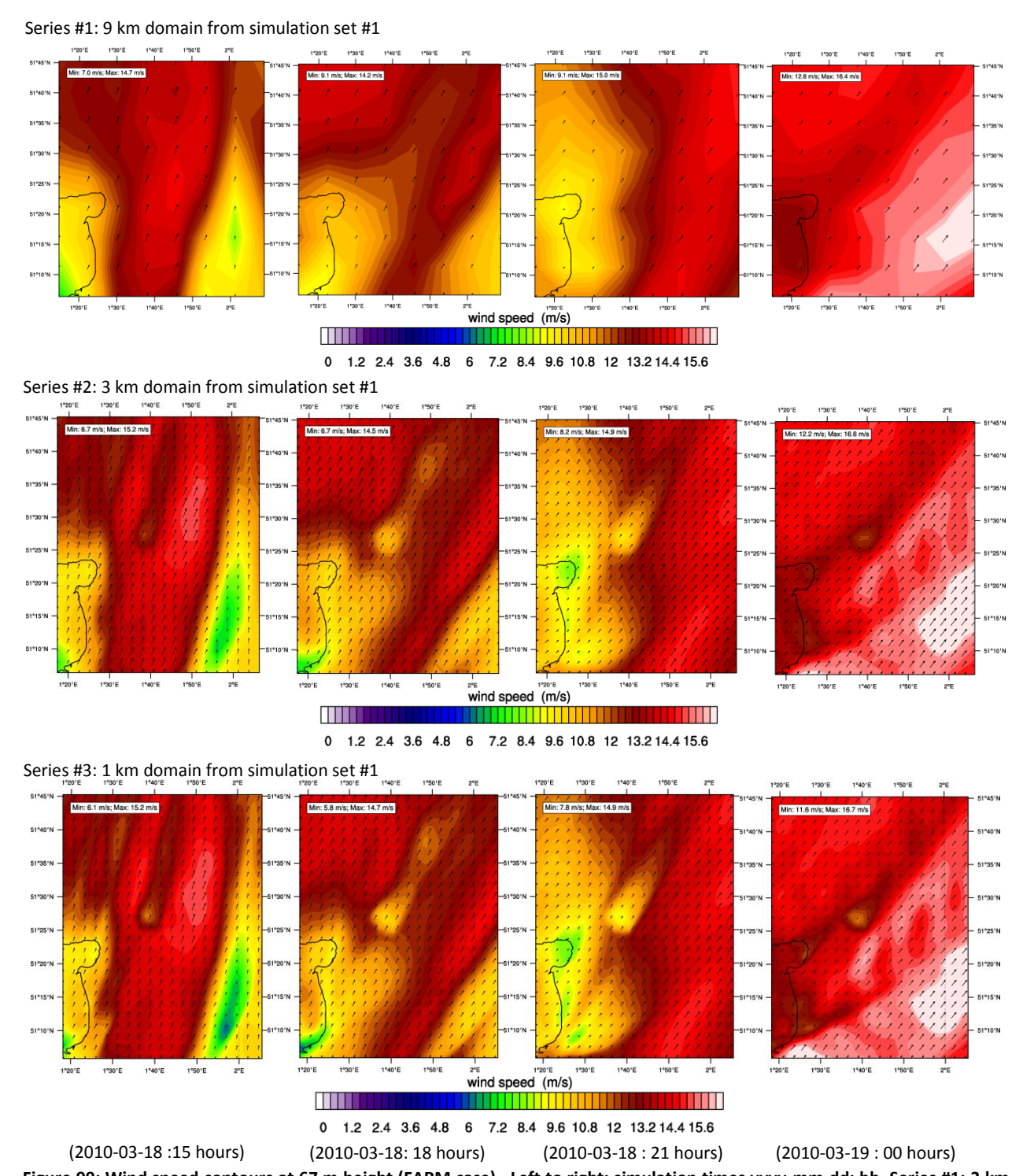


Figure 99: Wind speed contours at 67 m height (FARM case) . Left to right: simulation times yyyy-mm-dd: hh. Series #1: 3 km domain from simulation set #1. Series #2: 1 km domain from simulation set #1. Series #3: 500 m domain from simulation set #2.

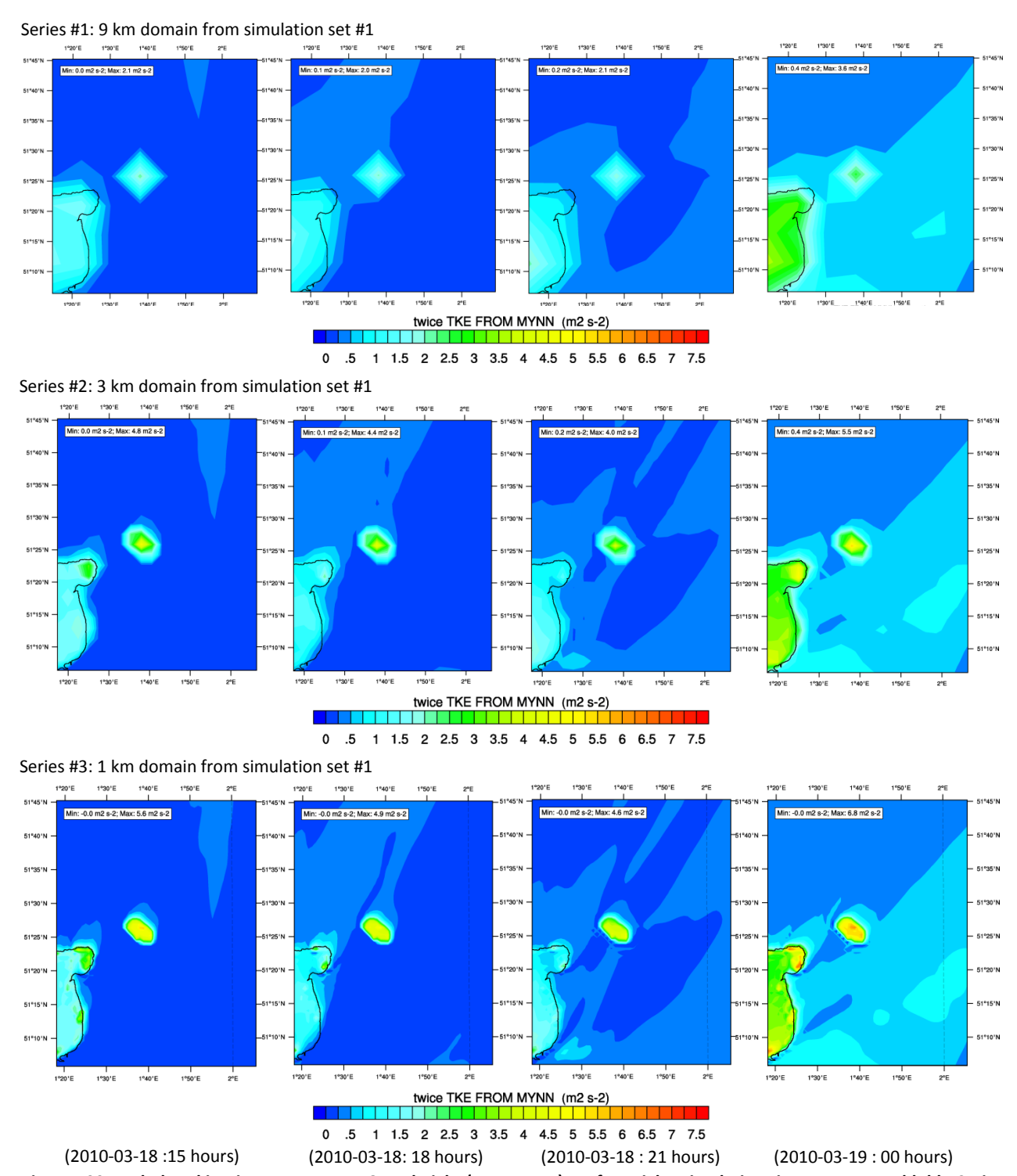


Figure 100: Turbulent kinetic energy TKE at 67 m height (FARM case) . Left to right: simulation times yyyy-mm-dd: hh. Series #1: 3 km domain from simulation set #1. Series #2: 1 km domain from simulation set #1. Series #3: 500 m domain from simulation set #2.

A.M. Striedinger P.

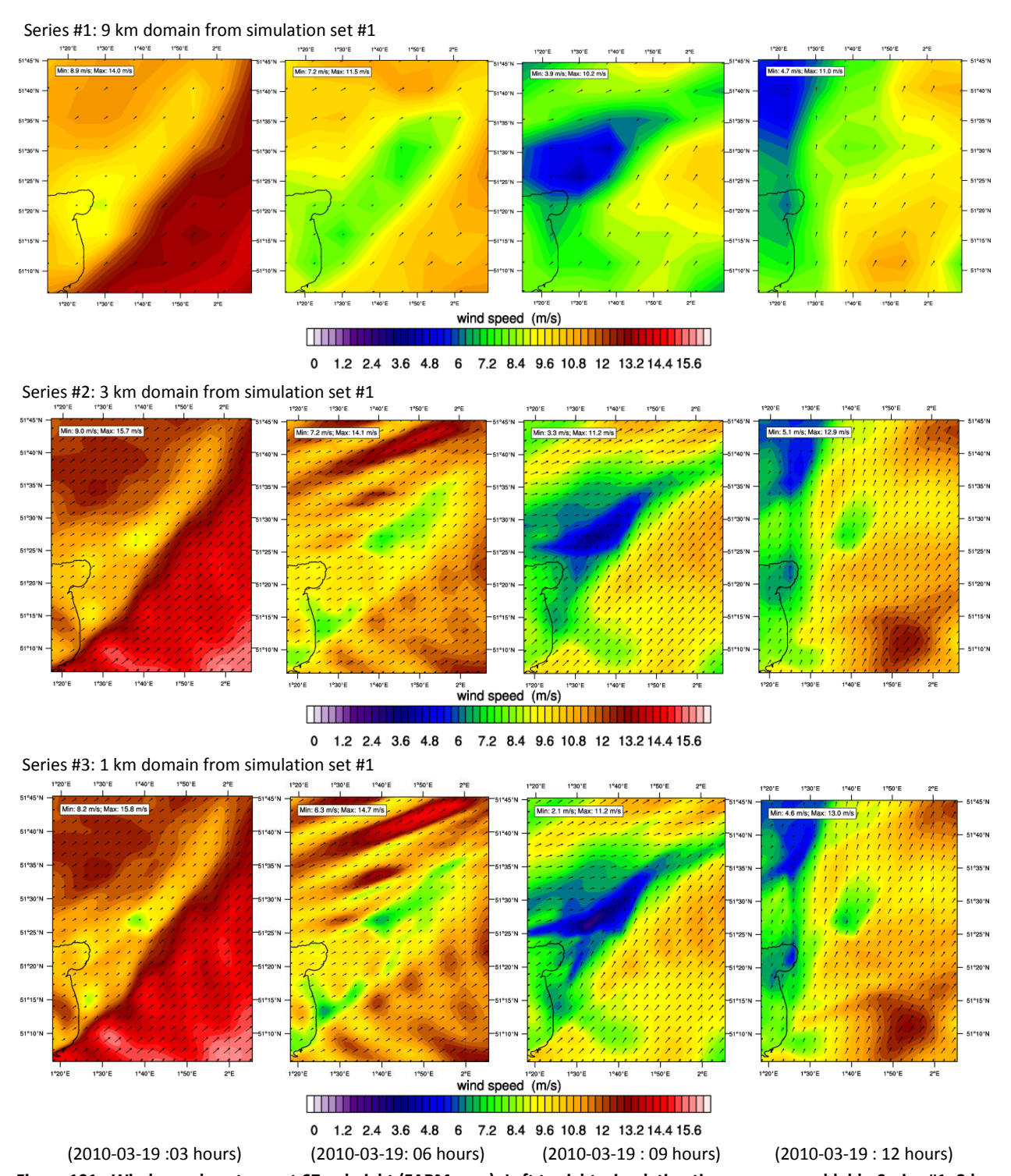


Figure 101: Wind speed contours at 67 m height (FARM case). Left to right: simulation times yyyy-mm-dd: hh. Series #1: 3 km domain from simulation set #1. Series #2: 1 km domain from simulation set #1. Series #3: 500 m domain from simulation set #2.

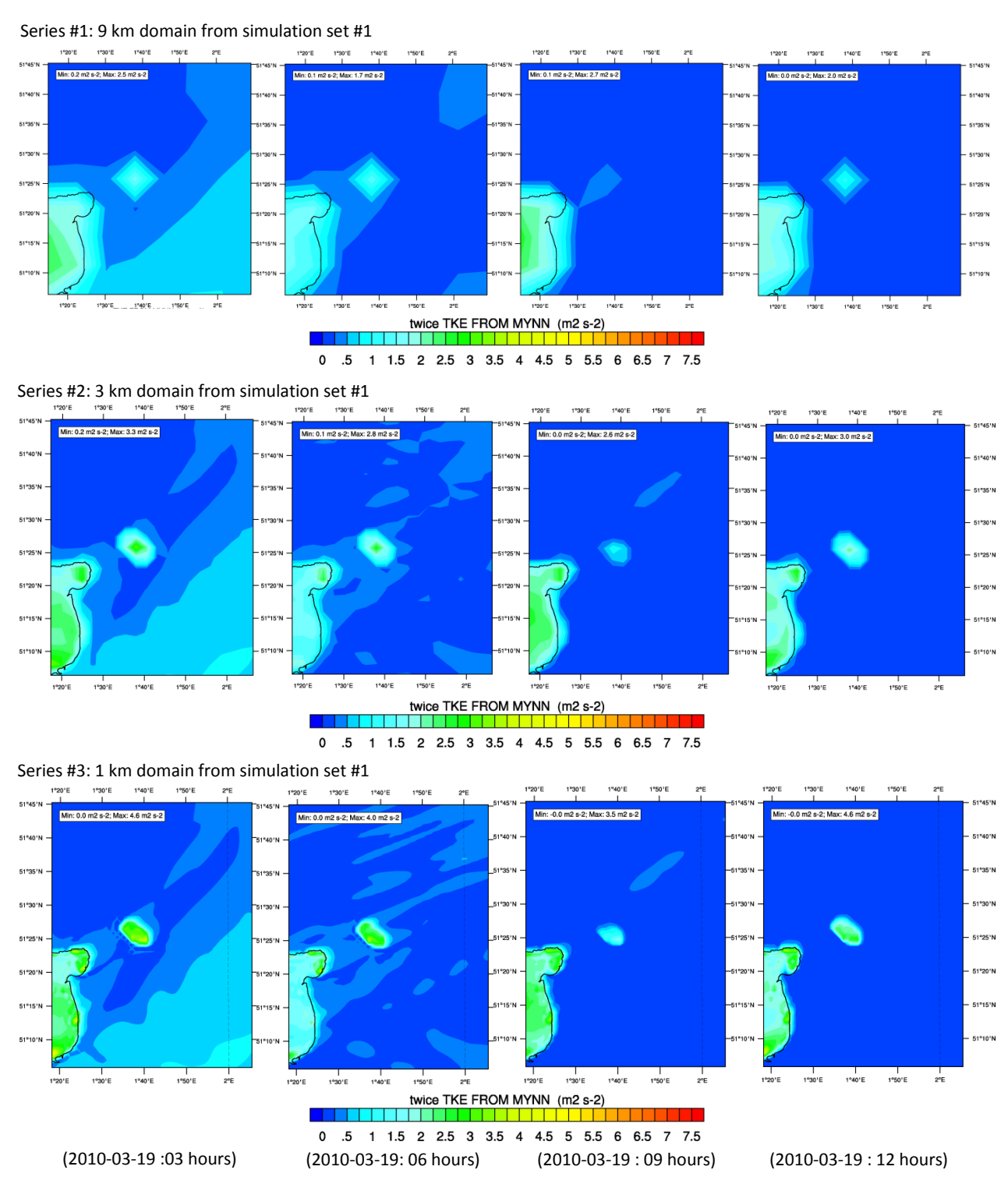


Figure 102: Turbulent kinetic energy TKE at 67 m height (FARM case) . Left to right: simulation times yyyy-mm-dd: hh. Series #1: 3 km domain from simulation set #1. Series #2: 1 km domain from simulation set #1. Series #3: 500 m domain from simulation set #2.

B-4. **Examples of Local Changes in Meteorology**

The predicted changes in local meteorology at the offshore site are expressed in the variables of temperature, upward surface-heat flux $H_{\mathcal{S}f}$, the planetary boundary layer height h_* , and vorticity. The first 12 hours of simulation time are known as "spin-up time". This time is required by the model to adjust to all initial conditions and ensure the dynamics of the model. Results within the spin-up time are therefore not considered accurate by definition.

The vertical gradient in temperature was found throughout the complete simulation, showing the same pattern: cooler air masses above hub height, and hotter air masses below and near the sea surface; see Figure 103. The main effect in H_{sf} , is a decrease inside the turbine array, with a small increase in front of it. Behind the array, changes in H_{sf} remain negative, but in the downstream the changes are positive. Therefore, indicating a wave that propagates ;see Figure 104. The same situation occurs for the changes in h_* but in opposite values; see Figure 105. The boundary layer inside the turbine array increase due to a sudden expansion of the flow, and decrease further downstream.

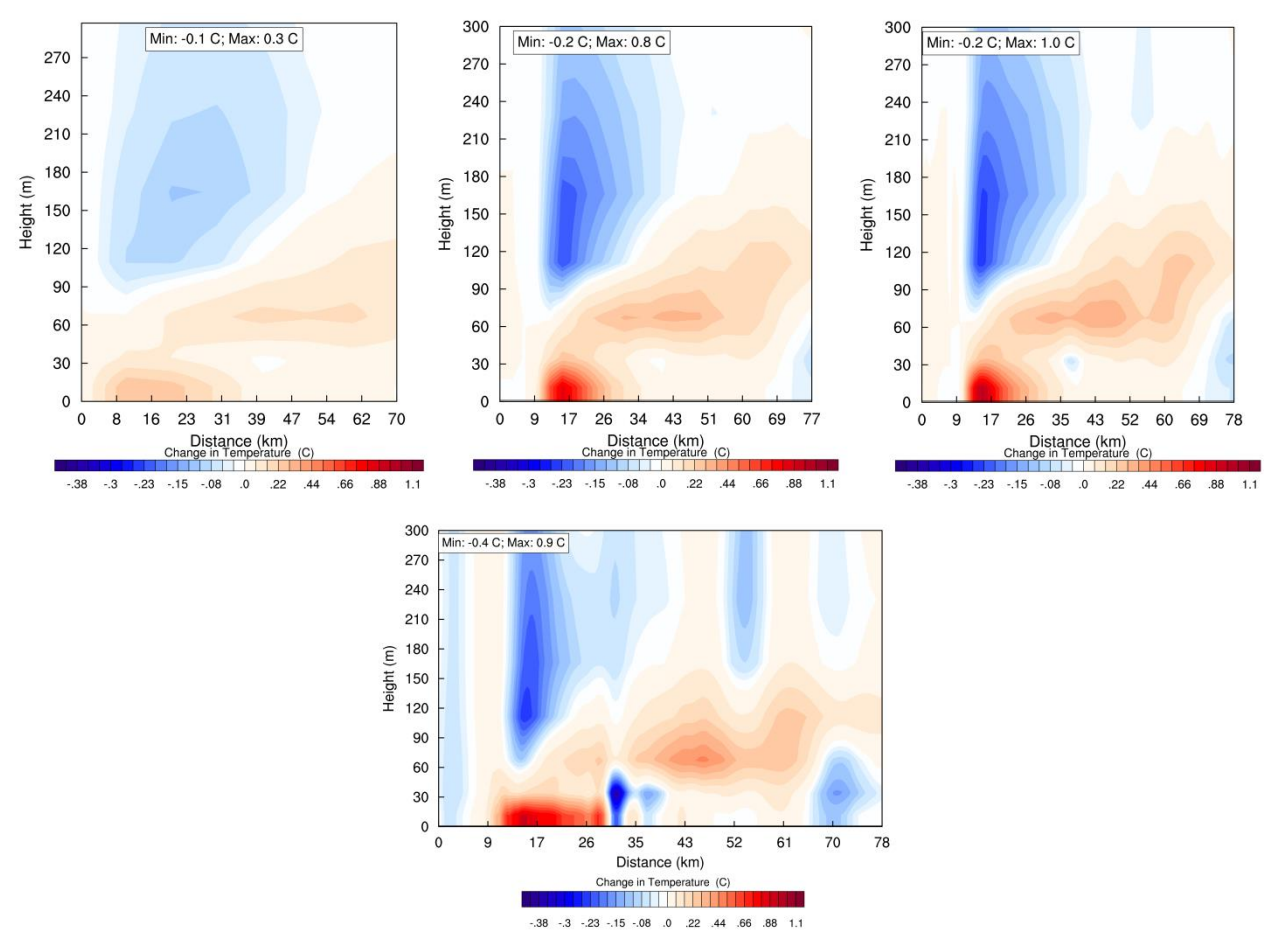


Figure 103: Vertical contours of Temperature (FARM - BACKGROUND case). Left to right: 9 km, 3 km, 1 km domains from set #1, and 500 m domain from set #2 (below). Values indicate a change in air temperature.

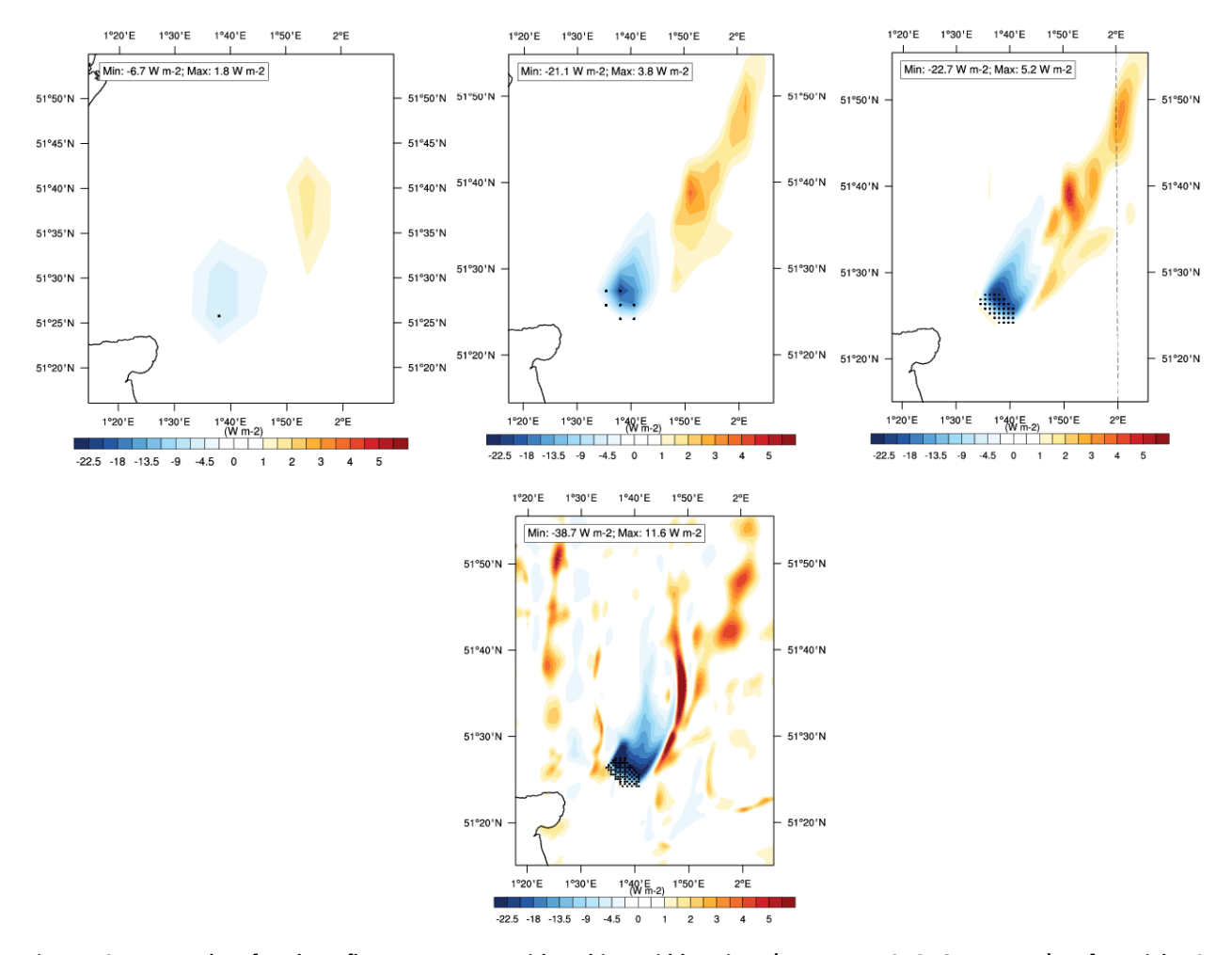


Figure 104: Upward surface-heat flux H_{sf} contours with turbine grid locations (FARM – BACKGROUND case). Left to right: 9 km, 3 km, 1 km domains from set #1, and 500 m domain from set #2 (below). Values indicate changes in H_{sf} .

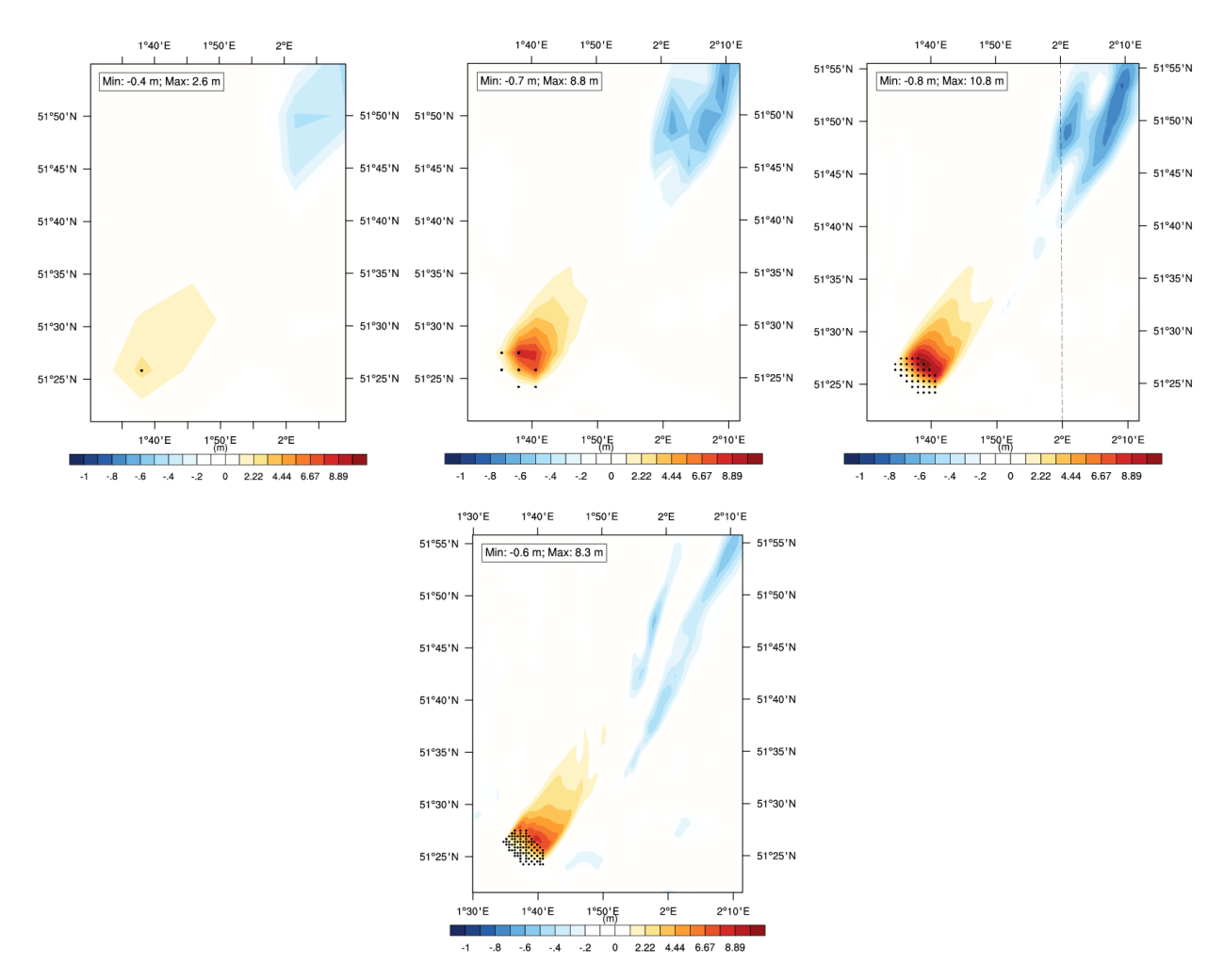


Figure 105: Planetary boundary layer height h. contours with turbine grid locations (FARM - BACKGROUND case). Left to right: 9 km, 3 km, 1 km domains from set #1, and 500 m domain from set #2 (below).

Local changes in meteorology are well captured on the 3 km, and 1 km domains from set #1. On the 500 m domain from set #2, the changes in meteorology are also captured with a much turbulent nature, and different patterns than on other domains. Finally, results at different hours are shown in Figure 106 to Figure 111 for each variable and grid domain. These results support the statements about the local changes in meteorology.

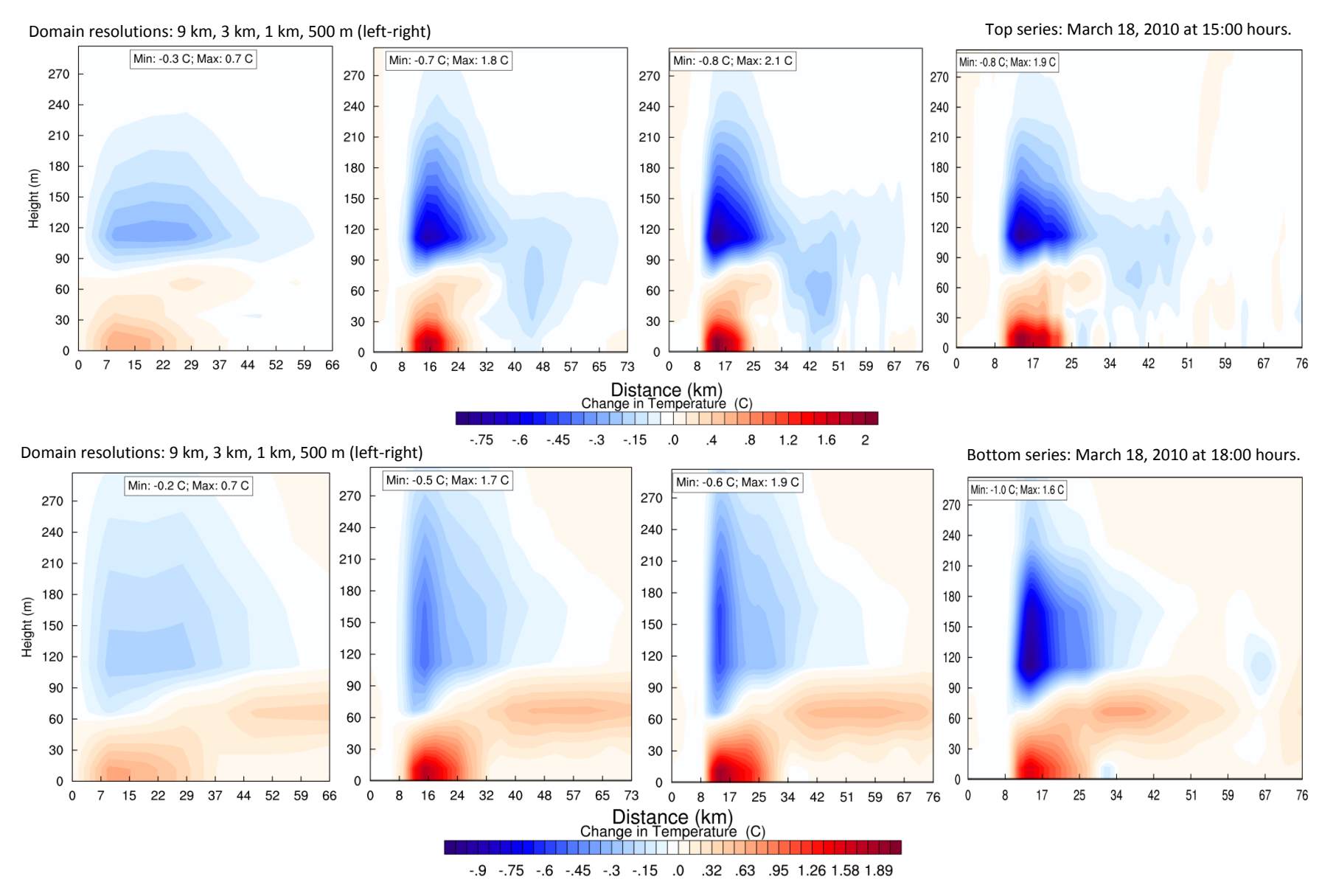


Figure 106: Vertical contours of Temperature (FARM – BACKGROUND case). Left to right: 9 km, 3 km, 1 km domains from set #1, and 500 m domain from set #2. Top series is at simulation time of March 18, 15:00 hours, 2010. Bottom series at 18:00 hours. Farm is located from the 10th km, and profiles are oriented in the flow direction at each simulation time.

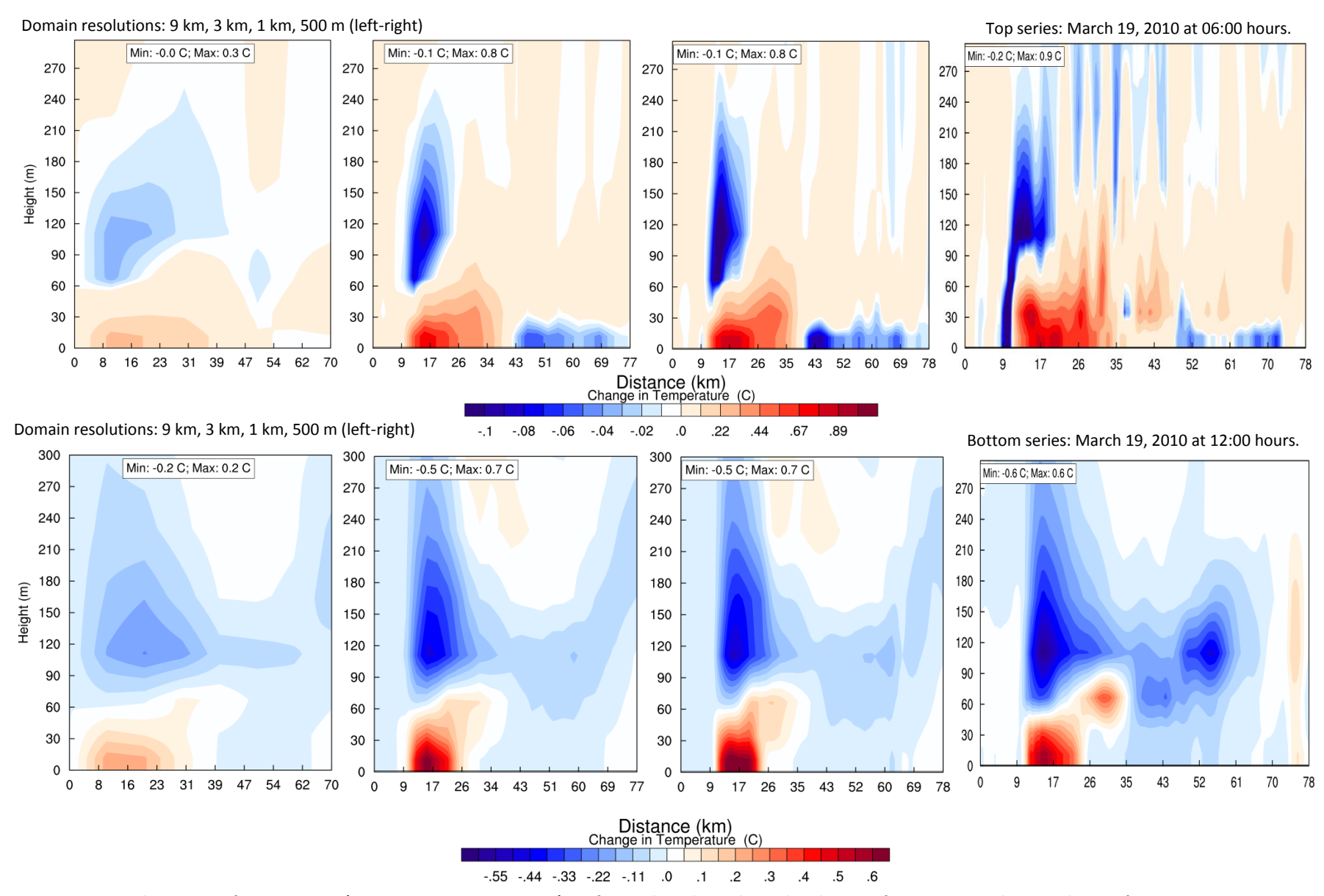


Figure 107: Vertical contours of Temperature (FARM – BACKGROUND case). Left to right: 9 km, 3 km, 1 km domains from set #1, and 500 m domain from set #2. Top series is at simulation time of March 19, 06:00 hours, 2010. Bottom series at 12:00 hours. Farm is located from the 10th km, and profiles are oriented in the flow direction at each simulation time.

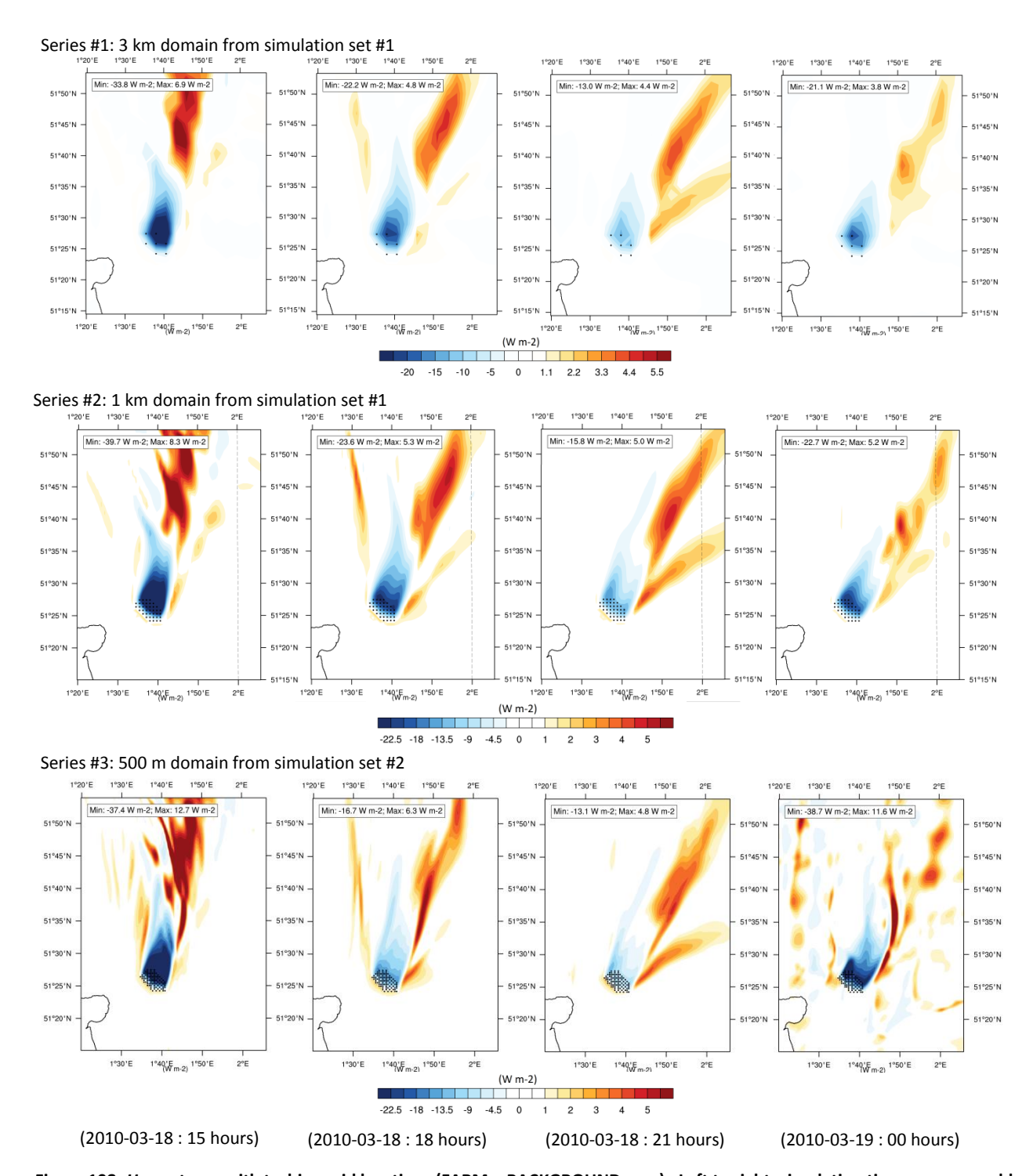


Figure 108: H_{sf} contours with turbine grid locations (FARM – BACKGROUND case) . Left to right: simulation times yyyy-mm-dd: hh. Series #1: 3 km domain from simulation set #1. Series #2: 1 km domain from simulation set #1. Series #3: 500 m domain from simulation set #2.

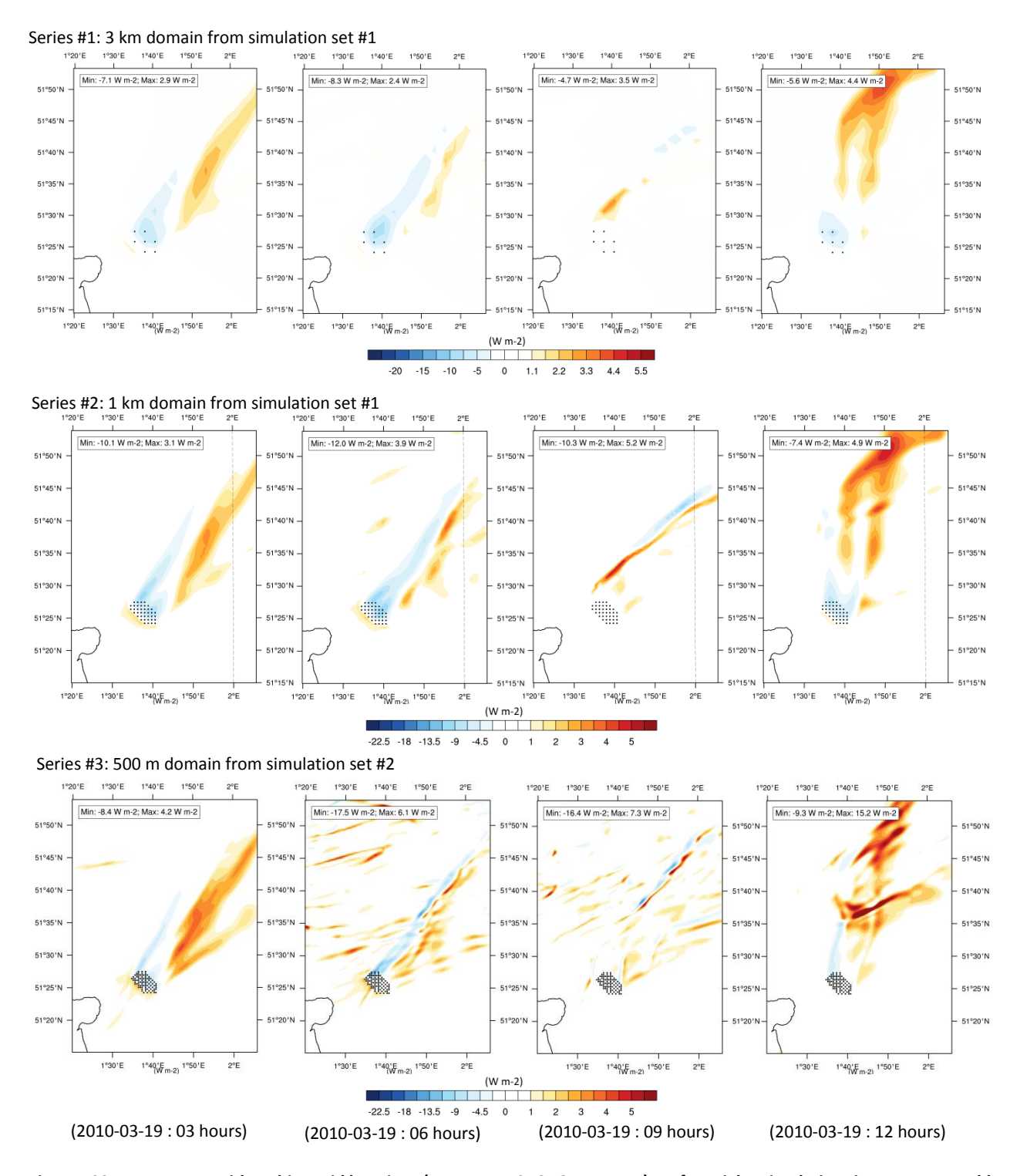


Figure 109: H_{sf} contours with turbine grid locations (FARM – BACKGROUND case) . Left to right: simulation times yyyy-mm-dd: hh. Series #1: 3 km domain from simulation set #1. Series #2: 1 km domain from simulation set #1. Series #3: 500 m domain from simulation set #2.

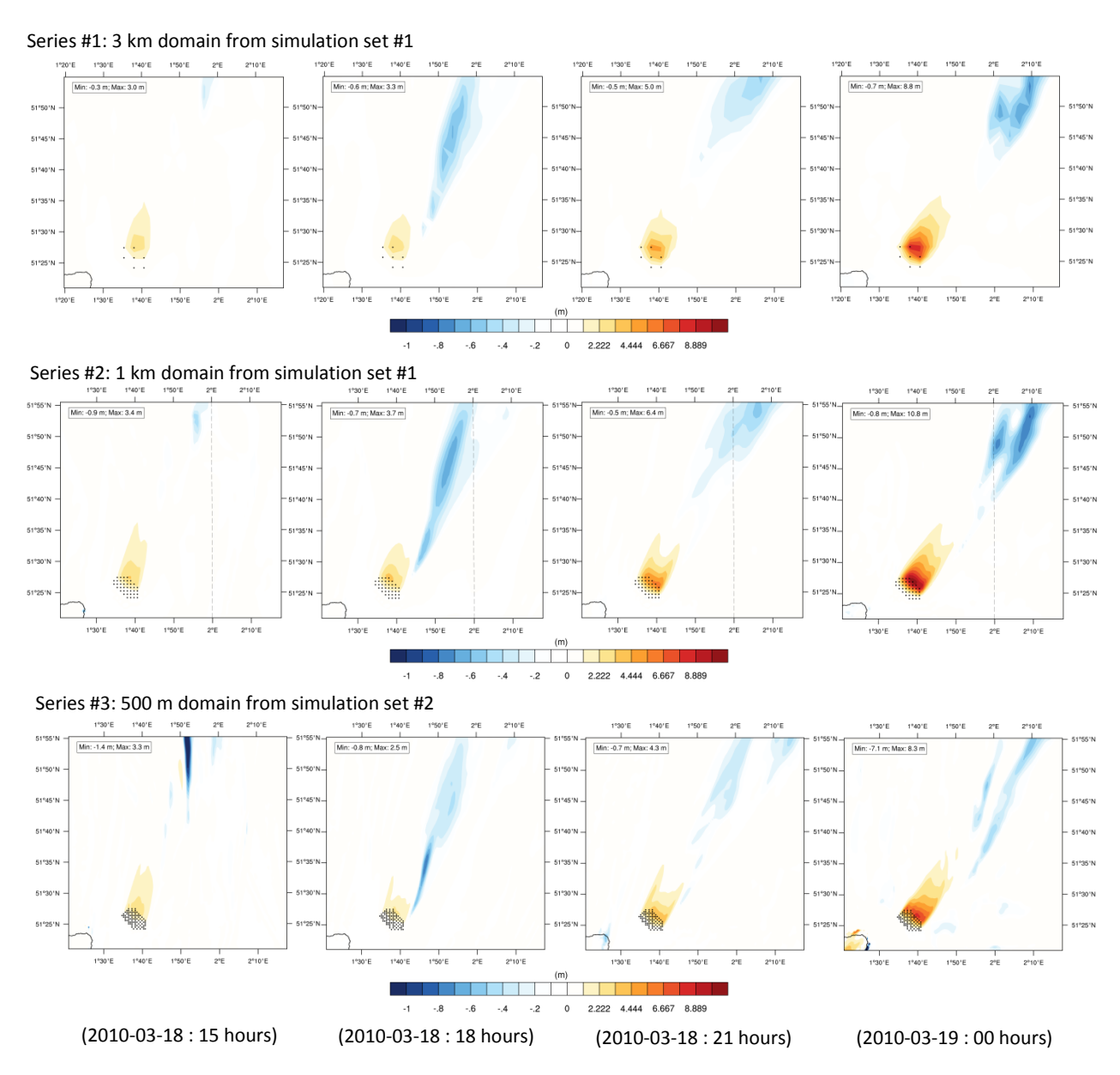


Figure 110: PBLH contours with turbine grid locations (FARM – BACKGROUND case) . Left to right: simulation times yyyy-mmdd: hh. Series #1: 3 km domain from simulation set #1. Series #2: 1 km domain from simulation set #1. Series #3: 500 m domain from simulation set #2.

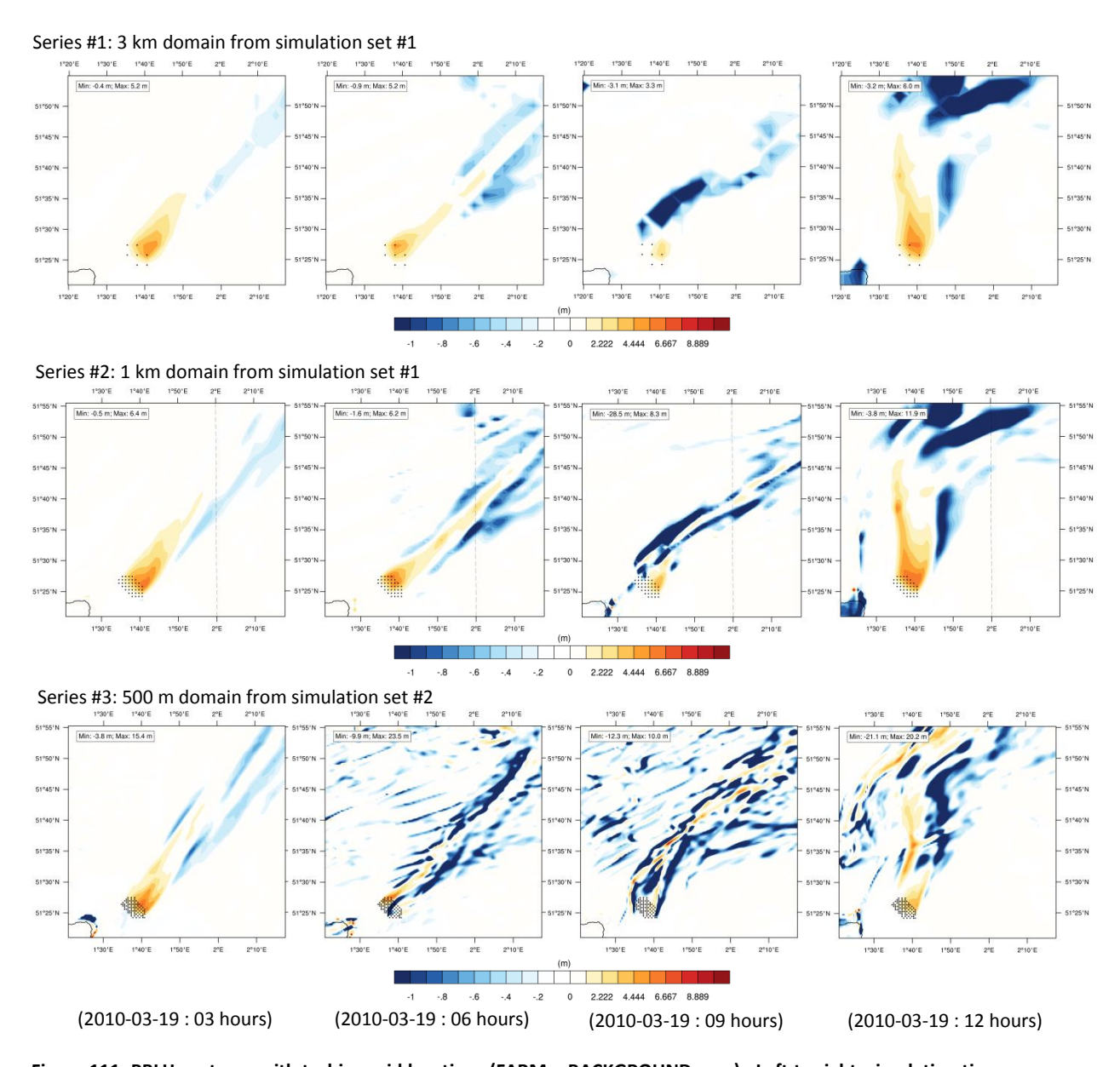


Figure 111: PBLH contours with turbine grid locations (FARM – BACKGROUND case) . Left to right: simulation times yyyy-mmdd: hh. Series #1: 3 km domain from simulation set #1. Series #2: 1 km domain from simulation set #1. Series #3: 500 m domain from simulation set #2.

Appendix-C. Information on Middelgrunden

This section contains general information on the MIDD offshore wind farm and additional results from the WRF simulations performed at MeteoGroup. Information from the MIDD offshore wind farm was collected from public sources, and no private right is to be derived from them. Turbine and Farm information can be found in the following web sites:

http://www.lorc.dk/offshore-wind-farms-map/middelgrunden

http://www.middelgrunden.dk/middelgrunden/?q=en/node/35

The next tables summarize the general information regarding the farm site, and location of turbine on the simulation domains. Additional plots of TKE and wind speed contours are given at the end.

Table 24: Thanet offshore wind farm configuration and general information.

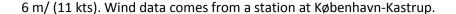
		A 6 6 11	
Location		Array Configuration	
Name	Middelgrunden Offshore Wind Farm	Not Uniform	Slightly curved
Phase	Commissioned	Number of rows	1
Location	Amager	Number of Columns	
Region	Copenhagen, Sjaelland	Number of Turbines	20
Country	England / U.K	Inline turbine spacing	184 m
Sea	The Sound	Between row spacing	
GPS Latitude	55.6909	Composition overview	
GPS Longitude	12.6708	(Number of rows/	1
Distance to Shore	2 km	turbines per row)	20
Water Depth	3 - 5 m		
Turbine Description ar	nd Energy Production	Annual Productions:	
Farm Power	40 MW	2009	92.3 GWh
Turbine Power	2 MW	2010	89.34 GWh
Turbine	Bonus 2M/76	2011	88.43 GWh
Rotor diameter	76 m	2012	90.74 GWh
Hub height	64 m	Historic Mean	89 GWh/yr.
Cut in speed (V_{in})	3 m/s	Annual mean speed	8.76 m/s
Cut out speed (V_{out})	25 m/s	10-yr mean (2000-2010)	10.06 m/s
Rated speed	15 m/s		

C-1. Site and Conditions of Middelgrunden

Located in Øresund between Denmark and Sweden, MIDD sets 2 km east of the Copenhagen harbor [80]. The main wind direction is from the south west with a wide distribution in that quadrant, and a prevailing wind from the east as well. For the simulation period that uses ERA-Interim data for the beginning of April, the transition from westerly winds to SE winds is captured. The wind rose of April indicates prevailing winds from the southwest: average magnitude of



Figure 112: Middelgrunden Offshore Wind Farm. Picture from Google Earth.



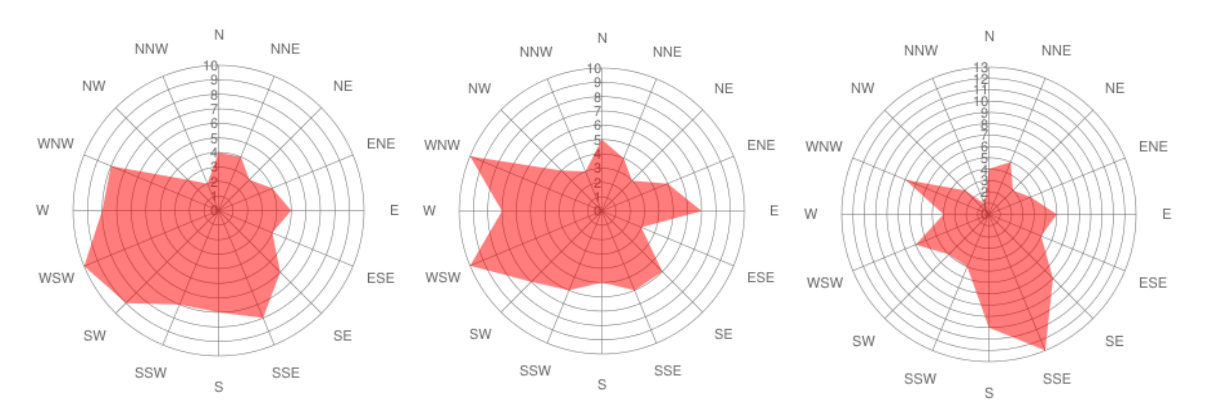


Figure 113: Wind roses for Middelgrunden site: Annual wind rose (left), for the period of March (middle), and for the period of April (right). All data from 2001-2014 from www.windfinder.com

Information on met mast of MIDD is better described by K.S Hansen from DTU [81], a ns is partially presented here for information purposes only. The meteorological mast was established in 1997 to provide turbulence characteristics for wind resources assessment on the wind farm to be built in 2000. The mast is located at 55° 42.1 North, 12° 39.45 East, and has a height of 50 m. All cup anemometers are installed on the westerly booms, and wind speed is measured at 10 m, 30 m, and 50 m. Wind speed data at 50 m is used together with wind direction measured at 30 m, at a 5 Hz sampling frequency.

Wind speed is at 30 m, 6 - 9 m/s 68% of the time and 10 - 11 m/s 18%, these wind speed values correspond to turbulence intensities between 0.05 and 0.01 72% of the time, with a highest occurrence at 0.07 (19%). Turbulences higher than 12% are unlikely to occur. As height increases (50 m), the low aerodynamic roughness of the site (z_0 = 0.03 m [30]) makes winds of 8 -9 m/s most often. According to the met mast measurements wind is most frequent from the south but almost even from the SE and SW directions. In contrast to the wind roses provided earlier for the 2001-2014 period in Figure 113. The met mast falls short, mostly because it was operational for few years only. The next plots illustrate probability distributions measurements form the met mast at different heights.

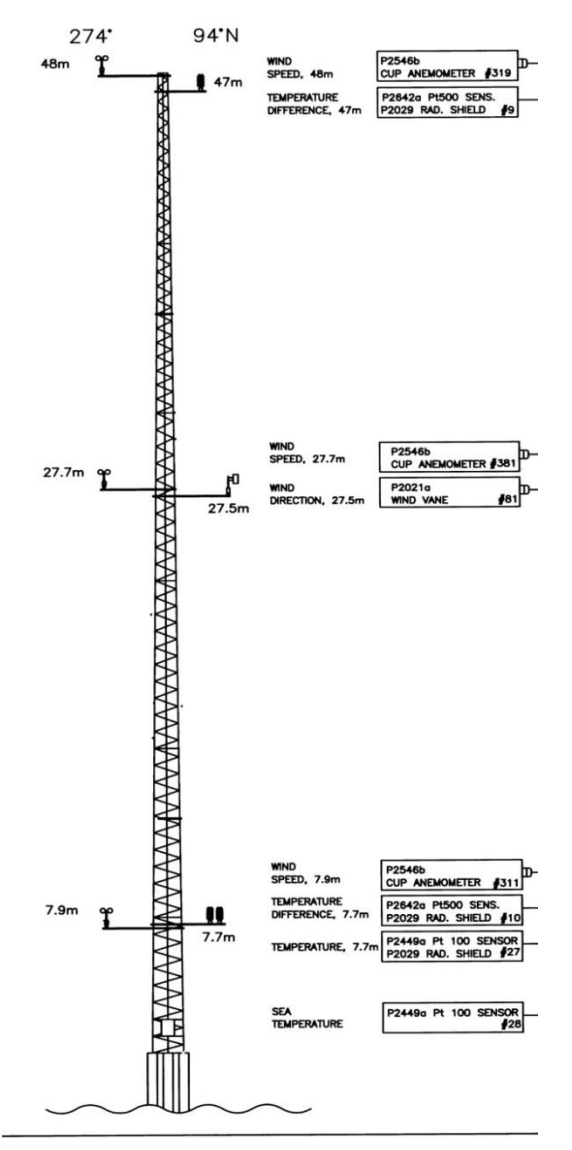


Figure 114: Meteological mast layout [79].

Master of Science Thesis A.M. Striedinger P.

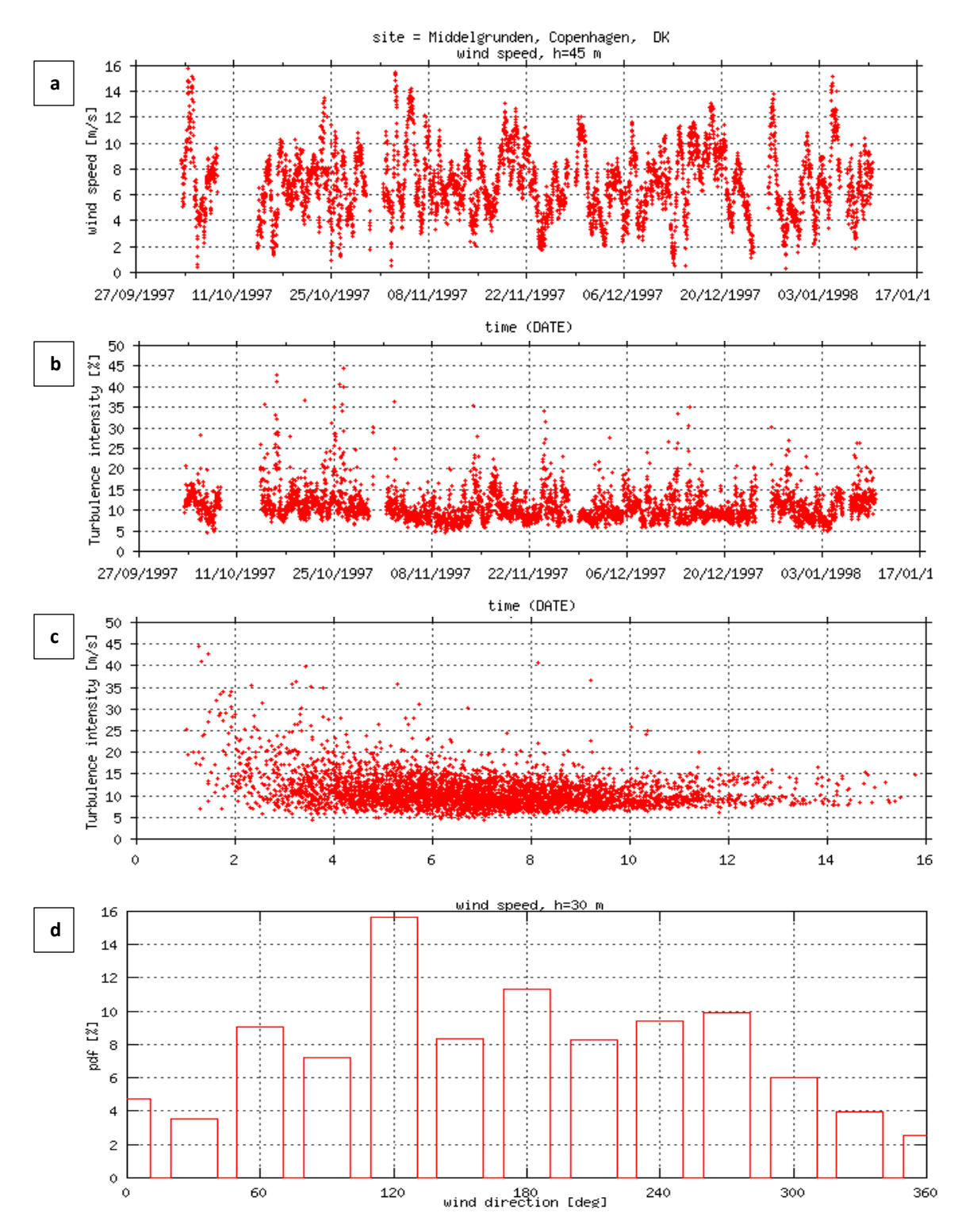


Figure 115: Sactter widn speed for different dates (a), scatter turbulence intensity for different dates (b), scatter turbuelnce intsnity with respect to wind speed at 45 m (c), and wind direction histogram at 30 m heihgt (d). Raw data is extacted from [80]. All plots are met mast measurements.

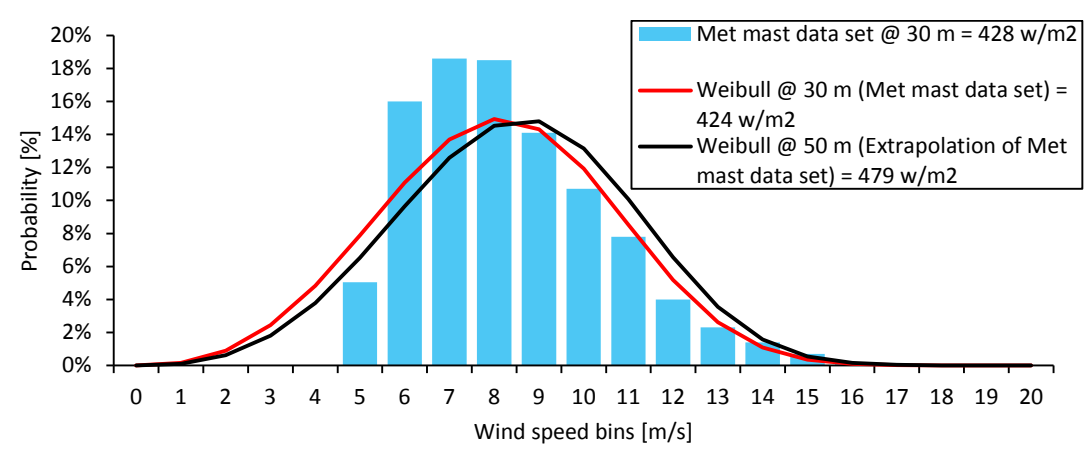


Figure 116: Extrapolation of wind speed distribution from 30 m to 50 m using z_0 of 0.03 m. Weibull fits are shown.

Turbulence intensity is also extracted from the data sets for the validation and from the WRF simulations. Nevertheless, it is not a direct measurement contain within the data set, it has to be derived from other variables. Additionally, to represent the frees stream, data from turbines in the deep array cannot be used, only data from the south and north turbine are used according to the methodology established in Chapter-5, and section 5.2. Basically the use of turbine data implies that the predicted turbulence of the free stream is higher than in reality as it includes effects of the added turbulence intensity by the north and /or south turbines; see Figure 117. It was found during the simulations that the turbulence intensity was barely higher than 0.2 for wind speed higher than 4 m/s; see Figure 118.

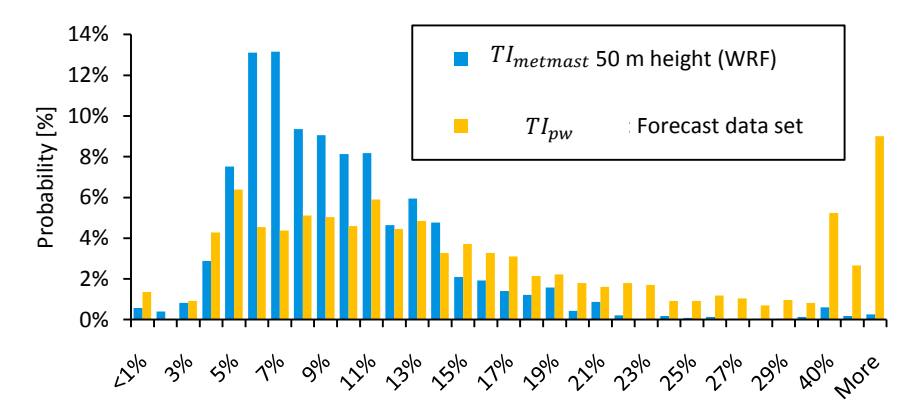


Figure 117: Probability distribution of turbulence intensity of the free stream from the Forecast data set, and from the simulations in WRF.

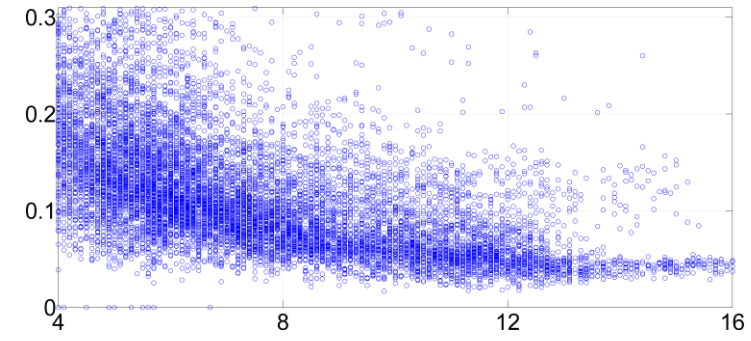


Figure 118: Zoom in turbulence intensity with respect to wind speed from WRF simulations at met mast location, 50 m height.

Master of Science Thesis A.M. Striedinger P.

By removing all cases of turbulence intensity higher than 0.2 from the data set, we can isolate the cases for lower turbulence intensity in the free stream, and compare them to the results obtain form simulations. The comparison is shown in Figure 119, and it both distributions are remarkably similar. Thus, this comparison verifies that the method used for TI_{pw} is at least theoretically correct (or according to the physical schemes in WRF, and input data); see Figure 119.

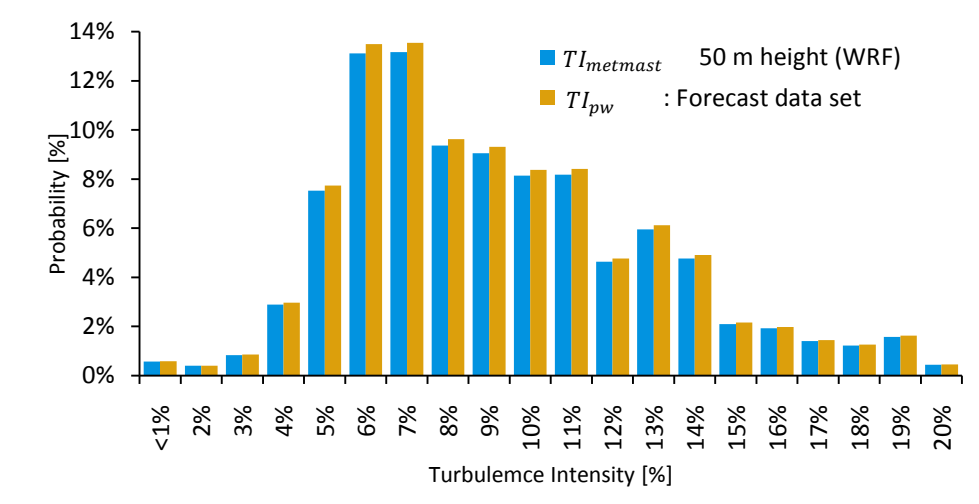


Figure 119: Probability distribution of turbulence intensity from forecast data set, and from simulations. The data set has been filtered to avoid readings from added turbulence due to the turbines.

C-2. Calculation of Turbulence Intensity from Turbine Data

Turbulence intensity is deduced from turbine power data in order to have an approximation of the free stream conditions when direct measurements of the free stream are not available. Under such cases the fluctuations of the active power are related to the fluctuations of wind speed through the rotor. More specifically, it is a direct relation of the changes in lift distribution along the blades, to the variations in the output torque. Neglecting, this relation is circumvented by using the momentum approach, with power as $P=0.5\rho C_p A_{rot} V^3$, and so is its standard deviation: $\sigma_p \propto \rho C_p A_{rot} (V^3-V_{avg}^3)$. The following formulation and steps express the previous σ_p relation.

$$\frac{\sigma_p}{P_{avg}} = \frac{\sqrt{\frac{1}{N} \sum \left(P' - P_{avg}\right)^2}}{P_{avg}}$$

Equation 51: Definition of standard deviation.

Using manufacturer data on c_p coefficients, $rac{\sigma_p}{P_{ava}}$ is redefined with the equation of P as :

$$\frac{\sigma_{p}}{P_{avg}} = \frac{\sqrt{\frac{1}{N}\sum_{i}^{N}\left(\frac{1}{2}c_{p(i)}\rho A_{rot}V_{i}^{3} - \frac{1}{2}c_{p(o)}\rho A_{rot}V_{avg}^{3}\right)^{2}}}{\frac{1}{2}c_{p(o)}\rho A_{rot}V_{avg}^{3}}$$

Equation 52: Standard deviation of power generation from a time series.

Where V_{ava} does not represent the average wind speed in the time series, but rather the average wind speed that would produce P_{avg} , and $c_{p(o)}$ is the power coefficient yielding this power. Each wind speed in the series is noted as V_i . But for short time series, V_{avg} may yield P_{avg} . This is the case or rather the assumption when analysis the commonly used 10 min wind speed average. On WRF the output is set every 10 min, so to use the same approach.

$$\begin{split} \frac{\sigma_{p}}{P_{avg}} &= \frac{\frac{1}{2}\rho A_{rot}\sqrt{\frac{1}{N}\sum_{i}^{N}\left(c_{p(i)}V_{i}^{3} - c_{p(o)}V_{avg}^{3}\right)^{2}}}{\frac{1}{2}c_{p(o)}\rho A_{rot}V_{avg}^{3}} = \frac{\sqrt{\frac{1}{N}\sum_{i}^{N}\left(c_{p(i)}V_{i}^{3} - c_{p(o)}V_{avg}^{3}\right)^{2}}}{c_{p(o)}V_{avg}^{3}} \\ &\frac{\sigma_{p}}{P_{avg}} &= \frac{c_{p(o)}G_{(v,\sigma_{v})}\sqrt{\frac{1}{N}\sum_{i}^{N}\left(V_{i}^{3} - V_{avg}^{3}\right)^{2}}}{c_{p(o)}V_{avg}^{3}} = G_{(v,\sigma_{v})}\left(\frac{\sigma_{(v^{3})}}{V_{avg}^{3}}\right) \end{split}$$

Equation 53: Deviation of power generation as function of wind speed and factor G.

Where the differences between $c_{p(i)}$, and $c_{p(o)}$ in the formulation is accounted for with the introduction of the factor $G_{(v,\sigma_v)}$, as a function of mean wind speed V_{avg} , and the wind deviation σ_v about it. $G_{(v,\sigma_v)}$ may be considered as 1, the variation of $c_{p(i)}$ does not contribute significantly to σ_p (high winds).

$$V_a^3 = V_{avg}^3 - \sigma_{(v^3)}$$

$$V_b^3 = V_{avg}^3 + \sigma_{(v^3)}$$

Equation 54: Boundaries of the mean power generation from wind speed distribution.

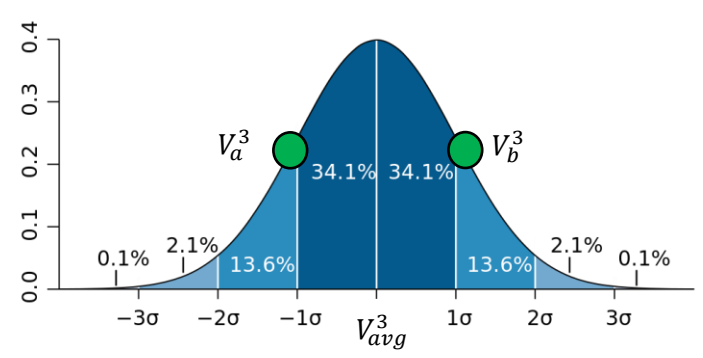


Figure 120: Standard deviation diagram with area coverage in [%]

By definition, any σ establishes a range covering most of the values inside the normal distribution it represents. Such representation is symmetrical, and bounds in this case, $\sigma_{(v^3)}$ to wind speeds V_a , and V_b as in Equation 54 and Figure 120, such that $\sigma_v \neq \sigma_{(v^3)}$. To proceed with the calculation V_b will be used to replace $\sigma_{(v^3)}$ in a numerical sense to produce Equation 55.

$$\frac{\sigma_{p}}{P_{avg}} = G_{(v,\sigma_{v})} \frac{\left(V_{b}^{3} - V_{avg}^{3}\right)}{V_{avg}^{3}} = G_{(v,\sigma_{v})} \frac{\left(V_{b} - V_{avg}\right)\left(V_{b}^{2} + V_{b} \cdot V_{avg} + V_{avg}^{2}\right)}{V_{avg}^{3}}$$

Equation 55: Deviation of power generation as a function of $\boldsymbol{V_b}$.

Turbulence intensity TI_{pow} is defined as $\frac{\sigma_v}{V_{ava}}$, and rewritten into Equation 56. This is the turbulence intensity to be used in further calculations, and is proposed to represent the turbulence intensity in the rotor area. Until this moment, the mathematical expressions are approximations having the next assumptions to be demonstrated:

- lacktriangle The turbulence intensity TI_{pow} based on V_{avg} is to represent the turbulence intensity I_O with wind speed V_{huh}
- lacktriangle The mean power P_{ava} must be a function of the mean wind speed V_{ava}

Basically, the applicability of the model lay in how representative is the mean wind speed with respect to the mean power.

$$\begin{split} \frac{\sigma_p}{P_{avg}} &\cong G_{(V_i,\sigma_v)} * TI_{pow} \frac{\left(V_b^2 + V_b \cdot V_{avg} + V_{avg}^2\right)}{V_{avg}}; \\ for \, F_{(v,TI)} &= \frac{\left(V_b^2 + V_b \cdot V_{avg} + V_{avg}^2\right)}{V_{avg}} = \left[1 + \left(1 + TI_{pow}\right)^2 + 1 + TI_{pow}\right] \\ &\Rightarrow \frac{\sigma_p}{P_{avg}} \cong G_{(v,\sigma_v)} * TI_{pow} * F_{(v,TI)} \end{split}$$

Equation 56: mathematical relation between active power and turbulence intensity.

The factor $F_{(v,TI)}$ is found to be a function of the turbulence intensity. Therefore, the resultant TI_{pow} is found through an iteration process. To speed up the procedure, factor $F_{(v,TI)}$ has been simplified onto a simpler fit, enabling the direct use of Equation 56 without an iteration process. The fit was found in Matlab, and $F_{(v,TI)}$ was found to follow a power-law distribution with V_{avg} (1 m/s to 26 m/s), and directly proportional to TI_{pow} (0.04 to 0.44).

$$F_{(v,TI)} = \frac{a}{V_{avg}} + m(TI_{pow} - 0.04) + c$$

Equation 57: Expression for conversion factor $F_{(v,T)}$. Coefficients $a=1.04,\ c=2.082,\ m=2.67$.

The function coefficients are particular for each turbulence intensity value but they remain nearly constant. Introducing Equation 57 into Equation 56, and taking $G_{(v,\sigma_v)}$ as 1, produces the following quadratic expression.

$$\frac{\sigma_p}{P_{avg}} \cong m \, T I_{pow}^2 + T I_{pow} \left(\frac{a}{V_{avg}} + C - 0.04m \right)$$

Equation 58: Final expression for Turbulence intensity as a function of active power. Coefficients a = 1.04, c = 2.082, m = 2.67.

See Table 25, and Figure 121 for the distribution of $F_{(v,TI)}$. The offset presented in calculating $F_{(v,TI)}$ is shown in Figure 122, where the real actor is defined as $F_{(v,TI)} * (1 + Offset)$.

Table 25: Distribution of factor $F_{(v,TI)}$ as function of turbulence and wind speed: $1+\left(1+TI_{pow}\right)^2+rac{1}{V_{avg}}+rac{TI_{pow}}{V_{avg}}$ 0,31 Vavg / TI 0,04 0,05 0,06 0,1 0,11 0,12 0,13 0,14 0,15 0,16 0,32 0,33 0,34 0,35 0,44 3,41 3,12 3,15 3,31 3,34 3,37 3,44 3,47 3,51 4,03 4,06 4,10 4,14 4,17 1 3,18 4,51 2 2,60 2,63 2,65 2,76 2,79 2,81 2,84 2,87 2,90 2,93 3,37 3,40 3,43 3,47 3,50 3,79 3 2,43 2,45 2,48 2,58 2,60 2,63 2,65 2,68 2,71 2,73 3,15 3,18 3,21 3,24 3,27 3,55 4 2,34 2,37 2,51 2,53 2,56 2,58 2,61 2,64 3,04 3,07 3,10 2,39 2,49 3,13 3,16 3,43 5 2,29 2,31 2,34 2,43 2,45 2,48 2,50 2,53 2,55 2,58 2,98 3,01 3,03 3,06 3,09 3,36 2,25 2,28 2,30 2,39 2,42 2,44 2,47 2,49 2,51 2,54 2,93 2,96 2,99 3,02 3,05 3,31 6 2,23 2,25 2,28 2,37 2,39 2,44 2,46 2,49 2,90 2,93 2,99 7 2,41 2,51 2,96 3,02 3,28 2,42 2,47 2,49 8 2,21 2,23 2,35 2,37 2,39 2,44 2,88 2,91 2,94 2,96 2,99 2,26 3,25 2,33 9 2,20 2,22 2,24 2,36 2,38 2,40 2,43 2,45 2,47 2,86 2,89 2,94 2,97 2,92 3,23 10 2,19 2,21 2,23 2,32 2,34 2,37 2,39 2,41 2,44 2,46 2,85 2,87 2,90 2,93 2,96 3,22 11 2,20 2,36 2,40 2,18 2,22 2,31 2,33 2,38 2,43 2,45 2,84 2,86 2,89 2,92 2,95 3,20 2,21 2,30 2,17 2,19 2,32 2,35 2,37 2,39 2,42 2,44 2,83 2,85 2,91 2,94 12 2,88 3,19 2,32 2,39 2,82 2,90 13 2,16 2,18 2,21 2,29 2,34 2,36 2,41 2,43 2,84 2,87 2,93 3,18 2,29 2,31 2,38 2,81 2,92 2,16 2,18 2,20 2,33 2,36 2,40 2,43 2,84 2,86 2,89 14 3,18 2,31 2,38 15 2,15 2,17 2,19 2,28 2,33 2,35 2,40 2,42 2,80 2,83 2,86 2,88 2,91 3,17 16 2,15 2,17 2,19 2,28 2,30 2,32 2,35 2,37 2,39 2,42 2,80 2,82 2,85 2,88 2,91 3,16 2,14 2,27 2,30 2,32 2,34 2,37 2,41 2,79 2,82 2,90 17 2,16 2,19 2,39 2,85 2,87 3,16 18 2,14 2,16 2,18 2,27 2,29 2,32 2,34 2,36 2,39 2,41 2,79 2,82 2,84 2,87 2,90 3,15 19 2,14 2,16 2,18 2,27 2,29 2,31 2,34 2,36 2,38 2,41 2,79 2,81 2,84 2,87 2,89 3,15 2,29 2,31 2,33 2,36 2,78 2,89 20 2,13 2,16 2,18 2,27 2,38 2,40 2,81 2,84 2,86 3,15 21 2,13 2,15 2,17 2,26 2,28 2,31 2,33 2,35 2,38 2,40 2,78 2,81 2,83 2,86 2,89 3,14 22 2,13 2,15 2,17 2,26 2,28 2,31 2,33 2,35 2,37 2,40 2,78 2,80 2,83 2,86 2,88 3,14 23 2,13 2,15 2,17 2,28 2,30 2,33 2,35 2,37 2,40 2,77 2,80 2,83 2,85 2,88 2,26 3,14 24 2,12 2,15 2,17 2,26 2,28 2,30 2,32 2,35 2,37 2,39 2,77 2,80 2,82 2,85 2,88 3,13 25 2,12 2,14 2,17 2,25 2,28 2,30 2,32 2,35 2,37 2,39 2,77 2,80 2,82 2,85 2,88 3,13 2,12 2,14 2,25 2,27 2,32 2,34 2,37 2,77 2,79 2,82 2,85 2,87 26 2,16 2,30 2,39 3,13

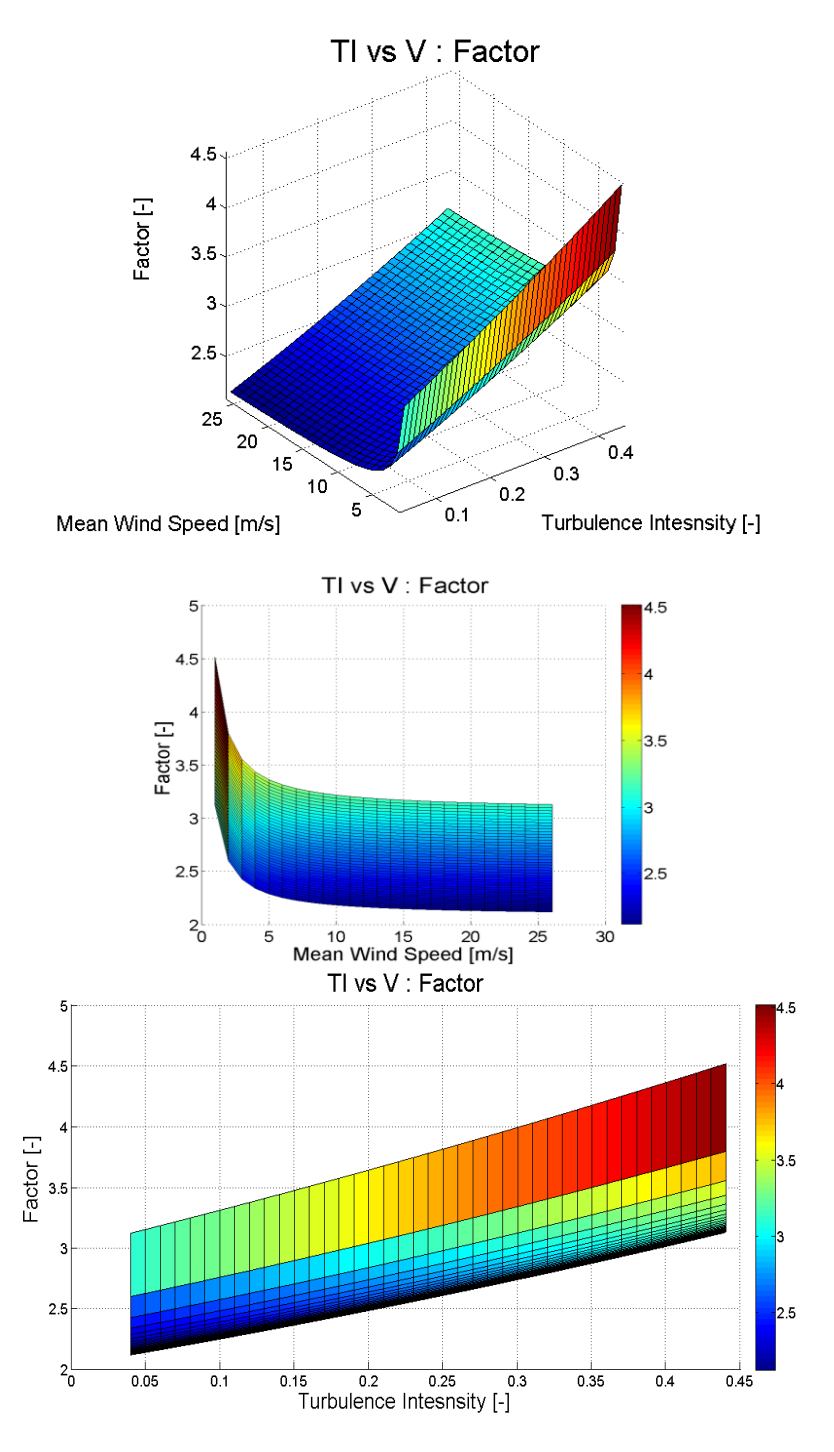


Figure 121: Factor $F_{(v,TI)}$ behavior with wind speed and turbulence intensity from Equation 56. The power –law distribution is seen on the left, and the linear relation on the right. Linear approach takes the slope into account to extrapolate the results of the power-law distribution to higher values of turbulence intensity: TI > 0.04.

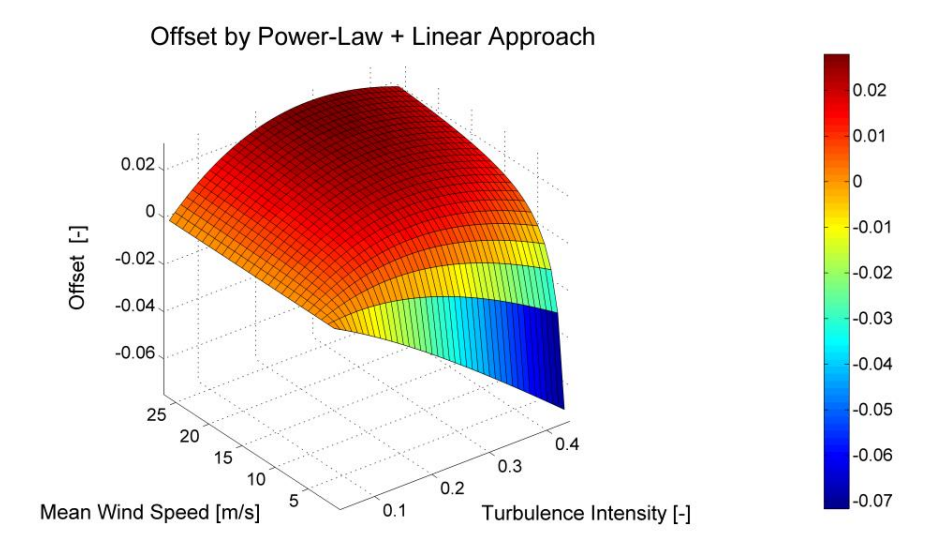


Figure 122: Resultant offset by using the power-law + linear distribution. Positive Offset indicate overestimation in the Factor, and negative Offset indicates underestimation of the Factor.

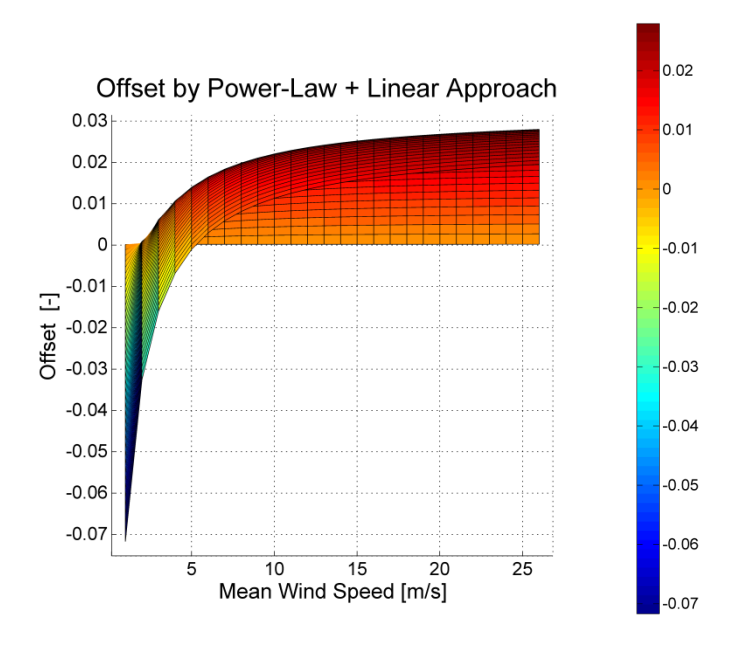


Figure 123: Resultant offset by using the power-law + linear distribution. Positive Offset indicate overestimation in the Factor, and negative Offset indicates underestimation of the Factor.

The factor $F_{(v,TI)}$, underestimates TI_{pow} at winds speeds lower than 5 m/s, specially at high values of turbulence intensity. Above 5 m/s, $F_{(v,TI)}$ overestimates TI_{pow} with by a maximum of 2 %. More can be said on the error distribution of $F_{(v,TI)}$ with respect to the exact solution of the method here presented. But how accurate the method is, is really established by the factor $G_{(v,\sigma_v)}$. It was presented before that $G_{(v,\sigma_v)}$ is affected by the variation in c_p due to σ_v in a short time series. Hence, $G_{(v,\sigma_v)}$ also depends on the turbulence intensity TI_{pow} . An option to evaluate $G_{(v,\sigma_v)}$ is to implement Equation 53 on the power curve of a wind turbine; for example, the AN Bonus 2 MW-76 installed in MIDD.

Master of Science Thesis A.M. Striedinger P.

First, calculate the relative change of V^3 due to a change δ in wind speed (i.e. $\frac{+}{2}$ 1 m/s), around each wind speed bin over the power curve of the turbine (i.e. V_{in} , 4 , 5, 6, $\cdots V_{out}$). If δ is considered as the standard deviation σ_v of wind speed around a V_{avg} equal the speed bin, the change of V^3 could be considered as the standard deviation $\sigma_{(v^3)}$. Normalizing it, would produce $\frac{\sigma_{(v^3)}}{V_{ava}^3}$. Second, calculate the analogous σ_p , and $\frac{\sigma_{(p)}}{P_{avg}}$ corresponding to δ on each bin. As a consequence, $\frac{\sigma_{(v^3)}}{V_{avg}^3}$ and $\frac{\sigma_{(p)}}{P_{avg}}$ are now associated to some turbulence intensity values of $\frac{\sigma_v}{V_{ava}}$, or namely an approximation of TI_{pow} . In the process, $G_{(v,\sigma_v)}$ is obtained. The next table and plots are illustrated for an approximated σ_v of 1m/s.

Table 26: Approximation of $G_{(v,\sigma_v)}$ through imposed changes in wind speed over the power curve of the AN Bonus 2 MW-76 wind turbine for MIDD, with 1 m/s bins.

V_{avg}	C_p	V_{avg}^3	$\sigma_{(v^3)}$	$\frac{\sigma_{(v^3)}}{V_{avg}^3}$	P_{avg}	σ_p	$rac{oldsymbol{\sigma}_{(p)}}{oldsymbol{P}_{avg}}$	$\left(\frac{\sigma_{(p)}}{P_{avg}} - \frac{\sigma_{(v^3)}}{V_{avg}^3}\right)$	$\frac{\delta}{V_{avg}}$	$G_{(v,\sigma_v)}$
[m/s]	[-]	[m ³ /s ³]	[m ³ /s ³]	[%]	[kW]	[kW]	[%]	[%]	[-]	[-]
4	0.311535	64	49	76.6%	55.4	58.60	105.8%	29.2%	0.250	1.382
5	0.365078	125	76	60.8%	126.8	84.50	66.6%	5.8%	0.200	1.096
6	0.373892	216	109	50.5%	224.4	137.05	61.1%	10.6%	0.167	1.210
:	:	:	÷	:	:	÷	÷	÷	:	÷
20	0.089974	8000	1201	15.0%	2000	5.97E-07	0.0%	-15.0%	0.050	0.000
21	0.077723	9261	1324	14.3%	2000	7.62E-07	0.0%	-14.3%	0.048	0.000
22	0.067599	10648	1453	13.6%	2000	1.59E-06	0.0%	-13.6%	0.045	0.000
:	:	:	:	:	÷	:	:	:	÷	÷

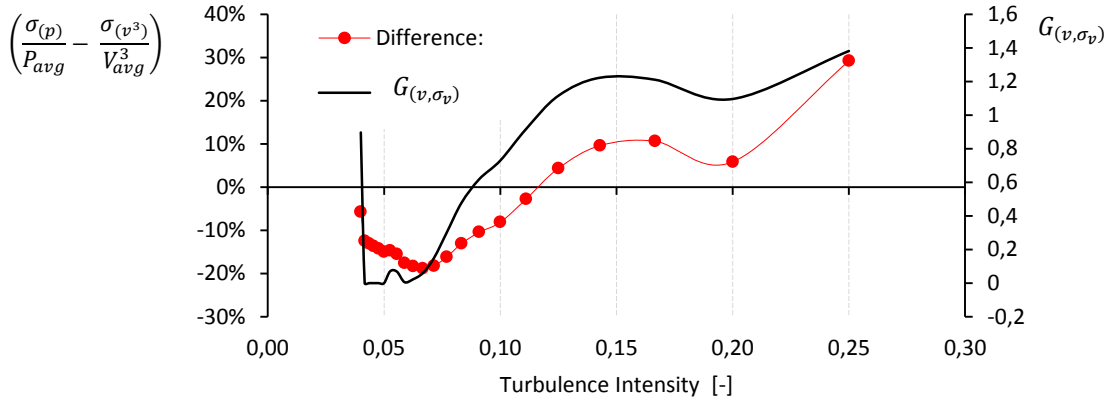


Figure 124: Approximation of $G_{(v,\sigma_v)}$, and $\left(\frac{\sigma_{(p)}}{p_{avg}}-\frac{\sigma_{(v^3)}}{v_{ava}^3}\right)$ over the power curve with 1 m/s bins.

Figure 124 indicates that at speeds less than 8 m/s, $G_{(v,\sigma_v)}$ is more than 1, and hence TI_{pow} is overestimated. This is the case when the predicted TI_{pow} is more than 0.125. For $G_{(v,\sigma_v)}$ less than 1, the opposite occurs. Therefore, $G_{(v,\sigma_n)}$ and $F_{(v,TI)}$ compensate one another in most cases for the AN Bonus 2 MW-76 wind turbine. The plots also show why the method is not to be used near V_{out} , as the change in nominal power cannot be accounted for. In reality, the method should not be used for $V > V_{rated}$ because at that speed the power becomes nominal regardless of the increase in wind, and $\sigma_{(p)}$ is zero.

C-3. Data scattering from the sample data and from WRF

A comparison on maximum efficiency: based on maximum unit power, regardless of position. It is WT20 or WT01 for WRF, but often times max power is found at WT10,WT15, for Data sample. Wind speeds between 50° and 70° were on that frequent in either simulation or the data set. This is clear in Figure 125. In addition, some efficiencies derived from the data set were much higher than 2, some even reaching 100 or more. These were cases for which neither turbine was representative for the free stream but were rather in the wake. This is an indirect consequences of using turbine data only to derived the free stream. Nevertheless less these cases were around 5.

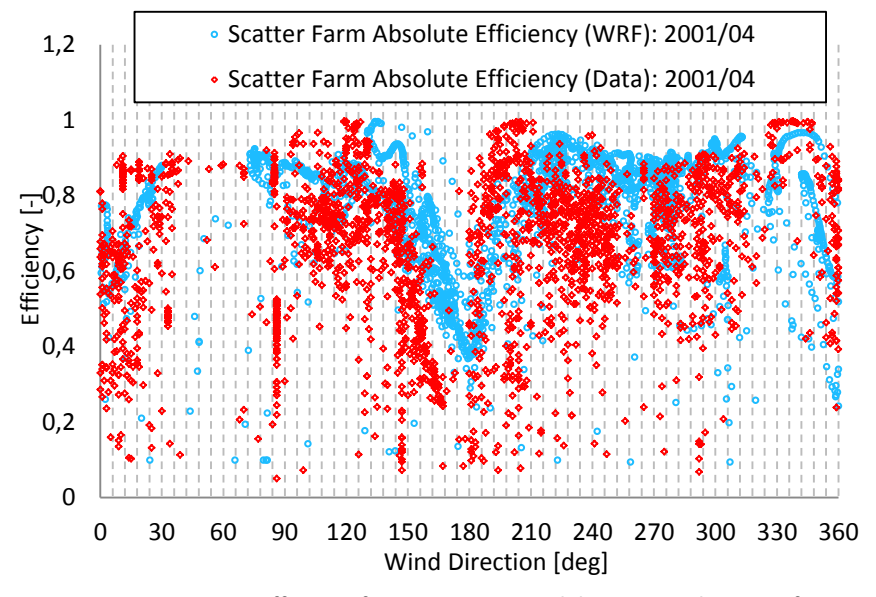


Figure 125: Farm efficiency from Case 2 vs. wind direction in the MIDD farm.

C-4. Input File to WRF

The next is the input file that contains the turbine information about MIDD. It Additionally contains information to be used on the proposed parameterization. If used for the Fitch scheme under WRF, the code will ignore the additional variables. The additional variables are Curve, V_{vaw} , Yaw_init, and Blades. S1 and S2 are the same as in Frandsen's formulation. The power curve parameters like ap, and rpm are also additional.

!Power_Curves= specific !no_cp_curves= 1 !*-----Wind Turbine input data for WRF-----!*Wind Farm: Middelgrunden Offshore *******GPS Latitude: 55.6909 !*Location: Amager, Denmark (Copenhagen, Sjaelland)*GPS Longitude: 12.6708

Master of Science Thesis A.M. Striedinger P.

```
!*Distance From Shore: 2 km approx. (3-5) km water depth
!* Number of Turbines: 20 turbines (single row) Boomerang shape
!* Turbine Name and Rating: 2 MW Bonus wind turbines
!* Spacing: 2.4 D ~ 154 m ( low!!!)
!id Lat Lon Hub Dia Ct(o) Power Cut-in Cut-out Curve V_ya
w S1 S2 Yaw init Blades
4\,55.70682985\,12.66837293\,60.000\,76.000\,0.1590000\,2.000000\,3.00000\,25.00000\,1\,0.6000
2,4000 24,00 62,5000 3
4 55.70520569 12.66885758 60.000 76.000 0.1590000 2.000000 3.00000 25.00000 1 0.6000
2.4000 24.00 62.5000 3
4 55.70358343 12.66927868 60.000 76.000 0.1590000 2.000000 3.00000 25.00000 1 0.6000
2.4000 24.00 68.0000 3
4 55.70195365 12.66965126 60.000 76.000 0.1590000 2.000000 3.00000 25.00000 1 0.6000
2.4000 24.00 63.0000 3
4 55.70032577 12.66996031 60.000 76.000 0.1590000 2.000000 3.00000 25.00000 1 0.6000
2.4000 24.00 59.0000 3
4\ 55.69868987\ 12.67023673\ 60.000\ 76.000\ 0.1590000\ 2.000000\ 3.00000\ 25.00000\ 1\ 0.6000
2.4000 24.00 52.0000 3
4 55.69704692 12.67044878 60.000 76.000 0.1590000 2.000000 3.00000 25.00000 1 0.6000
2.4000 24.00 75.0000 3
4 55.69540588 12.67059732 60.000 76.000 0.1590000 2.000000 3.00000 25.00000 1 0.6000
2.4000 24.00 64.0000 3
4 55.6937658 12.67071409 60.000 76.000 0.1590000 2.000000 3.00000 25.00000 1 0.6000
2.4000 24.00 62.0000 3
4 55.69212762 12.67076735 60.000 76.000 0.1590000 2.000000 3.00000 25.00000 1 0.6000
2.4000 24.00 76.0000 3
4 55.69048239 12.67075628 60.000 76.000 0.1590000 2.000000 3.00000 25.00000 1 0.6000
2.4000 24.00 62.0000 3
4\ 55.68883811\ 12.67071346\ 60.000\ 76.000\ 0.1590000\ 2.000000\ 3.00000\ 25.00000\ 1\ 0.6000
2.4000 24.00 62.0000 3
4 55.68719575 12.67060715 60.000 76.000 0.1590000 2.000000 3.00000 25.00000 1 0.6000
2,4000 24,00 58,0000 3
4\,55.68555529\,12.67043737\,60.000\,76.000\,0.1590000\,2.000000\,3.00000\,25.00000\,1\,0.6000
2.4000 24.00 68.0000 3
4 55.68391578 12.67023586 60.000 76.000 0.1590000 2.000000 3.00000 25.00000 1 0.6000
2.4000 24.00 57.0000 3
4 55.68228715 12.66997173 60.000 76.000 0.1590000 2.000000 3.00000 25.00000 1 0.6000
2,4000 24,00 39,0000 3
4\,55.68065147\,12.6696433\,60.000\,76.000\,0.1590000\,2.000000\,3.00000\,25.00000\,1\,0.6000
2.4000 24.00 64.0000 3
4 55.6790257 12.669284 60.000 76.000 0.1590000 2.000000 3.00000 25.00000 1 0.6000
2.4000 24.00 65.0000 3
4\,55.67739287\,12.66886042\,60.000\,76.000\,0.1590000\,2.000000\,3.00000\,25.00000\,1\,0.6000
2.4000 24.00 61.0000 3
4 55.67577988 12.66837508 60.000 76.000 0.1590000 2.000000 3.00000 25.00000 1 0.6000
2.4000 24.00 76.0000 3
!Power Curve for MIDD
!-----Power curve starts from cut-in wind speed: !!!!!!!!!!
!Make sure it is the same as in turbine input file
!Make sure the cut-in and cut-out wind speeds in this file match the speeds
!declared in the turbine data
!Organize the matrix in an ascending order.
!Turbine : 2mW Bonus Wind Turbine
!Data Source: Virtual wakes lab
!Read as: v, cp, ct
!Curve_num = 1
I# 1
!V Cp Ct ap rpm
3 0.1279629696 0.159292000 0.034304027 10.26363636
4 0.3115348468 0.856195000 0.095118015 10.8
5 0.3650783521 0.858407000 0.117080254 11.33636364
6 0.3738918017 0.809735000 0.120970371 11.87272727
```

7 0.4206479505 0.851770000 0.143278967 12.40909091 8 0.4550011424 0.869469000 0.161969273 12.94545455

```
9\,0.4665810283\,0.809735000\,0.168854756\,13.48181818
10 0.4418081478 0.756637000 0.154510109 14.01818182
11 0.4012662992 0.600078466000 0.133657922 14.55454545
12 0.3601457795 0.585546000 0.114940617 15.09090909
13 0.3109814680 0.511799000 0.094904203 15.62727273
14 0.2612786175 0.438053000 0.076607481 16.16363636
15 0.2159588383 0.383481000 0.061267034 16.7
16 0.1792889369 0.336283000 0.049625562 16.94
17 0.1496355092 0.299410000 0.040645905 17.18
18 0.1261733640 0.268437000 0.033788025 17.42
19 0.1049412019 0.243363000 0.027754534 17.66
20 0.0899739630 0.222714000 0.023593647 17.9
21 0.0777228921 0.206490000 0.020241841 18.14
22 0.0675987701 0.193215000 0.017507255 18.38
23 0.0591593411 0.178466000 0.015251388 18.62
24 0.0520682656 0.169617000 0.013372313 18.86
25 0.0460666690 0.157817000 0.011793186 19.1
```

After successfully declaring the turbine locations, the resultant grid configuration is presented in Table 27, and applies to the preliminary validation of WRF turbine parameterization with Fitch scheme. Data described as: (grid points) = (i,j) - Number of Turbine units. Example: Turbine Designation in grid point settings: $(i,j) = (12, 19) - 2 \mid WTXX = 19, 20$, where 19, and 20 represent turbine number designations.

Table 27: Grid locations of MIDD turbines (West-East, South-North) coordinate system in (I,j)

(13, 19) 1 WTXX = 18
(14, 19) 2 WTXX = 16, 17
(15, 19) 2 WTXX = 14, 15
(16, 19) 1 WTXX = 13
(17, 19) 2 WTXX = 11, 12
(18, 19) 2 WTXX = 09, 10
(19, 19) 1 WTXX = 08
(20, 19) 2 WTXX = 06, 07
(20, 19) 2 WTXX = 06, 07
(21, 19) 2 WTXX = 04, 05
(22, 19) 1 WTXX = 03
(23, 19) 2 WTXX = 01, 02

C-5. Reanalysis time series examples

The Following figures provide the prediction of power and hub wind speed of few turbines in the Middelgrunden offshore wind farm. The prediction is really a Reanalysis with ERA-Interim model input data. The result are compared to the measured data from the wind farm for the reanalysis period. Measurements for comparison are provided by Middelgrundens Vindmollelaug through the Indiana Virtual Wake Lab. Information comes with no support.

Master of Science Thesis A.M. Striedinger P.

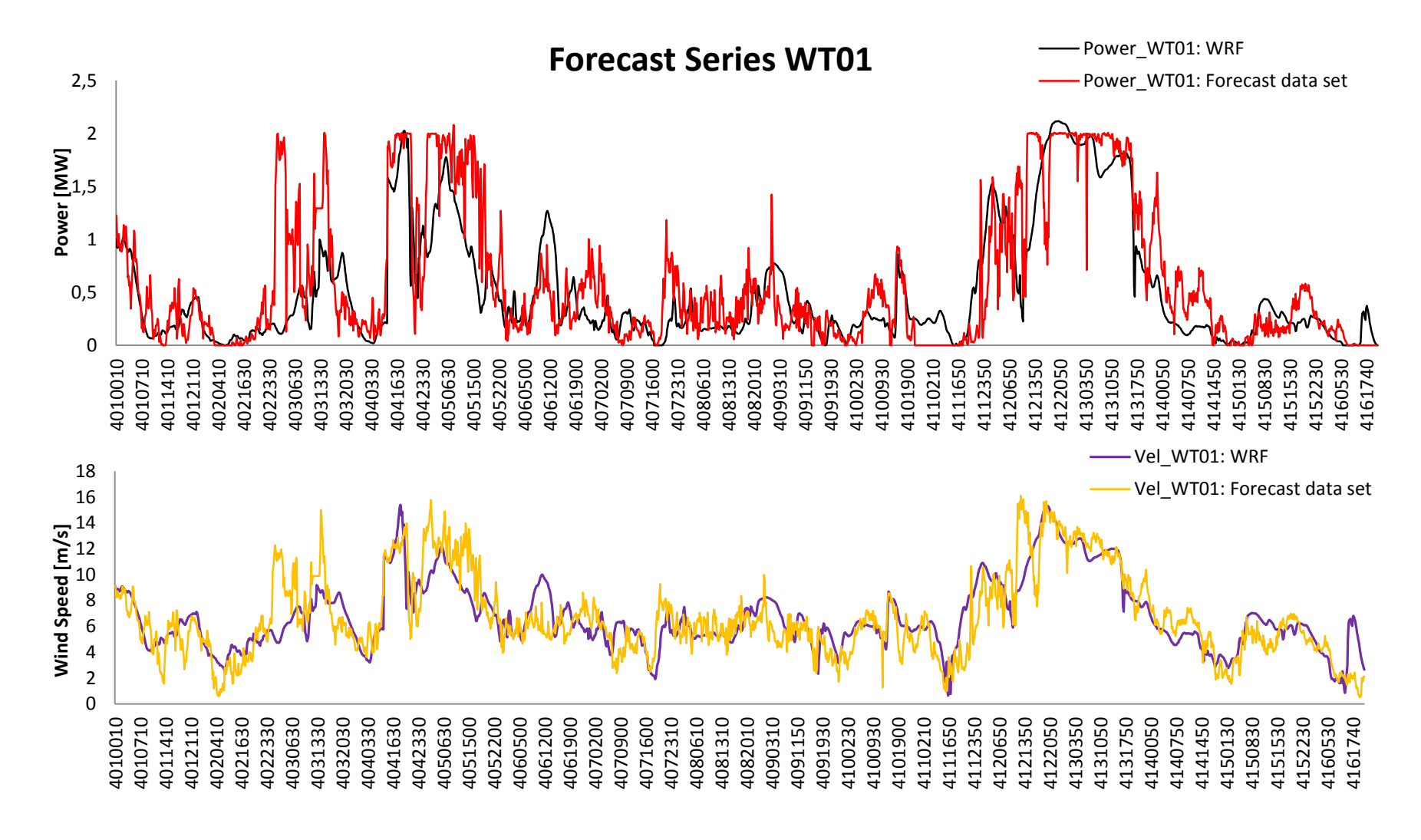


Figure 126: Reanalysis time series of total turbine power output and wind speed for turbine WT01: North turbine.

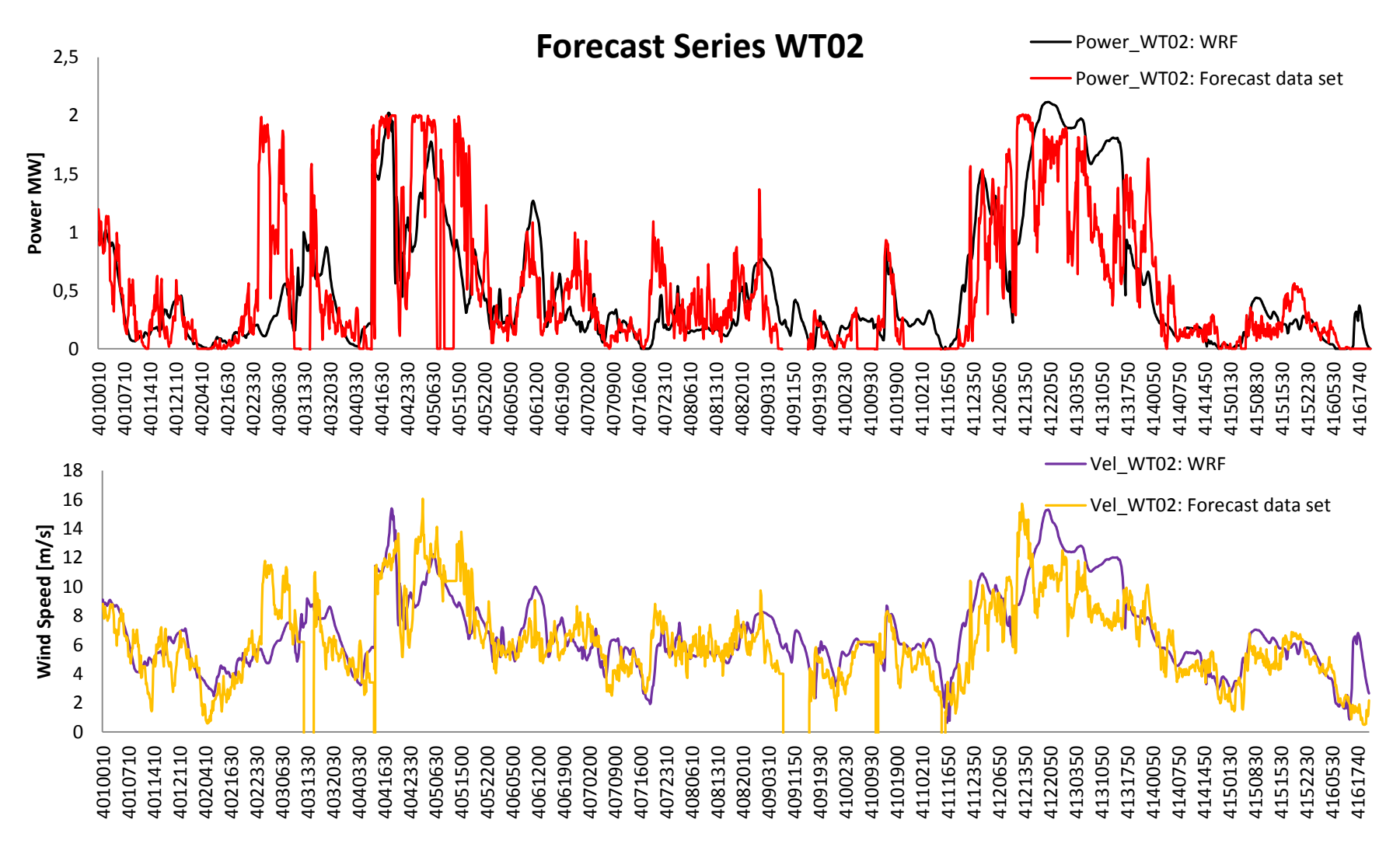


Figure 127: Reanalysis time series of total turbine power output and wind speed for turbine WT02.

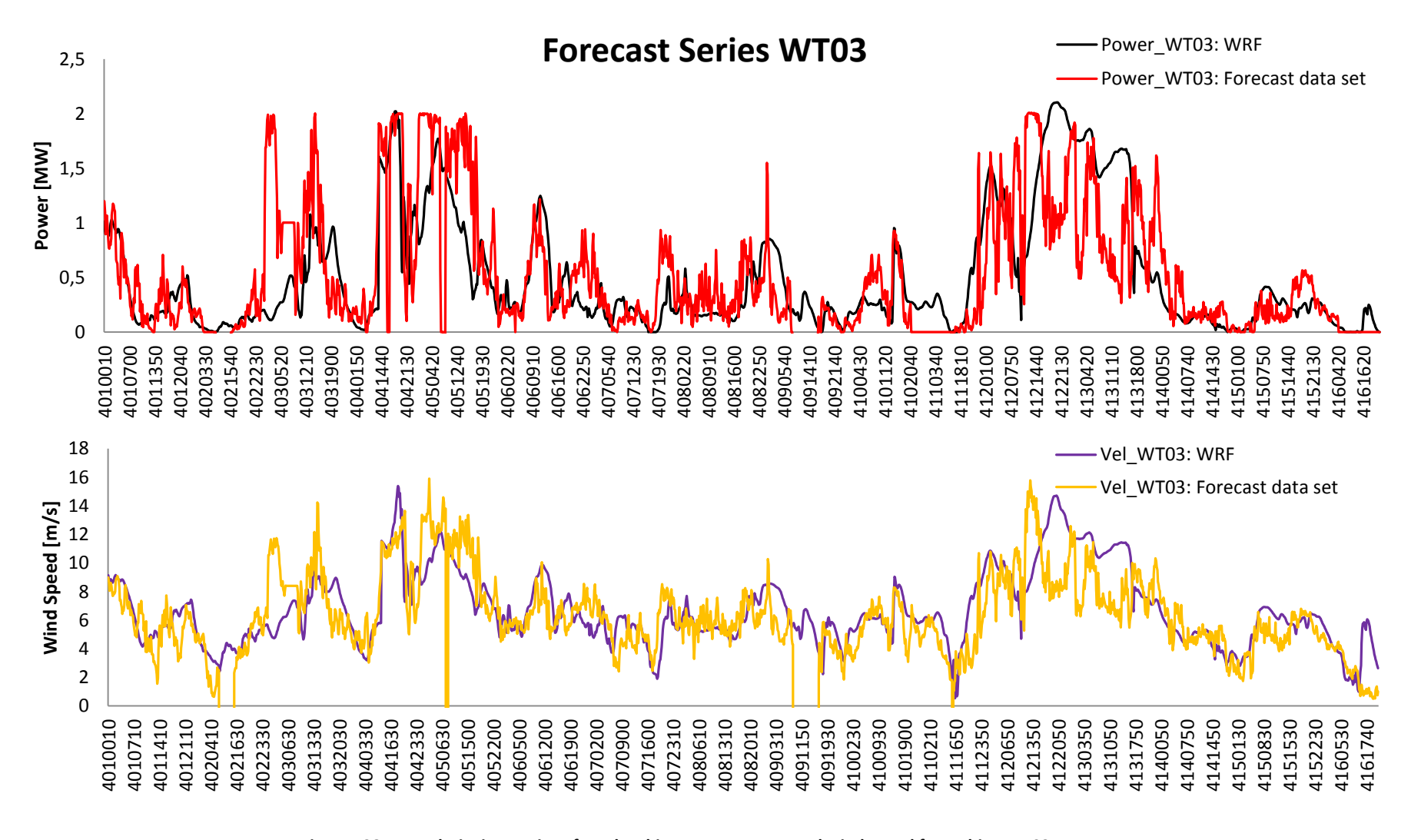


Figure 128: Reanalysis time series of total turbine power output and wind speed for turbine WT03.

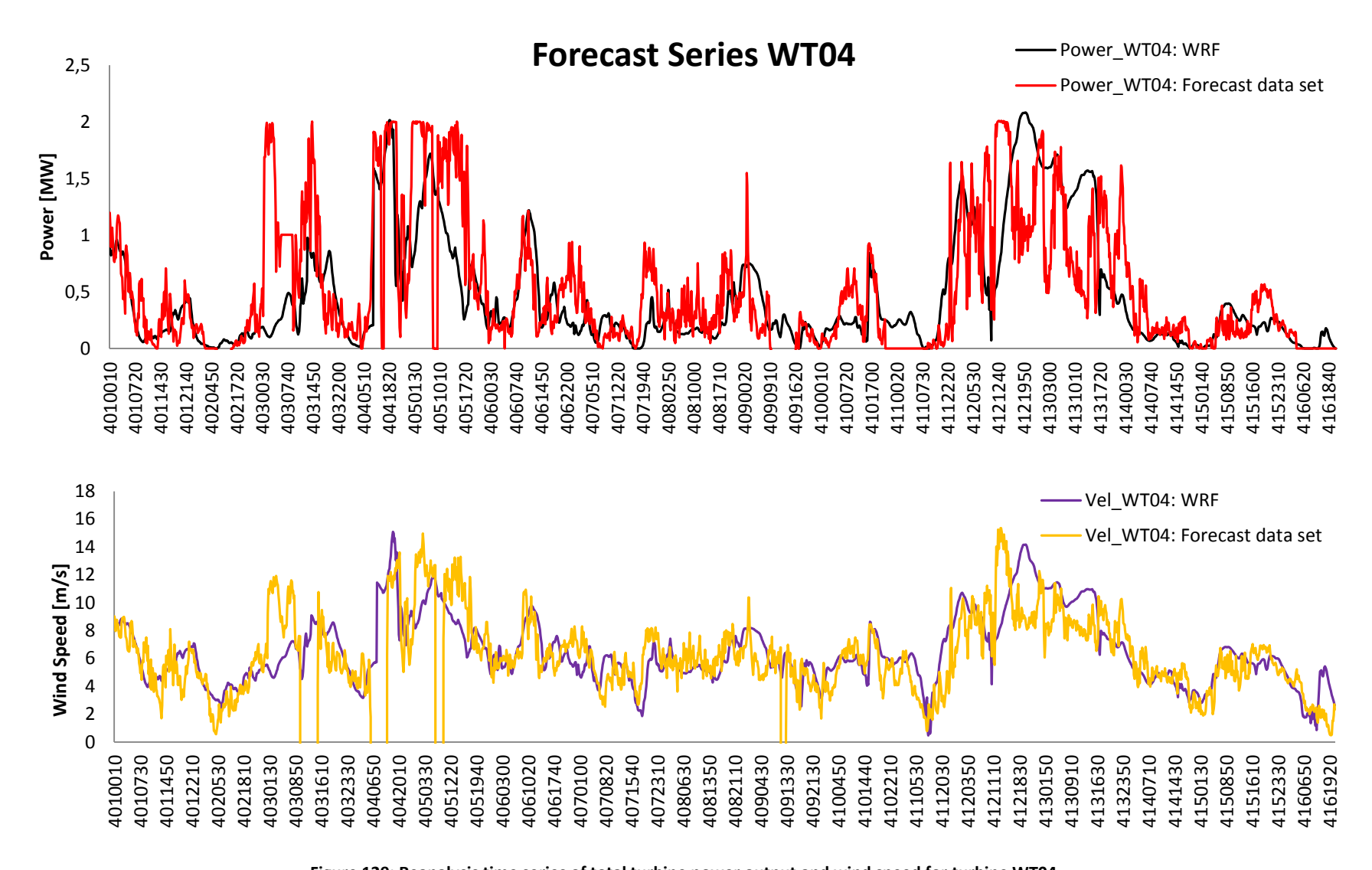


Figure 129: Reanalysis time series of total turbine power output and wind speed for turbine WT04.

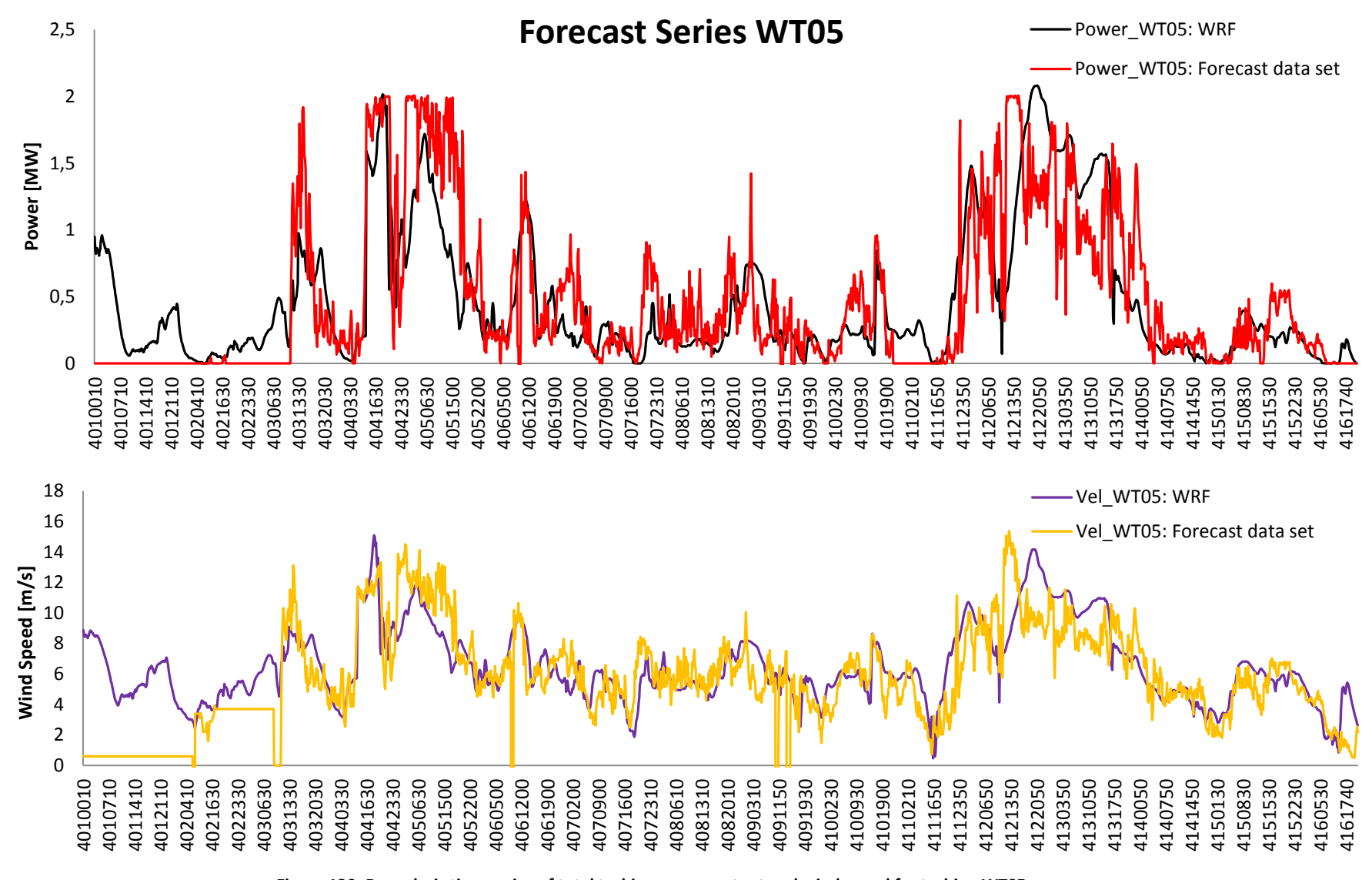


Figure 130: Reanalysis time series of total turbine power output and wind speed for turbine WT05.

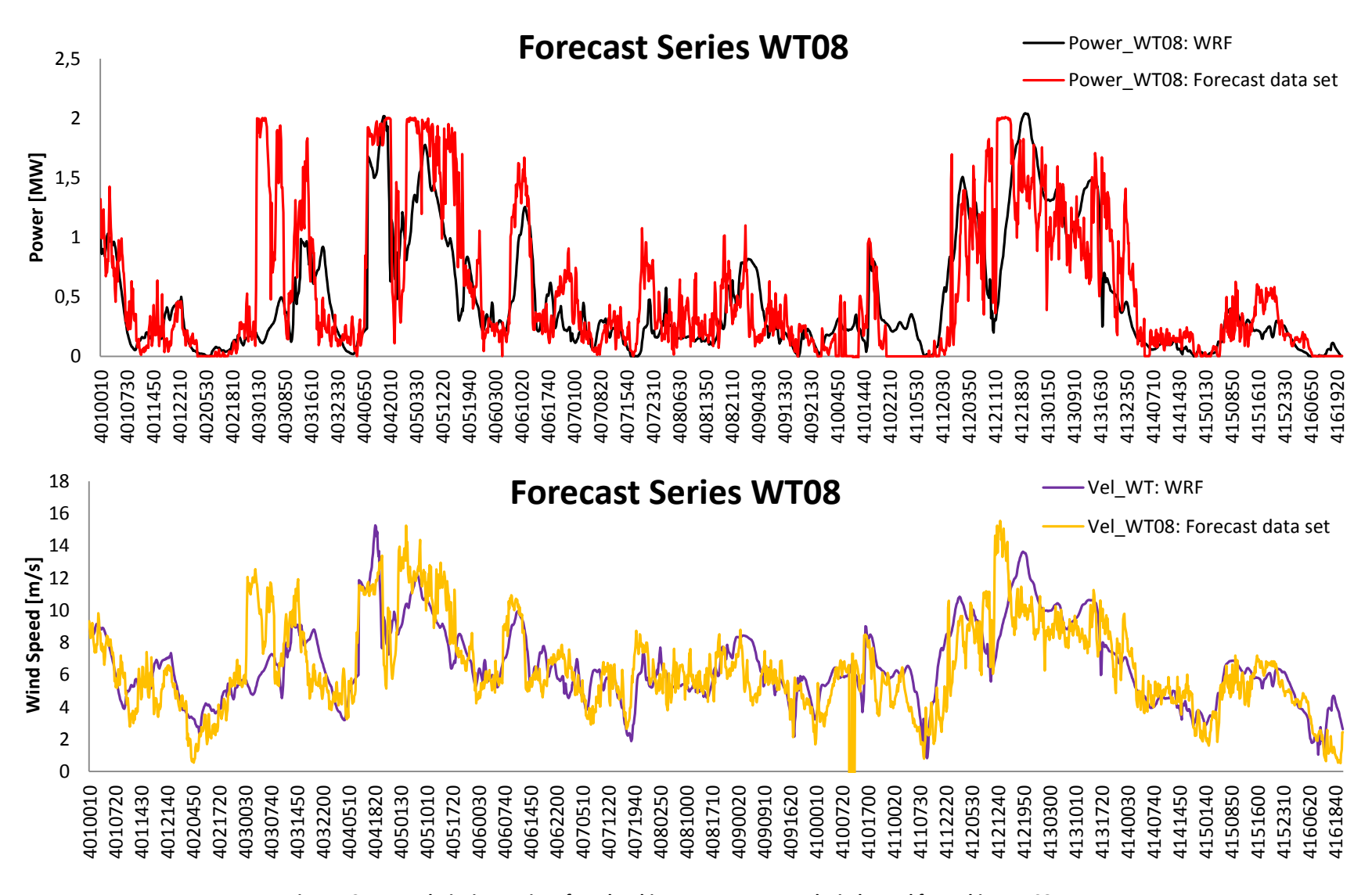


Figure 131: Reanalysis time series of total turbine power output and wind speed for turbine WT08.

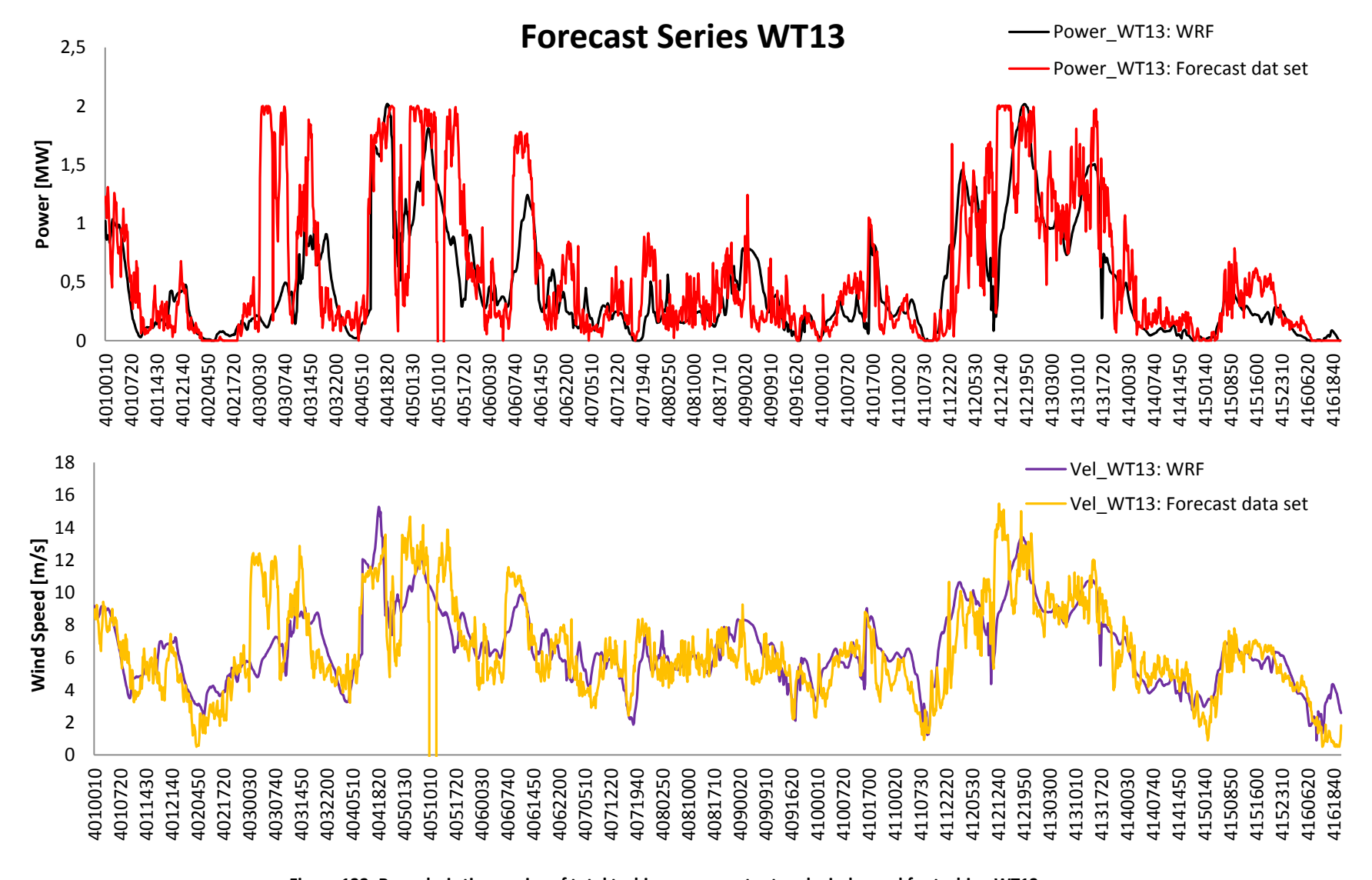


Figure 132: Reanalysis time series of total turbine power output and wind speed for turbine WT13.

Appendix-D. Optional Turbine Scheme

The Fitch scheme [12] has been modified in an attempt to provide a more detailed interaction between the turbines and the wind, such that the turbine parameterization could be implemented for real time forecasts. Therefore, the new scheme is based on formulations of similarity theory, empirical relations of atmospheric stability, performance and operational data from turbine manufacturers, wind farm configuration, Vermeulen's model for the near wake (Equation 19), and Frandsen's model for added turbulence intensity (Equation 62). Nevertheless, the new scheme is currently biased by the atmospheric modelling of the MYNN PBL and surface layer schemes, such that the turbulent kinetic energy of the flow and atmospheric stability are initially derived from the schemes.

The dependence on the MYNN schemes can be turned off by modifying few lines in the code, but a formulation for the flow turbulent kinetic energy **qke** must exist. The reason for this condition is that the new parameterization is governed by the flow turbulence intensity, which is related to the turbulent kinetic energy.

A key aspect to validate the scheme for forecasts is its ability to correctly track turbine yaw angles, and that ability should be tuned up. In case of not tuning up the turbine yaw tracking section of the parameterization scheme results can still be used for wind farm effects in a statistical manner. For example, the model prediction can be grouped per wind speed bins, stability, and direction to compare with measured data under the same classification. To better understand the turbine scheme and flow model the user should become familiar to the WRF "calling tree", and a basic knowledge of FORTRAN prior to reading the documents.

Figure 133 illustrates the proposed calling tree for using the parameterization scheme based on turbulence intensity. The inputs are depicted on the left side and the algorithm or procedure to yield the resultant added turbulence intensity per turbine rotor sections is depicted on the right. All input variables lay in the same input file for the current scheme in WRF.

Additional variables for the surface heat flux H_{sf} , and the aerodynamic roughness z_o may be needed in case not extracted from WRF, and model independently to yield the Monin-Obukhov Length L_* . Additionally, the turbine orientation labelled as $\theta_{turb(i,j)}$ is to be tracked to yield the yaw mismatch distribution along the rotor γ_{ijk} per turbine according to the flow direction $heta_{flow}$ at hub height. Exact code amendments were handed to MeteoGroup after having a successful compilation.

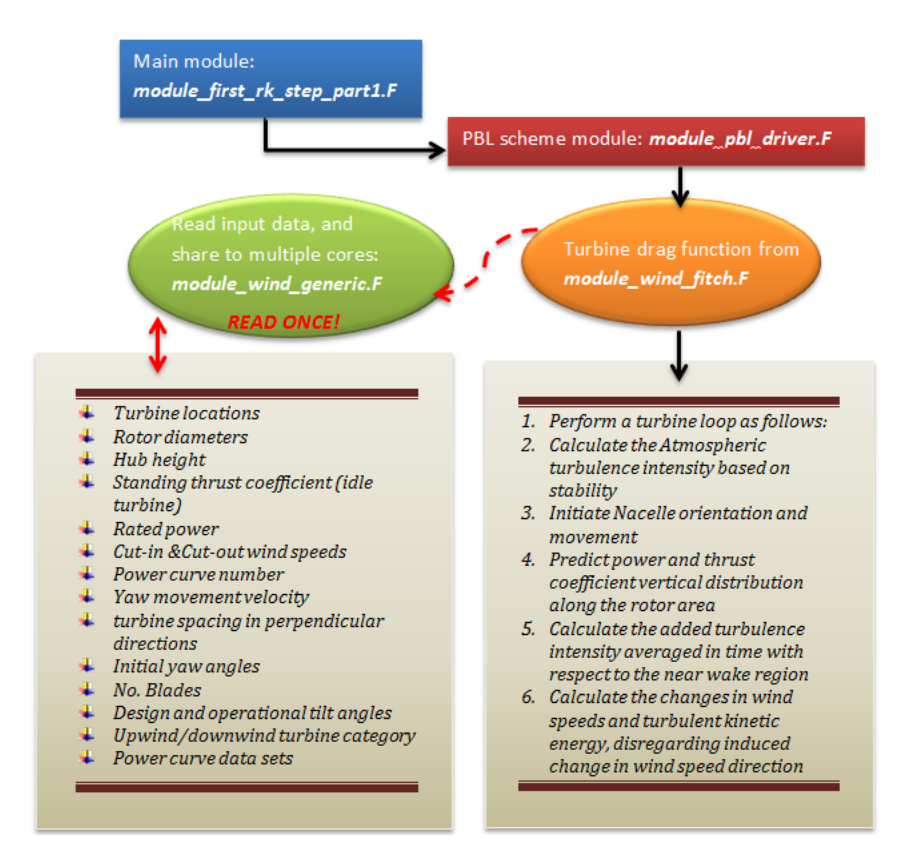


Figure 133: Calling Tree between turbine scheme and flow model in WRF

D-1. **Definitions of Input Variables**

The file section containing the turbine independent information contains addition variables besides those required by the current Fitch scheme. The complete set of these variables are used explanatory block diagrams, and are as follows

- Turbine Locations: grid locations of the turbines.
- Hub height, and rotor diameter D
- Ct(o) stands for the standing thrust coefficient of each turbine for velocities lower than the Cutin wind speed and greater that then Cut-out wind speed.
- Rated Power in MW of each turbine
- Curve, a number that stands for individual power curves
- $\Psi_{(vaw)}$ indicates the nominal turbine yaw movement velocity in deg/s. This velocity is found in Turbine manufactures data sheet.
- \$1, and \$2 stand for the orthogonal turbine spacing. The order of the values does not matter for the code. The only aspect that is important is their relation to the turbine layout. Their values are assigned such that they describe an ellipse around each turbine enclosing the 4 nearest turbines:

A.M. Striedinger P.

- 2 in-lines, and 2 transverse. If the eclipse is not closed, a value of 12 or 24 D is to be taken per missing spacing⁶⁵; see example with OWEZ wind farm starting at Figure 135.
- ullet $m{ heta}_{o\;(i,j)}$ or yaw_o stands for the initial turbine orientation to the simulation. For simplicity in the code, each angle points the direction where the wind flows to, and is defined in Cartesian coordinates: 0° for west-east direction, 90° for a north -south direction, and their respective opposites.
- Blades: Number of turbine blades. It is recommended to use always the same number of blades as there is no real example of a wind farm containing different number of blades per turbine.
- lacktriangle is the design tilt angle design per turbine, and $\Delta oldsymbol{eta}$ is the its fixed change in that angle. If the conditions are the same as in design $\Delta \beta = 0$.
- Up/Down stand for the definition of Upwind or Downwind wind turbines. Upwind turbines are numbered as -1, and Downwind turbines as 1. Upwind turbines are those where the rotor is located between the incoming flow and the nacelle.

Power curve data is written in matrix form with wind speed bins V, power coefficients c_p , Thrust coefficients c_T , axial induction factors a for power generation, and corresponding rpm in steady operation. It is important for the user to previously obtain this data from the manufacturer, and to obtained values for the axial induction factors by applying BEM theory, whilst disregarding cases of heavily loaded rotors as these are treated inside the code.

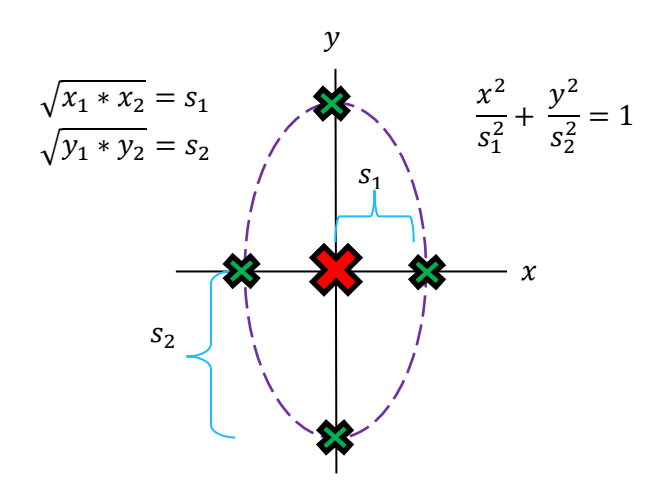


Figure 134: Elliptic configuration of turbulence intensity distribution based on turbine spacing parameters s_1 and s_2 . Green crosses represent the nearest turbines to the turbine under analysis.

The elliptic configuration is chosen due to the turbine pacing parameters. The ellipse is the only smooth geometrical shape that explains the doubly symmetrical added turbulence intensity from Frandsen's model. In this manner turbine spacing s_1 , and s_2 are related to an affected area; see Figure 134. Because the model requires both turbine spacing, it cannot be directly applied to turbines on the perimeter of the farm. For such cases, like WT01 in Figure 135 x_i and y_i should be changed to an

 $^{^{65}}$ In the example of MIDD in Chapter-5 , a transverse spacing of 7 D was implemented to reproduce wake with Frandsen's model. If possible, s_1, s_2 should be tuned-up with validation data for the selected wind farm.

artificial distance between 12 D and 24 D to account for the missing turbines. The distance is such that a turbine located at it will not considerably affect the wake development of the turbine under analysis.

For example, according to an ECN report [81] wakes losses account for 45% in power drop of the first four turbines on all rows when the wind comes from 140°. The in-line spacing for these cases is 7 D, and the transverse is 11 D. For which no differences in power loses was found between each row. Hence there was virtually no interference between parallel wakes. Thus only greater turbine spacing should be used to nullify the power drop. It is for this reason that distances > 12D are sued for x_i , and y_i in the absence for turbines. 24 D is added as a safety factor of 2, which in turn is greater than the common far wake length [22].

In the following example of the OWEZ wind farm, the artificial spacing is set to 24D; Table 28 shows the input parameters for the modified scheme, and Table 29 shows the resultant turbine spacing s_1 and s_2 for all OWEZ turbines in WRF.

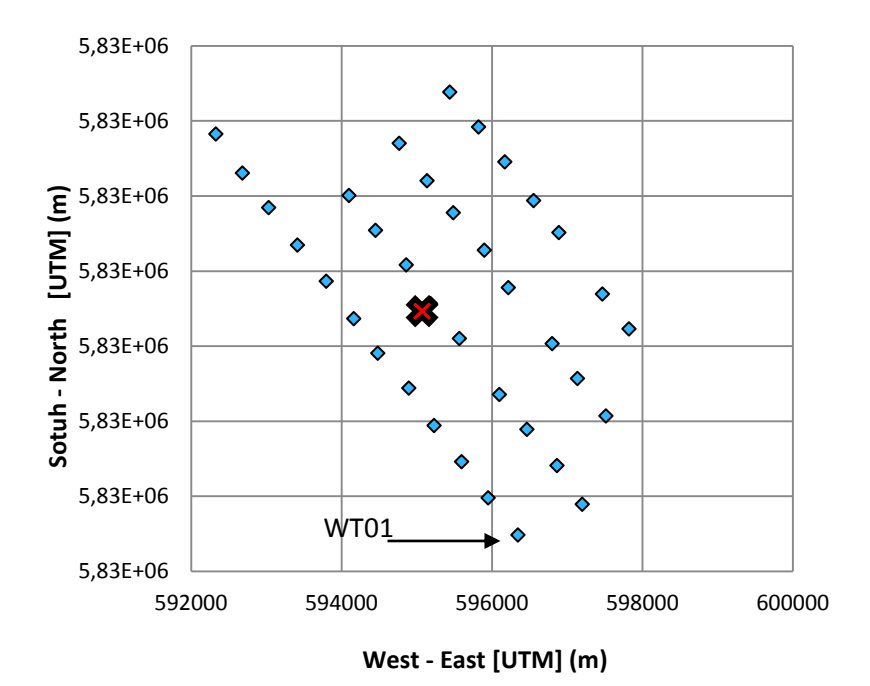


Figure 135: OWEZ Offshore Wind Farm as digitized from available information on the web.

	ruble 20. Turbine rocutions at the orisinore site of OVE2 with input parameters.																
No	LAT	LON	Hub	Dia	Ct(o)	Power	V_{in}	V_{out}	No	LAT	LON	Hub	Dia	Ct(o)	Power	V_{in}	V_{out}
1	52.580	4.438	70	90	0.065	3	4	25	20	52.616	4.407	70	90	0.065	3	4	25
2	52.584	4.431	70	90	0.065	3	4	25	19	52.612	4.413	70	90	0.065	3	4	25
3	52.588	4.425	70	90	0.065	3	4	25	20	52.616	4.407	70	90	0.065	3	4	25
4	52.593	4.419	70	90	0.065	3	4	25	21	52.621	4.400	70	90	0.065	3	4	25
5	52.597	4.414	70	90	0.065	3	4	25	22	52.594	4.459	70	90	0.065	3	4	25
6	52.602	4.407	70	90	0.065	3	4	25	23	52.597	4.453	70	90	0.065	3	4	25
7	52.606	4.401	70	90	0.065	3	4	25	24	52.602	4.448	70	90	0.065	3	4	25
8	52.610	4.401	70	90	0.065	3	4	25	25	52.609	4.438	70	90	0.065	3	4	25
9	52.615	4.389	70	90	0.065	3	4	25	26	52.613	4.432	70	90	0.065	3	4	25
10	52.619	4.382	70	90	0.065	3	4	25	27	52.618	4.425	70	90	0.065	3	4	25
11	52.624	4.377	70	90	0.065	3	4	25	28	52.623	4.419	70	90	0.065	3	4	25
12	52.628	4.371	70	90	0.065	3	4	25	29	52.627	4.413	70	90	0.065	3	4	25

Table 28: Turbine locations at the offshore site of OWEZ with input parameters.

13	52.583	4.453	70	90	0.065	3	4	25	30	52.604	4.465	70	90	0.065	3	4	25
14	52.588	4.447	70	90	0.065	3	4	25	31	52.608	4.460	70	90	0.065	3	4	25
15	52.592	4.441	70	90	0.065	3	4	25	32	52.615	4.449	70	90	0.065	3	4	25
16	52.596	4.435	70	90	0.065	3	4	25	33	52.620	4.443	70	90	0.065	3	4	25
17	52.603	4.425	70	90	0.065	3	4	25	34	52.624	4.437	70	90	0.065	3	4	25
18	52.608	4.419	70	90	0.065	3	4	25	35	52.628	4.431	70	90	0.065	3	4	25
19	52.612	4.413	70	90	0.065	3	4	25	36	52.633	4.424	70	90	0.065	3	4	25

	Table 29: Turbine locations at the offshore site of OWEZ with input parameters.												
No	V_{yaw}	$\mathbf{s_1}$	\mathbf{s}_2	$\boldsymbol{\theta}_{o(i,j)}$	В	Curve	No	V_{yaw}	$\mathbf{s_1}$	\mathbf{s}_2	$\boldsymbol{\theta}_{o(i,j)}$	В	Curve
1	0,5	13,145	16,25	60	3	1	20	0,5	7,200	11,00	60	3	1
2	0,5	7,200	16,25	60	3	1	21	0,5	13,145	11,00	60	3	1
3	0,5	7,200	16,25	60	3	1	22	0,5	13,145	16,25	60	3	1
4	0,5	7,200	16,25	60	3	1	23	0,5	7,200	11,00	60	3	1
5	0,5	7,200	16,25	60	3	1	24	0,5	7,200	11,00	60	3	1
6	0,5	7,200	16,25	60	3	1	25	0,5	7,200	11,00	60	3	1
7	0,5	7,200	16,25	60	3	1	26	0,5	7,200	11,00	60	3	1
8	0,5	7,200	16,25	60	3	1	27	0,5	7,200	11,00	60	3	1
9	0,5	7,200	16,25	60	3	1	28	0,5	7,200	11,00	60	3	1
10	0,5	7,200	24,00	60	3	1	29	0,5	13,145	11,00	60	3	1
11	0,5	7,200	24,00	60	3	1	30	0,5	13,145	16,25	60	3	1
12	0,5	13,145	24,00	60	3	1	31	0,5	7,200	16,25	60	3	1
13	0,5	13,145	16,25	60	3	1	32	0,5	7,200	16,25	60	3	1
14	0,5	7,200	11,00	60	3	1	33	0,5	7,200	16,25	60	3	1
15	0,5	7,200	11,00	60	3	1	34	0,5	7,200	16,25	60	3	1
16	0,5	7,200	11,00	60	3	1	35	0,5	7,200	16,25	60	3	1
17	0,5	7,200	11,00	60	3	1	36	0,5	13,145	16,25	60	3	1
18	0,5	7,200	11,00	60	3	1	20	0,5	7,200	11,00	60	3	1
19	0,5	7,200	11,00	60	3	1	21	0,5	13,145	11,00	60	3	1

D-2. **Model Expression and Derivation**

The model derivation is divided into 5 sections that deal with the calculation of ambient turbulence intensity I_o in front of the turbine rotors, an equivalent centroid for each rotor section as seen from the hub r_{eq} , the estimation of the near wake length x_n , at the height of each rotor section, the change in wind speed components du, dv, and the added turbulent kinetic energy as dqke.

D-2.1. **Calculation of the Ambient Turbulence Intensity**

Often time the offshore h_* is very low, and turbulence above it can be very uniform, such that qke is nearly isotropic. In addition, its component on the horizontal plane is the most relevant for the wake effects affecting power production. If turbulence is not isotropic then σ_v , σ_u , σ_w are calculated based on Equation 9 depending on the atmospheric stability (Table 2, Equation 4). See Equation 59.

$$I_o = rac{\sqrt{rac{2}{3}qke_{\langle total
angle}}}{V_o} \ or \ I_o = rac{\sqrt{\sigma_v^2 + \sigma_u^2}}{V_o}$$

Equation 59: Ambient turbulence intensity for isotropic flow where qke = 2TKE, and for non-isotropic flow (left).

D-2.2. Calculations of central radial positions per turbine rotor section (for power, thrust coefficients, and averaged turbine rpm)

To find the proper c_p and c_T per rotor section, this is evaluated through a balance in area-moment of inertia producing a representative centroid. This position is used to estimate tip loses, axial induction

factors, and the near wake distance associated to that rotor section. The distributions of coefficients become more detailed as the vertical resolution increases.

$$r_{eq} = \frac{\sum \left(\frac{+}{-} r_i A_i\right)}{Area_{eq}}$$

Equation 60: Area moment analysis of rotor sections.

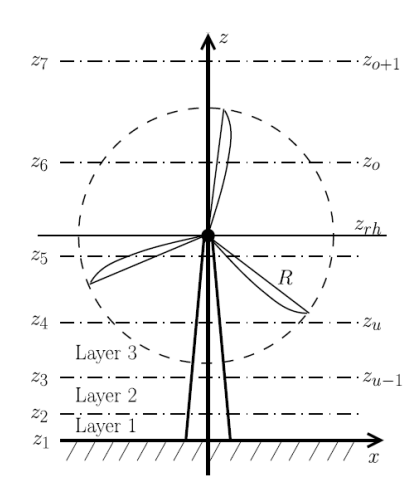


Figure 136: Turbine vertical levels intersecting rotor area.

The centroid r_{eq} is calculated with Equation 60, and as each rotor section is symmetrical in the vertical axis, finding its true geometric centroid erases the horizontal component and that is not suitable to represent an artificial radial blade position. Therefore, only half of each rotor section is considered. This approach has no conflicts when blades are aligned vertically or horizontally, as during such alignment the blades are still bounded to a unique Cartesian quadrant and not to two at the same time as they would be if the complete rotor section is considered; see Figure 136. Suffice to say there are two scenarios to calculate r_{eq} :

- Rotor section is either below or above hub height; see Figure 137
- Rotor section intersects hub height; see
- Figure 138

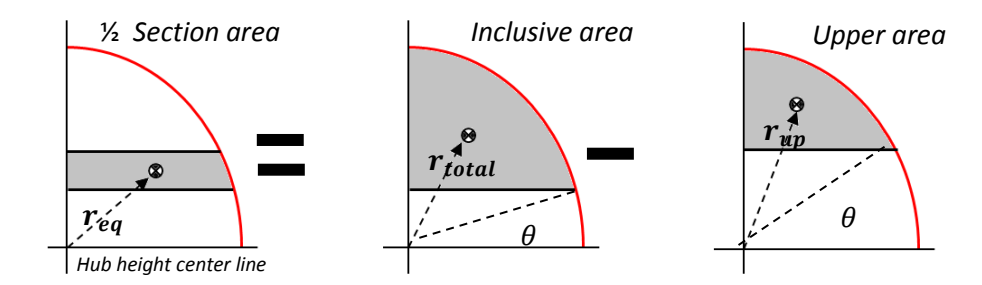


Figure 137 Illustration of area moment analysis of rotor section above or below hub height.

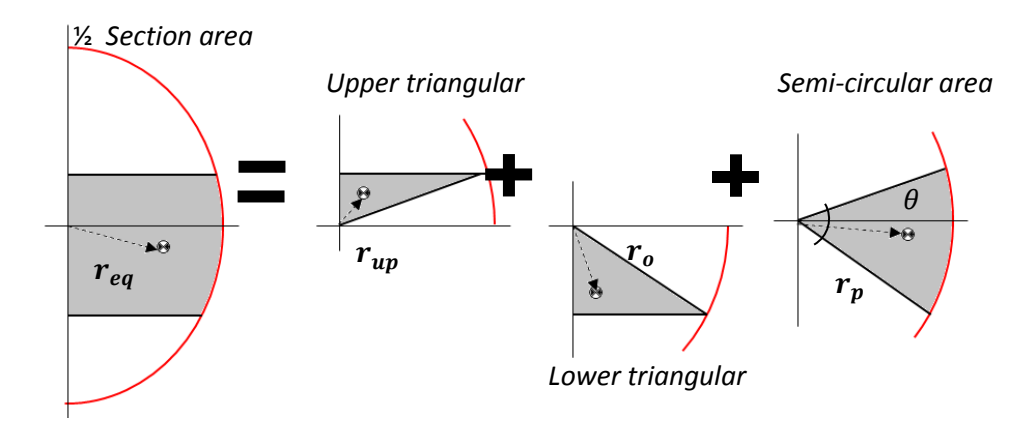


Figure 138: Illustration of area moment analysis for rotor section crossing hub height.

After r_{eq} is calculated, the wind speed components are used together with $\theta_{o(i,j)}$ or yaw_o and Ψ to predict c_p and c_T coefficients per rotor section through Equation 13 to Equation 16: momentum balance, tip loses, heavy or not heavy loaded blade, tilt angle and yaw mismatch γ . This is an iterative process executed by the FORTRAN code executed in WRF. Iterations started by guessing from the tabulated c_p and c_T provided by the user previous to the simulation. Finally, wind speed is used to interpolate the rpm from the tabulated list. The complete list must contain c_n , c_T , a, rpm per wind speed bin.

D-2.3. Calculation of the near wake length associated to each rotor section

The near wake length x_n is a function of c_T , c_p , blades, rpm, D, V, and I_o ; see line 398 for the FORTRAN subroutine with same input order. According to Vermeulen [50] x_n can be calculated in two ways: the first is when turbines are operational, and the second they are not. Vermeulen proposed an empirical relation considering wake growth contributions from atmosphere, from shear-generated turbulence, and from mechanical turbulence induced by the rotor blades by including the instantaneous tip speed ratio. Such contribution are : $\left(\frac{dr}{dx}\right)_{\alpha}$, $\left(\frac{dr}{dx}\right)_{m}$, and $\left(\frac{dr}{dx}\right)_{\lambda}$ respectively. The formulation is shown in Equation 60, and an illustration of the near wake and the far wake is shown in Figure 139.

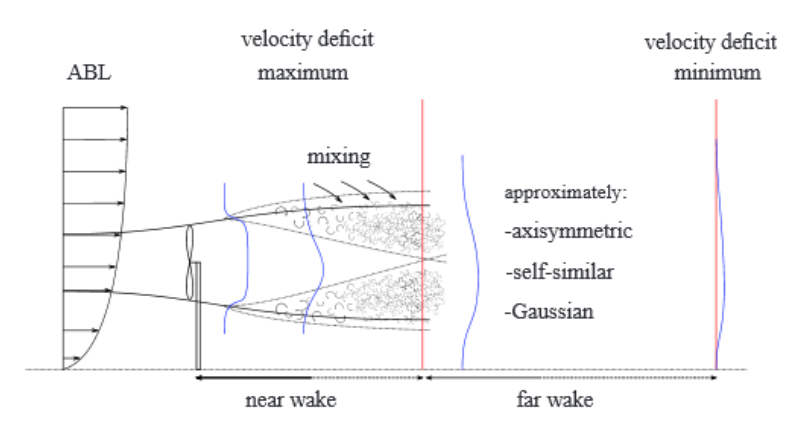


Figure 139: Wind speed profile in the wake of a wind turbine [44]

Master of Science Thesis A.M. Striedinger P.

$$x_{n} = \frac{n r_{o}}{\sqrt{\left(\frac{dr}{dx}\right)_{\alpha}^{2} + \left(\frac{dr}{dx}\right)_{m}^{2} + \left(\frac{dr}{dx}\right)_{\lambda}^{2}}} \qquad \left(\frac{dr}{dx}\right)_{m} = \frac{(1-m)\sqrt{1.49 + m}}{9.76(1+m)}$$

$$n = \frac{\sqrt{0.214 + 0.144m}(1 - \sqrt{0.134 + 0.124m})}{(1 - \sqrt{0.214 + 0.144m})\sqrt{0.134 + 0.124m}} \qquad \left(\frac{dr}{dx}\right)_{\alpha} = 2.5I_{o} + 0.005$$

$$m = \frac{1}{\sqrt{1 - C_{T}}}$$

$$r_{o} = \frac{D}{2} \sqrt{\frac{m+1}{2}}$$

Equation 61: Vermeulen's Expression for the near wake region X_n in terms of atmospheric turbulence intensity, turbine tip speed ratio, rotor diameter, and thrust coefficient.

D-2.4. Calculation of the changes in horizontal wind speed, and turbulent kinetic energy per

Frandsen's empirical expression of turbulence intensity in the deep turbine arrays has been tested on distances in the far wake region where each turbine is surrounded by other in-line and transverse turbine; see Equation 62.

$$\Delta I_T \cong \frac{1}{2} \left(I_o + \sqrt{I_o^2 + \left(\frac{0.36}{1 + 0.2\sqrt{s_1 s_2/C_T}} \right)^2} \right)$$

Equation 62 Frandsen's expression applied at the end of the near wake region x_n

Because WRF treats the atmospheric flow dynamics, the turbine-flow interaction captured by the Frandsen's model must also be a dynamic expression (a function of time). Therefore, the following interpretation is taken:

Turbulence intensities in Farndsen's expression from the far wake region have a Gaussian vertical profile. The formulation takes the near wake into account, and therefore the expression produces a quasi-state value of turbulence intensity from an unknown time-space development starting at the end of the near-wake regions. But, if time is sufficiently small, such development can be modelled as linearly dependent on time only: a straight line. This assumption is off course open for debate, but it will be considered true at the moment.

The previous is the key assumption to introduce Frandsen's formulation inside the new turbine scheme. Furthermore, the computational time-step (in the order of few seconds) can be set as constant by the user. The following equations and figures illustrate the assumptions in mathematical form on the ambient conditions (V_0, σ_0) at the end of the near wake (x_n) , and after the wake has been sufficiently developed for a quasi-static approach: at time T, and (V_{avg}, V_w, σ_T)

$$\left\| \vec{V} \right\| = \left\| (\vec{u} + \vec{v}) \right\| = \bar{V} + V'$$

$$\overline{V_o'} \cong \sigma_o \quad ; \quad \overline{V_w'} \cong \sigma_T \quad ; \quad \Delta \sigma_T = \sigma_T \quad - \sigma_o \quad ; \quad \Delta \sigma = \sigma - \sigma_o$$

Equation 63: wind speed and turbulence relations.

$$\sigma = \left(\frac{dt}{T}\right) \Delta \sigma_T + \sigma_o$$
 ; $fr = \left(\frac{dt}{T}\right)$

Equation 64: Proposed expression for wind speed turbulence at height h.

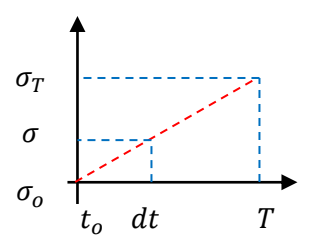


Figure 140: Time linearization of turbulence

One way ot calculate T is by the averaging wind speed between the inflow and the wake along the near wake region corresponding to a time dt. The validity of using an average velocity to represent the flow in the near wake is plausible due to the porposed time linearization of turbulence; see Equation 65. In addition it yields the theoretial mean wind speed through the rotor baldes provided by BEM theory.

$$V_{avg} = \frac{V_o + V_w}{2} = V_o(1 - a)$$

$$T = \frac{V_{avg}}{x_n} = f_r = \frac{dt \, V_o(1-a)}{x_n}$$

Equation 65: Final expression for the time fraction or turbulence development fraction at time $t_o + dt$

 I_p represents the change in turbulence ($\Delta\sigma$) within dt, a time small enough to consider the wind speed V_{avg} behind the rotor to represent the flow, and therefore its turbulence intensity; see Equation 66. Such change in turbulence intensity is also a fraction of the total change at time T on the edge of the near wake x_n .

$$\Delta I = \frac{\sigma}{V} - \frac{\sigma_o}{V_o} \cong \frac{\sigma - \sigma_o}{V} = \frac{\Delta \sigma_o}{V_{avg}} = f_r \left(\frac{\Delta \sigma_T}{V_{avg}}\right) = f_r \Delta I_T$$
$$\Delta \sigma \cong f_r \Delta \sigma_T = f_r \left(\Delta I_T V_{avg}\right) = I_p$$

Equation 66: Final expression for the added turbulence per turbine, and applied per rotor section

Once the added turbulence is calculated, the change in the **MYNN** turbulent kinetic energy and wind speed components are easily predicted from an energy balance in Equation 67, and Equation 68.

$$\frac{d(qke)}{dt} = \frac{d}{dt} \sigma^2 = 2\sigma * \frac{d\sigma}{dt} \cong 2 I_o V \left(\frac{fr\Delta\sigma_T}{dt}\right)$$

Equation 67: Change in twice MYNN turbulent kinetic energy (qke) due to turbine operation

$$\frac{dV}{dt} \cong -\frac{1}{2}c_p \left(\frac{A_{rot}}{V}\right) V_o^2 - I_o \frac{fr\Delta\sigma_T}{dt}$$
$$dv \cong \frac{v}{V} \left(\frac{dV}{dt}\right) \; ; \; du \cong \frac{u}{V} \left(\frac{dV}{dt}\right)$$

Equation 68 Change horizontal wind speed change due to the turbine operation

D-2.5. **Derivation of the Energy Balance**

The expression for the changes in turbulent kinetic energy (Equation 69), assumes no direct effects on the vertical direction due to the turbine parameterization alone because the flow is mainly in the horizontal direction. All changes and effects in the vertical direction are calculated separately by the physics schemes in WRF to satisfy the equation of continuity and energy balances. For example, σ_w^2 will be affected by the flow model inside WRF, and as such is not considered by turbine parameterization.

The following equations depict the solution procedure for horizontal wind speed changes in any grid cell containing a turbine. If the analysis is conceptualized to take initial conditions as the ambient conditions, such that $I_o=rac{\sigma_o}{v}$, and $d\sigma_o$ as a fraction of the total change $f_r\Delta\sigma_T$ at time T after the flow passes through the turbine and reaches the end of the near wake region x_n , the wind speed change from Equation 70 can be implemented inside the turbine parameterization through Equation 72.

$$\begin{split} &\frac{dKE}{dt} + \frac{dTKE}{dt} = -P - E_{defromation} \quad ; \quad E_{deformation} = 0 \\ &\frac{dKE}{dt} = \frac{d}{dt} \left(\frac{1}{2}\rho \Psi V^2\right) = \rho \Psi V \frac{dV}{dt} \\ &\Rightarrow \frac{dTKE}{dt} = \frac{d}{dt} \left(\frac{1}{2}\rho \Psi qke\right) = \frac{1}{2} \ \rho \Psi \frac{d(qke)}{dt} \\ &\frac{d(qke)}{dt} = \frac{d}{dt} (\sigma_u^2 + \sigma_v^2 + \sigma_w^2) \ ; \quad \sigma_u^2 + \sigma_v^2 = \sigma^2 \quad ; \quad \frac{d}{dt} \sigma_w^2 = 0 \\ &\Rightarrow \frac{d(qke)}{dt} = \frac{d}{dt} \sigma^2 = 2\sigma^2 * \frac{d\sigma}{dt} \end{split}$$

Equation 69 Proposed Energy balance due to turbine-flow interaction

$$P = \frac{1}{2}\rho V \frac{d(qke)}{dt} + \rho V V \frac{dV}{dt} = \frac{1}{2}\rho c_p A_{rot} V^3$$

$$\Rightarrow -\frac{1}{2}\rho c_p A_{rot} V^3 = \rho V \left[\frac{1}{2} \frac{d(qke)}{dt} + V \frac{dV}{dt} \right]$$

$$\Rightarrow -\frac{1}{2}c_p \left(\frac{A_{rot}}{V} \right) V^3 = \frac{1}{2} \frac{d(qke)}{dt} + V \frac{dV}{dt}$$

$$\Rightarrow \frac{dV}{dt} = \frac{-\frac{1}{2}c_p \left(\frac{A_{rot}}{V} \right) V^3 - \frac{1}{2} \frac{d(qke)}{dt}}{V} = -\frac{1}{2}c_p \left(\frac{A_{rot}}{V} \right) V^2 - \frac{1}{2V} 2\sigma * \frac{d\sigma}{dt}$$

Equation 70 General solution for induced wind speed change per grid cell per turbine rotor section

$$\frac{d(qke)}{dt} = \frac{d}{dt} \sigma^2 = 2\sigma * \frac{d\sigma}{dt} \cong 2 I_o V \frac{fr\Delta\sigma_T}{dt}$$

Equation 71 Change in MYN turbulent kinetic energy due to turbine operation

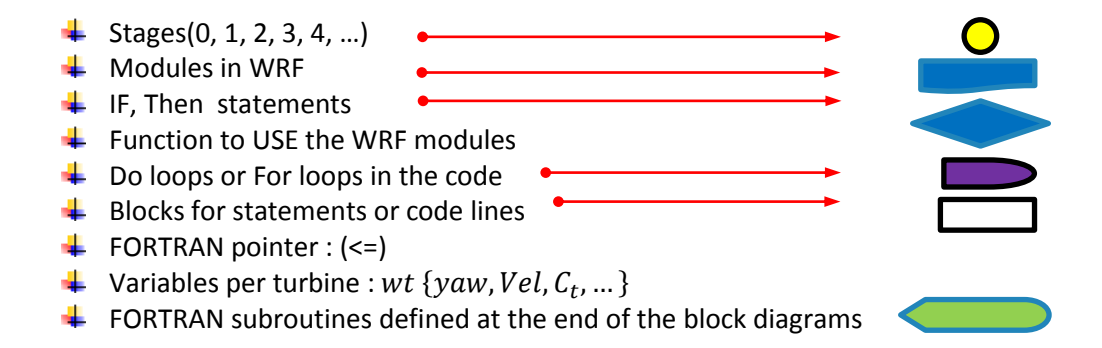
$$\frac{dV}{dt} \cong -\frac{1}{2}c_p \left(\frac{A_{rot}}{\Psi}\right) V_o^2 - I_o \frac{fr\Delta\sigma_T}{dt}$$

Equation 72 Change horizontal wind speed change

D-3. **Implementation Procedure**

The following block diagrams describe the implementation of the additional turbine parameterization scheme developed in the previous section of the appendix. The implementation is done in FORTRAN because that is the program language of WRF.

The diagrams include the initial procedures of calling the functions, doing the loops through turbine rotor sections, finding the appropriate turbine power and thrust coefficients, and providing the changes in output variables. The block diagrams use the symbols for the input variables together with IF and LOOP blocks. All set # are groups of WRF variables defined in the registry file. They are not shown in this appendix in order to protect the confidentiality of the code given to MeteoGroup.. Furthermore, the block diagrams make use of the current structure of the turbine scheme in WRF in order to incorporate the new concepts and methods. For illustrative purposes, some loops of the current Fitch turbine scheme in WRF are still presented and used. That is to smooth the code transition. No rights are to be derived from the following information.



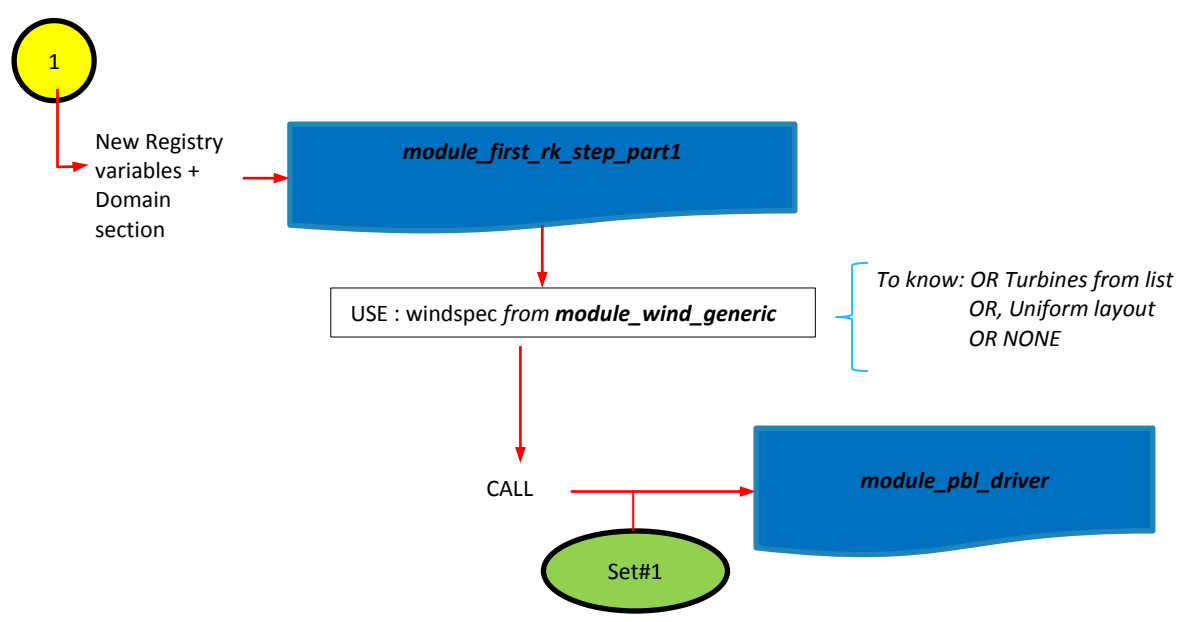


Figure 141: Entry modules in the structure

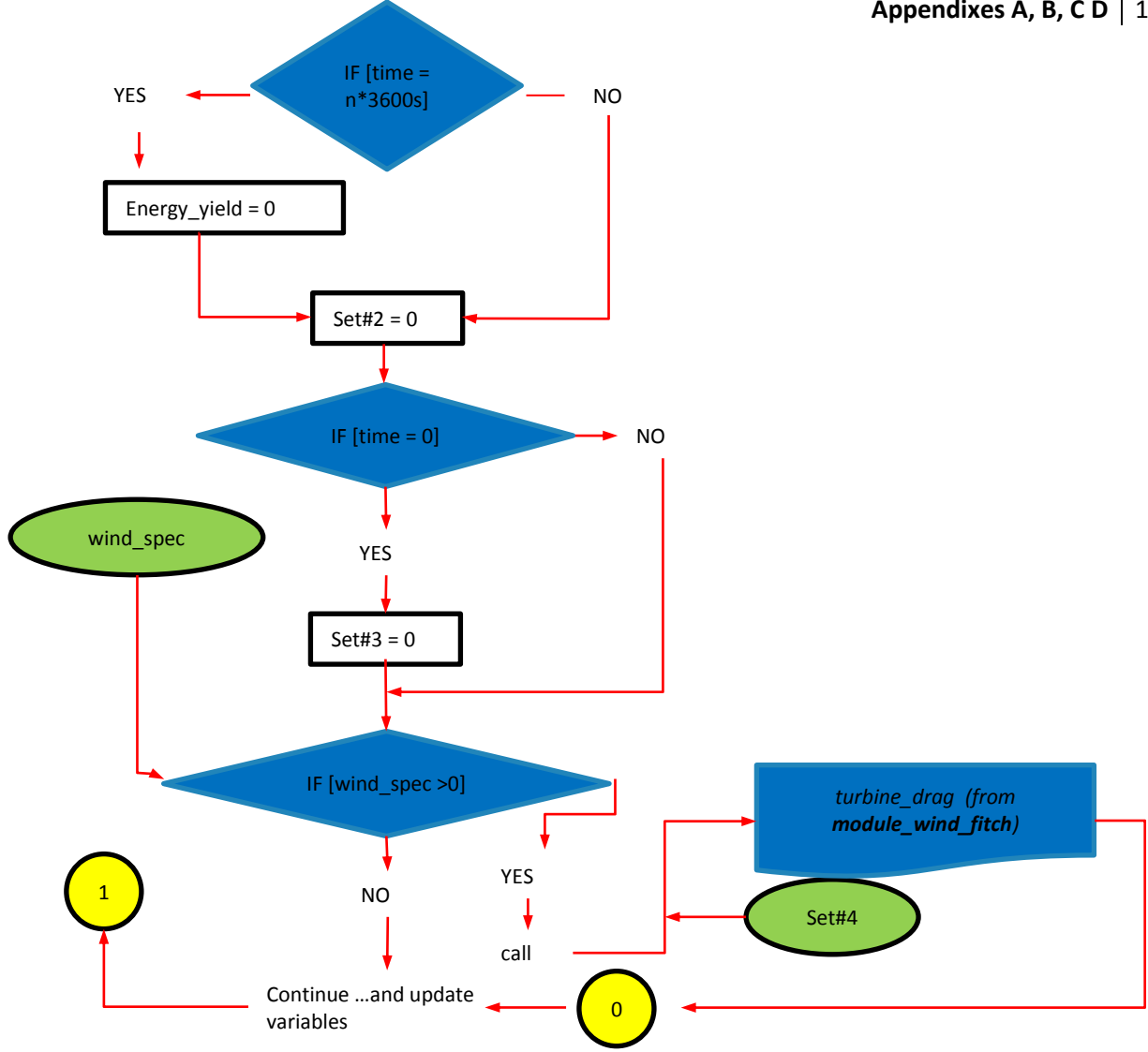


Figure 142: Algorithm inside the first module that calls the turbine scheme modules and dependencies

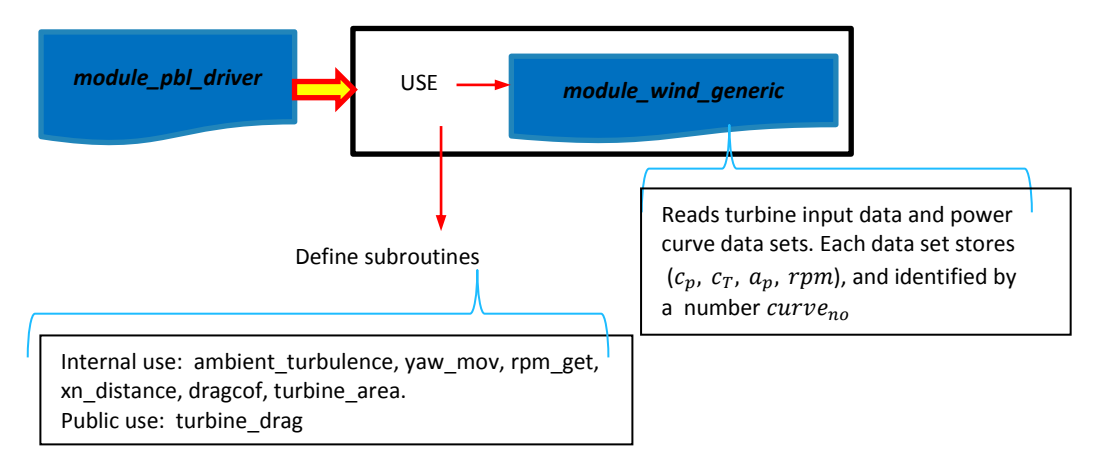


Figure 143: Tree for calling the PBL scheme and using variable from the module that reads the turbine information

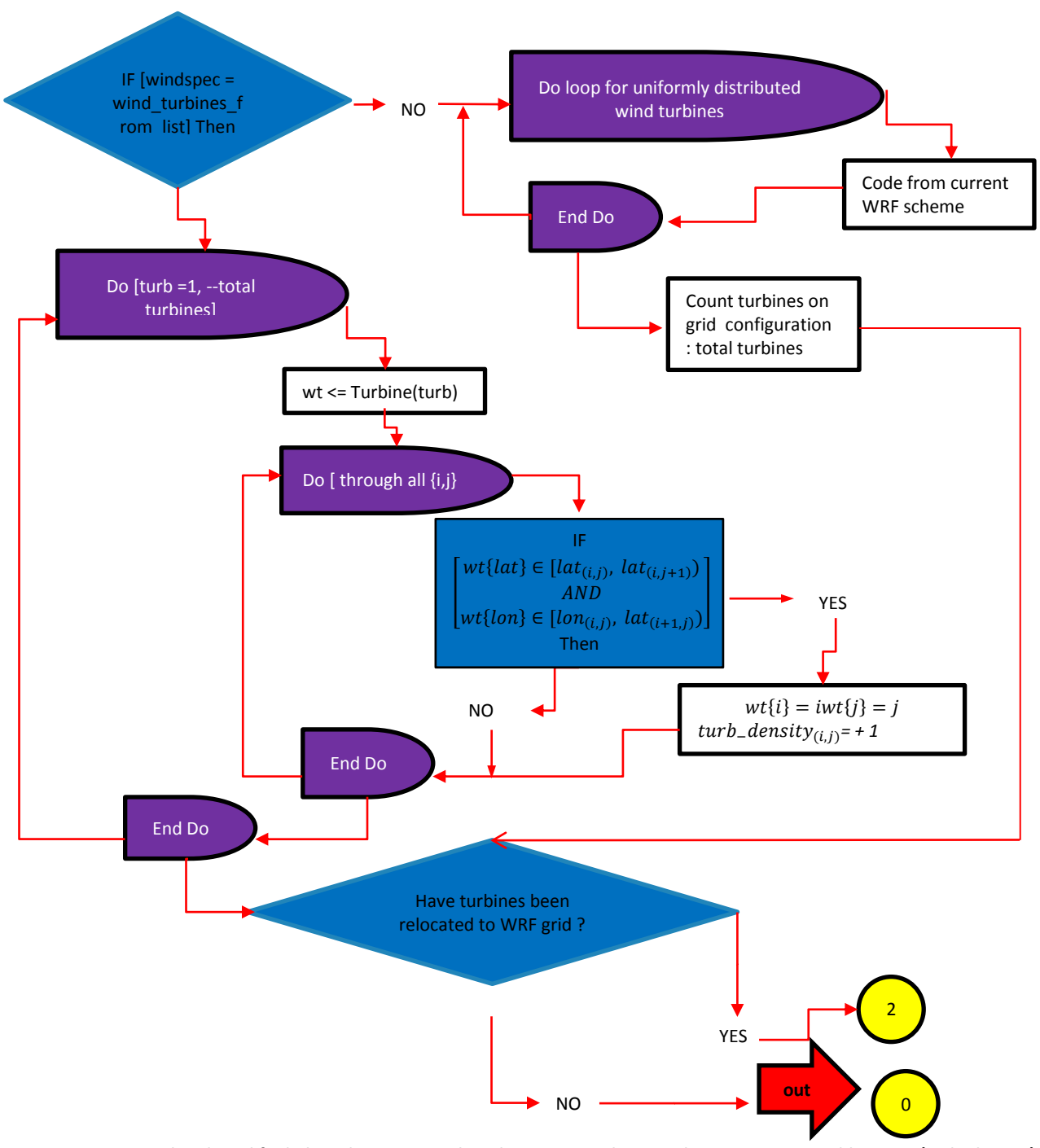


Figure 144: Original and modified algorithm to set turbine locations to obtain turbines units per grid location (turb_density) and total number.

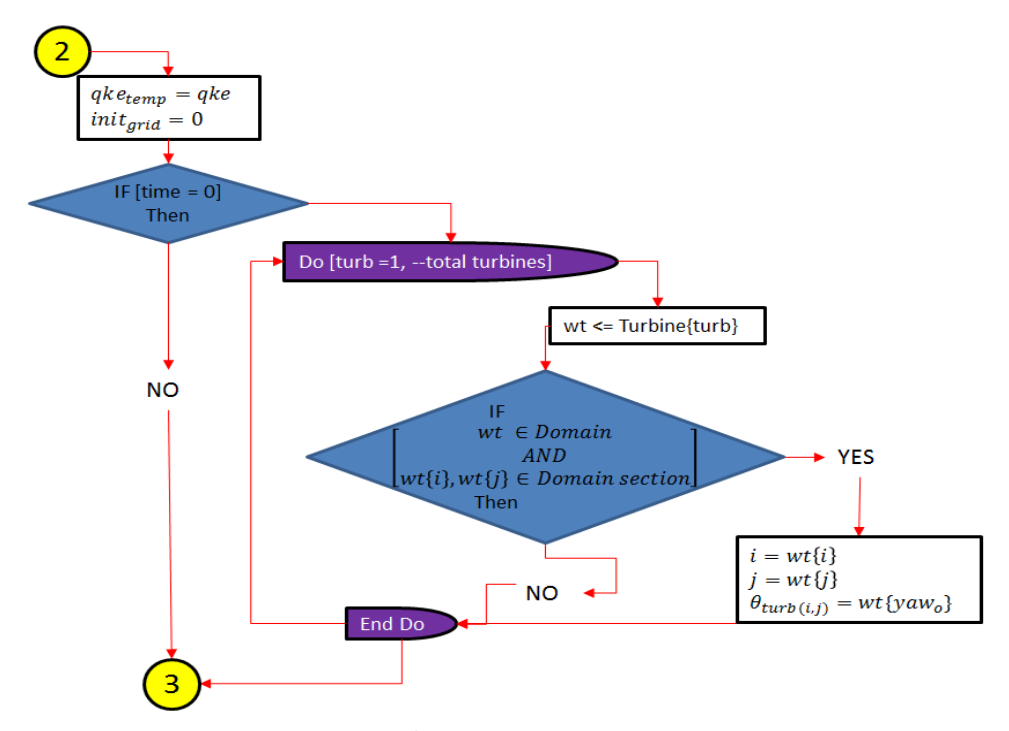


Figure 145: Initialization of qke , and turbine orientation per grid location $heta_{turb}$

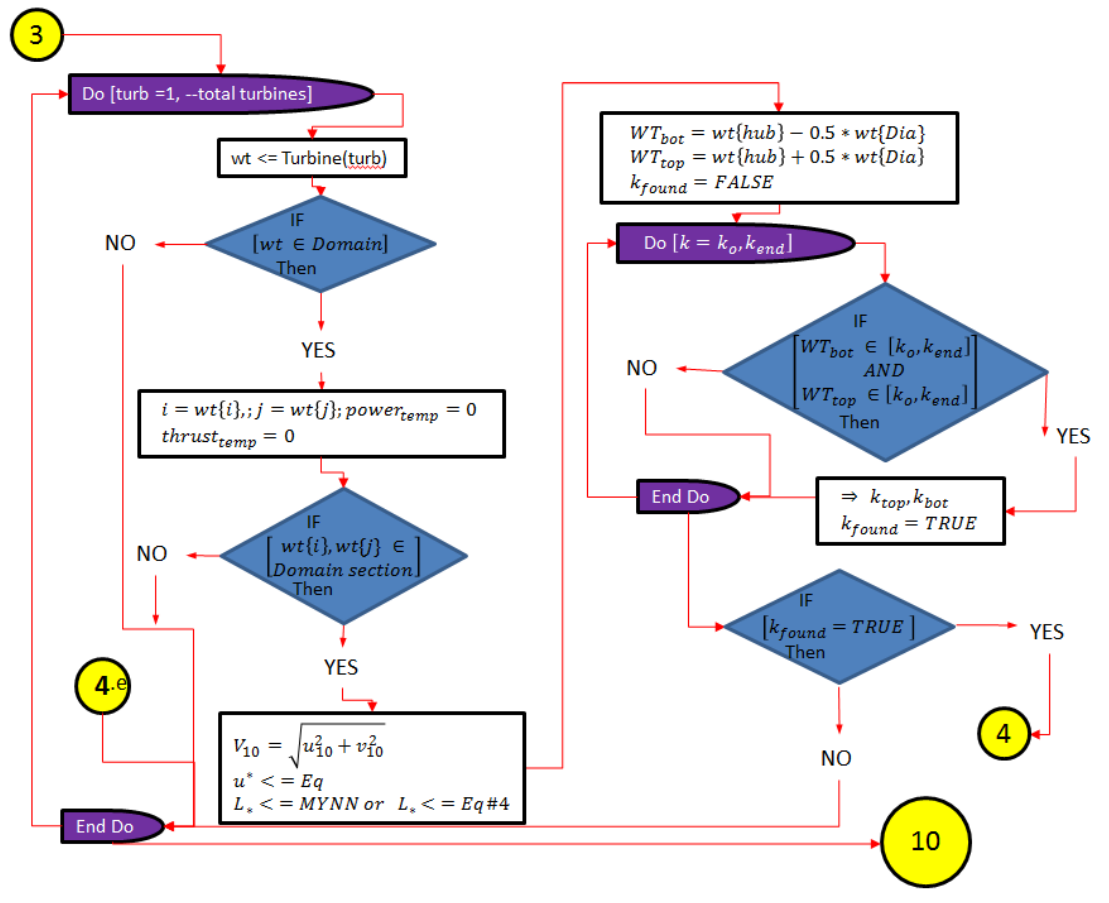


Figure 146: Initialization of power, thrust, atmospheric stability and loop through rotor sections within k levels.

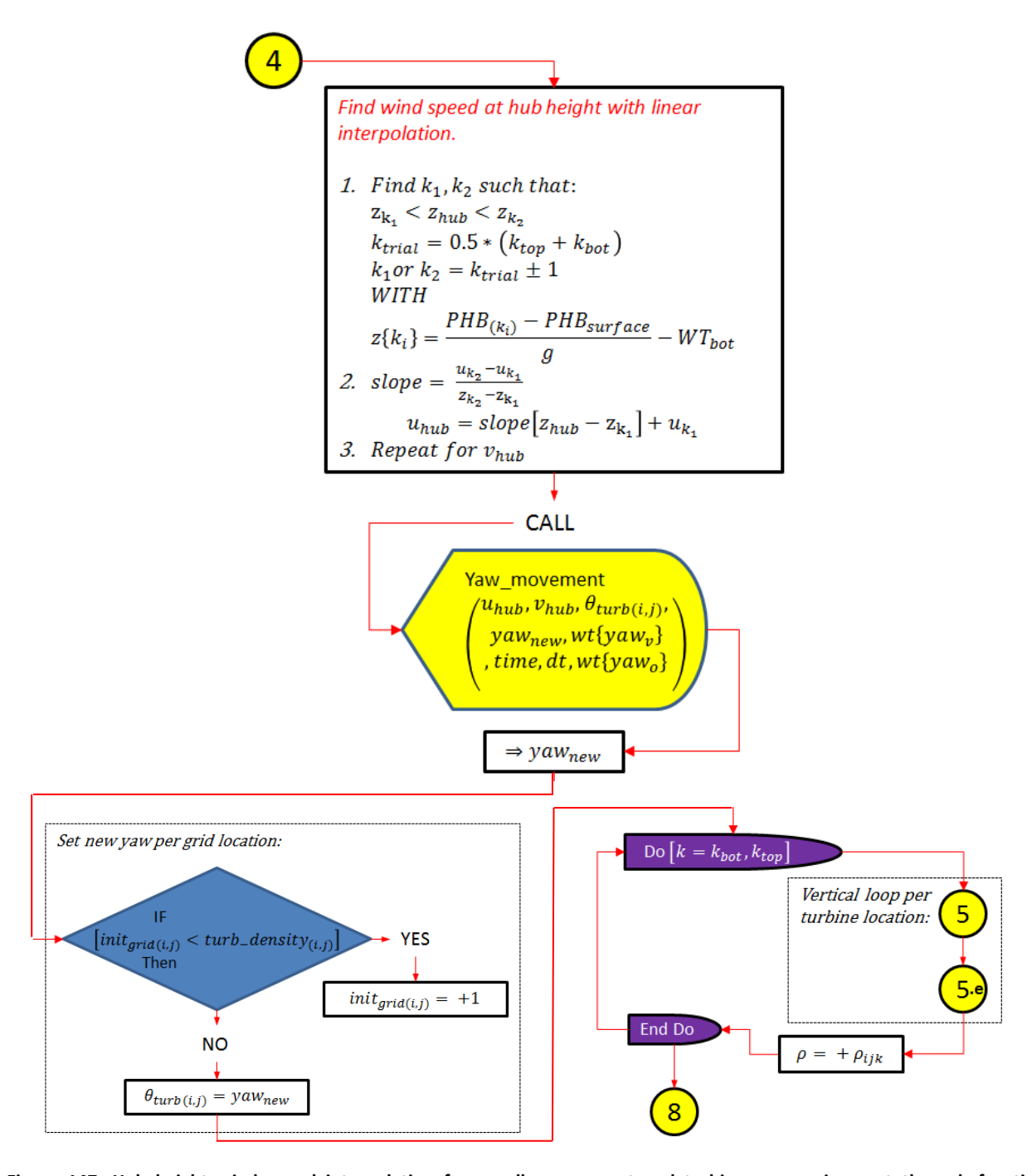


Figure 147: Hub height wind speed interpolation for nacelle movement and turbine yaw assignment through function Yaw_movement, and air density reading

A.M. Striedinger P.

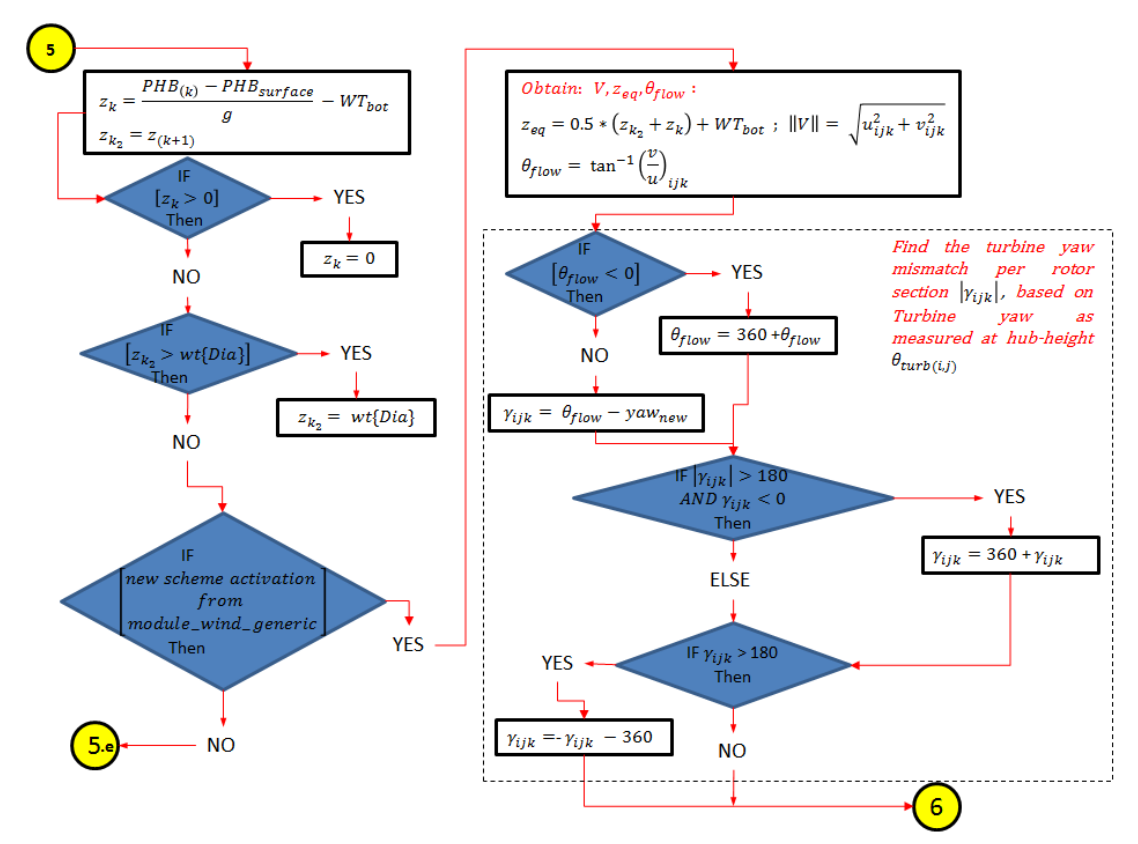


Figure 148: Section to correct turbine nacelle orientation

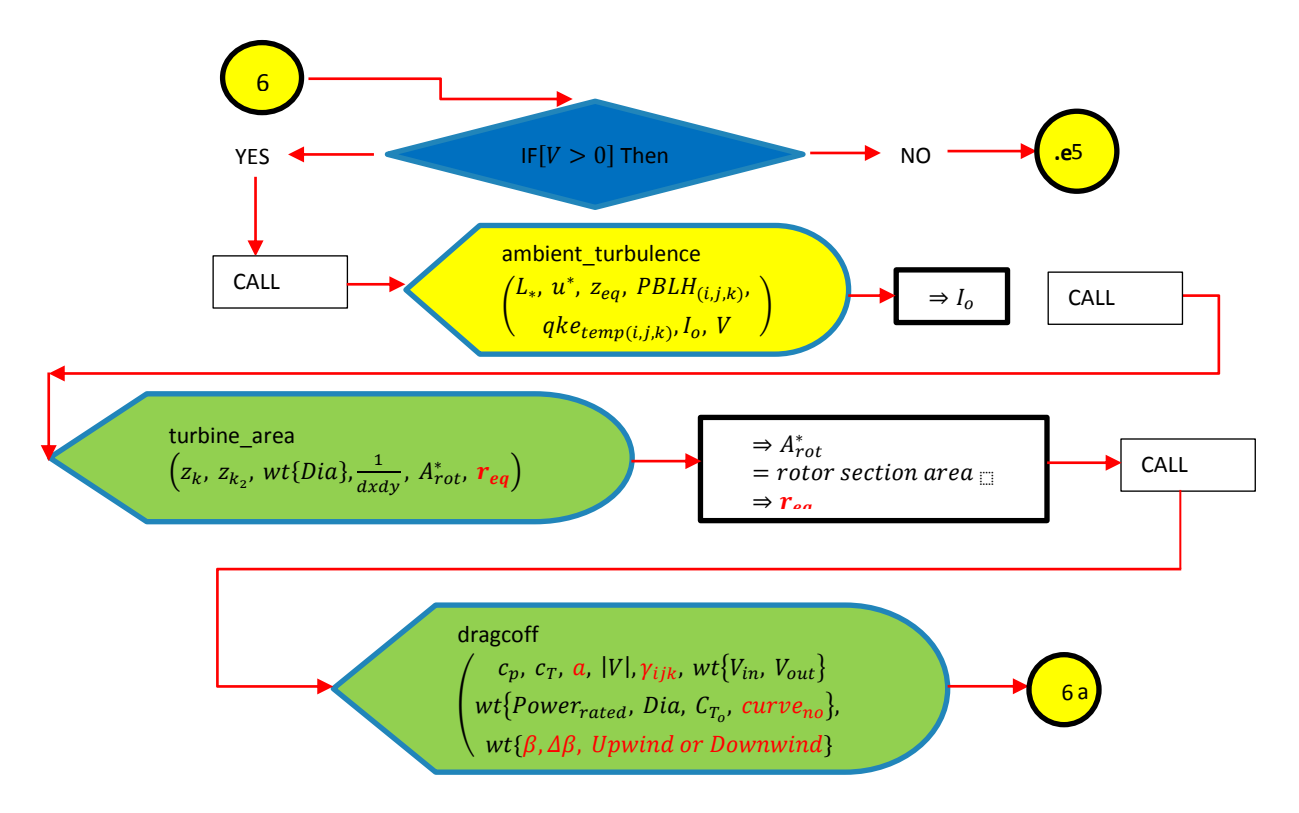


Figure 149: Final section to calculate ambient turbulence, and turbine performance coefficients

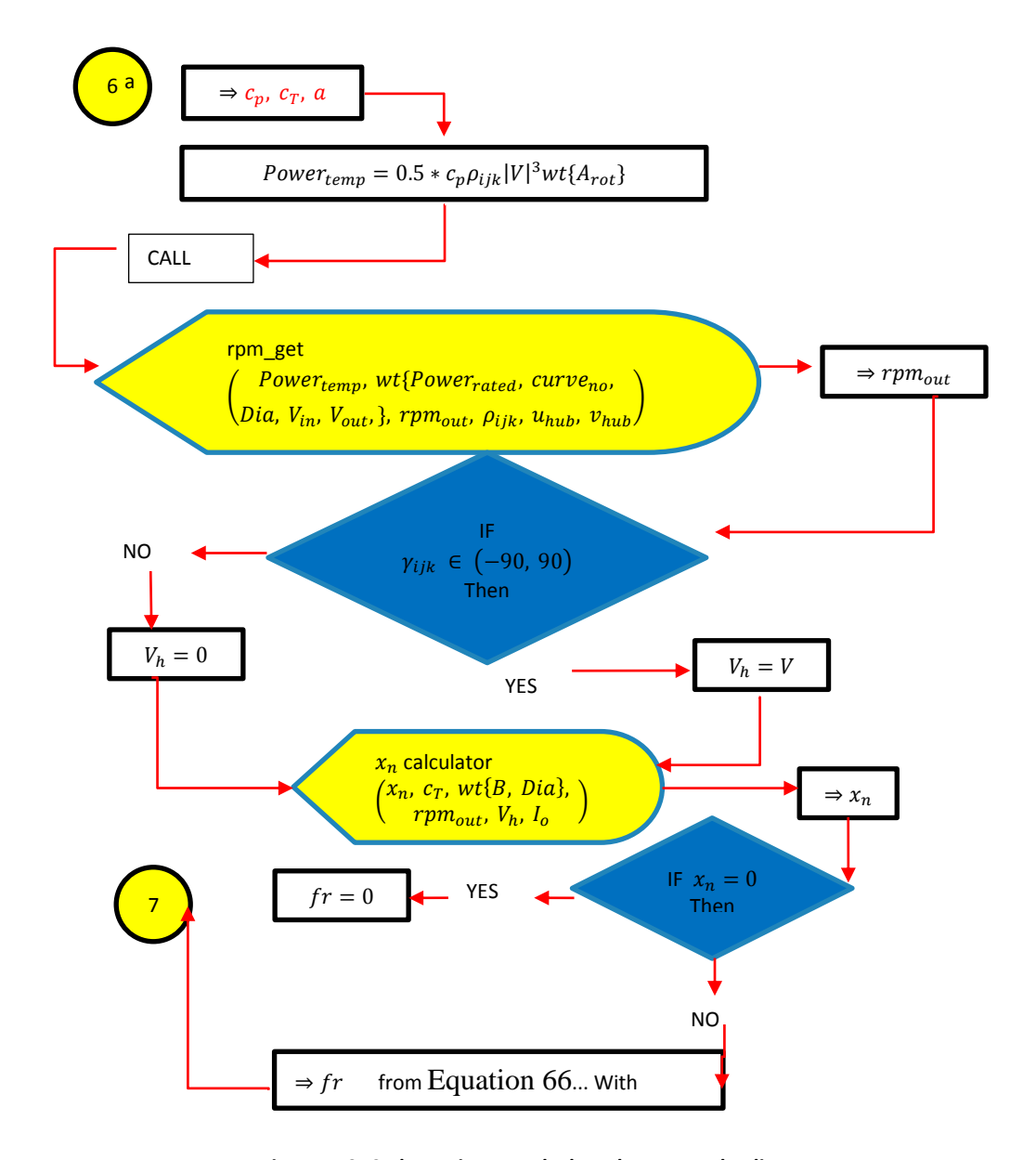


Figure 150: Code section to calculate the near wake distances

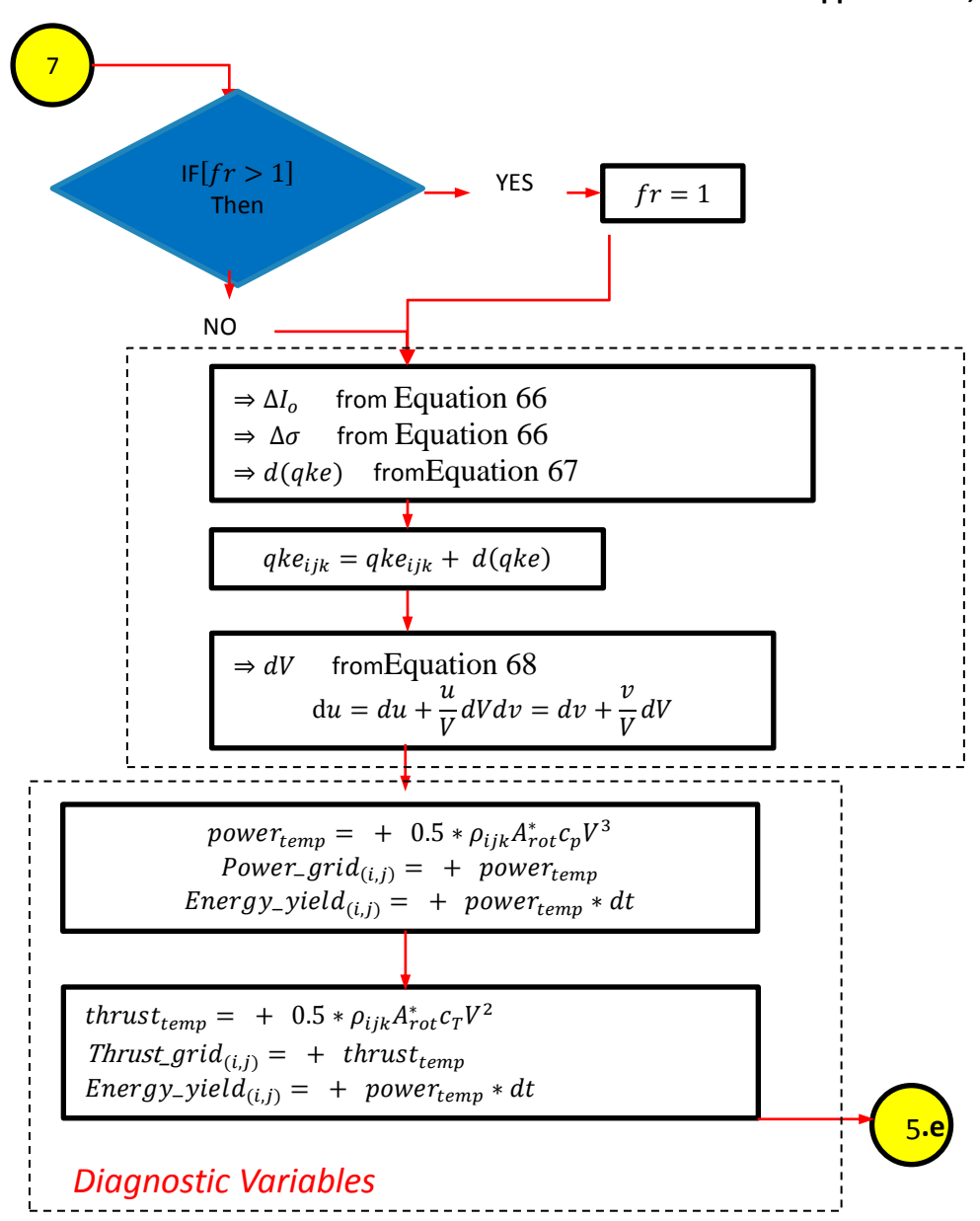


Figure 151: Code section for added turbulence intensity

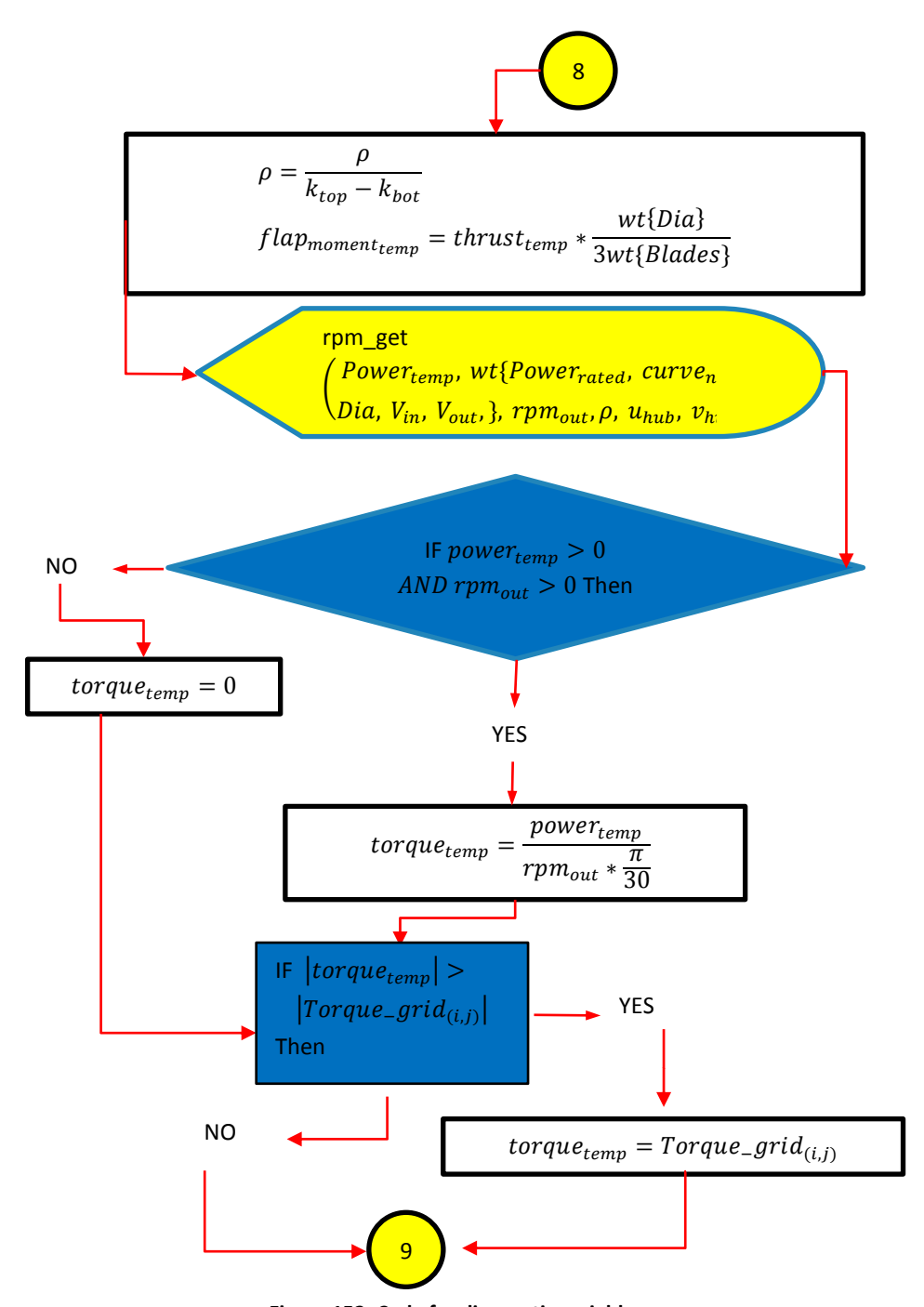


Figure 152: Code for diagnostic variables

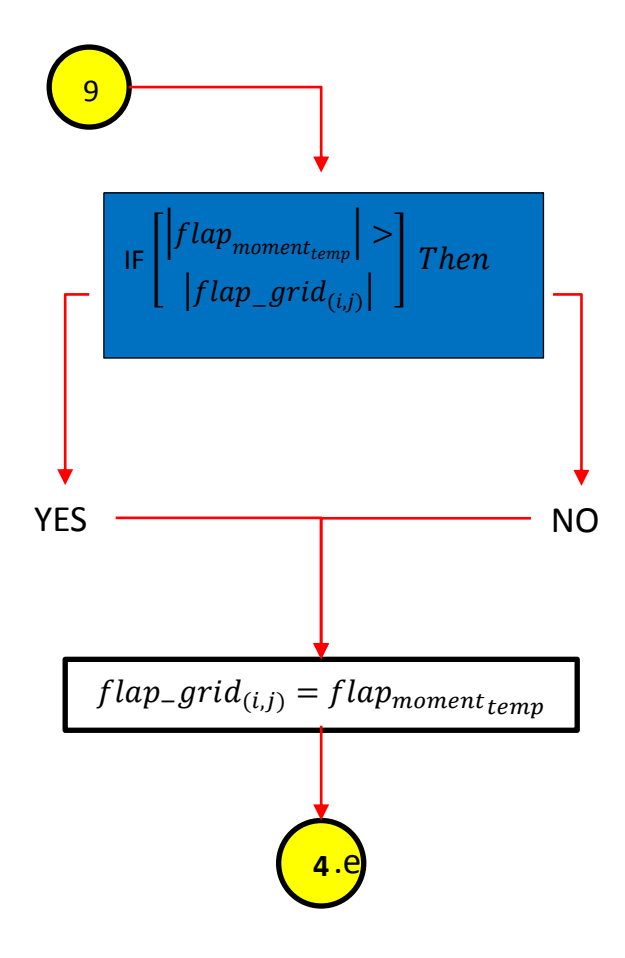


Figure 153: Final code to yield the average flapping moment

Bibliography

- [1] J. Manwell, J. Mcgowan and A. Rogers, Wind Energy Explained, Wiley, 2009.
- [2] C. Rindt, J. v. Berkel, G. Boxem, M. Creatore, W. v. Helden, E. hensen, J. v. Oijen and R. C. v. Zolingen, "General Introduction," in Renewable Energy Sources 4P510 Course, Department of Mechanical Engineering / Eindhoven University of Technology, 2011,
- [3] G. van Bussel and W. Bierbooms, Course Offshore wind farm design OE 5662. Module 4, Offshore Wind Climate, Delft: Faculty of Aerospace Engineering / Delft University of Technology, 2004.
- [4] D. W. Keith, J. F. DeCarolis, D. C. Denkenberger, D. H. Lenschow, S. L. Malyshev, S. Pacala and P. J. Rasch, "The influence of large-scale wind power on global climate," Proceedings of the national academy of sciences of the United States of America, vol. 101, no. 46, pp. 16115-16120, 2004.
- [5] D. B. Barrie and D. Kirk-Davidoff, "Weather response to a large wind turbine array," Atmos. Chem. Phys, vol. 10, pp. 769-775,
- [6] H. Lettau, "Note on aerodynamic roughness-parameter estimation on the basis of roughness-element description," Research and Development Technical Report', p. 163, 1969.
- [7] R. Macdonald, R. Griffiths and D. Hall, "An improved method for the estimation of surface roughness of obstacle arrays," Atmospheric environment, vol. 32, no. 11, pp. 1857-1864, 1998.
- [8] S. Baidya Roy, "Simulating impacts of wind farms on local hydrometeorology," Journal of Wind Engineering and Industrial Aerodynamics, vol. 99, no. 44, pp. 491-498, 2011.
- [9] M. Brower, B. HW, S. B and E. DL, "4.2 MESO-SCALE MODELING AS A TOOL FOR WIND RESOURCE ASSESSMENT AND MAPPING," in 14 th Conference on Applied Climatology, 2004.
- [10] A. Adams and D. Keith, "Wind energy and climate: Modeling the atmospheric impacts of wind energy turbines," in AUG Fall Meeting Abstracts, 2007, p. 08.
- [11] U. Blahak, B. Goretzki and J. Meis, "A simple parameterization of drag forces induced by large wind farms for numerical weather prediction models," in Proc. European Wind Energy Conf. and Exhibition 2010, 2010.
- [12] A. C. Fitch, J. B. Olson, J. K. Lundquist, J. Dudhia, A. K. Gupta, J. Michalakes and I. Barstad, "Local and Meso-scale Impacts of Wind Farms as Parameterized in a Meso-scale NWP Model," Monthly Weather Review-Boston, vol. 140, no. 9, p. 3017, 2012.
- [13] B. Lange, S. Larsen, J. Hoistrup and R. Barthelmie, "Importance of thermal effects and sea surface roughness for offshore wind resource assessment," Journal of wind engineering and industrial aerodynamics, vol. 92, no. 11, pp. 959-988, 2004.
- [14] M. Motta, R. Barthelmie and P. Volund, "The influence of non-logarithmic wind speed profiles on potential power output at Danish offshore sites," Wind Energy, vol. 8, no. 2, pp. 219-236, 2005.
- [15] J. Summer and C. Masson, "Influence of atmospheric stability on wind turbine power performance curves," Journal of solar energy engineering, vol. 128, no. 14, pp. 531-538, 2006.
- [16] A. Sathe and W. Bierbooms, "Influence of different wind profiles due to varying atmospheric stability on the fatigue life of wind turbines," Journal of Physics: Conference Series, vol. 75, no. 1, p. 012056, 2007.
- [17] Stefan, Ivanel, "Numerical Computations of Wind Turbine Wakes," Elforsk, Stockholm, 2009.
- [18] M. Calaf, C. Meneveau and J. Meyers, "Large eddy simulation study of fully developed wind-turbine array boundary layers," Physics of Fluids, vol. 22, p. 015110, 2010.
- [19] J. Meyers and C. Meneveau, "Optimal turbine spacing in fully developed wind farm boundary layers," Wind Energy, vol. 15, no. 2, pp. 305-317, 2011.
- [20] R. B. Cal, J. Lebrón, L. Castillo, H. S. Kang and C. Meneveau, "Experimental study of the horizontally averaged flow structure in a model wind-turbine array boundary layer," Journal of Renewable and Sustainable Energy, vol. 2, p. 013106, 2010.
- [21] H. Lu and F. Porté-Agel, "Large-eddy simulation of a very large wind farm in a stable atmospheric boundary layer," Physics of Fluids, vol. 23, p. 065101, 2011.
- [22] Y.-T. Wu and F. Porté-Amgel, "Large-eddy simulation of wind-turbine wakes: evaluation of turbine parametrisations," Boundary-layer meteorology, vol. 138, no. 3, pp. 345-366, 2011.
- [23] B. Sanderse, S. van der Pijl and B. Koren, "Review of computational fluid dynamics for wind turbine wake aerodynamics," Wind

- Energy, vol. 14, no. 7, pp. 799-819, 2011.
- [24] J. Mann, "Wind Field Simulation," Probabilistic engineering mechanics, vol. 13, no. 4, pp. 269-282, 1998.
- [25] B. A, "Large-eddy simulation of atmospheric flow over complex terrain.," PhD. Thesis, Technical University of Denmark, 2006.
- [26] L. Vermer and J. C. A. Sorensen, "Wind turbine wake aerodynamics," Progress in aerospace sciences, vol. 39, no. 6, pp. 467-510, 2003.
- [27] R. B. Stull, Meteorology for Scientists and Engineers, Brooks/Cole, 2000.
- [28] S. Emeis, Wind Energy Meteorology. Atmospheric Physics of Wind Power Generation, Springer, 2013.
- [29] "Lintas Zona Baca," [Online]. Available: http://lintaszonabaca.blogspot.nl/2011/04/macam-macam-lapisan-atmosfer.html.
- [30] P. E. J.W. Wagnaar, "Measurements of Wind, Wave and Currents at the Offshore Wind Farm Egmond aan Zee," Energy Research Center of the Netherlands, 2009.
- [31] D. B. Kirk-Davidoff and D. W. Keith, "On the Climate Impact of Surface Roughness Anomalies," Journal of the Atmospheric Sciences, vol. 65, no. 7, pp. 2215-2234, 2008.
- [32] J. Wieringa, "Updating the Davenport roughness classification," Journal of Wind Engineering and Industrial Aerodynamics, vol. 41, no. 1-3, pp. 357 -- 368, 1992.
- [33] R. Barthelmie, S. Pryor, S. Frandsen and S. E. Larsen, "Analytical modelling of large wind farm clusters," in *The science of making* torque from wind, Delft, The Netherlands, 2004.
- [34] A. M. Society, "Meteorology Glossary," American Meteorology Scociety, 25 April 2012. [Online]. [Accessed 2013].
- [35] A. Van Wijk, A. Beljaars, A. Holtslag and W. Turkenburg, "Evaluation of stability corrections in wind speed profiles over the North Sea," Journal of Wind Engineering and Industrial Aerodynamics, vol. 33, no. 3, pp. 551--566, 1990.
- [36] A. Peña and S.-E. Gryning, "Charnock's Roughness Length Model and Non-dimensional Wind Profiles Over the Sea," Boundary Layer Meteorology, vol. 128, no. 2, pp. 191-203, 2008.
- [37] International Electrotechnical Commission, "IEC 61400-1: Wind turbines Part 1: Design requirements," IEC, 2005.
- [38] H. Zhang, J. Chen and S.-U. Park, "Turbulence structure in unstable conditions over various surfaces," Boundary-layer meteorology, vol. 100, no. 2, pp. 243--261, 2001.
- [39] R. B. Stull, "Boundary Layers," in Meteorology for Scientists and Engineers, 2nd ed., Cengage Learning, 2000, pp. 66-89.
- [40] F. Nieuwstadt, "The steady-state height and resistance laws of the nocturnal boundary layer: Theory compared with Cabauw observations," Boundary-Layer Meteorology, vol. 20, no. 1, pp. 3-17, 1981.
- [41] M. O. Hansen, Aerodynamics of Wind Turbines, Earthscan, 2008.
- [42] Vestas Wind sYSTEMS, "General Specification V112-3.0 MW 50.60 Hz. Document no :0011-9181 V05," Vestas , Randers SV. Denmark, 2011.
- [43] P. J. Moriarty and A. C. Hansen, AeroDyn theory manual, Golden, Colorado, USA: National Renewable Energy Laboratory, 2005.
- [44] S. B., "Aerodynamics of wind turbine wakes. literature review," Energy Research Center of the Netherlands, 2009.
- [45] J. Marshal L. Huhl, "A New Empirical Relationship between Thrust Coefficient and Induction Factor for the Turbulent Windmill State," National Renewable Energy Laboratory, Golden, Colorado, 2005.
- [46] O. Rathmaan, "Wind farm Wake-effect model in WAsP8," VEA/ Win Power Meteorology, 2004.
- [47] P. Vermeulen, "An experimental analysis of wind turbine wakes," in 3rd International Symposium on Wind Energy Systems, 1980.
- [48] J. Højstrup, "Spectral cpherence in wind turbine wakes," Journal of Wind Engineering and Industrial Aerodynamics, vol. 80, pp. 137-146, 1999.
- [49] A. Crespo, J. Hernández and S. Frandsen, "Survay of modelling methods for wind turbine wakes and wind farms," Wind Energy, vol. 2, pp. 1-24, 1999.
- [50] T. G. Smith D, "Further analysis of turbine wake development and interaction data," in Proceedings of the 13th BWEA Wind Energy Conference, Swansea UK, 1991.
- [51] J. Sørensen, S. W.Z and R. Mikkelsen, "Wall Correction Model for Wind Tunnels with Open Test Section," American Institute of Aeronautics and Astronautics, vol. 44, no. 8, pp. 1890-1894, 2006.
- [52] G. H, "Airplane Propellers," in Aerodynamic Theory, New York, Durand, W. F., Dover, 1935, pp. 251-268.
- [53] C. Meneveau, "Wind turbine array fluid dynamics: measurements and modelling issues," in Cornell workshop on large-scale wind generated power, Cornell University, Ithaca, New York, 2009.
- [54] W. Hanns, Wind turbine aerodynamics in yaw: unravelling the measured rotor wake, Delft: Delft Univerity of Technology, 2011.
- [55] C. L. Archer, M. Sina and L. Sang, "Quatifying the sensitivity of wind farm performance to array layout options using large-eddy

- simulation," Geophysical Research Letters, vol. 40, no. 18, pp. 4963-4970, 2013.
- [56] M. J. Churchfield and e. al., "A large-eddy simulation of wind-plant aerodynamics," in Proceedings 50th AIAA Aerospace Science Meeting including the New Horizons Forum and Aerospace Exposition, 2012.
- [57] T. Burton, N. Jenkins, D. Sharpe and E. Bossanyi, Wind Energy Handbook, Wiley, 2011.
- [58] S. T. Frandsen, Turbulence and turbulence-generated structural loading in wind turbine clusters, Riso National Laboratory,
- [59] L. P. Chamorro and F. Porté-Agel. "A Wind-Tunnel Investigation of Wind-Turbine Wakes: Boundary-Laver Turbulence Effects." Boundary Layer Meteorology, vol. 132, no. 1, pp. 129--149, 2009.
- [60] P. Rèthore, B. Martinez, D. Cavar, F. Zahle, J. Berg, N. Sorensen, M. Kelly and A. Bechmann, "Comparison of OpenFoam and EllipSys for modelling the wind resources in complex terrain," in EWEA: Europe's Premier Wind Energy Event, Copenhagen,
- [61] C. Hasager, H. P. Madsen, P. Réthoré, L. Faiella, D. Cabezon, G. Giebel, J. Schepers and D. Luga, "Design Tools for Offshore wind farm Clusters," in European Research Alliance.
- [62] P. Volker, J. Badger, A. Hahman and S. Ooo, "Wind Farm parameterization in the meso-scale model WRF," DTU Wind Energy,
- [63] T. Hamill, "Introduction to Numerical Weather Predition and Ensemble Weather Forecasting," in International Hydrological Ensemble Prediction Experiment (HEPEX) Workshop, 2004.
- [64] J. Marchall, C. Hill, L. Perelman and A. Adroft, "Hydrostatic, quasi-hydrostatic, and nonhydrostatic ocean modeling," Journal of Geophysical Research, vol. 102, no. 03, pp. 5733-5752, 1997.
- [65] National Center for Geographic Information and Analysis, "NCGIA.ucsb.edu," [Online]. Available: http://www.ncgia.ucsb.edu/education/curricula/giscc/units/u014/tables/table01.html.
- [66] F. H. Harlow and J. E. Welch, "Numerical calculation of time-dependent viscous incompressible flow or fluid with free surface," Physics of fluids, vol. 8, p. 2182, 1965.
- [67] A. Simmons, S. Uppala and K. S. Dee D, "ERA-Interim: New ECMWF reanalysis products from 1989 onwards," ECMWF Newsletter, vol. 110, pp. 26-35, 2006.
- [68] M. Nakanishi and N. H, "Development of an improved turbulence closure model for the atmospheric boundary layer," Journal of the Meteorological Society of Japan, vol. 87, no. 5, pp. 895--912, 2009.
- [69] G. o. t. UK, "Met Office," [Online]. Available: http://www.metoffice.gov.uk/climate/uk/so/print.html. [Accessed 2013].
- [70] I. Svetlozar, Array Losses and Array Benefits at Offshore Wind Parks, Delft: Delft University of Technology, 2014.
- [71] G. C. Larsen, H. A. Madsen, K. Thomsen and T. J. Larsen, "Wake Meandering: A Pragmnatic Approach," WIND ENERGY, vol. 11, no. 4, pp. 377--395, 2008.
- [72] L. S. C. A. Sciences, "Lyndon State College Meteorological Department Bookmarks and Links," [Online]. Available: http://apollo.lsc.vsc.edu/classes/met455/notes/section4/1.html.
- [73] Y. Lisan, X. Jin and R. A. Welles, "Multidecade Global Flux Datasets from the Objectively Analyzed Air-sea Fluxes (OAFlux) Project: Latent and Sensible Heat Fluxes, Ocean Evaporation, and Related Surface Meteorological Variables," OAFlux Project, 2008.
- [74] N. C. O. a. M. (. program, "WHOI OAFlux project," [Online]. Available: http://oaflux.whoi.edu/data.html.
- [75] J. Dudhia, "UCAR," [Online]. Available: http://www.mmm.ucar.edu/wrf/users/tutorial/200807/WRF_Physics_Dudhia.pdf.
- [76] W. Langhans, J. Schmidli and B. Szintai, "A Smagorinsky-Lilly turbulence closure for COSMO-LES: Implementation and comparison to ARPS," COSMO newsletter, vol. 12, pp. 20-31, 2012.
- [77] T. K. Chow, "American Meteorological Society," 1 August 2010. [Online]. Available: http://www.ametsoc.org/Meet/fainst/2010shortcoursewindenergypresentations/Lecture5_Chow_Wind_Energy_AMS_SC.pdf.
- [78] K. Carrol, W. Capehart and M. Hjelmflet, "High Resolution Modeling in WRF to Determine the Impact of Terrain Resolution on Low-Level Winds in Complex Terrain," Institute of Atmospheric Sciences, South Dakota School of Mines and Technology.
- [79] M. Buzzi, "Challenges in operational numerical weather prediction at high resolution in complex terrain," Eidgenossische Technische Hochschule ETH Zurich, Zurich, 2008.
- [80] S. F. M. N. R.J. Barthelmie, "Modelling and Measurements of Power Losses and Turbulence Intensity in Wind Turbines Wakes at Middelgrunden Offshore Wind Farm," Wind Energy, pp. 517 - 528, 2007.
- [81] K. S. Hansen, "Middelgrunden -stide documentation," Unpusblished Unpublished Unpublished. [Online]. Available: http://130.226.56.150/extra/web docs/midgrund/midgrund.pdf. [Accessed 2014].
- [82] P. v. d. W. A. Curvers, "OWEZ Wind Farm Efficiency," ECN, 2009.

- [83] A. Boilley and J.-F. Mahfouf, "Assimilation of low-level wind in a high-resolution meso-scale using the back and forth mudging algorithm," Tellus A, vol. 64, 2012.
- [84] I. Stefan, J. Sorensen and D. Henningson, "Numerical computations of wind turbine wakes," Wind Energy, pp. 259-263, 2007.
- [85] M. R. Magdalena and M. Z. Jacobson, "New Parameterization ofr Wind Farm Effects on the Atmosphere," in AWEA WindPower, Huston, 2008.
- [86] S. M. Magdalena RV and M. Z. Jacobson, "Investigating the effect of large wind farms on energy in the atmosphere," Energies, vol. 2, no. 4, pp. 816-838, 2009.
- [87] M. O. L. Hansen, J. N. Sorensen, S. Voutsinas, N. Sorensen and H. Madsen, "State of the art in wind turbine aerodynamics and aeroelasticity," Progress in aerospace sciences, vol. 42, no. 4, pp. 285 --330, 2006.
- [88] A. Holtslag, "Estimates of diabatic wind speed profiles from near-surface weather observations," Boundary-Layer Metorology, vol. 29, no. 3, pp. 225-250, 1984.
- [89] A. Blackadar and H. Tennekes, "Asymptotic Similarity in Neutral Barotropic Planetary Boundary Layers," Journal of Atmospheric Sciences, vol. 25, no. 6, pp. 1015--1020, 1968.
- [90] R. Van Rooij and W. Timmer, "Roughness sensitivity considerations for thick rotor blade airfoils," ASME JOURNAL OF SOLAR ENERGY ENGINEERING, vol. 125, no. 4, pp. 468--478, 2003.
- [91] J. W. Sumner and M. C. Chirsophe, "CFD in wind energy: the virtual, multiscale wind tunnel," Energies, vol. 3, no. 5, pp. 989--1013, 2010.
- [92] S. D, "Multiple wake measurements and analysis," National Power Technology and Environmental Center, Leatherhead, UK.

List of Symbols

Greek Symbols

φ	Blade angle of inflow Geo-potential	[deg] $[m^2/s^2]$
φ	Blade angle of attack	[//t /s] [deg]
α	Inverse density of air or specific volume	$[m^3/kg]$
Ψ	Azimuth angle	[/// /// [deg]
β	Rotor tilt angle	[deg]
γ	Yaw mismatch	[deg]
k,λ	Shape and scale factors for the Weibull distribution	[-], [m/s]
Ω_{earth}	Earth rotational speed	[rad/s]
Ω	Turbine rotation	[<i>rad/s</i>], rpm
φ	Latitude	[deg°, min, sec]
η	Eta-levels in	[-]
μ_d	Hydrostatic pressure ration in a dry atmosphere.	[-]
ρ	Air density or gas-mixture density	$[kg/m^3]$
ρ_d	Dry air density	$[kg/m^3]$
τ	stresses	[kg]
		$\left \frac{1}{ms^2}\right $
$arepsilon_t$	Eddy diffusivity	$[m^2/s]$
α_c	Charnock's constant	[-]
κ	von Karman constant	[-]
ψ_m	Stable gradient function from similarity theory	[-]
σ_u , σ_v , σ_w	Standard deviations of wind speed in a 10 min series.	[m/s]
σ_p	Standard deviations of active power in 10 min series	MW, kW, W
σ_o	Total standard deviation of free stream wind speed in a 10 min series	[m/s]
σ_T	Change in σ_o from behind the rotor to the end of the near-wake, for	[m/s]
	steady uniform and steady inflow conditions	
$\sigma_{(v^3)}$	Standard fluctuations of V_o^3	[m/s]
θ	Potential temperature	K
θ	Blade twist angle	[deg]
$ heta_{turb}$	Turbine orientation at a given time	[deg]
$ heta_{flow}$	Wind speed direction in front of each turbine at a given time	[deg]
ξ	Downstream rotor distance from a single turbine	[-]
δ	Wind speed bin = 1	[m/s]

Wind Speed Symbols

U_g	Geostrophic wind	[m/s]
U_{10}	10 m wind speed	[m/s]
u^*	Friction velocity	[m/s]

$u_{(z)}$	Horizontal wind speed from similarity theory	[m/s]
V	Wind velocity for turbine parameterization	[m/s]
U, V, W	Corrected wind speed components for momentum equations in WRF	[m/s]
$V_{\langle in \rangle}, V_{\langle out \rangle}$	Cut-in ,and cut-out wind speeds of each turbine	[m/s]
$V_{\langle rated \rangle}$	Rated wind speed of each turbine	[m/s]
V_{res}	Relative wind speed of the following a turbine blade	[m/s]
V_{w}	Velocity in the wake	[m/s]
V_n	Velocity near wind tunnel wall	[m/s]
V_{∞} ,	Velocity in the free stream	[m/s]
V_o	Free stream velocity in a wind tunnel	[m/s]
$V_{\infty \langle WRF \rangle}$	Frees stream wind speed from WRF simulations, at met last grid location	[m/s]
$V_{\infty \langle data \rangle}$	Frees stream wind speed derived from the forecast data set	[m/s]
V_{hub}	Wind speed at hub height	[m/s]
u, v, w	Cartesian wind speed components	[m/s]
u', v', w'	Turbulent velocities	[m/s]

Turbulence and Stability Symbols

I_o	Ambient turbulence intensity	[-]
I_u	Turbulent intensity in the x direction	[-]
$I_{(u,x)}$	Turbulence intensity behind the turbine, in the x direction as a function of distance: Frandsen's model	[-]
I_{ref}	Reference turbulence intensity from IEC standard	[-]
I_{0na} I_{opw}	Turbulence intensity calculated from Nacelle wind speed measurements Turbulence Intensity using Jorgensen method	[-] [-]
I_{0met}	Turbulence intensity measurements from MIDD met mast (1997-1999)	[-]
I_p	Added turbulence intensity per rotor section at a given time and a given time-step dt	[-]
TI	Turbulence intensity from models	[-]
$TI_{metmast}$	Turbulence Intensity at MIDD met mast location, as derived from WRF	[-]
TI_{pw}	Turbulence intensity derived from South and North WTs from forecast data set	[-]
TKE	Flow turbulent kinetic energy	$[m^2/s^2]$
gke,	Twice TKE from MYNN scheme in WRF	$[m^2/s^2]$
x_n	Near-wake distance or length	[m]
z_o	Aerodynamic or surface roughness	[m]
$\overset{\circ}{h_*}$	Planetary boundary layer height	[m]
L_*	Monin-Obukhov Length	[<i>m</i>]

Thermodynamic Symbols

T	Air temperature	°C, K
∂T	Lapse rate	°C °C
$\overline{\partial z}$		\overline{m} ' \overline{km}
T_{v}	Virtual temperature	K
$T_{v}{}'$	Turbulent part of Virtual temperature	K
H_{sf}	Upward surface-heat flux	$[W/m^2]$

Turbine related Symbols

a a' k F P	Axial induction factor for BEM Tangential induction factor for BEM Jensen's wake constant Combined tip and hub loss factor Pressure Power	[-] [-] [-] Pa MW, kW, W
P, P _{avg}	Wind farm power efficiencies	[-]
E, E_{c_p}, E_v	Phase errors: Power, power coefficient, and free stream velocity.	[-]
P_{∞}	Pressure in the free stream	Pa
P^+, P^-	Pressure differences on the rotor area	Pa
p_{nw}	Pressure near wind tunnel walls, in the wake	Pa
C_p , C_T	Turbine power and thrust coefficients	[-]
$C_{T(o)}$	Standing thrust coefficient from Fitch Scheme	[-]
C_{pi}	Transition function of the power coefficient. Formula in WRF	[-]
A_{rot}	Turbine rotor area	$[m^2]$
A_i	Half area of rotor section inside a grid cell	$[m^2]$
D_o , Dia	Turbine rotor diameter	[m]
R	Turbine rotor radius	[m]
s_1, s_2	Transverse and in-line turbine spacing in a wind farm	[-]
V_{yaw}	Yawing speed of turbine. From manufacturers data	[deg/s]
λ_{tip}	Tip speed ratio	[-]

WRF Symbols

ṁ	Mass flow	[kg/s]
m_x , m_y	Map scale factor for spherical projections in WRF	[-]
x	Function(x) for similarity theory	[-]
x	Distance in the horizon	[m], [km]
$\Delta x, \Delta y, \Delta z$	Grid dell size in WRF	[m]
i, j, k	Numerical grid locations in WRF	[-]
$N_{tc\langle i,j\rangle}$	Number of turbines per grid location in WRF	[-]

f_c	Coriolis factor	$[s^{-1}]$
C_r	Maximum Courant number for advections	[-]
g	Gravitational acceleration = 9.8	$[m/s^2]$

Other Symbols

Z_i	Capping inversion height	[m]
z_R	Reference height	[m]
dt	Small time-step	
fr	Time fraction factor for turbine parameterization scheme for given timestep dt	
$F_{(v,TI)}$	Conversion factor the simplification, and calculation of TI_{pw}	[-]
¥	Volume	$[m^3]$
$E_{deformation} \\$	Energy rate spent in deforming the fluid	watts
$G_{(v,\sigma_v)}$	Factor G used for the simplification and calculation of TI_{pw}	[-]
l	Prandtl mixing length	[m]
$r_p, r_o,$	Geometrical centroids for rotor section analysis	[m]
r_{up}, r_{down}		